universität
innsbruck

Fakultät für Technische
Wissenschaften

Numerical modeling approaches to the oscillation roller-subsoil interaction problem

Dipl.-Ing. Ivan Paulmichl

Innsbruck, October 2019

Dissertation

eingereicht an der Leopold-Franzens-Universität Innsbruck,
Fakultät für Technische Wissenschaften,
zur Erlangung des akademischen Grades

Doktor der Technischen Wissenschaften

Erster Beurteiler: Univ.Prof. Dipl.-Ing. Dr.techn. Christoph Adam
Universität Innsbruck
Institut für Grundlagen der Technischen Wissenschaften
Arbeitsbereich für Angewandte Mechanik

Zweiter Beurteiler: Priv.Doz. Dipl.-Ing. Dr.techn. Fritz Kopf
Technische Universität Wien
Institut für Geotechnik, Forschungsbereich Grundbau, Boden- und Felsmechanik
VCE Vienna Consulting Engineers ZT GmbH

Hauptbetreuer: Univ.Prof. Dipl.-Ing. Dr.techn. Christoph Adam
Universität Innsbruck
Institut für Grundlagen der Technischen Wissenschaften
Arbeitsbereich für Angewandte Mechanik

Zweiter Betreuer: Univ.Prof. Dipl.-Ing. Dr.techn. Dietmar Adam
Technische Universität Wien
Institut für Geotechnik
Forschungsbereich Grundbau, Boden- und Felsmechanik

Dritter Betreuer: Univ.-Prof. i.R. Dr. Dr. h.c. Michael Oberguggenberger
Universität Innsbruck
Institut für Grundlagen der Technischen Wissenschaften
Arbeitsbereich für Technische Mathematik

Acknowledgment

The financial support granted by the German manufacturer of compaction equipment HAMM AG, D-95643 Tirschenreuth, Hammstraße 1, made the research on oscillation rollers possible and is gratefully acknowledged.

Kurzfassung

Die *Bodenverdichtung* stellt bei der Herstellung verschiedenster Ingenieurbauwerke eine entscheidende und gleichzeitig kritische Bauphase dar. Denn die Qualität von Auffüllungen im Zuge von Gründungsarbeiten im Hallen- und Industriebau sowie bei der Herstellung von Bodenauswechslungen, Dämmen und Tragschichten im Straßen-, Eisenbahn- und Flughafenbau hängt vom Verfüllmaterial und insbesondere vom Einbauvorgang ab. Dynamische *Walzen* sind mittlerweile zum bevorzugten Gerät für die *oberflächennahe Verdichtung* geworden, um zukünftige Schäden an Bauwerken, die mit einem lageweisen hergestellten Erdbauwerk verbunden bzw. darauf gegründet sind, steigende Instandhaltungskosten und eine geringere Lebensdauer des jeweiligen Bauwerks zu vermeiden. Während die Verdichtungswirkung einer *statischen Walze* im Wesentlichen vom Eigengewicht der Maschine und gegebenenfalls von der Bandagengeometrie und -oberfläche bestimmt wird, lässt sich bei *dynamischen Walzen* die Effizienz der Untergrundverdichtung durch die dynamische Anregung der Bandage erhöhen.

In Abhängigkeit von der Art der Bandagenanregung lassen sich grundsätzlich zwei Typen von dynamischen Walzen unterscheiden, nämlich Vibrations- und Oszillationswalzen. In einer *Vibrationsbandage* erzeugt eine Unwuchtmasse, die in der Bandagenachse angeordnet und mit einer festgelegten Frequenz um die Achse rotiert, eine schnell wechselnde Aufwärts-Abwärts-Bewegung. Der Untergrund wird durch die von der Bandage ausgeübten, vorwiegend vertikal gerichteten Schläge verdichtet. In einer *Oszillationsbandage*, die Gegenstand der vorliegenden Arbeit ist, sind zwei Unwuchtmassen mit derselben Größe und Exzentrizität punktsymmetrisch zur Bandagenachse angeordnet, die synchron in die gleiche Richtung drehen. Die daraus resultierende wechselnde hochfrequente Vorwärts-Rückwärts-Rotation der Bandage (rotatorische Schwingung) wird der Fahrbewegung (rollende Bandage unter der statischen Achslast) überlagert. Infolge Reibung in der Kontaktfläche zwischen Bandage und Untergrund werden hauptsächlich dynamische Schubkräfte in den Boden übertragen, wodurch die Untergrundsteifigkeit erhöht wird.

Das Fehlen von Echtzeit-Informationen über den Verdichtungszustand kann sowohl zu einer Unter- als auch zu einer Überverdichtung und darüber hinaus zu einem erhöhten Verschleiß der Bandage von Oszillationswalzen führen. Daher ist eine sofortige Kontrolle der erzielten Verdichtung von besonderer Bedeutung. Ein umfassendes Qualitätsmanagementsystem erfordert eine kontinuierliche Kontrolle der Verdichtungsqualität im gesamten verdichteten Bereich, die nur durch arbeitsintegrierte Verfahren

erreicht werden kann. Die Überwachung der Bandagenschwingung wird seit über 40 Jahren bei der Walzenverdichtung eingesetzt, um eine sogenannte *Flächendeckende Dynamische Verdichtungskontrolle (FDVK)* zu realisieren. Die FDVK ist mittlerweile zur Standardtechnologie für die arbeitsintegrierte und kontinuierliche Beurteilung der mittels Vibrationswalzen erzielten Verdichtung geworden. Für Oszillationswalzen gab es jedoch bis vor kurzem kein ausgereiftes FDVK-System, obwohl bereits vor fast vier Jahrzehnten erste diesbezügliche Entwicklungsansätze erfolgten. Das vor wenigen Jahren vorwiegend auf Basis von Feldversuchen vorgeschlagene FDVK-System wurde weder durch analytische noch durch numerische Untersuchungen verifiziert. Die vorliegende Dissertation zielt daher darauf ab, diese Forschungslücke zu schließen, wobei zwei Modellierungsstrategien verfolgt werden, nämlich mechanische Modellierung und Finite-Elemente-Modellierung.

Das *mechanische Modell* des dynamischen Interaktionssystems Oszillationswalze-Untergrund ermöglicht die Simulation der Schwingungsantwort einer Oszillationsbandage mit geringem numerischen Aufwand. Der Verdichtungsprozess selbst wird nicht modelliert, es werden aber unterschiedliche Verdichtungsgrade durch Variation der Bodensteifigkeit berücksichtigt. Die Walze wird durch die Oszillationsbandage und ihre viskoelastische Verbindung zum Rahmen (Gummipuffer) repräsentiert. In der gewählten Modellierungsstrategie wird die Krümmung der Bodenoberfläche unterhalb der Bandage vorgegeben. Auf diese Weise kann auch die vertikale Bandagenschwingung simuliert werden. Das diskrete viskoelastische Untergrundmodell besteht aus einem vertikalen und einem horizontalen *Kelvin-Voigt* Element. Der Kontakt zwischen Bandage und Untergrund wird mittels *Coulomb*'schen Reibungsgesetz beschrieben. Somit kann die *Haftgleitbewegung* der Bandage simuliert werden. Die hochgradig nichtlinearen Bewegungsgleichungen dieses Drei-Freiheitsgrade-Modells werden getrennt für die *Haftphase* und die *Gleitphase* der Bewegung hergeleitet. Die detaillierte Untersuchung des Bewegungsverhaltens für einen ausgewählten Walzentyp zeigt, dass das vorgeschlagene Modell die in Feldversuchen gemessene Antwortcharakteristik einer mit dem Untergrund interagierenden Oszillationsbandage grundsätzlich widerspiegelt. Die Ergebnisse einer umfassenden Parameterstudie mit vier verschiedenen Oszillationswalzen bestätigen im Wesentlichen den Verdichtungsindikator für die betrachteten Oszillationswalzen in einer weiten Bandbreite der Bodensteifigkeit. Die ermittelten Anwendungsgrenzen dieses Wertes werden von den Geräteparametern und der Betriebsfrequenz deutlich beeinflusst.

Das vorgeschlagene *Finite-Elemente-Modell* ermöglicht erstmals die gleichzeitige numerische Berechnung des Bewegungsverhaltens und der Verdichtungswirkung einer Oszillationswalze im Zuge der oberflächennahen Verdichtung von nichtbindigen Böden. Im entwickelten zweidimensionalen Modell erfasst das hypoplastische Stoffgesetz mit intergranularen Dehnungen das nichtlineare Verhalten des Bodens unterhalb der Bandage. Auf die freie Bodenoberfläche wird eine "Schutzfolie" aufgebracht, um die numerische Stabilität der mittels der Finite-Elemente-Software *ABAQUS/Standard* durchgeführten Simulationen zu gewährleisten. Die berechneten Spannungen, Dehnungen und Änderungen der Porenziffer im potentiellen Verdichtungsbereich, die repräsentativ für die Verdichtungswirkung ist, sowie das Bewegungsverhalten der Bandage werden im Detail analysiert. Darüber hinaus werden berechnete dynamische Spannungskomponenten im Boden und Beschleunigungen im Bandagenzentrum mit Daten aus Feldversuchen verglichen. Es wird gezeigt, dass das entwickelte Finite-Elemente-Modell quali-

tativ und teilweise auch quantitativ die grundlegenden, in Feldversuchen beobachteten Antwortcharakteristika des Interaktionssystems Oszillationswalze-Untergrund vorhersagt. Die Ergebnisse einer umfassenden Sensitivitätsstudie bestätigen, dass die aus dem Bewegungsverhalten der Bandage abgeleiteten Größen grundsätzlich als Indikatoren für die FDVK mit Oszillationswalzen geeignet sind. Darüber hinaus zeigen die Ergebnisse eindrucksvoll, dass die Fahrgeschwindigkeit der Walze sowohl das Bewegungsverhalten der Bandage als auch die erzielbare Bodenverdichtung signifikant beeinflusst.

Abstract

Soil compaction is a fundamental and critical construction phase of a wide variety of engineering structures, since the quality of fills in foundation work of hall and industrial facilities, soil replacements, dam and base layers in road, railway and airport construction depends on the built-in material and in particular on the realization of earthwork. Dynamic *roller* compaction has become the common method for proper *near-surface compaction* to prevent future damage of constructions connected to layered earth structures, failure of long-term pavement performances and increasing maintenance costs. While a *static* roller uses only its weight to compact filled layers, a *dynamic* roller enhances the efficiency of subsurface compaction through dynamic excitation of the drum.

Depending on the drum excitation, two basic types of dynamic rollers do exist, i.e. vibratory rollers and oscillation rollers. In a *vibrating* drum a single unbalance mass, which is attached concentrically to the drum axis, generates a rapidly alternating upward-downward motion of the drum. The subgrade is compacted by the dynamic pressure applied by the drum. The drum of an *oscillation roller*, as considered in the present thesis, is equipped with two offset eccentric masses, which rotate synchronously in the same direction. The resulting alternating high-frequency forward-backward motion of the drum (oscillatory drum motion) is superposed with the translational roller motion (moving drum under the static axle load). Due to the frictional contact between drum and subsoil mainly dynamic shear forces are transmitted to the soil, which in turn increase the subgrade density, also known as *shear force compaction.*

The lack of real-time compaction information may lead to both under- and over-compaction and, moreover, to an increased wear of the drum of oscillation rollers. Thus, instant *compaction control* is of particular importance. A high-leveled quality management requires continuous control of the soil compaction in the entire compacted area, which can be achieved only by work-integrated methods. Roller vibration monitoring has been used for over 40 years during soil compaction to provide what is referred to as *Continuous Compaction Control (CCC).* CCC has become the standard technology for assessing work-integrated and continuously the achieved compaction by vibratory rollers. For oscillation rollers, however, until recently no mature CCC system did exist, although initial approaches to a CCC system were already proposed almost four decades ago. The recently developed CCC technique has neither been verified by analytical nor by numerical studies. The present doctoral thesis therefore aims to fill this gap by pursuing two modelling strategies, *lumped parameter modeling* and *Finite Element modeling*.

The proposed *lumped parameter model* of the interacting oscillation roller-subsoil system facilitates the response simulation of an oscillation drum with the least numerical effort. The compaction process itself is not captured, but different degrees of compaction are considered by varying the soil stiffness. The roller is represented by the oscillation drum and its viscoelastic connection to the roller frame. In the chosen modeling strategy, the curvature of the soil surface below the drum is prescribed. In this way, also the vertical drum acceleration can be computed. The discrete viscoelastic subsoil model consists of a vertical and a horizontal *Kelvin-Voigt* element. Contact between drum and soil surface is described by means of dry friction according to *Coulomb*'s law. As such, the *stick-slip* motion of the drum can be simulated. The highly nonlinear equations of motion of this three degrees-of-freedom model are derived separately for the *stick* and the *slip* phase of the motion. A detailed response study of one selected roller type shows that this model captures the fundamental response characteristics of the drum-subsoil interaction system observed in the field. The results of a comprehensive parametric study based on four different oscillation rollers essentially confirm the compaction indicator for the considered oscillation rollers in a wide range of soil stiffness. The found application limits of this value are clearly influenced by the device parameters and the operating oscillation frequency.

The presented *Finite Element model* allows for the first time the numerical prediction of both the dynamic response acceleration and the compaction effect of an oscillation roller during near-surface compaction of non-cohesive soils. In the developed plane-strain model, the intergranular strain enhanced hypoplastic constitutive model captures the nonlinear behavior of the soil below the drum. A “protective foil” is applied to the soil surface to ensure the numerical stability of the model solved with the Finite Element software suite *ABAQUS/Standard*. The derived stresses, strains, and change of the void ratio in the subsoil representative for the compaction effect as well as the dynamic response of the drum center are analyzed in detail. In addition, computed dynamic stress components in the soil and drum accelerations are compared with data recorded in field tests. It is shown that the developed model qualitatively and partially also quantitatively predicts the fundamental response characteristics of the interacting oscillation-subsoil system observed in field tests. The outcomes of a comprehensive sensitivity study confirm that the quantities derived from the drum response are basically suitable as indicators for CCC with oscillation rollers. Moreover, the results impressively demonstrate that the roller speed has a significant effect on both drum response and achievable soil compaction.

Contents

1 Introduction **1**
1.1 Soil compaction with dynamic rollers 1
1.2 Roller-integrated compaction control 2
1.3 Motivation 4
1.4 Modeling strategies 6
1.5 Fundamentals and content 7

2 Lumped parameter modeling **9**
2.1 Considered oscillation rollers 9
2.2 Mechanical model 11
2.2.1 Basic structure and operation mode of an oscillation roller 11
2.2.2 Representation of roller and subsoil 11
2.2.3 Modeling of excitation and loading 13
2.3 Governing equations 15
2.3.1 Kinematics 15
2.3.2 Dynamic substructuring 16
2.3.3 Equations of motion 19
2.3.4 Procedure of solution 21
2.4 Detailed response study for a specific roller 21
2.4.1 Pure rolling (stick) motion of the drum 22
2.4.2 Stick-slip motion of the drum 26
2.5 Parametric studies 32
2.5.1 Influence of slip phases on the drum motion 33
2.5.2 Influence of subsoil on the drum motion 35
2.5.3 Influence of the device parameters on the compaction indicator . 40
2.5.4 Influence of the coefficient of friction on the compaction indicator 43

3 Finite Element modeling **45**
3.1 Considered oscillation roller 45
3.2 Numerical model with hypoplastic soil behavior 46
3.2.1 General modeling strategy 46
3.2.2 Spatial and temporal discretization 48

3.2.3 Contact between soil and drum 49
3.2.4 Initial conditions 49
3.2.5 Analysis steps 50
3.2.6 Loading, movement, and excitation of the oscillation drum . . . 50
3.2.7 Constitutive soil model and numerical implementation 50
3.2.8 Modeling approach to maintain numerical stability 51
3.3 Results and discussion 52
3.3.1 First observations 53
3.3.2 Stress and strain components in the soil 53
3.3.3 Compaction effect in terms of void ratio change 59
3.3.4 Drum response 70

4 Summary, conclusions, and outlook 91
4.1 Summary and conclusions 91
4.1.1 Lumped parameter modeling 91
4.1.2 Finite Element modeling 92
4.2 Outlook 94

A Dynamic decoupling 97

B Coefficients of the discrete soil model 99

C Abbreviations 105
C.1 Spiral-shaped settlement trough 105
C.2 Semi-circular settlement trough 105
C.3 Semi-circular fixed settlement trough 108

D State-space representation of the equations of motion 113
D.1 Spiral-shaped settlement trough 113
D.2 Semi-circular settlement trough 116

E Lissajous curves 121

F Finite Element model assuming linear elastic soil behavior 125
F.1 Numerical model 125
F.2 Results 126

G Hypoplastic constitutive model 127
G.1 Basic hypoplastic constitutive model 127
G.2 Extended hypoplastic constitutive model 130

H UMAT for the extended hypoplastic constitutive model 133

I Numerical modeling 137
I.1 Finite Element Models 137
I.2 Results based on “model A” with and without “surface dampers (SD)” . 139
I.3 Results based on “model B” without “protective measures” 148
I.4 Results based on “model B” with “surface dampers (SD)” 153

I.5 Results based on “model B” with “protective foil (PF)” 155

Abbreviations **161**

Lumped parameter modeling 161

Finite Element modeling 163

List of Figures **166**

List of Tables **175**

Bibliography **177**

Chapter 1

Introduction

1.1 Soil compaction with dynamic rollers

The quality of layered earth structures, such as dams and embankments for roads, railways, and airfields, depends on the built-in material and in particular on the construction work. The layers must be compacted properly in order to prevent future damage of the structure connected to the earth structure, failure of long-term pavement performances and increasing maintenance costs. Therefore, *soil compaction* is a very important and critical step in the construction process of various civil structures. Dynamic roller compaction has become the common method for *near-surface compaction*, since it is much more efficient compared to compaction using static rollers.

A *roller*, also often referred to as roller-compactor, is a heavy piece of equipment used for near-surface compaction of soil and asphalt layers in the construction of various civil structures. A *static* roller uses only its weight to compact the layer, whereas a *dynamic* roller enhances the efficiency of subsurface compaction through dynamic excitation of the drum. Depending on the drum excitation, two basic types of dynamic rollers exist, i.e. vibratory rollers and oscillation rollers. They differ in design, mode of operation, and how the medium to be compacted is loaded.

In a *vibrating drum* a single unbalance mass, which is attached concentrically to the drum axis, generates a rapidly alternating upward-downward motion of the drum. The subgrade is compacted by the dynamic pressure applied by the drum. The concept of *vibratory excitation* for drums was implemented for the first time in 1958 [Kappel, 2012] and has become the commonly used type of excitation for dynamic drums.

The drum of an *oscillation roller* is equipped with two offset eccentric masses, which rotate synchronously in the same direction (see Fig. 11). The resulting alternating high-frequency forward-backward motion of the drum (oscillatory drum motion), is superposed with the translational roller motion (moving drum under the static axle load). Due to the friction in the contact area between drum and soil mainly dynamic shear forces are transmitted to the soil, which in turn increase the subgrade density. Thus, compaction is achieved by “massaging” [Kearney, 2006] the soil, also known as *shear force compaction* [Thurner and Sandström, 2000]. Unlike with vibrating drums, the compaction force acts continuously on the subsoil because the drum remains in constant contact with the soil at all times. Therefore, the drum does not bounce like a conventional vibratory roller drum. Moreover, an oscillation drum reduces subsoil

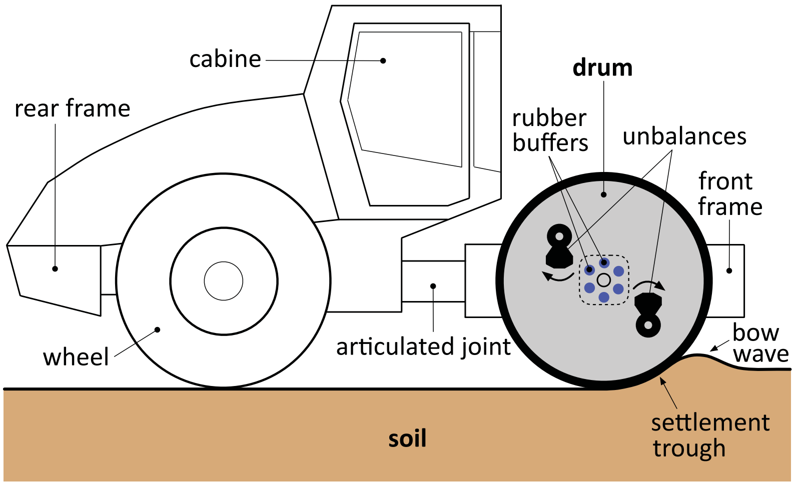

Figure 11: Principal components of an oscillation roller compactor with smooth drum

vibrations significantly compared to a vibratory roller and can therefore ideally be used in sensitive areas, such on construction sites in urban areas.

The first oscillation roller was developed by the Swedish company Geodynamik AB in the early 1980s ([Geodynamik AB, 1982], [Sandström, 1993]), i.e. the first *shearing force roller* [Geodynamik AB, 2018]. Today the only producer of this type of roller is the German company HAMM ([HAMM AG, 2018a], [Adam and Pistrol, 2016]).

1.2 Roller-integrated compaction control

The lack of real-time compaction information may lead to both over- and undercompaction. Moreover, the inappropriate use of oscillation rollers, i.e. continuing the compaction work despite reaching the state of maximum compaction, results in an increased wear of the oscillating drum [Pistrol, 2016]. Thus, instant *compaction control* is of particular importance. An extensive quality management requires continuous control of the soil compaction in the entire compacted area, which can be achieved only by work-integrated methods. Roller vibration monitoring has been used for over 40 years now during soil compaction to provide what is referred to as *Continuous Compaction Control* (CCC) ([Forssblad, 1980], [Thurner and Sandström, 1980], [Adam, 1996], [Kopf, 1999]). Real-time monitoring of the compaction quality during the compaction process yields the target compaction uniformly and continuously and results in time and cost savings. This control technique is based on the dynamic response of the interacting drum-subsurface system recorded during the roller pass, and thus, allows an instant continuous assessment of the compaction quality. In this method, the roller is used as compaction device as well as measuring device at the same time. During operation, CCC links one or more compaction indicators derived from the response of the roller (in the literature also referred to as *roller measured value* (RMV) [Imran et al, 2017], *roller-measured soil property* [Mooney and Rinehart, 2009] or *CCC-value* ([Adam, 1996], [Kopf, 1999])) to the degree of compaction of the soil. The parameters that influence the motion behavior of the drum also have an influence on the CCC indicators. Therefore, the first premise for a CCC technique is to keep the roller parameters of the compaction process such as roller speed, excitation frequency and excitation amplitude constant during the CCC measurements. Secondly, the motion of the drum needs to be recorded in terms of accelerations, velocities or displacements. Assuming constant parameters during the compaction process, a CCC technique assesses reliably the actual soil compaction, based on an analysis of the motion of the dynamically excited drum. The CCC indicators are *relative values*, which represent the evolution of the material stiffness in the compacted area. These indicators are calibrated to relate them to traditional compaction parameters such as deformation modulus of static and dynamic plate load tests defined in provisions and standards [Adam and Pistrol, 2016]. Thus, CCC overcomes the disadvantages of spot like compaction testing methods.

The concept of CCC for vibratory rollers was first investigated by H. Thurner of the Swedish Road Administration in 1974 by relating drum harmonics to soil compaction properties [White and Vennapusa, 2010]. In 1975, H. Thurner and Å. Sandström founded the company Geodynamik AB to continue research and development on CCC [White and Vennapusa, 2010]. In 1976, the *Compactometer* device based on the compaction indicator referred to as *Compaction Meter Value* (CMV) was developed by Geodynamik AB in cooperation with the Dynapac Research Department [White and Vennapusa, 2010]. Numerous studies by other researchers ([Adam, 1996], [Kopf, 1999]) and numerous research projects on CCC with vibrating rollers have been carried out since then, resulting in optimized vibrating rollers and other developments such as feedback controlled rollers and systems for CCC. While in the early years of CCC, roller-based measures of soil compaction were *heuristically determined relative indices* [Mooney and Rinehart, 2009] (e.g. the CMV value), more recently, roller vibration data has been used to extract continuous measurement of the actual soil stiffness ([Kröber et al, 2001], [Anderegg and Kaufmann, 2004], [Mooney and Adam, 2007], [Mooney and Rinehart, 2007], [National Academies of Sciences, Engineering, and Medicine, 2010]). Currently, there are three leading CCC systems for vibratory rollers on the market, the *Compactometer*, the *Terrameter* and the *ACE system*, which differ in their measurement principle and theoretical background [Pistrol, 2016]. Consequently, CCC has become the standard technology for assessing work-integrated and continuously the achieved compaction by means of vibratory rollers.

For oscillation rollers, however, no mature CCC system has been developed yet, although initial approaches to a CCC system were already proposed almost four decades ago [Thurner and Sandström, 2000]. The *Oscillometer*, introduced by the Swedish company Geodynamik AB in 1997 [Adam and Pistrol, 2016], is based on the so-called *Oscillometer Value* (OMV), i.e. a dimensionless value obtained from the amplitude of the horizontal acceleration of the drum. The OMV value reflects the horizontal force transferred from the drum to the soil [Thurner and Sandström, 2000]. The complication due to *slip* between drum and soil is considered by the built-in signal analysis of the *Oscillometer* using a special algorithm [Sandström, 1993]. HAMM AG adopted the OMV measurement technology [Thurner and Sandström, 2000] for the use on their smooth drum oscillation rollers. Kopf [1999] investigated the reliability of the OMV value by analyzing measurement data and performing parametric studies based on a single-degree-of-freedom lumped parameter model that considers frictional contact between drum and soil. He found that the *Oscillometer* does not reliably predict the soil stiffness compared to the results of CCC systems for vibratory rollers [Kopf, 1999]. Therefore, the CCC system using the OMV value was never used in engineering practice. Kopf [1999] also showed that an *imbalanced drum* causes motion patterns that repeat with every full rotation of the drum. This behavior is called *periodicity* of a drum [Kopf, 1999]. As this periodicity of a drum usually can also be observed in CCC values, it reduces their significance. Moreover, the investigations of the motion behavior of an oscillation drum in terms of horizontal drum accelerations considering *Coulomb* friction in the contact area between drum and soil, revealed that an oscillation roller exhibits two *operating modes*: i.e. the operating mode *stick* and the operating mode *slip* [Kopf, 1999]. Depending on the speed of the drum, the soil stiffness, and the friction between drum and soil the following modes of response may be observed: *one-sided slip*, *asymmetric slip*, and *symmetric slip* [Kopf, 1999]. Furthermore, Kopf [1999] showed that the vertical acceleration component of the oscillation drum center plotted against its horizontal counterpart, measured during compaction of granular soil, yields a figure in the shape of a *"recumbent eight"*. Based on the findings of Kopf, a comprehensive research project on the compaction with oscillation rollers was launched by the German roller manufacturer HAMM AG in 2011 in cooperation with the Institute of Geotechnics at TU Wien. The aims of the project, which ended in September 2016, were to obtain a better understanding of the motion behavior of an oscillating drum and its impact on the compacted soil as well as the development of a reliable CCC method for oscillation rollers and, moreover, the indication of wear of the drum during operation. Within this project large-scale in-situ tests were performed with a HAMM HD$^+$ 90 VO tandem roller [HAMM AG, 2011] possessing an oscillation drum and a vibrating drum in a gravel pit near Vienna International Airport. Analyzing the measurement data, Pistrol [2016] found that the *area enclosed in the "recumbent eight"* can be used as a characteristic quantity for the compaction degree of the subsoil, which increases with increasing soil stiffness, and thus, may serve as a CCC indicator. The reason for the formation of this figure is the vertical drum acceleration, which contains in addition to the excitation frequency also its double frequency as a result of the roller motion in the *settlement trough* and the development of a *bow* and a *rear wave* in the soil during compaction [Pistrol, 2016]. As a final outcome, based on the area of this response representation, in [Pistrol and Adam, 2018] a working roller integrated compaction control method was proposed also for oscillation rollers.

1.3 Motivation

Since experiments provide only a narrow insight into the response behavior of the entire parameter space, a complete picture of the drum response and its parameter interdependency can only be gained from the outcomes of comprehensive parametric numerical studies. In the meanwhile, only some attempts have been made to confirm the proposed CCC technique, which was mostly found empirically, supported by a few semi-analytical (e.g. [Pistrol, 2016]) and numerical studies (e.g. [Capraru et al, 2014]).

The literature on *mechanical modeling* of roller-compactors for numerical response simulation is quite scarce. Basically, it can be distinguished between lumped parameter models (e.g. [Wolf, 1994], [Beainy et al, 2013], [Li et al, 2018], [van Susante and Mooney, 2008]) and Finite Element (FE) models (e.g. [Cao et al, 2013], [Kenneally et al, 2015]) of the dynamic interacting roller-subsurface system. The focus of most FE models is to predict the subsurface compaction, and depending on the degree of sophistication, they allow only selective insight into the system response, like experimental studies. On the contrary, lumped parameter models are often used to predict the response of the compaction device for predefined subsurface condition or (over)simplified soil compaction models.

A first modeling attempt of the oscillation drum-soil system was presented in [Zuwang et al, 1997], where a single degree-of-freedom (SDOF) *lumped parameter model* captures slip between drum and subsurface, considering the suspension elements between drum and frame. This paper also explains the basic principle of oscillation compaction and some basic response phenomena such as “peak cut” of the horizontal drum acceleration. In a similar approach, Kopf [1999] studied the influence of the slip motion on the horizontal drum accelerations, using also a SDOF lumped parameter model. A few years ago, Pistrol [2016] presented a three degrees-of-freedom (3DOF) lumped parameter model for the drum in pure rolling motion, i.e. rolling without slipping, that delivers the horizontal and also the vertical acceleration response of the drum. An approach to solve this 3DOF model is presented in [Pistrol, 2016] for the operating mode stick. Lately, in [Li et al, 2018] the amplitude frequency characteristics of a tandem oscillation roller have been studied based on a 5DOF model in pure rolling motion. From this brief literature survey it can be concluded that, so far, no reliable lumped parameter model that predicts both realistically and efficiently the dynamic response of an oscillation drum operating at *stick-slip* motion is available.

There is an extensive body of literature available for the *Finite Element modeling* of dynamic soil compaction by means of vibrating rollers (e.g. [Yoo and T. Selig, 1977], [Yoo and T. Selig, 1979], [Pietzsch and Poppy, 1992], [Kelm, 2004], [Erdmann and Adam, 2014]) including CCC application (e.g. [Grabe, 1993], Anderegg and Kaufmann [2004], [Kenneally et al, 2015], [Adam and Pistrol, 2016]). However, literature on numerical modeling of the interacting system composed of oscillation roller and underlying soil is quite rare. Capraru et al [2014], for instance, used the modified *Drucker-Prager* cap plasticity model to simulate the compaction of a sandy soil layer resting on a gravel-like linear elastic subsoil. In their study, the inelastic volume change of the soil due to the oscillation drum serves as an indicator for soil compaction, provided that the soil compaction is related to the plastic strains. Based on this plane-strain FE model, the tribological behavior of an oscillation drum was investigated by Pistrol [2016]. On the other hand, a plasticity constitutive model can at best only indirectly simulate soil compaction. Alternatively, an anelastic constitutive model such as a *hypoplastic* constitutive law provides a direct measure of soil density. For example, in hypoplastic constitutive laws (e.g. [Gudehus and Kolymbas, 1979], [von Wolffersdorff, 1996], [Niemunis and Herle, 1997], [Mašín, 2019b]) the void ratio of the soil serves as an indicator of the predicted density, i.e. a reduction in the void ratio relative to the initial void ratio is referred to as soil *compaction.* Kelm [2004] was the first to use a hypoplastic constitutive model to predict the compaction effect of a vibratory roller. Soil compaction using vibratory and oscillation rollers equipped with different exciters was numerically investigated by Erdmann and Adam [2014]. In their FE model, a hypoplastic constitutive law with intergranular strain was implemented to simulate the soil compaction with parameters of Schlabendorf sand. Selected results for both a vibrating and an oscillation roller are presented in terms of contour plots of vertical soil displacements, stresses, and void ratios, respectively, and are qualitatively compared with the outcomes of a static roller. However, the compaction effect and the dynamic response of the drum are not addressed. From this brief literature survey it becomes clear that no reliable numerical model has yet been developed to predict the dynamic response of the complete highly nonlinear oscillation roller-soil interaction system, which covers both the actual compaction of non-cohesive soils and the response of the drum.

Thus, the novel CCC technique for oscillation rollers proposed by Pistrol [2016] has neither been verified by analytical nor by numerical studies. In order to fill this gap, the present dissertation aims to develop both a lumped parameter model that facilitates the response simulation of an oscillation drum with the least numerical effort capturing the observed *stick-slip motion* of the drum, and a FE model of the oscillation roller-subsoil system in an effort to predict and to assess for the first time simultaneously the soil compaction and the dynamic roller response with respect to the mentioned CCC indicator.

1.4 Modeling strategies

In the present work, two modeling strategies are pursued. On the one hand, *lumped parameter modeling* is applied with focus on the motion behavior of the drum in dependence of a priori defined soil parameters. On the other hand, *Finite Element modeling* is used with focus on simultaneous investigation of compaction effect and drum motion behavior. In both cases, parametric and sensitivity studies are performed with respect to the capabilities of the aforementioned CCC indicator. To support the proposed models, computed results are compared with corresponding experimental results based on measurement data recorded during in-situ field tests [Pistrol, 2016].

In the chosen *lumped parameter modeling* strategy, a curved dent, which approximates the settlement trough of the subsoil below the drum, is prescribed, supported by a discrete spring-damper soil model [Pistrol, 2016]. This curved dent that allows the simulation of the vertical motion of the drum is modeled as translatory movable, rigid track with asymmetric shape as observed in field tests [Pistrol, 2016]. The smooth drum is idealized as circular rigid body with spring-damper elements attached to its center, which represent the viscoelastic connection to the roller frame (suspension, also referred to as "rubber buffers") installed to decouple dynamically the drum from the remaining roller components. Modeling of frictional contact between drum and settlement trough, enables one to also consider the operating mode *slip*. Additionally to the sinusoidal excitation torque induced by the unbalance masses, a constant driving torque is imposed to the drum. As such, the effect of the translational motion of the roller on the response can be captured. The numerically obtained results of this 3DOF model in terms of drum center accelerations are evaluated for four oscillation rollers of the German roller manufacturer HAMM in an effort to explain the dynamic response of the interacting oscillation drum-soil system, and ultimately to validate the novel compaction measurement method for oscillation rollers taking into account the *stick-slip motion* of the oscillation drum.

In the chosen *Finite Element modeling* strategy, a two-dimensional (2D) model of the oscillation roller-subsoil system is developed for performing numerical simulations with the FE software suite *ABAQUS/Standard*, whereas the intergranular strain enhanced *hypoplastic* constitutive model is implemented to describe the complex nonlinear and inelastic material behavior of the granular soil. The numerically predicted change in void ratio serves as an indicator of the *compaction effect* achieved by the tandem roller type HAMM HD$^+$ 90 VO under consideration. Only those parts of the roller that are essential for soil compaction are modeled. These are the oscillating drum, the viscoelastic suspension, and the static and dynamic forces applied to the drum. Based on this plan-strain FE model, it is aimed to investigate the sensitivity of the predicted soil compaction to several parameter variations (soil, machine and operating parameters), the parameter dependency of the drum response, and consequently of the CCC indicator proposed in [Pistrol, 2016], considering the actual compaction state.

1.5 Fundamentals and content

This doctoral thesis is based on the following publications that were developed in the context of the current research project:

(1) “Analytical modelling of the motion of an oscillating roller during soil compaction assuming pure rolling contact”, co-authored by I. Paulmichl, C. Adam, D. Adam, and W. Völkel, published in D. Adam and S. Larsson (eds.), *Proc. Anniversary Symposium “40 Years of Roller Integrated Continuous Compaction Control (CCC)”, November 29th, Vienna*, Mitteilungen des Institutes für Geotechnik, Heft 4, S. 121-124, Vienna, 2018 (“paper 1”)

(2) “Analytical modeling of the stick-slip motion of an oscillation drum”, co-authored by I. Paulmichl, C. Adam, and D. Adam, published in Acta Mechanica, 230(9):3103-3126, doi:10.1007/s00707-019-02454-3, 2019 (“paper 2”)

(3) “Simulation of the stick-slip motion of an oscillatory roller”, co-authored by I. Paulmichl, C. Adam, and D. Adam, published as OnlineOpen in Proceedings in Applied Mathematics and Mechanics (PAMM), doi:10.1002/pamm.201900245, 2019 (“paper 3”)

(4) “Assessment of a compaction indicator for oscillation rollers with a lumped parameter model”, co-authored by I. Paulmichl, C. Adam, D. Adam, and W. Völkel, submitted for publication to ICE - Geotechnical Engineering for the *Roller integrated continuous compaction control* themed issue, tracking number: GE-D-19-00204, 08/2019 (“paper 4”)

(5) “Numerical simulation of the compaction effect and the dynamic response of an oscillation roller based on a hypoplastic soil model”, co-authored by I. Paulmichl, T. Furtmüller, C. Adam, and D. Adam, submitted for publication to Soil Dynamics and Earthquake Engineering, 09/2019 (“paper 5”)

(6) “Parametric study of the compaction effect and the response of an oscillation roller”, co-authored by I. Paulmichl, C. Adam, and D. Adam, submitted for publication to ICE - Geotechnical Engineering for the *Roller integrated continuous compaction control* themed issue, tracking number: GE-D-19-00209, 09/2019 (“paper 6”)

The present thesis is structured as follows. Chapter 2 describes the *lumped parameter modeling* of the oscillation roller-soil system based on papers 1, 2, 3 and 4. The considered types of oscillation rollers are outlined in Section 2.1. After a brief explanation of the basic components and the basic principles of an oscillation roller (Section 2.2.1), the proposed drum-subsoil interacting model (Section 2.2.2) and excitation model (Section 2.2.3) is presented. Based on the kinematic relations (Section 2.3.1), in a substructure approach (Section 2.3.2) the equations of motion of this 3DOF model are derived in Section 2.3.3 separately for the response mode *stick* and the response mode *slip* for an asymmetric (spiral-shaped) settlement trough. The numerical solution of these highly nonlinear equations is discussed in Section 2.3.4. Once the model has been established, the impact of the contact condition between drum and soil (pure rolling vs. stick-slip motion), soil stiffness, and driving torque on the response of the oscillation drum of a HAMM HD$^+$ 90 VO tandem roller is investigated in detail (Section 2.4). Moreover, the frequency content of selected computed results and drum accelerations recorded during in-situ field tests [Pistrol, 2016] is examined to support the proposed analytical model (Section 2.4). Subsequently, a comprehensive parametric study considering three additional types of HAMM oscillation rollers, i.e. a H7i VIO, HD13i VIO and HD$^+$ 140i VO roller, is performed (Section 2.5). The impact of the slip phases (Section 2.5.1), the soil stiffness (Section 2.5.2), the excitation frequency (Section 2.5.3), the suspension properties (Section 2.5.3), and the coefficient of friction between drum and soil surface (Section 2.5.4) on the drum response is investigated in detail.

Chapter 3 describes the *Finite Element modeling* of the dynamic interacting oscillation roller-soil system based on papers 5 and 6. After a brief description of the considered oscillation roller (Section 3.1), the developed numerical model of the oscillation roller-soil interaction system is explained in Section 3.2. An approach to increase the numerical stability related to the implemented *hypoplastic* constitutive law (Section 3.2.7) is presented in Section 3.2.8. Once a numerically stable and reliable model has been established (Section 3.3.1), predicted soil stress and strain components at selected depths are visualized and compared with the ones induced by a static roller. The aim is to reveal the soil depth-dependent compaction behavior of the considered oscillation roller (Section 3.3.2). Subsequently, the impact of selected soil properties, the coefficient of friction, the static axle load, and the roller speed on both the compaction effect (Section 3.3.3) and the drum response (Section 3.3.4) is investigated in detail. Selected computed results (stress components in the soil and drum center accelerations) are compared with corresponding experimental results based on in-situ field tests [Pistrol, 2016] to support and validate the proposed numerical model (Sections 3.3.2 and 3.3.4).

Finally, Chapter 4 summarizes the main findings and outcomes of the presented numerical simulations of the interacting oscillation roller-soil system and gives a brief outlook on open research questions of the considered “contact problem”.

Chapter 2

Lumped parameter modeling

2.1 Considered oscillation rollers

For the subsequent *lumped parameter modeling*, four oscillation rollers of the German roller manufacturer HAMM are considered:

(1) HD^+ 90 VO (“roller 1”)
(2) H7i VIO (“roller 2”)
(3) HD13i VIO (“roller 3”)
(4) HD^+ 140i VO (“roller 4”)

Rollers 1 and 4 are both articulated tandem rollers each with a vibratory drum (“V”) in the front and an oscillation drum (“O”) in the rear. While roller 1 possesses an operating weight of about 9 tons, roller 4 has an operating weight of around 14 tons. Rollers 2 and 3 are both compactors with a “VIO” smooth drum. The unbalance system of these rollers combines two compaction methods in a single drum allowing compaction either with vibration (“V”) or with oscillation (“O”). The operating weight of roller 2 is around 6 tons, while the operating weight of roller 3 is about 13 tons, and thus, more than twice as large. The main parameters of these rollers and the operating frequency of each roller are listed in Table 21. For further details see [Pistrol, 2016].

Roller 1, i.e. the HD^+ 90 VO tandem roller, is used to create the subsequently proposed 3DOF model in Section 2.4 in the framework of a detailed investigation of the drum motion because for this device acceleration response data of the drum center have been recorded in field tests [Pistrol, 2016]. The outcomes of these investigations are summarized in the papers 1, 2 and 3, see Section 1.5. Based on this detailed response study, in Section 2.5 the response of rollers 2, 3 and 4 is investigated in the same manner. The results of this parametric study are summarized in paper 4 (see Section 1.5).

			Type of oscillation roller			
Parameter	Symbol	Dimension	HD$^+$ 90 VO (roller 1)	H7i VIO (roller 2)	H13i VIO (roller 3)	HD$^+$ 140i VO (roller 4)
Radius of the drum	r	m	0.600	0.603	0.752	0.700
Width of the drum	b	m	1.68	1.68	2.14	2.14
Mass of the drum	m	kg	1851	1818	3499	2907
Mass moment of inertia of the drum	I	kg m^2	412	472	1290	863
Static axle load	P_0	N	45,224	36,935	73,575	64,305
Static axle load minus drum weight	F_z	N	27,066	19,100	39,250	35,787
Excitation frequency	$\bar{f}$	Hz	39	36	33	36
Amplitude of the oscillation moment	$M_{Mu}^{(0)}$	Nm	54,947	46,390	125,550	91,904
Suspension drum/frame - stiffness	k_d	N/m	4.0×10^6	2.8×10^6	5.8×10^6	5.3×10^6
Suspension drum/frame - damping	c_d	Ns/m	3×10^2	3×10^2	3×10^2	3×10^2

Table 21: Roller parameters [Pistrol, 2016] and suspension properties ([HAMM AG, 2017], [HAMM AG, 2018b])

2.2 Mechanical model

2.2.1 Basic structure and operation mode of an oscillation roller

The main components of an oscillation roller shown in Fig. 11 are the rigid drum (at the front) equipped with two rotating unbalances (also referred to as unbalanced masses or eccentric masses), the driving wheels, the front and the rear frame, and the driver's cabin including processing, display and storing unit. Drum and front frame are separated by suspension elements (rubber buffers) to prevent the transmission of vibrations from the drum to the frame. A hinged connection between the front frame and the rear frame improves the maneuverability of the roller. To protect the driver from vibration, the cabin is detached from the rear frame by isolation mounts.

In the oscillation drum, two opposite eccentric masses, whose shafts are arranged excentrically to the drum axis, rotate synchronously in the same direction (see Fig. 11), driven by a toothed belt. Because these unbalance masses are offset by 180° relative to each other, the out-of-balance forces cancel out. The remaining spinning couple of forces induces a torsional moment around the drum axis, which changes its sign during the rotation of the eccentric masses. It causes the drum to rapidly move in a alternating forward-backward motion. This rotational motion and the translational motion of the roller moving with constant speed are superposed. The dynamic (alternating) tangential (shear) forces, imposed through friction in the contact area between drum and surface of the compacted medium, induce mainly shear waves in the subsurface, and compaction is achieved by "massaging" the material [Kearney, 2006], also referred to as *shear force compaction* [Thurner and Sandström, 2000]. Unlike in a vibrating drum, which may bounce during compaction ([Beainy et al, 2013], [van Susante and Mooney, 2008]), the compaction forces strain continuously the subsoil because oscillation drum and soil remain in permanent contact. An oscillation drum performs either a pure rolling motion or a *stick-slip motion*. As such, an oscillation roller continuously compacts the subsurface both dynamically by alternating (primarily) horizontal shear loading and statically by its weight in a vertical direction. During the forward motion, the static weight of the drum deforms the soil surface asymmetrically as shown in Fig. 11, subsequently referred to as "settlement trough". This curved contact zone between drum and subsoil is the reason why the oscillation drum also responds in a vertical direction.

2.2.2 Representation of roller and subsoil

The main objective of the roller-soil model to be developed is to allow for a comprehensive parametric study of the response behavior of the drum for a given subsoil condition (i.e. the compaction process in the soil is not simulated). Consequently, in the desired computationally efficient model all parts of the roller with minor effects on the dynamic drum response are omitted. During operation, both the horizontal and vertical vibrations of the rear and front frame are negligible because drum and front frame are dynamically decoupled by the deeply tuned rubber buffers. For further details see Appendix A. Based on this observation, it is reasonable to reduce the whole roller to the oscillation drum that is connected through spring-damper elements to the static frame, taking into account the dead weight of the front frame. The drum is assumed to be a planar rigid smooth circular body of radius r with mass m and mass moment of inertia I (with respect to the drum center M). One vertical and one horizontal spring-damper element attached to the drum center, both of same stiffness (k_d) and viscous damping (c_d) properties, capture the effect of the suspension (rubber buffers), as shown in Fig. 21.

In the utilized modeling strategy, the shape of the soil surface below the drum, which has a significant impact on the roller response, and the soil parameters depending on the degree of soil compaction need to be a priori defined (see, for instance, [Kopf, 1999], [Pistrol, 2016]). The settlement trough is prescribed as an asymmetric rigid curved track according to a logarithmic spiral. At the bottom of the settlement trough (point A in Fig. 21), in a common approach the effect of the elastic continuous halfspace (subsoil) is captured simplified through two discrete *Kelvin-Voigt* bodies, one arranged in vertical (subscript sv) and one in horizontal (subscript sh) direction. This simplified viscoelastic soil model, first introduced by Lysmer and Richart [1966], is commonly used to model soil behavior in foundation vibrations ([Gazetas, 1983], [Wolf, 1994]) as well as in roller-soil interaction modeling ([Yoo and T. Selig, 1979], [Pietzsch and Poppy, 1992], [Grabe, 1993], [Adam, 1996], [Facas et al, 2010], [Beainy et al, 2013]). The settlement trough exhibits a translational motion in both horizontal and vertical direction, its rotation is, however, constrained. In [Gazetas, 1991] and [Wolf, 1994], the reduction of the elastic soil halfspace to spring-dashpot damper elements in parallel is discussed in detail, and thus, not repeated here. The expressions for soil spring coefficients k_{sh} and k_{sv}, and soil damping parameters c_{sh} and c_{sv} are listed in Appendix B. In the current roller-soil model, the soil mass is not considered because its effect is negligible if *Poisson*'s ratio ν of the soil is less than 1/3 [Wolf, 1994]. This is the case in the current study where only non-cohesive soils are considered. For larger

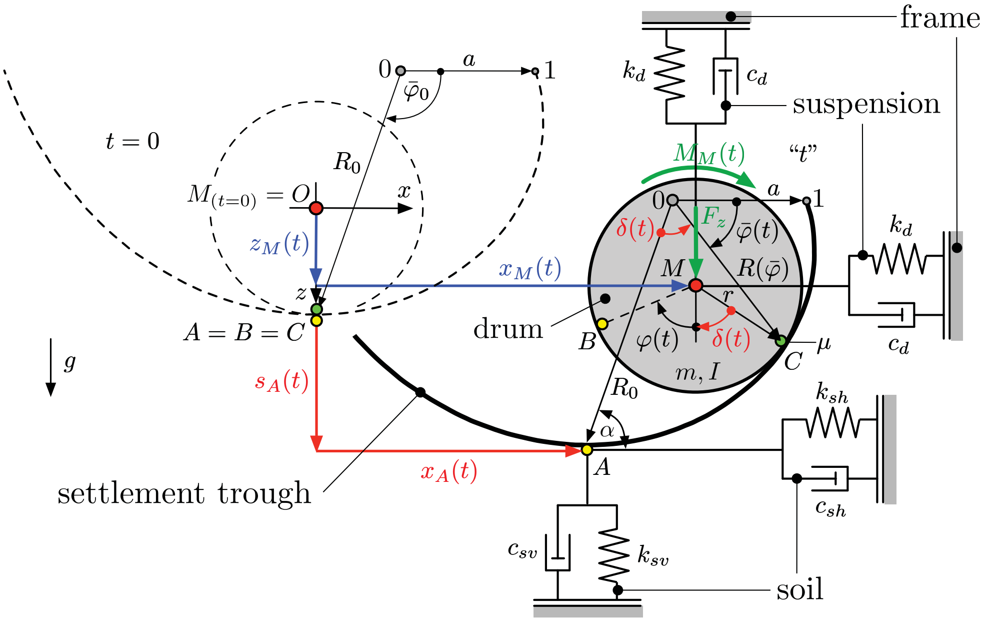

Figure 21: 3DOF lumped parameter model of the interaction system oscillation roller-subsoil (spiral-shaped settlement trough)

Poisson's ratio, a trapped soil mass is added to the vertical spring-dashpot damper elements, as explained in [Wolf, 1994].

The contact between drum and subsoil is described by means of dry friction according to *Coulomb*'s law with constant coefficient of friction μ. As such, both the *stick* phase and *slip* phase between drum and soil can be simulated by the roller-soil interaction model shown in Fig. 21, which has 3DOF.

2.2.3 Modeling of excitation and loading

The two rotating eccentric shafts inside the drum with each two imbalances (see Fig. 11) can be each represented by two equal eccentric lumped masses, $m_{u1} = m_{u2} = 2m_u$, with distance e_u from the center of rotation (see Fig. 22). The amplitude F_u of the centripetal force generated by each unbalanced shaft rotating with constant angular velocity $\bar{\nu}$ is

$$F_{u1} = F_{u2} = F_u = 2m_u e_u \bar{\nu}^2 \tag{2.1}$$

where $\bar{\nu}$ is 2π times the excitation frequency $\bar{f}$. Decomposition of the centripetal force at time t into component $F_{u\|}$ in parallel and component $F_{u\perp}$ perpendicular to the line that connects the center of rotation (denoted as RC in Fig. 22) and the drum center M yields

$$F_{u\|} = F_u \cos(\bar{\nu}t) \quad , \quad F_{u\perp} = F_u \sin(\bar{\nu}t) \tag{2.2}$$

Since the unbalance masses m_{u1} and m_{u2} are offset by 180° relative to each other and the shafts rotate in the same direction, the components of the corresponding unbalance forces

$$\vec{F}_{u\|1} = -F_{u\|}\vec{e}_{\|} \quad , \quad \vec{F}_{u\perp 1} = -F_{u\perp}\vec{e}_{\perp} \tag{2.3}$$

$$\vec{F}_{u\|2} = F_{u,\|}\vec{e}_{\|} \quad , \quad \vec{F}_{u\perp 2} = F_{u\perp}\vec{e}_{\perp} \tag{2.4}$$

cancel out. In the above equations, $\vec{e}_{\|}$ and $\vec{e}_{\perp}$ denote the unit vectors depicted in

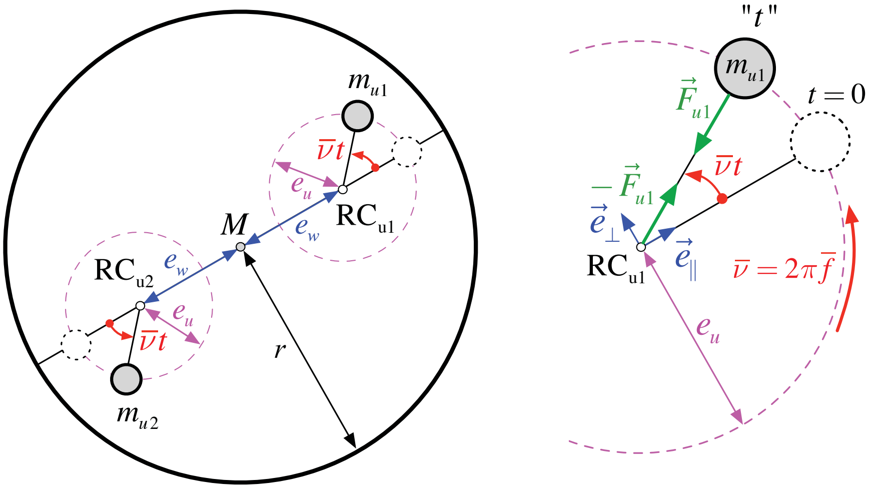

Figure 22: Drum with unbalanced shafts (left), and circular motion of one unbalance mass with constant circular frequency $\bar{\nu}$ (right)

Fig. 22. The counteracting normal forces $\vec{F}_{u\perp 1}$ and $\vec{F}_{u\perp 2}$ with distance $2e_w$ result in the sinusoidal torque $M_{Mu}(t)$ around the drum axis with the amplitude $M_{Mu}^{(0)}$,

$$M_{Mu}(t) = M_{Mu}^{(0)} \sin(\bar{\nu}t) \quad , \quad M_{Mu}^{(0)} = 4m_u e_u e_w \bar{\nu}^2 \tag{2.5}$$

In Fig. 23, the relation between the excitation torque $M_{Mu}(t)$ and the location of the rotating unbalanced shafts is depicted for discrete time instants visualizing the basic principle of an oscillation drum.

The total drum excitation applied at the drum center is composed of the unbalanced shaft moment $M_{Mu}(t)$ and the constant driving torque M_{Md} imposed by the roller engine,

$$M_M(t) = M_{Mu}(t) + M_{Md} \tag{2.6}$$

Application of the constant torque M_{Md} allows to control the location of the drum in the settlement trough. Since the oscillation drum motion is superposed to the translational motion of the drum with constant roller velocity, the drum does not oscillate around the bottom of the settlement trough but on its slope in driving direction. In addition, the vertical load F_z, i.e. the static axle load P_0 of the frame minus drum weight mg,

$$F_z = P_0 - mg \tag{2.7}$$

is applied to the drum center. Variable g denotes the acceleration of gravity.

In contrast to a simpler roller model presented in [Pistrol, 2016], the model proposed here allows to simulate the stick-slip motion of the drum, to take into account the suspension between drum and roller, to consider the effect of driving velocity by application of a constant driving torque, and to study the motion of the oscillation drum in its asymmetric settlement trough.

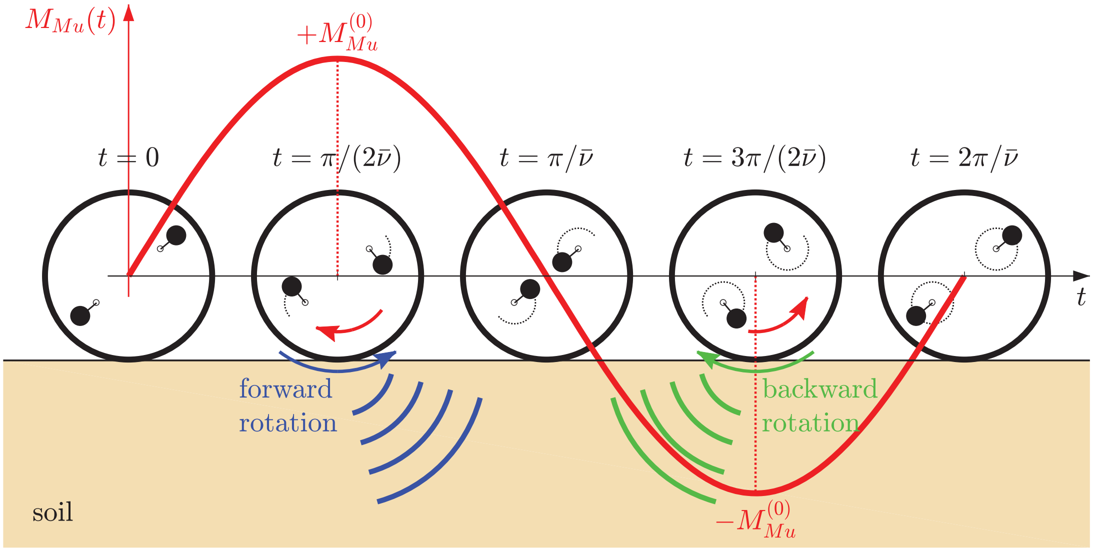

Figure 23: Excitation torque $M_{Mu}(t)$ in an oscillation drum and corresponding location of the unbalance at discrete time instants, based on Zuwang et al [1997]

2.3 Governing equations

2.3.1 Kinematics

Before the equations of motion are derived, the kinematic relations for the drum motion and soil-drum interaction need to established. The distance R from the origin of the logarithmic spiral (point 0) describing the settlement trough to the contact point C at time t reads as [Weisstein, 2018]

$$R(t) = a \exp\left[k\bar{\varphi}(t)\right] \quad , \quad \bar{\varphi}(t) = \bar{\varphi}_0 - \delta(t) \tag{2.8}$$

with spiral parameters a and k calibrated to the actual shape of the soil surface. Angle $\bar{\varphi}_0 = \pi - \alpha$ represents the inclination of the connection line between 0 and C at time $t = 0$, $\alpha = \arctan(1/k)$ is the angle between the tangent and radial line at point $(R_0,\bar{\varphi}_0)$, and $\delta(t)$ defines the position of the drum in the settlement trough at time t (see Fig. 21). It is assumed that at time $t = 0$ the drum is at the bottom of the rigid settlement trough, as indicated by dashed lines in Fig. 21. This position $(R_0,\bar{\varphi}_0)$ is defined by the radius $R_0 = a \exp(k\bar{\varphi}_0)$ and angle $\bar{\varphi}_0$. For $k \to 0$, $\alpha \to \pi/2$, the spiral approaches a circle with radius a (see Fig C1 in Appendix C.2). Thus, the proposed model allows the simulation of both a symmetric semicircular and an asymmetric spiral-shaped settlement trough.

In the *stick* phase of the drum, the following three independent coordinates are chosen to describe the motion of 3DOF model shown in Fig. 21, i.e. the displacement components $x_A(t)$ and $s_A(t)$ of support point A, and the position angle $\delta(t)$. In this phase, continuous rolling contact can be assumed, and the relative velocity between drum surface and settlement trough is zero. Consequently, the arc length L_{AC} along the settlement trough (between support point A and the contact point C, see Fig. 21),

$$L_{AC} = \frac{\sqrt{1+k^2}}{k} R_0 \left[1 - \exp(-k\delta)\right] \tag{2.9}$$

and the arc length L_{BC} along the drum surface (between contact point C and point B on the drum, see Fig. 21),

$$L_{BC} = (\varphi + \delta)\, r \tag{2.10}$$

are equal, $L_{AC} = L_{BC}$. In Eq. 2.10, $\varphi(t)$ denotes the total rotation angle of the drum [Marguerre, 1968]. Rewriting this *rolling condition* yields for the *stick* phase the relationship between the drum rotation angle φ and the position angle δ,

$$\varphi = \frac{\sqrt{1+k^2}}{kr} R_0 \Big[1 - \exp(-k\delta)\Big] - \delta \tag{2.11}$$

The first and the second time derivative read

$$\dot{\varphi} = f_5 \dot{\delta} \quad , \quad \ddot{\varphi} = f_5 \ddot{\delta} + f_6 \dot{\delta}^2 \tag{2.12}$$

The functions f_5 and f_6, which depend on the angle $\delta(t)$, the spiral parameters R_0 and k, and the drum radius r are listed in Appendix C.1.

Slip of the drum on the soil surface results in a relative motion between drum and soil. Thus, in the *slip* phase lengths L_{AC} (Eq. 2.9) and L_{BC} (Eq. 2.10) are dissimilar.

Differentiation of the difference $L_{AC} - L_{BC}$ with respect to time t results in the relative velocity v_{rel} between drum and subsoil (slip velocity),

$$v_{rel} = \dot{\delta} f_5 r - \dot{\varphi} r \tag{2.13}$$

Since in the *slip* phase $v_{rel} \neq 0$, the angles $\delta(t)$ and $\varphi(t)$ become independent variables. However, the tangential friction contact according to *Coulomb*'s law at point C couples in this phase the variables x_A and s_A, which are, therefore, no independent variables, as it is seen later.

For deriving the equations of motion, it is convenient to express the horizontal and vertical displacement components x_M and z_M, respectively, of the drum center M at time t as a function of the coordinates $x_A(t)$, $s_A(t)$, and $\delta(t)$,

$$x_M = x_M^{(\mathrm{roll})} + x_A \quad , \quad z_M = z_M^{(\mathrm{roll})} + s_A \tag{2.14}$$

$$x_M^{(\mathrm{roll})} = -R_0 \exp(-k\delta)\cos(\alpha + \delta) - r\sin\delta + R_0 \cos\alpha \tag{2.15}$$

$$z_M^{(\mathrm{roll})} = R_0 \exp(-k\delta)\sin(\alpha + \delta) - r\cos\delta - (R_0 \sin\alpha - r) \tag{2.16}$$

where $x_M^{(\mathrm{roll})}$ and $z_M^{(\mathrm{roll})}$ are the corresponding displacement components of M relative to the settlement trough, which are superposed to the displacement components of the settlement trough, x_A and s_A, respectively. Differentiation of Eqs 2.14 with respect to time t yields the components of the drum center velocity,

$$\dot{x}_M = f_1 \dot{\delta} + \dot{x}_A \quad , \quad \dot{z}_M = f_3 \dot{\delta} + \dot{s}_A \tag{2.17}$$

and repeated differentiation the acceleration components,

$$\ddot{x}_M = f_1 \ddot{\delta} + f_2 \dot{\delta}^2 + \ddot{x}_A \quad , \quad \ddot{z}_M = f_3 \ddot{\delta} + f_4 \dot{\delta}^2 + \ddot{s}_A \tag{2.18}$$

in terms of $x_A(t)$, $s_A(t)$, and $\delta(t)$. The functions f_1, f_2, f_3, and f_4, which depend on the angle $\delta(t)$, the spiral parameters a, k, α, R_0, and the drum radius r, are specified in Appendix C.1.

2.3.2 Dynamic substructuring

To derive efficiently the equations of motion, the model of Fig. 21 is separated into the subsystem drum (“I”) and the subsystem soil (“II”) including the settlement trough. At contact point C, the normal component N and the tangential component T of the interface force are applied as external forces, as shown in Fig. 24.

Subsystem I: Drum
Two equations are obtained by application of conservation of momentum [Ziegler, 1995] to the subsystem drum in horizontal (x) and vertical direction (z), compare with Fig. 24 (I),

$$T\cos\delta - N\sin\delta - c_d \dot{x}_M - k_d x_M = m\ddot{x}_M \tag{2.19}$$

$$(mg + F_z) - T\sin\delta - N\cos\delta - c_d \dot{z}_M - k_d z_M = m\ddot{z}_M \tag{2.20}$$

Solving this coupled system of equations for N and T yields,

$$N = \Big[(mg + F_z) - (m\ddot{z}_M + c_d\dot{z}_M + k_d z_M)\Big]\cos\delta \\ - (m\ddot{x}_M + c_d\dot{x}_M + k_d x_M)\sin\delta \quad (2.21)$$

$$T = \Big[(mg + F_z) - (m\ddot{z}_M + c_d\dot{z}_M + k_d z_M)\Big]\sin\delta \\ + (m\ddot{x}_M + c_d\dot{x}_M + k_d x_M)\cos\delta \quad (2.22)$$

A third equation is obtained by application of the conservation of angular momentum [Ziegler, 1995] with respect to the drum center M,

$$I\ddot{\varphi} = M_M(t) - Tr \quad (2.23)$$

where φ denotes the total rotation angle [Marguerre, 1968] of the drum (see Fig. 24).

Subsystem II: Subsoil

Conservation of momentum in horizontal (x) and vertical (z) direction to the soil subsystem shown in Fig. 24 (II) leads to

$$N\sin\delta - T\cos\delta = k_{sh}x_A + c_{sh}\dot{x}_A \quad (2.24)$$

$$N\cos\delta + T\sin\delta = k_{sv}s_A + c_{sv}\dot{s}_A \quad (2.25)$$

This set of equations is solved for N,

$$N = (k_{sh}x_A + c_{sh}\dot{x}_A)\sin\delta + (k_{sv}s_A + c_{sv}\dot{s}_A)\cos\delta \quad (2.26)$$

Coupling of the subsystems

The compatibility conditions at contact point C between both subsystems depend on the motion phase (stick or slip) of the drum. In the *stick* phase, where kinematic relations Eqs 2.11 and 2.12 are applicable, the sliding friction force T_f between drum and soil according to *Coulomb*'s law of dry friction [Steiner, 2014]

$$T_f = -\mu N \operatorname{sign}(v_{rel}) \quad (2.27)$$

is not exceeded at any time,

$$|T| \leq |T_f| = \mu N \quad (v_{rel} = 0) \quad (2.28)$$

It is assumed, that the coefficient of kinetic friction μ_k is approximately equal to the coefficient of static friction μ_s [Popov, 2017] and, thus, $\mu = \mu_k \approx \mu_s$.

If $|T| = \mu N$ and there is a relative motion between drum and subsoil with relative velocity v_{rel} according to Eq. 2.13, the motion switches from the *stick* to the *slip* phase. In the *slip* phase, where $v_{rel} \neq 0$, the tangential contact force T corresponds to *Coulomb*'s force of friction T_f, depending on the sign of v_{rel},

$$T = |T_f| > 0 \quad (v_{rel} \leq 0^-) \quad , \quad T = -|T_f| < 0 \quad (v_{rel} \geq 0^+) \quad (2.29)$$

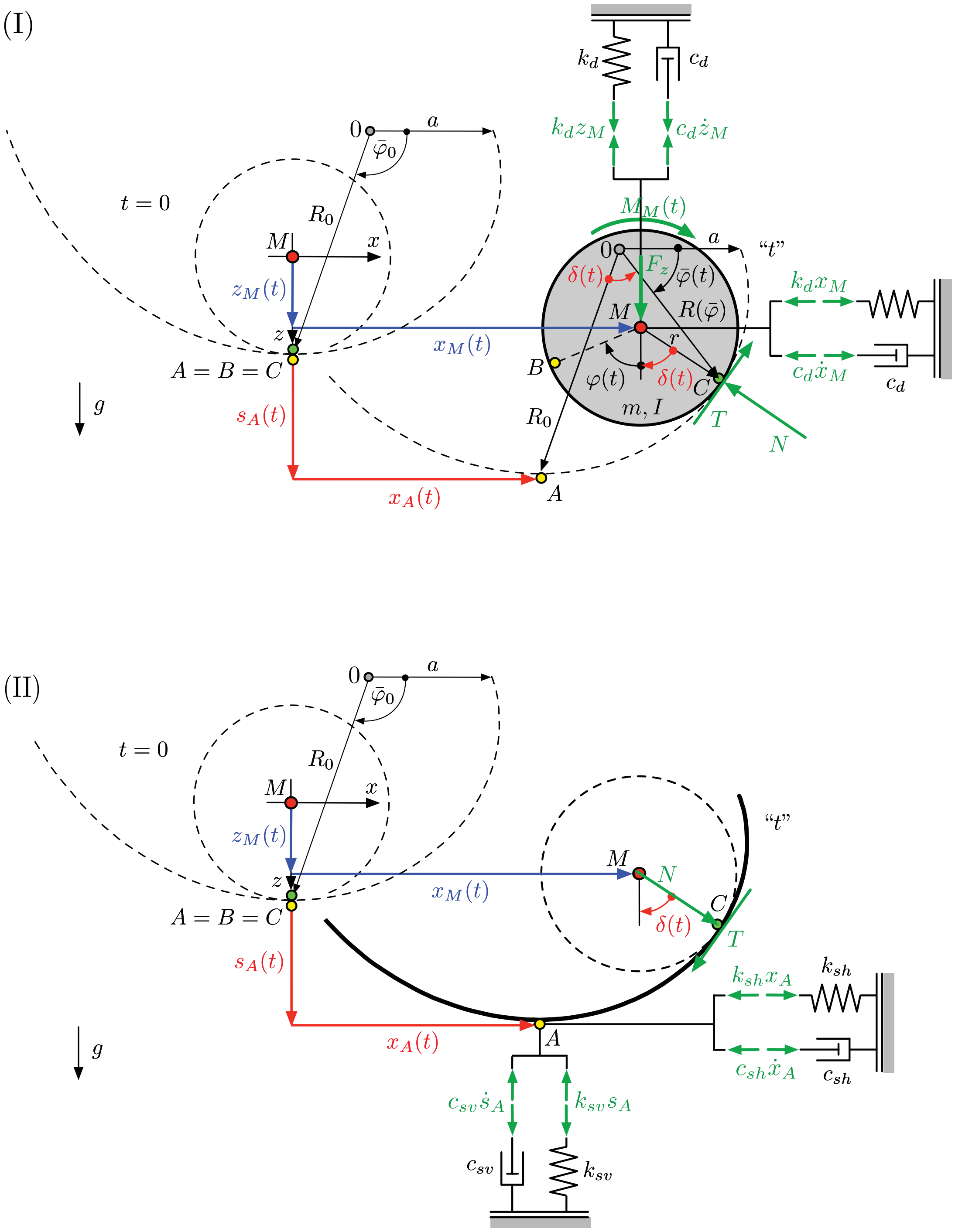
(I)
k_d
c_d
$k_d z_M$
$c_d \dot{z}_M$
0
a
$\bar{\varphi}_0$
$t = 0$
R_0
M
x
$z_M(t)$
z
$x_M(t)$
$A = B = C$
g
$s_A(t)$
$x_A(t)$
A
$M_M(t)$
0
a
"t"
$\delta(t)$
F_z
$\bar{\varphi}(t)$
M
$R(\bar{\varphi})$
r
B
$\varphi(t)$
$\delta(t)$
C
m, I
R_0
T
N
$k_d x_M$
$c_d \dot{x}_M$
c_d
(II)
0
a
$\bar{\varphi}_0$
$t = 0$
R_0
M
x
$z_M(t)$
z
$x_M(t)$
$A = B = C$
$s_A(t)$
g
$x_A(t)$
A
M
N
C
$\delta(t)$
T
"t"
$k_{sh} x_A$
k_{sh}
$c_{sh} \dot{x}_A$
c_{sh}
$c_{sv} \dot{s}_A$
$k_{sv} s_A$
c_{sv}
k_{sv}

Figure 24: Subsystem I (oscillation drum with suspension) and subsystem II (subsoil with settlement trough)

2.3.3 Equations of motion

Stick phase

Adding up Eq. 2.19 and Eq. 2.24, and replacing x_M and its first and second derivative by the independent coordinates δ and x_A and their derivatives through Eqs. 2.14, 2.17, and 2.18, leads to the first equation of motion in terms of δ and x_A,

$$f_1 m\ddot{\delta} + m\ddot{x}_A + f_2 m\dot{\delta}^2 + f_1 c_d\dot{\delta} + (c_{sh} + c_d)\,\dot{x}_A + (k_{sh} + k_d)\,x_A + k_d x_M^{(\mathrm{roll})} = 0 \quad (2.30)$$

Similarly, Eqs 2.20 and 2.25 are added up, and z_M and its derivatives are expressed by δ and s_A through Eqs 2.14, 2.17, and 2.18, respectively, yielding the second equation of motion,

$$\begin{aligned} f_3 m\ddot{\delta} + m\ddot{s}_A + f_4 m\dot{\delta}^2 + f_3 c_d\dot{\delta} + (c_{sv} + c_d)\,\dot{s}_A& \\ + (k_{sv} + k_d)\,s_A + k_d z_M^{(\mathrm{roll})} &= mg + F_z \quad (2.31) \end{aligned}$$

To obtain the third equation of motion in terms of the independent coordinates δ, x_A and s_A, in Eq. 2.23, T is substituted with Eq. 2.22 and $\ddot{\varphi}$ with Eq. 2.12. Then, x_M and z_M and their time derivatives are replaced by the relations of Eqs 2.14, 2.17, and 2.18, resulting after some algebra in

$$\begin{aligned} \left(f_5\frac{I}{mr} + \tilde{f}_1\right) m\ddot{\delta} + m\ddot{x}_A\cos\delta - m\ddot{s}_A\sin\delta + \left(f_6\frac{I}{mr} + \tilde{f}_2\right) m\dot{\delta}^2& \\ + c_d\Big[\tilde{f}_1\dot{\delta} + \dot{x}_A\cos\delta - \dot{s}_A\sin\delta\Big] + k_d\Big[\left(x_M^{(\mathrm{roll})} + x_A\right)\cos\delta& \\ - \left(z_M^{(\mathrm{roll})} + s_A\right)\sin\delta\Big] &= \frac{M_M(t)}{r} - (mg + F_z)\sin\delta \quad (2.32) \end{aligned}$$

with

$$\tilde{f}_1 = f_1\cos\delta - f_3\sin\delta \quad , \quad \tilde{f}_2 = f_2\cos\delta - f_4\sin\delta \quad (2.33)$$

Eqs 2.30, 2.31 and 2.32 represent three coupled second order nonlinear ordinary differential equations (ODEs), which describe the motion of the 3DOF roller-soil interaction model in the *stick* phase and for pure rolling. For efficient numerical solution, this coupled set of equations is written in the state space, as described in Appendix D.1.

Note that for an immovable semicircular settlement trough (i.e. $k = 0$, $k_{sh} \to \infty$ and $k_{sv} \to \infty$), the presented 3DOF lumped parameter model simplifies to a SDOF lumped parameter model with “fixed settlement trough” (see Fig. C2 in Appendix C.3). In this case, Eq. 2.32 approaches to the solution presented in [Ziegler, 1995] (example A7.2, pp 461-462), i.e. Eq. C.44 as derived in Appendix C.3. On the other hand, if the settlement trough becomes horizontal (i.e. $R \to \infty$), Eq. 2.32 reduces to the equation of motion of a model proposed by Kopf [1999].

Slip phase

To derive the first equation of motion of the 3DOF model in the *slip* phase, in Eqs 2.19 and 2.20 the tangential force component T is replaced by the expression of Eq. 2.27, representing the friction force T_f. These equations are combined by eliminating the normal force component N. Then, x_M and z_M and their time derivatives are expressed by means of the coordinates δ, x_A, s_A and their time derivatives according to Eqs 2.14, 2.17, and 2.18, leading to

$$\begin{aligned}(f_1 f_{\mu 1} - f_3 f_{\mu 2})\, m\ddot{\delta} + f_{\mu 1} m \ddot{x}_A - f_{\mu 2} m \ddot{s}_A + (f_2 f_{\mu 1} - f_4 f_{\mu 2})\, m\dot{\delta}^2 \\ + c_d \Big[(f_1 f_{\mu 1} - f_3 f_{\mu 2})\, \dot{\delta} + f_{\mu 1} \dot{x}_A - f_{\mu 2} \dot{s}_A \Big] + k_d \Big[f_{\mu 1} \left(x_M^{(\mathrm{roll})} + x_A \right) \\ - f_{\mu 2} \left(z_M^{(\mathrm{roll})} + s_A \right) \Big] = -f_{\mu 2} (mg + F_z) \qquad (2.34)\end{aligned}$$

with

$$f_{\mu 1} = \cos\delta - \operatorname{sign}(v_{rel})\, \mu \sin\delta \quad , \quad f_{\mu 2} = \sin\delta + \operatorname{sign}(v_{rel})\, \mu \cos\delta \qquad (2.35)$$

The second equation of motion is based on Eq. 2.23 derived by conservation of angular momentum, where T is likewise replaced by T_f according to Eq. 2.27, and N is substituted with Eq. 2.21. In the resulting relation, x_M and z_M and their time derivatives are substituted as before, with the outcome

$$\begin{aligned}\operatorname{sign}(v_{rel})\, \mu m (\tilde{f}_3 \ddot{\delta} + \ddot{x}_A \sin\delta + \ddot{s}_A \cos\delta) + \frac{I}{r} \ddot{\varphi} - \operatorname{sign}(v_{rel})\, \mu \Big\{ (mg + F_z) \cos\delta \\ - \tilde{f}_4 m \dot{\delta}^2 - \tilde{f}_3 c_d \dot{\delta} - c_d (\sin\delta\, \dot{x}_A + \cos\delta\, \dot{s}_A) - k_d \Big[\left(x_M^{(\mathrm{roll})} + x_A \right) \sin\delta \\ + \left(z_M^{(\mathrm{roll})} + s_A \right) \cos\delta \Big] \Big\} = \frac{M_M(t)}{r} \qquad (2.36)\end{aligned}$$

with

$$\tilde{f}_3 = f_1 \sin\delta + f_3 \cos\delta \quad , \quad \tilde{f}_4 = f_2 \sin\delta + f_4 \cos\delta \qquad (2.37)$$

The third equation of motion results from coupling of the two subsystems. To this end, Eqs 2.21 and 2.26 are combined through N. Considering Eq. 2.37, also this equation of motion is written in terms of the kinematic variables δ, x_A, s_A, and their time derivatives,

$$\begin{aligned}m \tilde{f}_3 \ddot{\delta} + m \ddot{x}_A \sin\delta + m \ddot{s}_A \cos\delta + c_d \tilde{f}_3 \dot{\delta} + (c_{sh} + c_d)\, \dot{x}_A \sin\delta + (c_{sv} + c_d)\, \dot{s}_A \cos\delta \\ + m \tilde{f}_4 \dot{\delta}^2 + (k_{sh} + k_d)\, x_A \sin\delta + (k_{sv} + k_d)\, s_A \cos\delta \\ + k_d \Big[x_M^{(\mathrm{roll})} \sin\delta + z_M^{(\mathrm{roll})} \cos\delta \Big] = (mg + F_z) \cos\delta \qquad (2.38)\end{aligned}$$

Eqs 2.34, 2.36, and 2.38 of the 3DOF system express the motion in the *slip* phase in terms of the four coordinates x_A, s_A, δ and φ. Thus, a forth equation, which captures coupling between x_A and s_A due to tangential friction contact at point C, needs to be established. To this end, Eqs 2.24 and 2.25, where T has been replaced by T_f (Eq. 2.27), are combined by eliminating the normal force component N, which leads after some algebra to

$$f_{\mu 1} (c_{sh} \dot{x}_A + k_{sh} x_A) = f_{\mu 2} (c_{sv} \dot{s}_A + k_{sv} s_A) \qquad (2.39)$$

The set of nonlinear ODEs 2.34, 2.36, 2.38, and 2.39 describes the motion of the interacting roller-soil model in the *slip* phase. The state space representation of these equations for efficient numerical solution is introduced in Appendix D.1.

2.3.4 Procedure of solution

The response is obtained numerically by switching between the set of the first order ODEs for the *stick* phase (Eq. D.2) and the set of ODEs for the *slip* phase (Eq. D.11), basically as described in [Leine et al, 1998]. In the *stick* phase, the outcomes of Eq. D.2 (i.e. x_A, s_A, δ, $\dot{x}_A$, $\dot{s}_A$, $\dot{\delta}$), are substituted into the original equations of motion 2.30, 2.31 and 2.32, which are solved for the accelerations $\ddot{x}_A$, $\ddot{s}_A$, and $\ddot{\delta}$ (see Appendix D.1). Accelerations $\ddot{x}_A$, $\ddot{s}_A$, $\ddot{\delta}$, $\ddot{\varphi}$ of the *slip* phase given in Appendix D.1 are obtained by rearranging of Eqs 2.34, 2.36, 2.38, and D.9, where the outcomes of Eq. D.11 (i.e. x_A, s_A, δ, φ, $\dot{x}_A$, $\dot{s}_A$, $\dot{\delta}$, and $\dot{\varphi}$) have been inserted. In both phases of the stick-slip motion, the desired acceleration components $\ddot{x}_M$ and $\ddot{z}_M$ of the drum center M are obtained by evaluation of Eqs 2.18. This analysis continues until the steady state response is reached.

2.4 Detailed response study for a specific roller

The subsequent studies are based on the machine properties of the HD$^+$ 90 VO tandem roller [HAMM AG, 2011] listed in Table 21 (roller 1) because for this device acceleration response data of the drum center M recorded in field tests are available [Pistrol, 2016]. Note that in contrast to the parameters specified in Table 21 the subsequent investigations are based on a viscous suspension damping of $c_d = 3 \times 10^3$ Ns/m [HAMM AG, 2017], i.e. then times the value given in Table 21. However, the studies in Section 2.5, where the suspension properties are varied, show that this has no significant effect on the results. It is assumed that all considered non-cohesive soil conditions exhibit a *Poisson*'s ratio ν of 0.3 and a density ρ of 1900 kg/m^3. The shear modulus G of the soil is varied in steps of 5 MN/m^2 between 5 and 70 MN/m^2. The soil parameters (shear modulus G, density ρ, *Poisson*'s ratio ν), and the corresponding half contact length a_0 (see Fig. B1) between drum of the four considered oscillation rollers and soil are listed in Table B1 in Appendix B. The resulting coefficients k_{sh} and k_{sv} (Eq. B.2), and damping parameters c_{sh} and c_{sv} (Eq. B.4) are listed in Table B2, see Appendix B. Note that c_{sh} and c_{sv} do not change with increasing soil stiffness because *Poisson*'s ratio ν and soil density ρ are assumed to be constant, compare with Eq. B.4 given in Appendix B. In the base case, a semicircular shaped settlement trough with radius $R = 0.606$ m is assumed, which is slightly larger than the drum radius $r = 0.60$ m. The corresponding spiral parameters representing a semicircle are $k = 0$ and $a = R$ (see Appendix C.2).

In the following, the steady state acceleration components of the drum center M, $\ddot{x}_M$ and $\ddot{z}_M$, and thereof derived characteristic response quantities (e.g. plot $\ddot{z}_M$ over $\ddot{x}_M$) are presented and analyzed because they serve as basis of a novel CCC methodology [Pistrol, 2016], as discussed in the introduction. The area inside the plot $\ddot{z}_M$-$\ddot{x}_M$ is calculated using the Matlab function *inploygon* [Mathworks, 2018] assuming a sample size of at least 1×10^5. The results are verified by application of *Green*'s theorem [Nykamp, 2018].

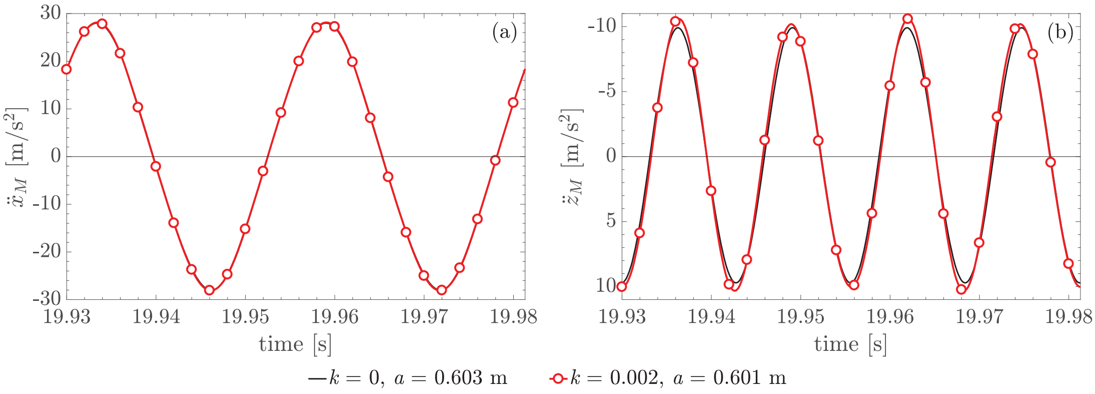

Figure 25: Time history of the (a) horizontal and (b) vertical acceleration in the drum center; soft soil $G = 5$ MN/m^2; $M_{Md} = 0$; pure rolling motion; symmetric vs. asymmetric settlement trough

2.4.1 Pure rolling (stick) motion of the drum

At first, the influence of the geometry of the settlement trough on the predicted accelerations of a drum in pure rolling motion is investigated. That is, it is assumed that the tangential contact force T does not exceed the sliding friction T_f at any time. To this end, a semicircular settlement through ($k = 0$, $a = R = 0.603$ m) as well as an asymmetric settlement trough with the shape of a logarithmic spiral ($k = 0.002$, $a = 0.601$ m) are considered. In this study, no driving torque is applied, i.e. $M_{Md} = 0$. As an example, Fig. 25 shows for soil stiffness $G = 5$ MN/m^2 the steady state acceleration components $\ddot{x}_M$ and $\ddot{z}_M$ with respect to time t during two excitation periods for both settlement troughs. In Fig. 26 (a), the time history of the corresponding position angle δ is displayed, and in Fig. 26 (b) $\ddot{z}_M$ is plotted against $\ddot{x}_M$. The vertical acceleration ($\ddot{z}_M$) is a result of the up- and downward motion of the drum in the settlement trough during each period of excitation. Due to the nonlinear motion, the period of $\ddot{z}_M$ is half of the excitation period, i.e. two excitation periods correspond to four periods of vertical acceleration $\ddot{z}_M$. If the settlement trough is of semicircular shape (solid lines in black), both the horizontal and vertical acceleration components of M are symmetric with respect to the horizontal axis. The plot $\ddot{z}_M$ vs. $\ddot{x}_M$, represented in Fig. 26 (b) by a solid black line, has the shape of "recumbent eight", and is symmetric with respect to the vertical and horizontal axes. An asymmetric settlement trough results in a slightly asymmetric pattern of the position angle δ (see Fig. 26 (a), red line with circular markers), i.e. the amplitudes in the positive domain are larger than in the negative domain. Consequently, also the peak values of the vertical acceleration $\ddot{z}_M$ become slightly larger (see Fig. 25 (b)). The horizontal acceleration $\ddot{x}_M$, which has the same period as the excitation period, remains virtually unaffected from the shape of the settlement trough (see Fig. 25 (a)). Thus, the plot $\ddot{x}_M$-$\ddot{z}_M$ shown by a red line with circular markers becomes slightly asymmetric, as seen in Fig. 26 (b). Since these and further results not presented here have revealed that the asymmetry of the settlement trough has only a very small effect on the response, subsequently, the drum acceleration is examined based on a semicircular settlement trough (i.e. $k = 0$ and $a = R$, see Fig. C1 in Appendix C.2).

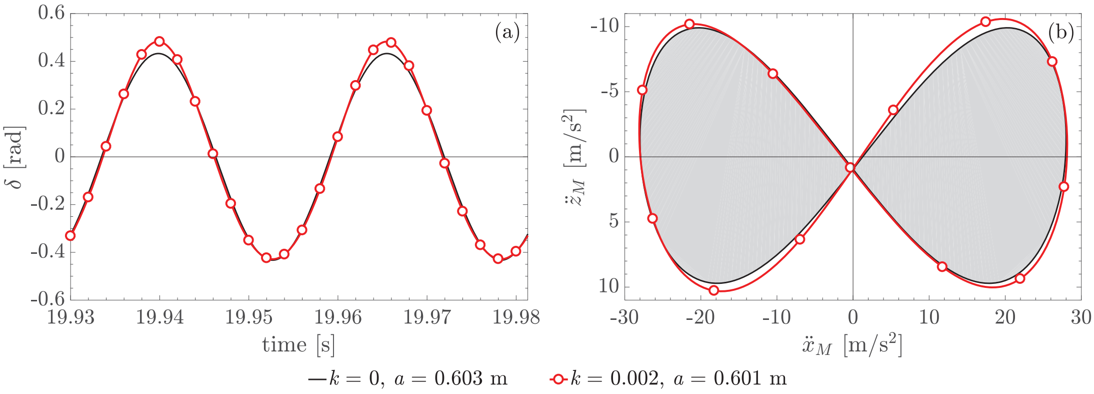

Figure 26: Time history of (a) position angle δ and (b) plot $\ddot{z}_M$ vs. $\ddot{x}_M$; soft soil $G = 5$ MN/m^2; $M_{Md} = 0$; pure rolling motion; symmetric vs. asymmetric settlement trough

Next, the influence of the radius R of a semicircular settlement trough on the drum center acceleration is investigated for all considered soil shear moduli G, for $M_{Md} = 0$. Fig. 27 shows the peak acceleration components, (a) $\ddot{x}_{M\max}$ and (b) $\ddot{z}_{M\max}$, respectively, as a function of G for four selected radii R ranging from 0.603 m to 0.65 m. As observed, the horizontal peak acceleration $\ddot{x}_{M\max}$ increases continuously from about $25 - 28$ m/s^2 ($G = 5$ MN/m^2) to about 56 m/s^2 at $G = 40$ MN/m^2, where the maximum is attained, and then slightly descends to 50 m/s^2 at $G = 70$ MN/m^2, almost unaffected by the radius R (Fig. 27 (a)). The vertical accelerations $\ddot{z}_{M\max}$ also increase with increasing stiffness G, however, they reach their maximum at lower stiffness of $G = 15 - 20$ MN/m^2, and then, decrease with increasing soil stiffness with a steep gradient (see Fig. 27 (b)). In contrast to $\ddot{x}_{M\max}$, the magnitudes of $\ddot{z}_{M\max x}$ are sensitive to the radius R of the settlement trough, i.e. the closer R is to the drum radius r, the larger $\ddot{z}_{M\max}$ becomes. In general, the vertical peak acceleration components are smaller than the corresponding horizontal ones. As observed, the ratio $\ddot{z}_{M\max}$ to $\ddot{x}_{M\max}$ decreases from 0.21 at $R = 0.603$ m to about 0.01 at $R = 0.65$ m. If $R = 0.606$ m, $\ddot{z}_{M\max}$ is about 10% of $\ddot{x}_{M\max}$. The following studies are based on a settlement trough radius of $R = 0.606$ m, i.e. one percent larger than the drum radius r.

Fig. 28 illustrates that also the phase lag between the harmonic excitation torque $M_{Mu}(t)$ and the drum rotation φ $(= \frac{R-r}{r}\delta)$ (see Eq. C.12 in Appendix C.2) strongly depends on the soil stiffness G. Fig. 28 (a) shows one period of the harmonic excitation torque $M_{Mu}(t)$ (dashed line) and the corresponding drum rotation φ for four values of the soil stiffness G, as specified in the legend. In this representation, the effect of G on both the phase lag and the amplitude of φ becomes apparent. The maximum value of the phase lag occurs at $G = 50$ MN/m^2 (Fig. 28 (b)). At the lowest considered soil stiffness, $G = 5$ MN/m^2, the phase lag is -0.84π. For $G \to 0$ (lifted drum), the phase lag converges towards $-\pi$. That is, an oscillation drum without soil contact conducts a pure forward-backward rotation with a phase lag $-\pi$ between $M_{Mu}(t)$ and φ.

The steady state acceleration components $\ddot{x}_M$ and $\ddot{z}_M$ (see Fig. 29 (a) and (b), respectively) of the drum center M demonstrate the effect of the soil stiffness on the peak response and phase lag, exemplarily shown for four selected shear moduli G and two excitation periods. While the maximum of $\ddot{x}_M$ is about the same for $G = 25$, 50 and 70 MN/m^2, the peak value of $\ddot{z}_M$ related to $G = 25$ MN/m^2 is about 3.3 and 8.4, respectively, times larger than for $G = 50$ and 70 MN/m^2. Another observation is that the period of $\ddot{z}_M$ is only half of the period of $\ddot{x}_M$, which corresponds to the excitation period. Additionally, in Fig. 210 the phase lag between $\ddot{x}_M$ and $\ddot{z}_M$ is depicted. As observed, the predicted phase lag is about 0.11 rad for the lowest shear modulus, the maximum of 0.64 is obtained at $G = 25$ MN/m^2, and with increasing soil stiffness it subsequently decreases. For stiff soils with $G \geq 60$ MN/m^2 the phase is negative. Note that a positive phase lag indicates that $\ddot{z}_M$ lags behind $\ddot{x}_M$. Plotting the vertical component $\ddot{z}_M$ against its horizontal counterpart $\ddot{x}_M$ results in another meaningful response representation, shown in Fig. 211 (a). The result is a so-called *Lissajous curve* (e.g. [Klotter, 1981], [Ferréol, 2017b]) (see Appendix E), whose shape is either similar to the *lemniscate of Gerono* [Lawrence, 1972], i.e. the *eight curve* [Lawrence, 1972] (for $G = 5$, 50 and 70 MN/m^2), or similar to a general *besace* [Ferréol, 2017a] (for $G = 25$ MN/m^2). In the latter case ($G = 25$ MN/m^2), the node of the resulting figure is shifted considerably along the vertical axis in the positive domain. This is a result of the phase lag between $\ddot{x}_M$ and $\ddot{z}_M$, which has its maximum at $G = 25$ MN/m^2 (see Fig. 210). All figures are symmetric with respect to the vertical axis because the driving torque is zero, i.e. $M_{Md} = 0$.

The response in the frequency domain for four selected subsoils (Figs 212 and 213) reveals that the frequency content (f) of the vertical accelerations $\ddot{z}_M$ is two-times the excitation frequency $\bar{f}$ if $M_{Md} = 0$ (Fig. 212 (b)). In Figs 212 and 213 the frequency f is normalized by the excitation frequency $\bar{f}$. In contrast, $\ddot{x}_M$ is governed by $\bar{f}$, see Fig. 212 (a). Since the dominating frequency content of $\ddot{z}_M$ and $\ddot{x}_M$ differs by a factor of two, the $\ddot{z}_M$-$\ddot{x}_M$ plot results in the *Lissajous curves* shown in the previous figure (see also Appendix E).

When additionally a constant driving torque of $M_{Md} = 0.05 M_{Mu}^{(0)}$ is applied to the drum, the spectrum of the vertical accelerations $\ddot{z}_M$ contains now two frequencies, one at $f = 2\bar{f}$ (as for $M_{Md} = 0$) and one at $f = \bar{f}$ (see Fig. 213 (b)). The spectral amplitudes of $\ddot{z}_M$ are largest for $f/\bar{f} = 1$, except for the softest subsoil ($G = 5$ MN/m^2). The ratio of the amplitude at $f = 2\bar{f}$ to the amplitude at operating frequency $\bar{f}$ decreases from 1.11

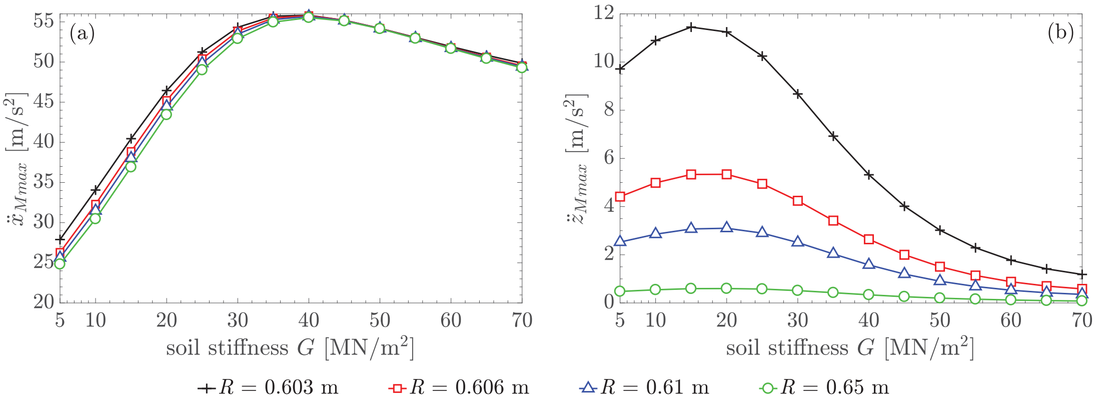

Figure 27: Peak of the (a) horizontal and (b) vertical acceleration in the drum center as a function of soil shear modulus G for selected radii R of a semicircular settlement trough; $M_{Md} = 0$; pure rolling motion

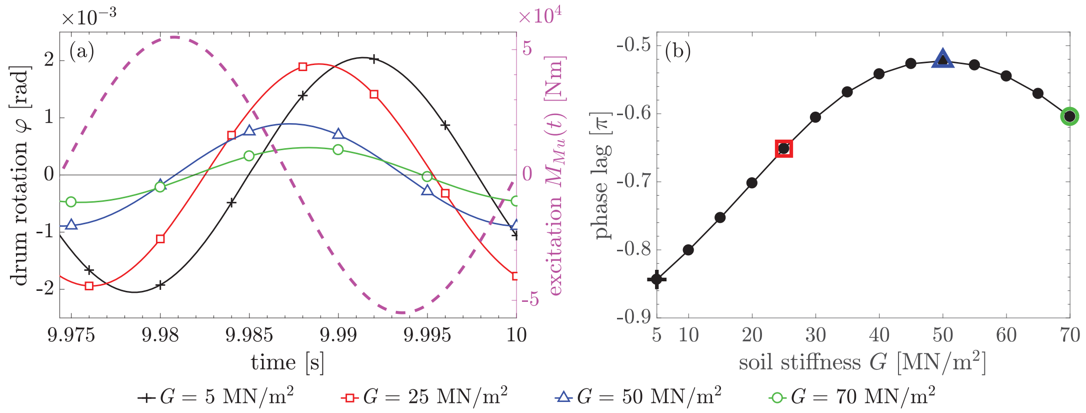

Figure 28: Phase lag between excitation torque $M_{Mu}(t)$ (dashed line) and drum rotation φ - (a) time histories for four selected soil shear moduli G, and (b) phase lag for the entire range of G; $M_{Md} = 0$; pure rolling motion

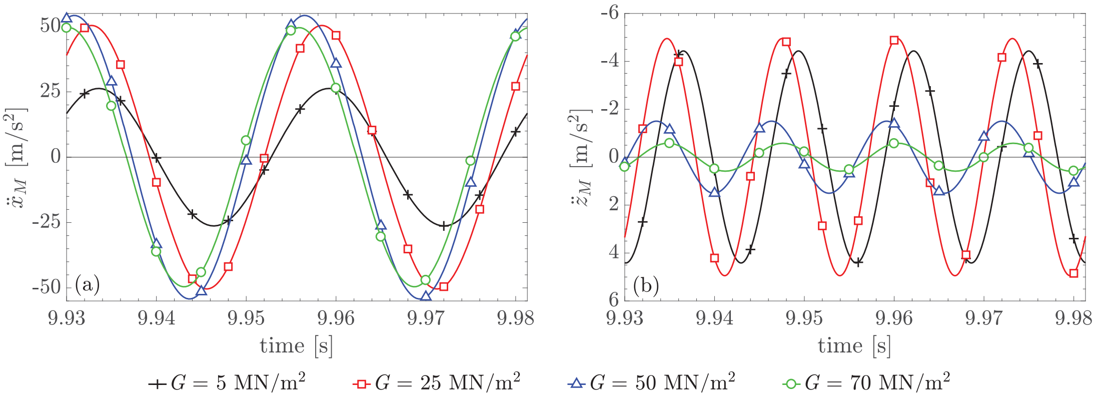

Figure 29: Steady state (a) horizontal and (b) vertical acceleration in the drum center for four selected soil shear moduli G; $M_{Md} = 0$; pure rolling motion

($G = 5$ MN/m^2) to 0.24 ($G = 70$ MN/m^2). The amplitudes at $f/\bar{f} = 2$ are virtually the same as for $M_{Md} = 0$ (compare Fig. 212 (b) with Fig. 213 (b)). The frequency spectrum of the horizontal accelerations $\ddot{x}_M$ is, however, virtually not affected by the driving torque M_{Md} (compare Fig. 212 (a) with Fig. 213 (a)). Thus, the application of the driving torque M_{Md}, which captures the effect of the translational drum motion with the roller driving speed, changes the shape of the $\ddot{z}_M$-$\ddot{x}_M$ plot, as seen in Fig. 211 (b). The *Lissajous curves* become asymmetric and distorted, depending on the soil stiffness and the ratio of the amplitude at $f = 2\bar{f}$ to the amplitude at operating frequency $\bar{f}$. For large soil stiffness, the asymmetric *Lissajous* similar curves degenerate into curves without node.

Another important response quantity is the area inside the $\ddot{z}_M$ over $\ddot{x}_M$ figure. Recent experimental studies have revealed that this area increases with increasing shear modulus G, and thus, has been proposed as performance indicator of the actual soil compaction [Pistrol, 2016]. For zero driving torque, i.e. $M_{Md} = 0$, the area inside the $\ddot{z}_M$-$\ddot{x}_M$ figure is equal to the product of two times the amplitudes of $\ddot{x}_M$ and twice the amplitude of $\ddot{z}_M$, i.e. $4|\ddot{X}_M(\bar{f})||\ddot{Z}_M(2\bar{f})|$, multiplied by a reduction factor that depends on the phase lag between $\ddot{x}_M$ and $\ddot{z}_M$ (for further details see Appendix E). In Fig. 214, this area is plotted against shear modulus G, both for simulations without driving torque (black line with "+" markers) and with driving torque (red line with circular markers). It is seen that for zero driving torque the maximum area is obtained at a quite low stiffness between $G = 20$ MN/m^2 and $G = 25$ MN/m^2. As such, this area would be an appropriate performance indicator only for soil compaction up to a soil stiffness of about $G = 25$ MN/m^2. However, in the more realistic modeling scenario, the driving torque $M_{Md} = 0.05 M_{Mu}^{(0)}$ shifts the maximum of the area to a stiffer subsoil with $G = 40$ MN/m^2. Thus, the applicability of the area as compaction control value is extended to a larger soil range.

2.4.2 Stick-slip motion of the drum

The following studies on the stick-slip motion are based on a coefficient of friction of $\mu = 0.50$ between drum and soil. Figs 215 and 216 show for two excitation periods the steady state time histories of $\ddot{x}_M$ and $\ddot{z}_M$ for four soil stiffness parameters G specified in the legend, and an excitation torque of $M_{Md} = 0$ (Fig. 215) and $M_{Md} = 0.05 M_{Mu}^{(0)}$ (Fig. 216), respectively. These results illustrate the grave effect of slip between drum and soil surface on the response. In general, in stick-slip motion the amplitudes of $\ddot{x}_M$ and $\ddot{z}_M$ are significantly smaller compared to pure rolling of the drum, compare Fig. 215 with Fig. 29. In the *slip* phase, both the positive and negative peaks of the horizontal drum center acceleration are cut (see Fig. 215 (a)). A kink in the time history of $\ddot{x}_M$ indicates the transition from the *stick* into the *slip* phase and vice versa. During the *slip* phase, both the horizontal and vertical acceleration component in the drum center decrease. Fig. 215 (a) also shows that the slope of $\ddot{x}_M$ in the slip phase is larger the lower the soil stiffness. In contrast to $\ddot{x}_M$, the component $\ddot{z}_M$ decreases significantly with increasing soil shear modulus (see Fig. 215 (b)).

The horizontal response without excitation torque (i.e. $M_{Md} = 0$) is almost symmetric with respect to the time axis, while for an excitation torque of $M_{Md} = 0.05 M_{Mu}^{(0)}$ the *slip* phase in the negative horizontal acceleration range is only about the half of the one in the positive range (compare Fig. 215 (a) with Fig. 216 (a)). Also, the

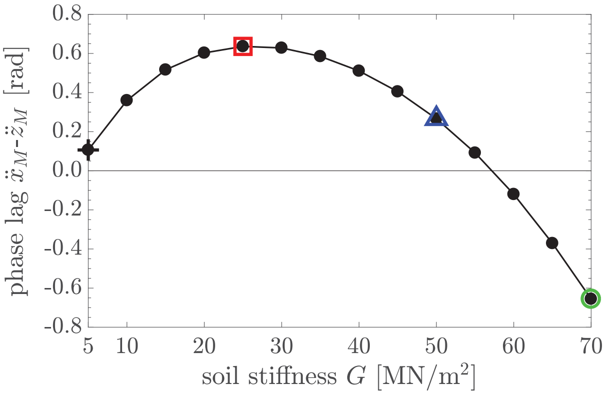

Figure 210: Phase lag between $\ddot{x}_M$ and $\ddot{z}_M$ as a function of shear modulus G; $M_{Md} = 0$; pure rolling motion

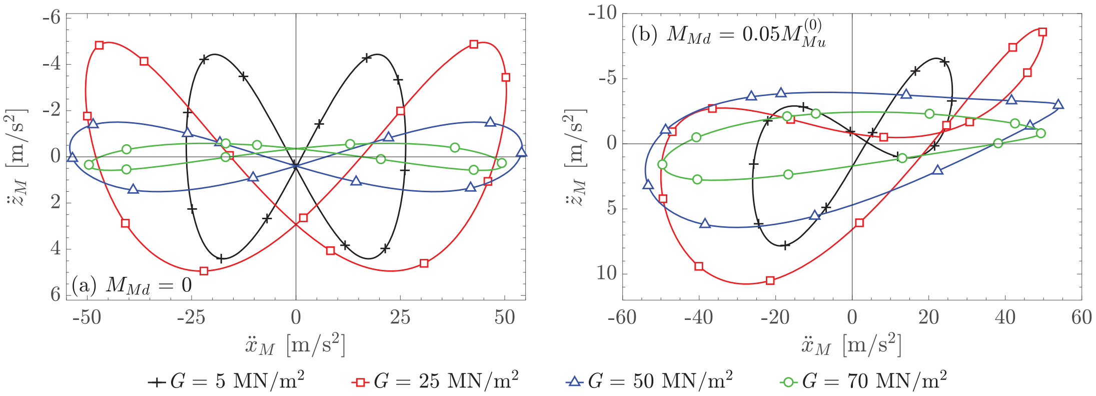

Figure 211: Plot $\ddot{z}_M$ over $\ddot{x}_M$; (a) $M_{Md} = 0$ vs. (b) $M_{Md} = 0.05M_{Mu}^{(0)}$; pure rolling motion

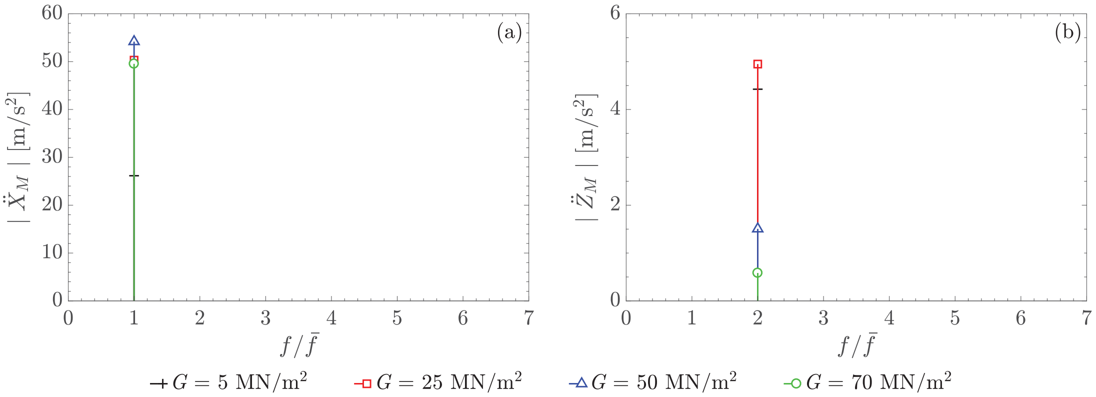

Figure 212: Frequency spectrum of the (a) horizontal and (b) vertical acceleration in the drum center for four selected shear moduli G; pure rolling motion; $M_{Md} = 0$

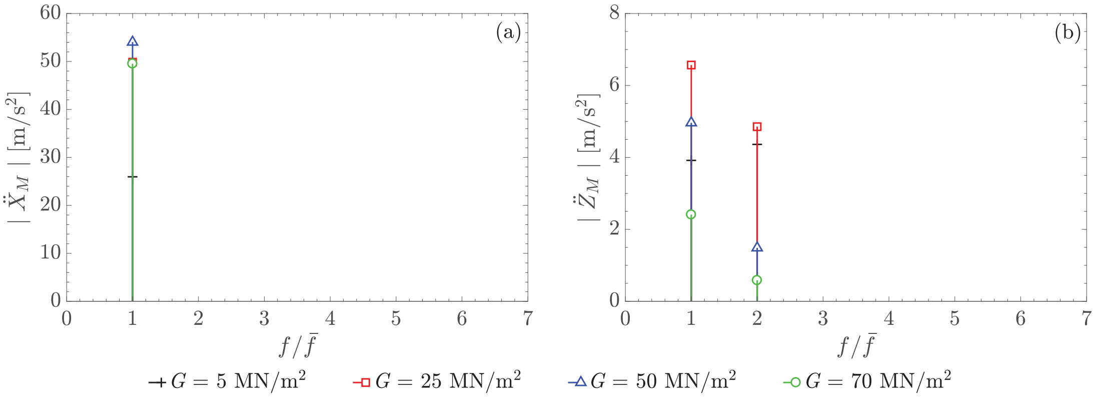

Figure 213: Frequency spectrum of the (a) horizontal and (b) vertical acceleration in the drum center for four selected shear moduli G; pure rolling motion; $M_{Md} = 0.05M_{Mu}^{(0)}$

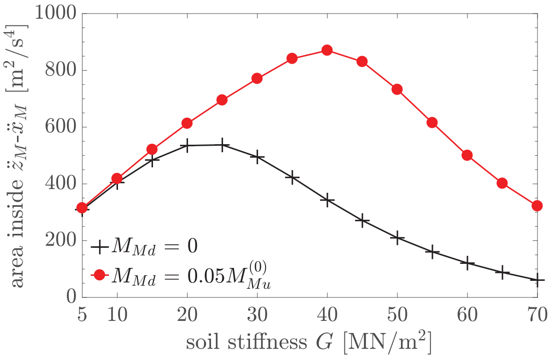

Figure 214: Area inside the $\ddot{z}_M$-$\ddot{x}_M$ figure as a function of soil shear modulus G; pure rolling motion; $M_{Md} = 0$ and $M_{Md} = 0.05M_{Mu}^{(0)}$, respectively

negative response amplitude is larger than the positive one. Another observation is that horizontal steady state stick-slip acceleration $\ddot{x}_M$ is only slightly affected by the soil stiffness parameter, and concerns the duration of the *slip* phase, which increases slightly with increasing soil stiffness. In contrast, both signature and amplitude of the vertical component $\ddot{z}_M$ depends strongly on the subsoil properties (see Fig. 216 (b)). The acceleration components $\ddot{z}_M$ look different in the positive and negative range, both for $M_{Md} = 0$ and $M_{Md} = 0.05M_{Mu}^{(0)}$. For $M_{Md} = 0$, the lowest shear modulus $G = 5$ MN/m^2 yields the largest vertical acceleration amplitude (see Fig. 215 (b)). Applying a driving torque of $M_{Md} = 0.05M_{Mu}^{(0)}$, yields the positive amplitudes of $\ddot{z}_M$ between 2 (for $G = 5$ MN/m^2) and 7.6 (for $G = 70$ MN/m^2) times larger than for $M_{Md} = 0$ (see Fig. 216 (b)). In the negative range, no characteristic response pattern is observed, i.e. the pattern depends strongly on the soil shear modulus G.

Figs 217 and 218 represent (a) $\ddot{x}_M$ and (b) $\ddot{z}_M$ in the frequency domain both for $M_{Md} = 0$ (Fig. 217) and $M_{Md} = 0.05M_{Mu}^{(0)}$ (Fig. 218). First, the spectral response without driving torque ($M_{Md} = 0$) is discussed. Fig. 217 (a), representing the horizontal drum accelerations $\ddot{x}_M$, contains only odd harmonics because in the *slip* phase the response is cut symmetrically. The overtones at uneven multiples of the excitation frequency ($f/\bar{f}$ = 3, 5, 7, ...) indicate that the drum motion includes *slip* phases, compare with the spectrum for pure rolling motion (see Fig. 212 (a)). The largest amplitude belongs to the operating frequency $\bar{f}$ (i.e. $f/\bar{f} = 1$). The spectrum of $\ddot{z}_M$ for $M_{Md} = 0$ (Fig. 217 (b)) contains only even harmonics ($f/\bar{f}$ = 2, 4, 6, ...), with the largest amplitude at f=2$\bar{f}$. The larger the soil stiffness the more pronounced become the higher harmonics in the response, both for $\ddot{x}_M$ and $\ddot{z}_M$. While with increasing shear modulus G the amplitudes in the frequency spectrum of $\ddot{x}_M$ increase, the amplitudes in the frequency spectrum of $\ddot{z}_M$ decrease.

When applying a driving torque of $M_{Md} = 0.05M_{Mu}^{(0)}$ to the drum, the spectra for $\ddot{x}_M$ and $\ddot{z}_M$ contain both odd and even harmonics (see Fig. 218). They are both dominated by the operating frequency $\bar{f}$, except for the stiffest subsoil $G = 70$ MN/m^2. The additional uneven harmonics in the spectrum of $\ddot{z}_M$ ($f/\bar{f}$ = 1, 3, 5, ...) result from the response asymmetry due to driving torque M_{Md}, whereas the new even harmonics ($f/\bar{f}$ = 4, 6, 8, etc.) come from the *slip* phase of the motion (see Fig. 218 (b)). In the same spectrum, the ratio of the amplitude at f=2$\bar{f}$ to the amplitude at operating

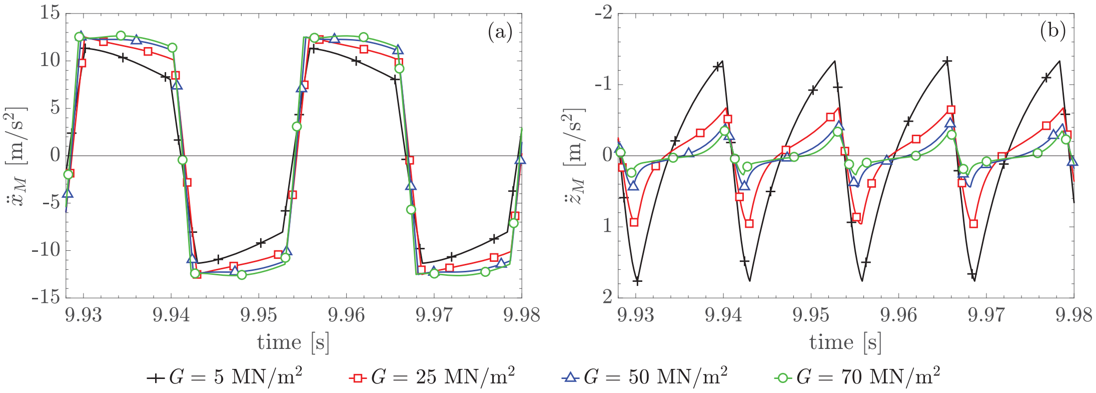

Figure 215: Steady state (a) horizontal and (b) vertical acceleration in the drum center for four selected soil shear moduli G; stick-slip motion ($\mu = 0.50$); $M_{Md} = 0$

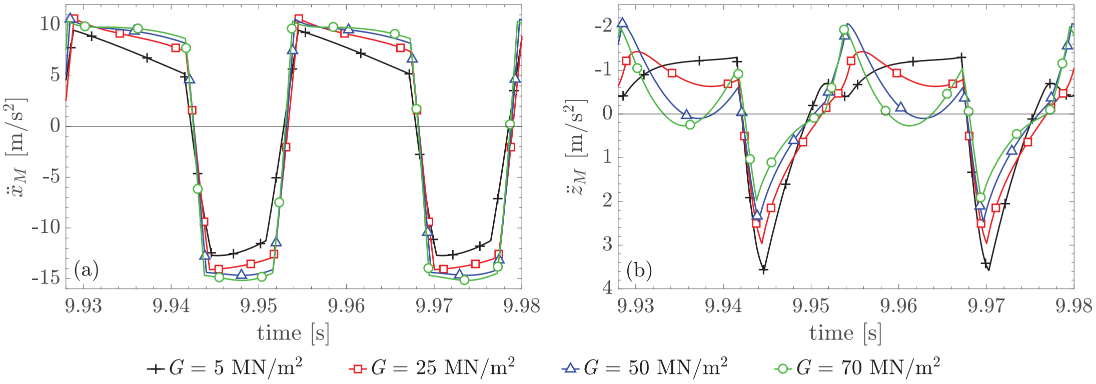

Figure 216: Steady state (a) horizontal and (b) vertical acceleration in the drum center for four selected soil shear moduli G; stick-slip motion ($\mu = 0.50$); $M_{Md} = 0.05 M_{Mu}^{(0)}$

frequency $\bar{f}$ decreases from 0.65 ($G = 5$ MN/m^2) to 0.38 ($G = 25$ MN/m^2) and then increases up to about 1.03 ($G = 70$ MN/m^2).

Comparing the $\ddot{z}_M$-$\ddot{x}_M$ plot for stick-slip motion and zero driving torque (see Fig. 219 (a)) with the corresponding plot for pure rolling motion (see Fig. 211 (a)) shows that the *slip* phase causes "peak cut" and distortion of the *Lissajous* similar curves, however, the symmetry with respect to the vertical axis is preserved. The resulting shape is similar to a "bow tie" (see Fig. 219 (a)). The effect of a driving torque of $M_{Md} = 0.05 M_{Mu}^{(0)}$ on the $\ddot{z}_M$-$\ddot{x}_M$ plot is visualized in Fig. 219 (b). The resulting curves are twisted and the symmetry gets lost. Moreover, with increasing soil stiffness the node in the curve moves to the right, and disappears completely for $G = 50$ and 70 MN/m^2. This behavior has already been observed in pure rolling motion, as shown in Fig. 211 (b).

Since in the stick-slip motion the amplitudes of the drum accelerations are smaller than for pure rolling motion, also the area inside the $\ddot{z}_M$-$\ddot{x}_M$ curves decreases. In Fig. 220 this area is depicted as a function of the underlying soil shear stiffness G. When the drum oscillates at the bottom of the settlement trough ($M_{Md} = 0$), this

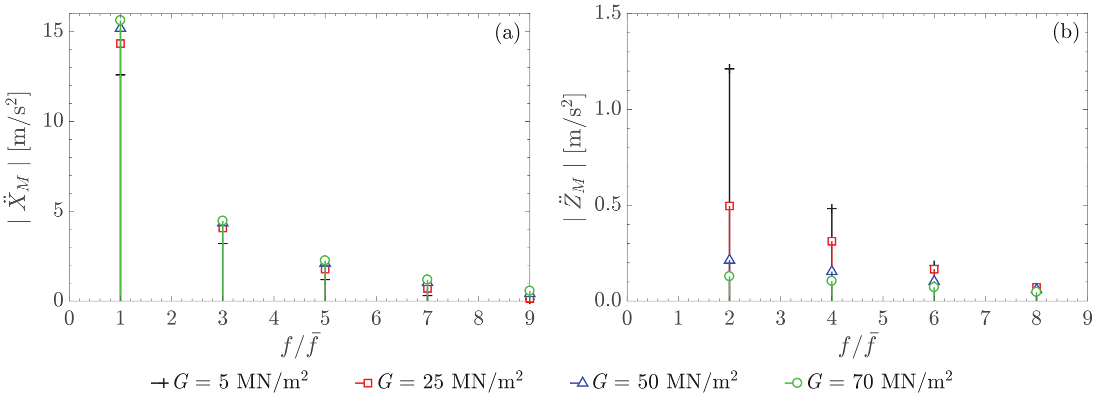

Figure 217: Frequency spectrum of the (a) horizontal and (b) vertical acceleration in the drum center for four selected shear moduli G; stick-slip motion ($\mu = 0.50$); $M_{Md} = 0$

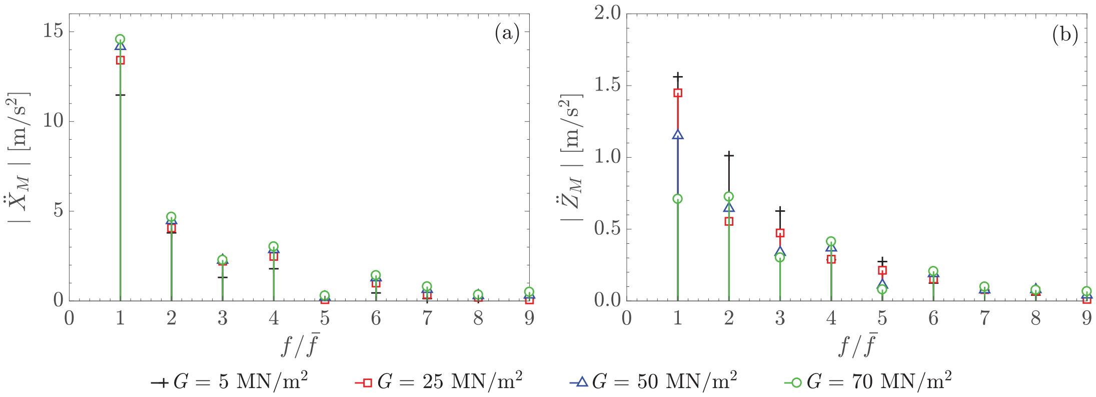

Figure 218: Frequency spectrum of the (a) horizontal and (b) vertical acceleration in the drum center for four selected shear moduli G; stick-slip motion ($\mu = 0.50$); $M_{Md} = 0.05 M_{Mu}^{(0)}$

area shown by a black line with "+" markers decreases continuously with increasing soil stiffness (see Fig. 220). This result is in contradiction to outcomes of field tests presented in [Pistrol, 2016]. A driving torque of $M_{Md} = 0.05 M_{Mu}^{(0)}$ increases the area in the whole considered soil parameter range compared to $M_{Md} = 0$, as seen in this figure. The red line with circular markers representing this area exhibits a minimum at $G = 20$ MN/m^2 and a maximum at $G = 45$ MN/m^2. For pure rolling motion the maximum occurs at slightly smaller soil stiffness of $G = 40$ MN/m^2 (see Fig. 214). However, the minimum only appears in the stick-slip motion.

To support the proposed analytical model, the frequency content of the computed results and of selected drum accelerations recorded during in situ field tests [Pistrol, 2016] is examined. Fig. 221 shows frequency spectra of (a) $\ddot{x}_M$ and (b) $\ddot{z}_M$ for a dense gravel, i.e. $G = 25$ MN/m^2. As observed, up to the third harmonic the computed and the recorded response are in good agreement. In the horizontal accelerations, the overtone at the second multiple of the excitation frequency is overestimated by the analytical model (see Fig. 221 (a)). In the frequency range $f/\bar{f} > 3$, the normalized amplitudes of the computed accelerations are larger than the ones of the measured

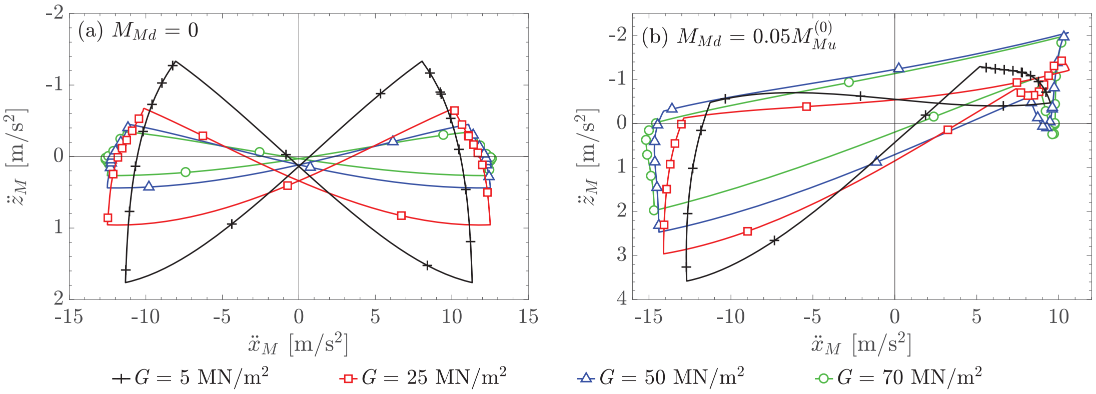

Figure 219: Vertical ($\ddot{z}_M$) over horizontal ($\ddot{x}_M$) acceleration in the drum center; stick-slip motion ($\mu = 0.50$); (a) $M_{Md} = 0$ and (b) $M_{Md} = 0.05M_{Mu}^{(0)}$

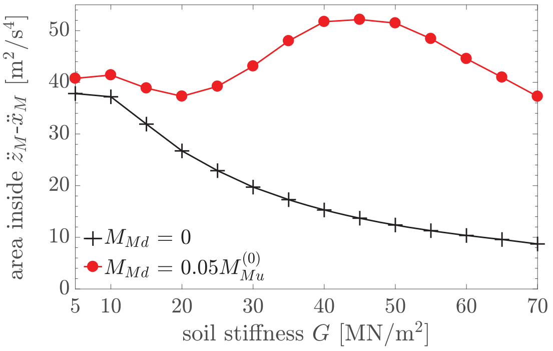

Figure 220: Area inside the $\ddot{z}_M$-$\ddot{x}_M$ figure as a function of soil shear modulus G; stick slip motion ($\mu = 0.50$); $M_{Md} = 0$ and $M_{Md} = 0.05M_{Mu}^{(0)}$, respectively

response. This is due to the fact that in the measured response the transition from the stick to *slip* phases is smoother than in the analytical model, consequently, the "peak cut" of the horizontal drum accelerations is less pronounced. One reason is the coefficient of friction between drum and subsoil, which is assumed to be constant in the analytical model. In the presented study, a constant value of $\mu = 0.50$ has been assumed, in reality, however, this parameter varies within a certain range. Nevertheless, the analytical model is capable of predicting the overall response behavior of the drum observed in the field.

The presented 3DOF lumped parameter model was validated based on a two-dimensional FE model that allows the simulation of the response of the drum oscillating in a defined semi-circular notch on the surface of a linear elastic soil halfspace. To this end, in Appendix F the frequency content of $\ddot{x}_M$ and $\ddot{z}_M$ is set in contrast. The evaluations demonstrate that the computed drum responses of the lumped parameter model and the FE model based on linear elastic soil behavior are in good agreement if the contact length $2a_0$ resulting from the FE simulations is used when calculating the parameters of the discrete springs and dampers (k_{sv}, k_{sh}, c_{sv}, c_{sh}), which represent the elastic soil halfspace.

2.5 Parametric studies

Based on the investigations of the tandem roller HD$^+$ 90 VO (roller 1) presented in Section 2.4, in the following the response of three additional types of oscillation rollers, i.e. a H7i VIO (roller 2), HD13i VIO (roller 3) and HD$^+$ 140i VO (roller 4) roller, is studied in the same way.

The parameters of the considered rollers are summarized in Table 21. Rollers 1 and 2 have virtually the same drum geometry with the same unbalance configuration. However, the drum weight of roller 1 is about 2 % and the operating weight (and therefore the static axle load) is 22 % higher. In addition, the operating frequency of roller 1 is slightly larger. Consequently, the amplitude of the oscillation moment of roller 1 is about 18 %) larger than the one of roller 2. In contrast, the drum width of rollers 3 and 4 is 27 % larger, and the drum radius is about 17 % (roller 4) and 25 % (roller 3), respectively, larger. Compared to roller 2, the drum weight of roller 4 is almost 60 % and of roller 3 almost 93 % larger. The static axle load of roller 4 is about 74 % and of roller 3 about 99 % higher. Moreover, the different unbalance configuration in combination with the standard operating frequency (which is the lowest for roller 4) leads to an almost 2 (roller 4) and 2.7 (roller 3), respectively, times larger amplitude of the oscillation moment compared to roller 2.

As in Section 2.4, the considered subsoil conditions differ only by the shear modulus G in the range between 5 and 70 MN/m^2 in steps of 5 MN/m^2, while *Poisson*'s ratio $\nu = 0.3$ and density $\rho = 1900\,\mathrm{kg/m^3}$ are the same for all soils. For each considered roller, the half contact length a_0 between drum and subsoil according to Eq. B.1 is given in Table B1 in Appendix B. The corresponding discrete soil stiffness coefficients k_{sh} and k_{sv} (Eq. B.2) and damping parameters c_{sh} and c_{sv} (Eq. B.3) are listed in Table B2, see Appendix B. The damping parameters c_{sh} and c_{sv} are the same for all subsoil conditions, since *Poisson*'s ratio ν and soil density ρ are the same, and shear stiffness G cancels when in Eqs B.3 variable a_0 is replaced by Eq. B.1. According with Section 2.4, it is assumed that the radius R of the semicircular shaped settlement trough is 1.01 times the drum radius r, i.e. $R/r = 1.01$. Moreover, the constant torque M_{Md} applied to simulate that the drum oscillates on the slope of the settlement trough

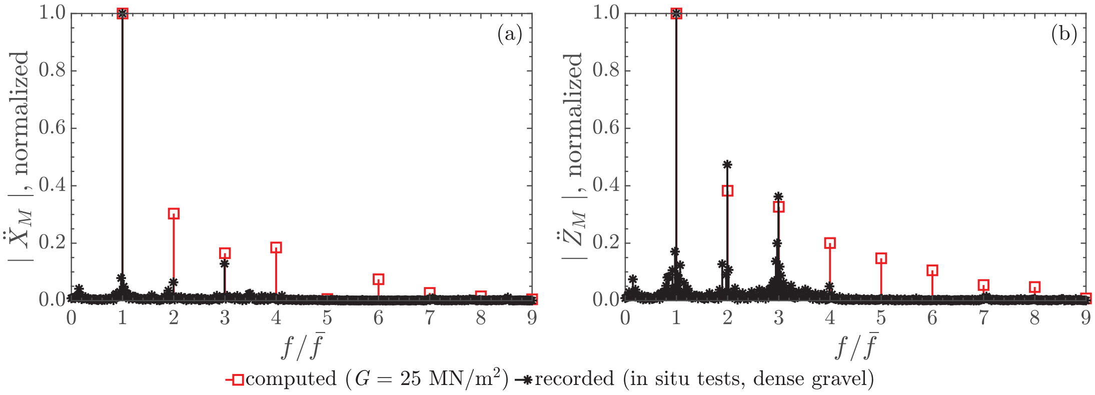

Figure 221: Frequency spectrum of the (a) horizontal and (b) vertical acceleration in the drum center; computed ($G = 25$ MN/m^2; $\mu = 0.50$; $M_{Md} = 0.05 M_{Mu}^{(0)}$) vs. recorded (in field tests, dense gravel, based on Pistrol [2016]) accelerations

is assumed to be 5 % of the oscillation moment amplitude $M_{Mu}^{(0)}$, i.e. $M_{Md}/M_{Mu}^{(0)} = 0.05$ (see Section 2.4). The default value of the coefficient of friction between drum and soil is $\mu = 0.50$. Additionally, the response is also analyzed for a lower coefficient of friction of $\mu = 0.30$.

In the following, the steady state acceleration components of the drum center M, $\ddot{x}_M$ and $\ddot{z}_M$, and characteristic response quantities derived from $\ddot{x}_M$ and $\ddot{z}_M$ are presented and discussed because they serve as the basis for the compaction indicator of the CCC technique presented in [Pistrol, 2016], as explained in the introduction.

2.5.1 Influence of slip phases on the drum motion

First, for roller 1 on soft soil ($G = 5\,\mathrm{MN/m^2}$) the effect of slip phases on the computed drum response is discussed. To this end, additionally to the steady state drum center acceleration components of roller 1 in stick-slip motion also the corresponding response of the roller in pure rolling motion are presented. However, in the field a pure rolling motion is very unlikely because it is assumed the shear force at the interface between drum and soil may grow unbounded. Fig. 222 shows the steady state drum center acceleration components (a) $\ddot{x}_M$ and (b) $\ddot{z}_M$ of roller 1 in pure rolling motion (black lines with “+” markers) and stick-slip motion, respectively, during two excitation periods. The stick-slip response prediction is depicted for coefficients of friction of $\mu = 0.50$ (blue line with “*” markers) and $\mu = 0.30$ (red line with circular markers). These results illustrate the grave effect of slip between drum and soil surface on the response. In general, in stick-slip motion the peak values of $\ddot{x}_M$ and $\ddot{z}_M$ are significantly smaller compared to pure drum rolling. It is also observed that a smaller coefficient of friction μ reduces both $\ddot{x}_M$ and $\ddot{z}_M$. The horizontal acceleration component $\ddot{x}_M$ shows the typical “peak cut” in the *slip* phase, in both positive and negative directions. A kink in $\ddot{x}_M$ indicates the transition from the stick into the slip phase and vice versa. Due to the application of the constant torque M_{Md}, the negative response amplitude of $\ddot{x}_M$ is larger than the positive one. Thus, the duration of the slip phase in the negative horizontal acceleration range is only about half of the one in the positive range. Another observation is that a smaller coefficient of friction μ prolongs the duration of the slip phase in the positive horizontal acceleration range, and simultaneously reduces this duration in the negative range.

To gain a deeper insight into the drum response characteristic, Fig. 223 shows the drum accelerations in the frequency domain normalized to a peak value of one and plotted against the ratio of frequency f over excitation frequency $\bar{f}$. It is readily seen that the frequency spectra of the stick-slip motion contain both odd and even harmonics. In the case of a pure rolling motion, the frequency spectra of $\ddot{x}_M$ contains only one amplitude at $\bar{f}$ and the frequency spectra of $\ddot{z}_M$ a second amplitude at $f/\bar{f} = 2$. For the considered low soil stiffness, the corresponding frequency content of $\ddot{z}_M$ is dominated by a frequency that is two-times the excitation frequency $\bar{f}$. The detailed study based on roller 1 (Section 2.4) has, however, shown that for larger soil stiffness the response is mostly dominated by $\bar{f}$. If slipping is admitted between drum and subsoil, in the spectra of $\ddot{x}_M$ additional harmonics appear at $f/\bar{f} = 2, 3, 4, ...$, with amplitudes much smaller than those at $f/\bar{f} = 1$. These harmonics are a result of the “peak cut” in the response. According to Pistrol [2016], the normalized amplitude at the third harmonic ($|\ddot{X}_M(3\bar{f})|/|\ddot{X}_M(\bar{f})|$) can be taken as a slip indicator. In the

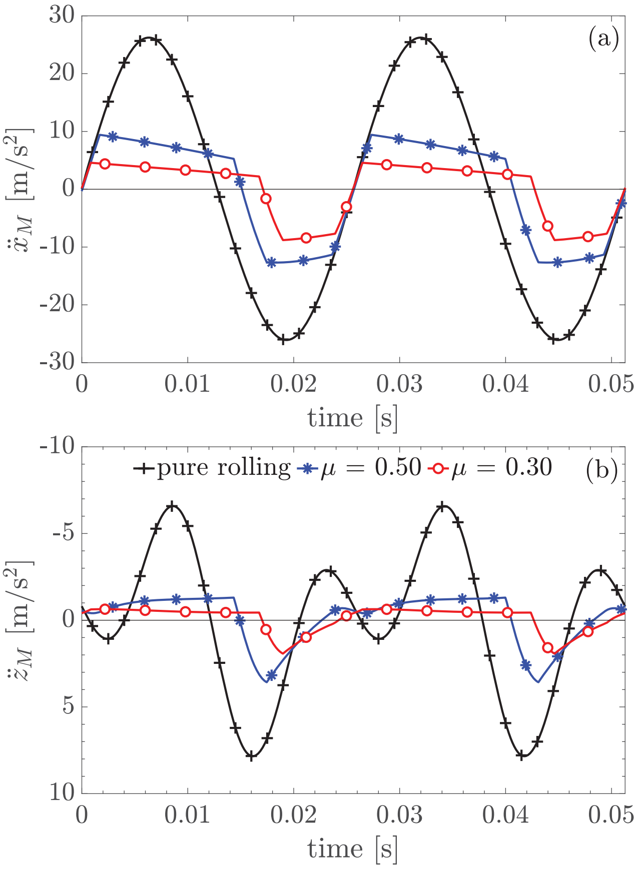

roller: HD$^+$ 90 VO, $\bar{f}$= 39 Hz – soil: $G = 5$ MN/m^2

Figure 222: (a) Horizontal and (b) vertical acceleration in the drum center with respect to time; roller 1; soft soil; pure rolling motion vs. stick-slip motion

considered case study, the amplitude at $f/\bar{f} = 3$ is about 0.114 times the amplitude at $f/\bar{f} = 1$ for $\mu = 0.50$, while the corresponding ratio is about 0.135 for $\mu = 0.30$. Thus, the normalized amplitude $|\ddot{X}_M(3\bar{f})|/|\ddot{X}_M(\bar{f})|$ increases by almost 20 % when the coefficient of friction μ is reduced from 0.50 to 0.30. The drum operates on the slope of the settlement trough, and thus, the $\ddot{z}_M$-spectra are dominated by the excitation frequency $\bar{f}$. The second harmonic in the $\ddot{z}_M$-spectra, i.e. $|\ddot{Z}_M(2\bar{f})|$, results from the up- and downward motion of the drum in the curved contact zone between drum and subsoil (“settlement trough”). The additional harmonics in the spectra of $\ddot{z}_M$ at $f/\bar{f} = 3$, 4, 5, ..., reflect the slip phases of the drum.

Plotting the vertical drum acceleration $\ddot{z}_M$ against its horizontal counterpart $\ddot{x}_M$, as shown in Fig. 224, results in another meaningful response representation that is fundamental to the CCC technique described in [Pistrol, 2016]. The result is a so-called *Lissajous curve* [Klotter, 1981] with one node and an asymmetric pattern resembling a *recumbent eight*, if the drum performs a pure rolling motion (black line with “+” markers in Fig. 224). Its shape is strongly influenced by the stiffness and damping of the subsoil as shown in Section 2.4. This will be discussed in detail in Section 2.5.2. Comparison of the $\ddot{z}_M$-$\ddot{x}_M$ plots for the stick-slip motion with the corresponding plot for pure rolling motion shows that the slip phases cause a “peak cut” of the *Lissajous*

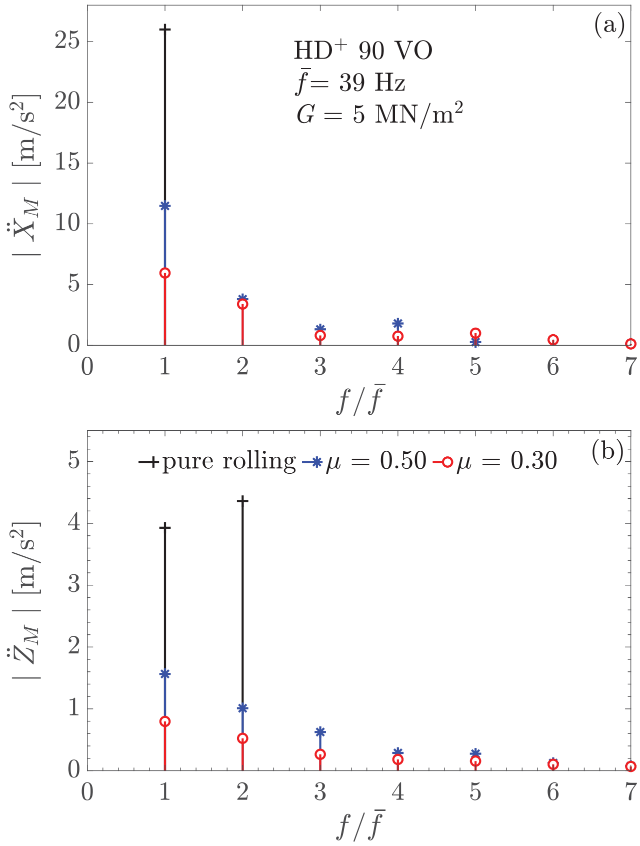

Figure 223: Frequency spectrum of the (a) horizontal and (b) vertical acceleration in the drum center; roller 1; soft soil; pure rolling motion vs. stick-slip motion

similar curve (see Fig. 224). This "cut" is more pronounced the lower the coefficient of friction μ is. The resulting shape is similar to a rotated, asymmetric "bow tie" whose enclosed area becomes smaller with decreasing μ (compare the blue line with "*" markers in Fig. 224 with the red line with circular markers).

2.5.2 Influence of subsoil on the drum motion

Next, the influence of the subsoil, characterized by the shear modulus G, on the stick-slip motion of the drum is discussed for the four rollers listed in Table 21. To this end, the stick-slip response in the drum center in terms of the $\ddot{z}_M$ over $\ddot{x}_M$ representation and frequency spectra are examined for the whole range of considered subsoil stiffness G. The underlying coefficient of friction is $\mu = 0.50$. Since the compaction indicator of the CCC methodology described in [Pistrol, 2016] is based on the $\ddot{z}_M$ over $\ddot{x}_M$ plot, Figs 225 (roller 2) and 226 (roller 4) show this response representation for four selected values of G. As it can be observed at first glance, the shape of the $\ddot{z}_M$-$\ddot{x}_M$ plots is strongly influenced by the subsoil characterized by G. For instance, the "peak cut" due to the slip phases is clearly illustrated. Moreover, with increasing soil stiffness the node observed in the curve for $G = 5\,\mathrm{MN/m^2}$ (black line with "+" markers in Figs 225 and 226) moves to the right (at $G = 35\,\mathrm{MN/m^2}$ for roller 4, see blue line with circular

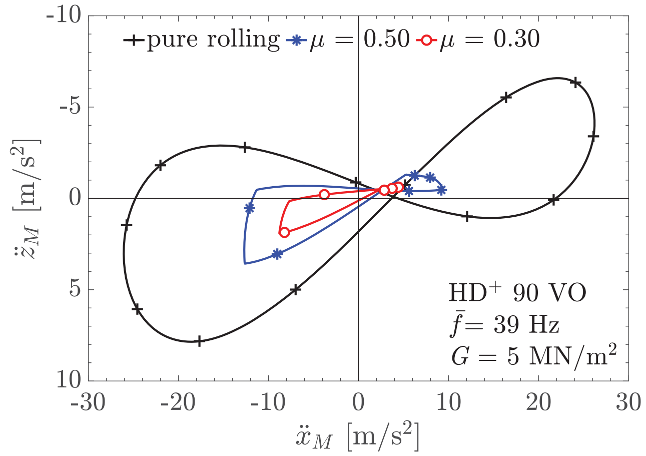

Figure 224: Plot vertical over horizontal acceleration in the drum center; roller 1; soft soil; pure rolling motion vs. stick-slip motion

markers in Fig. 226), and disappears completely for $G = 35\,\mathrm{MN/m^2}$ (roller 2) and 50 MN/m^2 (roller 4), respectively. Thus, the resulting shape is similar to a rotated, asymmetric "bow tie" for $G = 5\,\mathrm{MN/m^2}$, while for stiffer subsoils degenerated curves without node are observed that do not resemble a *Lissajous curve*. Notably, the area inside the $\ddot{z}_M$-$\ddot{x}_M$ figures becomes larger with increasing G. For roller 4, the increase of the area is apparently larger than for roller 2, e.g. compare the red lines with "*" markers in Figs 225 and 226. The influence of G on this area depending on the machine and operating parameters will be discussed in detail in Section 2.5.3.

As the shape of the $\ddot{z}_M$ over $\ddot{x}_M$ plot and consequently the enclosed area are strongly affected by the frequency content and amplitudes of the drum response (as shown in Section 2.4), $\ddot{x}_M$ and $\ddot{z}_M$ are subsequently analysed in the frequency domain up to a frequency ratio $f/\bar{f} = 3$. Figs 227 and 230 show the response amplitudes at excitation frequency $\bar{f}$ (i.e $|\ddot{X}_M(\bar{f})|$ and $|\ddot{Z}_M(\bar{f})|$) as a function of the soil stiffness G for the considered rollers. Black lines with "+" markers represent the response of roller 1,

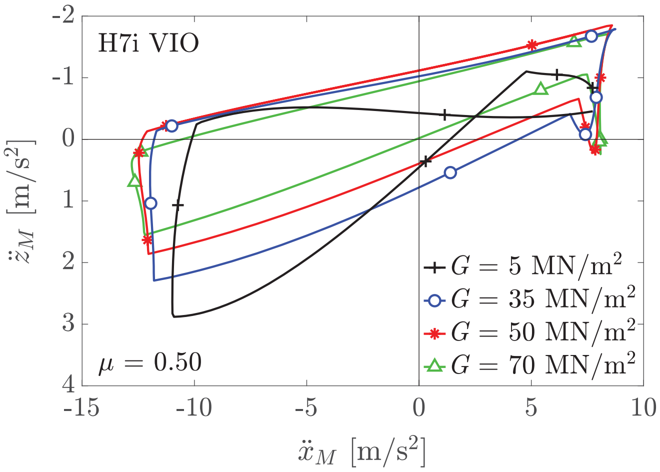

Figure 225: Plot vertical over horizontal acceleration in the drum center; roller 2

blue lines with circular markers of roller 2, red lines with "*" markers of roller 3, and green lines with triangular markers of roller 4. Note that this color and line style selection is retained for all of the following representations. It is readily seen that the amplitudes of the horizontal drum accelerations $|\ddot{X}_M(\bar{f})|$ become continuously larger with increasing G for all rollers. The simulations based on the parameters of roller 1 yield the largest values of $|\ddot{X}_M(\bar{f})|$ in the whole range of G with an increase of about 27 % from $11.5\,\mathrm{m/s^2}$ ($G = 5\,\mathrm{MN/m^2}$) to $14.6\,\mathrm{m/s^2}$ ($G = 70\,\mathrm{MN/m^2}$). The smallest values result from the simulations with the parameters of roller 2, except for $G = 5$ and $10\,\mathrm{MN/m^2}$, showing an increase of 23 % from $9.9\,\mathrm{m/s^2}$ ($G = 5\,\mathrm{MN/m^2}$) to $12.2\,\mathrm{m/s^2}$ ($G = 70\,\mathrm{MN/m^2}$). The values of $|\ddot{X}_M(\bar{f})|$ for roller 3 are virtually in the same order of magnitude, increasing from $9.4\,\mathrm{m/s^2}$ ($G = 5\,\mathrm{MN/m^2}$) to $12.3\,\mathrm{m/s^2}$ ($G = 70\,\mathrm{MN/m^2}$), i.e. an increase of about 31 %. The values for roller 4 are in between, increasing from $10.3\,\mathrm{m/s^2}$ ($G = 5\,\mathrm{MN/m^2}$) to $13.1\,\mathrm{m/s^2}$ ($G = 70\,\mathrm{MN/m^2}$) and thus, showing the same increase as predicted for roller 1. In contrast, the amplitudes of the vertical drum accelerations at excitation frequency $\bar{f}$ $|\ddot{Z}_M(\bar{f})|$ decrease with increasing G for all rollers, however, not continuously because in the medium stiffness range the curves show a plateau (see Fig. 230). This range with virtually constant $|\ddot{Z}_M(\bar{f})|$ is smallest for roller 2 ($G =$ 15-25 $\mathrm{MN/m^2}$) and largest for roller 4 ($G =$ 15-35 $\mathrm{MN/m^2}$). Before the plateau is attained, a decrease of $|\ddot{Z}_M(\bar{f})|$ of about 5 % (roller 2) to 7 % (rollers 1 and 3) is observed. The decrease $|\ddot{Z}_M(\bar{f})|$ with respect to G is similar for rollers 1 and 2 and more pronounced than for rollers 3 and 4. The total decrease of $|\ddot{Z}_M(\bar{f})|$ between $G = 5\,\mathrm{MN/m^2}$ and $G = 70\,\mathrm{MN/m^2}$ is about 50 % for rollers 3 and 4 and 64 % for roller 2. Similar to the horizontal amplitude $|\ddot{X}_M(\bar{f})|$, the largest values of the vertical amplitude $|\ddot{Z}_M(\bar{f})|$ are induced by roller 1 and the smallest ones by roller 2. Comparison of Figs 227 and 230 shows that the amplitudes $|\ddot{Z}_M(\bar{f})|$ are only about 0.15 times the amplitudes $|\ddot{X}_M(\bar{f})|$ at $G = 5\,\mathrm{MN/m^2}$ and approximately 0.05 times the amplitudes $|\ddot{X}_M(\bar{f})|$ at $G = 70\,\mathrm{MN/m^2}$, respectively.

Fig. 228 shows the response amplitudes $|\ddot{X}_M(2\bar{f})|$ at the double excitation frequency $2\bar{f}$ normalized by the amplitudes $|\ddot{X}_M(\bar{f})|$ at the excitation frequency $\bar{f}$ as a function of G. As can be observed at first glance, the normalized amplitudes $|\ddot{X}_M(2\bar{f})|/|\ddot{X}_M(\bar{f})|$

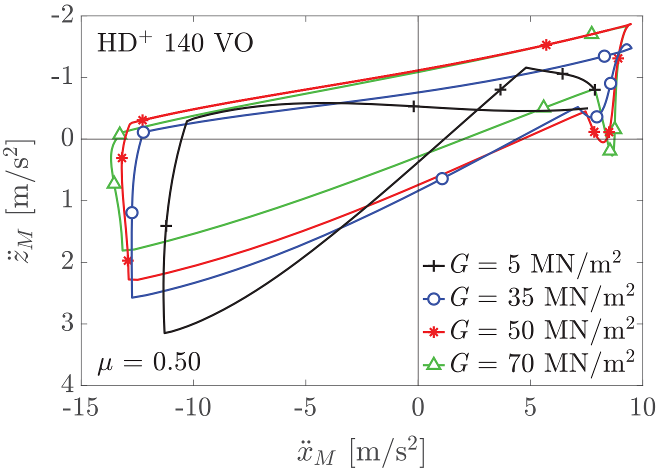

Figure 226: Plot vertical over horizontal acceleration in the drum center; roller 4

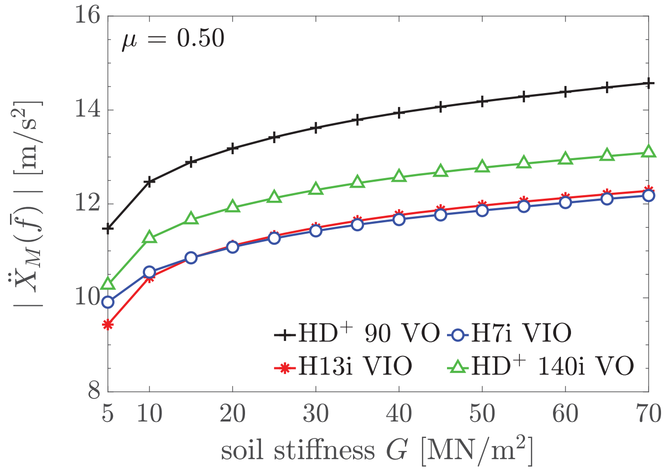

Figure 227: Amplitude of the horizontal drum accelerations at the excitation frequency as a function of soil stiffness

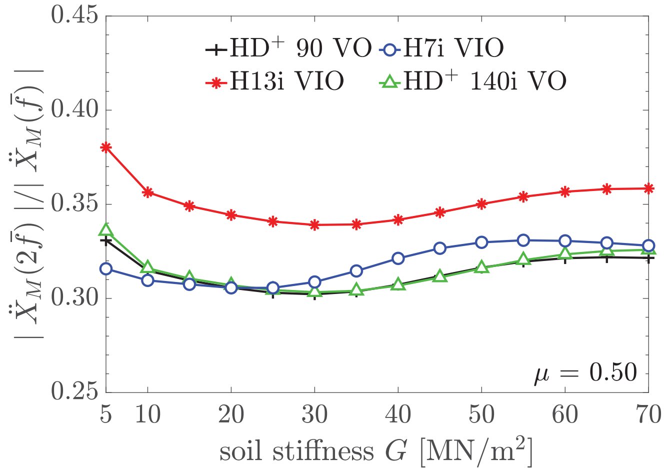

Figure 228: Amplitude of the second harmonic of the horizontal acceleration normalized by the amplitude at the excitation frequency as a function of soil stiffness

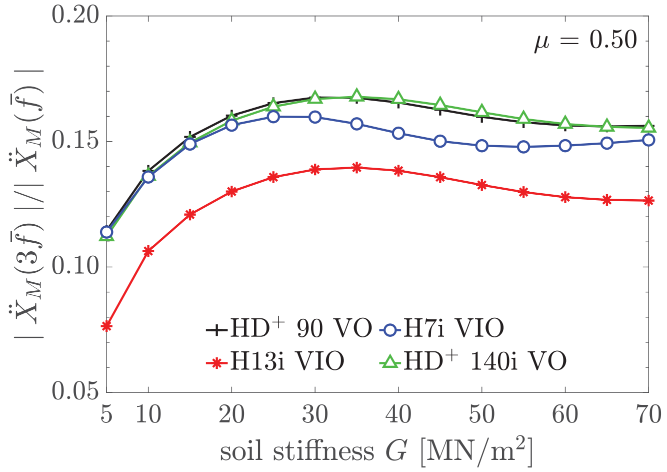

Figure 229: Amplitude of the third harmonic of the horizontal acceleration normalized by the amplitude at the excitation frequency as a function of soil stiffness

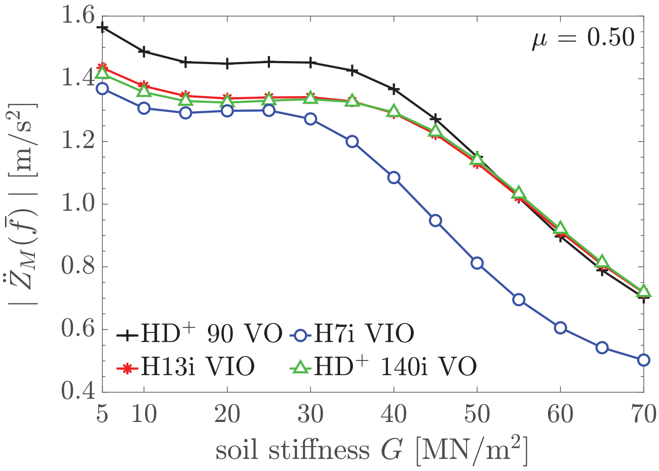

Figure 230: Amplitude of the vertical drum accelerations at the excitation frequency as a function of soil stiffness

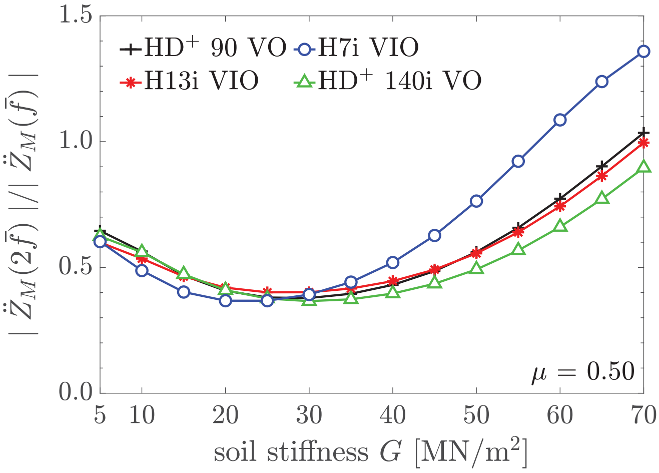

Figure 231: Amplitude of the second harmonic of the vertical acceleration normalized by the amplitude at the excitation frequency as a function of soil stiffness

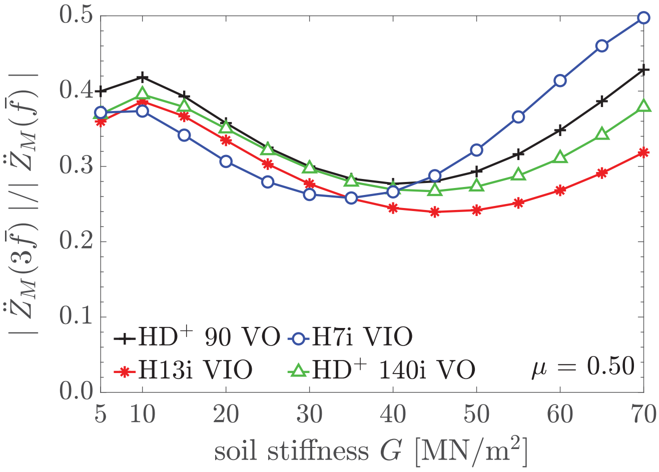

Figure 232: Amplitude of the third harmonic of the vertical acceleration normalized by the amplitude at the excitation frequency as a function of soil stiffness

are only slightly influenced by the soil stiffness G. Their values vary between 0.30 and 0.33 (rollers 1, 2 and 4) and 0.34 and 0.38 (roller 3), respectively. The outcomes based on rollers 1, 3 and 4 are qualitatively very similar, whereas the results due to rollers 1 and 4 match also quantitatively. The amplitudes $|\ddot{X}_M(2\bar{f})|/|\ddot{X}_M(\bar{f})|$ become smaller up to $G = 30\,\mathrm{MN/m^2}$ (i.e. a decrease of about 10 %) and start to continuously increase at $G \geq 35\,\mathrm{MN/m^2}$ (increase of approximately 7 %). In contrast, for roller 2 the amplitudes $|\ddot{X}_M(2\bar{f})|/|\ddot{X}_M(\bar{f})|$ decrease up to $G = 20\,\mathrm{MN/m^2}$ by about 3 % before becoming larger in the range $G =$ 25-50 MN/m^2 (increase of approximately 8 %) and show a local maximum $G \geq 50\,\mathrm{MN/m^2}$.

In Fig. 229 the third harmonic horizontal response amplitude $|\ddot{X}_M(3\bar{f})|$ normalized by corresponding first harmonic $|\ddot{X}_M(\bar{f})|$ is plotted against soil shear modulus G. It can be readily seen that the normalized amplitudes $|\ddot{X}_M(3\bar{f})|/|\ddot{X}_M(\bar{f})|$ are strongly influenced by the subsoil in the stiffness range up to $G =$ 25-35 MN/m^2. While in this stiffness range ratio $|\ddot{X}_M(3\bar{f})|/|\ddot{X}_M(\bar{f})|$ increases by 40 % (roller 2) to 83 % (roller 4), the numerically predicted decrease in the range $G >$ 25-35 MN/m^2 is only between ≈ 7 % (rollers 1, 2 and 4) and 10 % (roller 4). Similar to the previously discussed amplitude ratio $|\ddot{X}_M(2\bar{f})|/|\ddot{X}_M(\bar{f})|$, rollers 1, 3 and 4 yield amplitude ratios $|\ddot{X}_M(3\bar{f})|/|\ddot{X}_M(\bar{f})|$ of the same order of magnitude. In particular, the curves for rollers 1 and 4 are virtually identical. The peak values of $|\ddot{X}_M(3\bar{f})|/|\ddot{X}_M(\bar{f})|$ vary between 0.14 (roller 3) and 0.17 (rollers 1 and 4), respectively.

Next, the influence of G on the vertical drum response ($\ddot{z}_M$) in the frequency domain is examined in the same way, based on the normalized amplitudes $|\ddot{Z}_M(2\bar{f})|/|\ddot{Z}_M(\bar{f})|$ (see Fig. 231) and $|\ddot{Z}_M(3\bar{f})|/|\ddot{Z}_M(\bar{f})|$ (see Fig. 232). Fig. 231 shows that the amplitude ratios $|\ddot{Z}_M(2\bar{f})|/|\ddot{Z}_M(\bar{f})|$ are strongly affected by G. The response curves as a function of G are similar for all considered rollers, i.e. in the range $G =$ 20-30 MN/m^2 these curves show a minimum. At $G = 5\,\mathrm{MN/m^2}$ ratio $|\ddot{Z}_M(2\bar{f})|/|\ddot{Z}_M(\bar{f})|$ is about 0.60-0.65, and the minimum ratio is approximately 0.37-0.38. The largest amplitude ratio $|\ddot{Z}_M(2\bar{f})|/|\ddot{Z}_M(\bar{f})|$ occurs at the largest considered soil stiffness $G = 70\,\mathrm{MN/m^2}$. Notably, the ratio $|\ddot{Z}_M(2\bar{f})|/|\ddot{Z}_M(\bar{f})|$ due to roller 2 exceeds in the stiffness range $G > 55\,\mathrm{MN/m^2}$ the value of 1 with its maximum of 1.36 at $G = 70\,\mathrm{MN/m^2}$. Thus, for $G > 55\,\mathrm{MN/m^2}$ the frequency spectrum of the vertical drum response resulting from roller 2 is dominated by the second harmonic. In contrast, for the remaining rollers the corresponding peak ratio is less or equal than 1, i.e. the vertical drum response $\ddot{z}_M$ is dominated by the excitation $\bar{f}$.

Fig. 232 illustrates that also the normalized amplitudes $|\ddot{Z}_M(3\bar{f})|/|\ddot{Z}_M(\bar{f})|$ at three-times the excitation frequency strongly depend on G and they vary between 0.24 and 0.50. The global trend of this response quantity is the same for all rollers. The curves show a local maximum at $G = 10\,\mathrm{MN/m^2}$ and a global minimum at at $G =$ 35-50 MN/m^2. At the largest considered value of the soil stiffness $G = 70\,\mathrm{MN/m^2}$, for roller 3 the ratio $|\ddot{Z}_M(3\bar{f})|/|\ddot{Z}_M(\bar{f})|$ is 0.32 and for roller 2 about 0.50.

2.5.3 Influence of the device parameters on the compaction indicator

Recent experimental studies have revealed that the area inside the $\ddot{z}_M$ over $\ddot{x}_M$ figure becomes larger with increasing G, and thus, has been proposed as CCC indicator of the actual soil compaction [Pistrol, 2016]. In Fig. 233, this CCC response parameter (i.e. the "area") is plotted against the shear modulus G for all considered types of oscillation rollers. It is readily seen that the all curves representing different oscillation rollers are qualitatively very similar. In particular, the results due to rollers 3 and 4 are virtually the same. As can be observed, up to a soil stiffness of G = 15-20 MN/m^2, the compaction indicator slightly decreases (rollers 1, 2 and 3) or is almost constant (roller 4). Subsequently, this response quantity becomes continuously larger with increasing G, reaches a maximum at G = 35-40 MN/m^2 (roller 2), G = 45 MN/m^2 (roller 1), G = 45-50 MN/m^2 (roller 3) and G = 50 MN/m^2 (roller 4), respectively, and then decreases with increasing G. The simulations based on the parameters of roller 1 yield the largest compaction indicators in the whole range of G with a maximum value of about 53 m^2/s^4. The smallest values result from the simulations with the parameters of roller 2 showing a maximum of $\approx$ 39 m^2/s^4. The compaction indicators resulting from rollers 3 and 4 are in the same order of magnitude with a maximum of about 42 and 44 m^2/s^4, respectively. Notably, for rollers 1 and 2 the compaction indicator at the largest soil stiffness (G = 70 MN/m^2) is smaller than the corresponding value for soft soil (G = 5 MN/m^2).

Normalizing the compaction indicators by the corresponding compaction indicator for soft soil (G = 5 MN/m^2) results in the graphs shown in Fig. 234. This illustration clearly shows that the largest increase of the compaction indicator is observed for rollers 3 and 4, with a maximum increase of 45 %. The normalized compaction indicator due to roller 1 increases only by 30 % and due to roller 2 by almost 34 %. However, the gradient of the increase and the subsequent decrease is the strongest for roller 2. Thus, the resulting compaction indicator at G = 70 MN/m^2 is 26 % smaller than the corresponding value at G = 5 MN/m^2.

Next, the influence of operating frequency $\bar{f}$ on the considered compaction indicator is discussed based on rollers 1 and 4. To this end, the default value of $\bar{f}$, as listed in Table 21, is reduced and increased by 3 Hz, respectively. The corresponding normalized compaction indicators are depicted in Figs 235 (roller 1) and 236 (roller 4). As can be observed, a reduction of $\bar{f}$ results in a considerable decrease of the normalized compaction indicator in the entire range of soil stiffness G, while an increase of $\bar{f}$ also increases this indicator. Moreover, the maximum point of the curves is shifted to the right when the operating frequency $\bar{f}$ is increased. Thus, the maximum of normalized compaction indicator occurs at a larger soil stiffness. The computations based on roller 1 operated at a reduced excitation frequency of $\bar{f}$ = 36 Hz yield a maximum normalized compaction indicator of only 1.03 at a lower soil stiffness of G = 35-40 MN/m^2. This corresponds to a decrease in normalized compaction indicator of about 20 % compared to the operation with standard frequency $\bar{f}$ = 39 Hz. In comparison, the simulations based on the same roller but operated at the larger frequency $\bar{f}$ = 42 Hz lead to a maximum normalized compaction indicator of about 1.6 at a considerably larger value of the soil stiffness G = 50-55 MN/m^2, i.e. an increase of almost 25 % compared to the standard operating frequency. The change of the excitation frequency of roller 4 results in a change of the normalized compaction indicator that is quantitatively and qualitatively similar.

Additionally, the effect of suspension parameters k_d and c_d (which represent the suspension between drum and frame) on the normalized compaction indicator is studied exemplarily on roller 1. As shown in Fig. 237, the increase of stiffness k_d from its default value of 4 MN/m to 8 MN/m results in an increase of the normalized com-

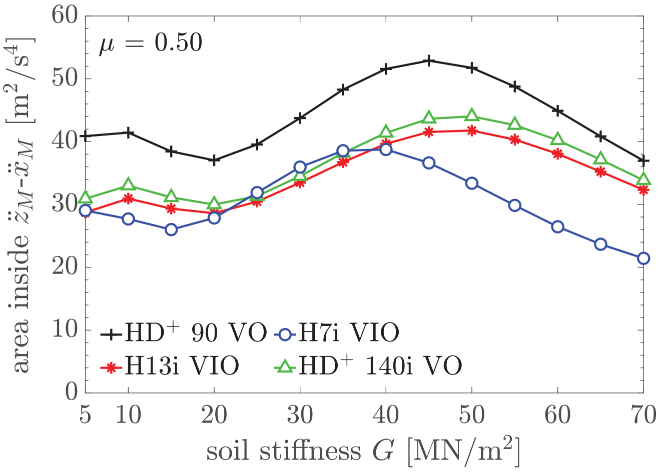

Figure 233: Compaction indicator as a function of soil stiffness

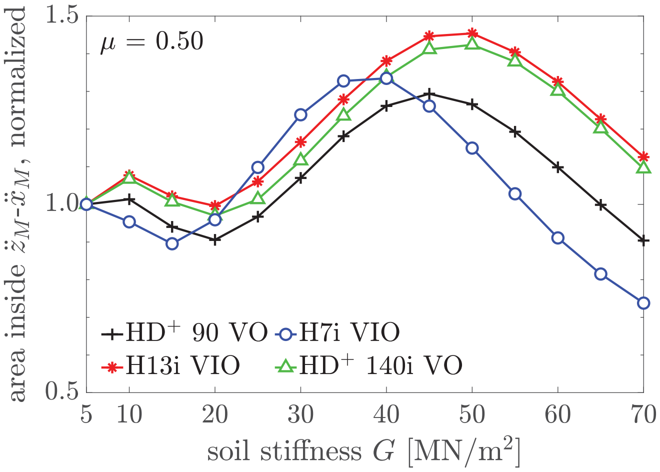

Figure 234: Normalized compaction indicator as a function of soil stiffness

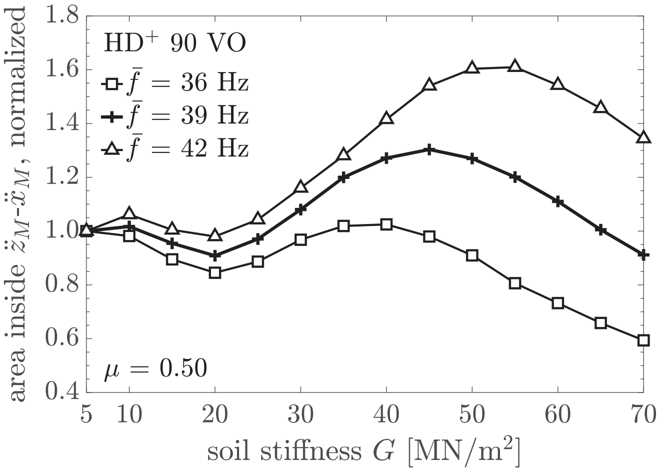

Figure 235: Normalized compaction indicator as a function of soil stiffness; variation of operating frequency for roller 1

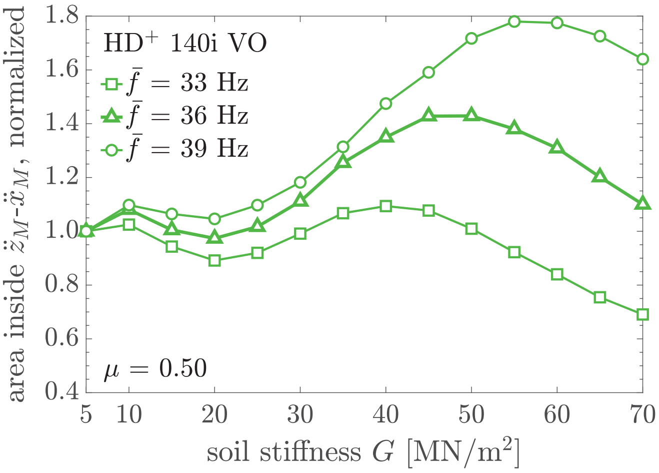

Figure 236: Normalized compaction indicator as a function of soil stiffness; variation of operating frequency for roller 4

paction indicator, and the decrease of the default value 4 MN/m to 2 MN/m reduces this indicator. The peak value of this indicator occurs for all values of k_d at the same soil stiffness G. The effect resulting from the variation of the damping parameter c_d is illustrated by Fig. 238. Simulations based on a suspension damping coefficient c_d that is 20 times larger than the default value listed in Table 1 show virtually no affect on the normalized compaction indicator. In the unrealistic case that c_d is 100 times higher than the default value, the maximum value of the normalized compaction indicator is reduced by about 9 % and shifted from $G = 45\,\mathrm{MN/m^2}$ to a slightly higher soil stiffness range of $G = 45\text{-}50\,\mathrm{MN/m^2}$, see Fig. 238.

2.5.4 Influence of the coefficient of friction on the compaction indicator

The influence of the coefficient of friction between drum and subsoil on the normalized compaction indicator is illustrated by comparing Fig. 239 ($\mu = 0.30$) with Fig. 234 ($\mu = 0.50$). The reduction in μ to 0.30 has virtually no effect on that soil stiffness G, where the maximum value of the normalized compaction indicator occurs. However, a reduction of μ increases the normalized compaction indicator for all rollers. Rollers 3 and 4 yield the largest maximum normalized compaction indicator. The smallest increase is observed for roller 2 with a maximum normalized compaction indicator of 1.53. Notably, this value is in the same order of magnitude as the value resulting from roller 1. In contrast to the outcomes based on $\mu = 0.50$, the minimum value of the normalized compaction indicator occurs both at the lowest and at the largest considered value of the soil stiffness. That is, at $G = 70\,\mathrm{MN/m^2}$ the indicator does not drop below the value at $G = 5\,\mathrm{MN/m^2}$.

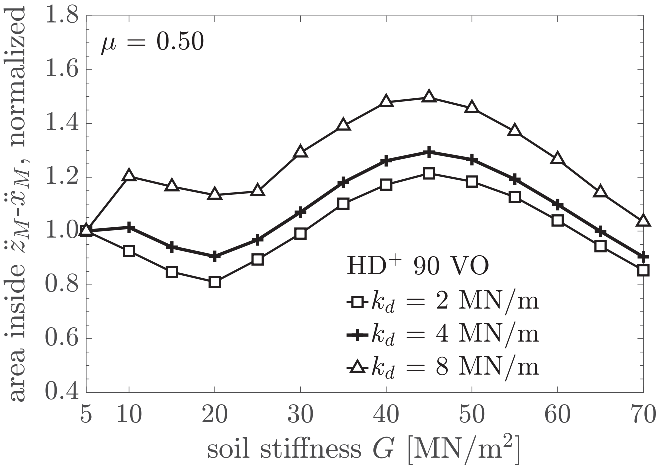

Figure 237: Normalized compaction indicator as a function of soil stiffness; variation of the suspension stiffness of roller 1

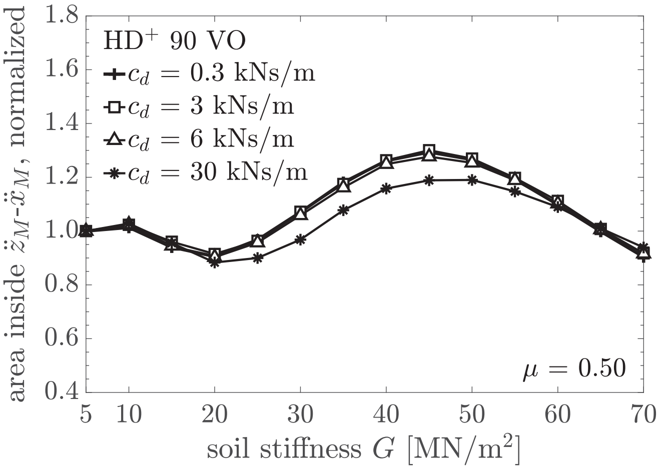

Figure 238: Normalized compaction indicator as a function of soil stiffness; variation of the suspension damping of roller 1

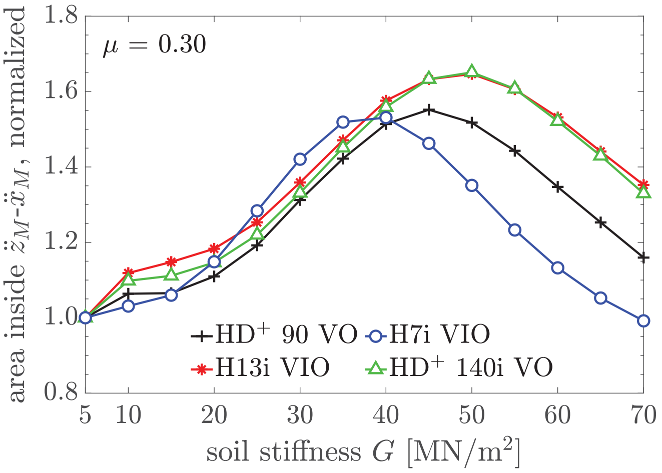

Figure 239: Normalized compaction indicator as a function of soil stiffness; standard operating frequency; coefficient of friction $\mu = 0.30$

Chapter 3

Finite Element modeling

3.1 Considered oscillation roller

For the *Finite Element modeling* of the dynamic interacting oscillation roller-soil system, roller 1 (i.e. the HD$^+$ 90 VO tandem roller) is used because for this device acceleration response data of the drum center as well as dynamic soil stress components have been recorded in field tests [Pistrol, 2016]. The default machine and operating parameters are listed in Table 31. Note that in contrast to the parameters specified in Table 21 the subsequent numerical investigations are based on a static axle load of $P_0 = 44{,}130\,\mathrm{N}$ [Pistrol, 2016], which is about 2.5 % smaller than the value of P_0 given in Table 21. However, the studies in Section 3.3.3, where the static axle load is varied, show that this has no significant effect on the results. The outcomes of the numerical study summarized in this chapter are based on papers 5 and 6, see Section 1.5.

Table 31: HD$^+$ 90 VO tandem roller parameters (based on Pistrol [2016])

Default parameters		Value	Dimension
Radius of the drum	r	0.60	m
Width of the drum	b	1.68	m
Mass of the drum	m	1851	kg
Mass moment of inertia of the drum	I	412	$\mathrm{kg\,m^2}$
Static axle load	P_0	44,130	N
Excitation frequency	$\bar{f}$	39	Hz
Amplitude of the oscillation moment	$M_{Mu}^{(0)}$	54,947	Nm
Suspension drum/frame - stiffness	k_d	4×10^6	N/m
Suspension drum/frame - damping	c_d	3×10^2	Ns/m
Roller speed	v_0	1.11	m/s

3.2 Numerical model with hypoplastic soil behavior

3.2.1 General modeling strategy

The drum and the front frame are dynamically decoupled by a deeply tuned suspension system (rubber buffers), and thus, both the horizontal and vertical vibrations of the rear and front frame are negligible during operation, as discussed in Section 2.2.2 (for further details see Appendix A). Based on this observation, the entire roller illustrated in Fig. 11 is reduced to the stiff oscillation drum connected through spring-damper elements to the quasi-static frame, which is moving horizontally at speed v_0. The spring-damper elements represent the viscoelastic properties of the rubber buffers. The static axle load P_0 applied to the center of the drum consists of the dead weight of the front frame and the drum weight. The effect of two eccentric and (with respect to the drum center) point-symmetric shafts inside the drum, each with two equal imbalances (same mass and same eccentricity) rotating in the same direction with constant angular velocity $\bar{\nu}$, is captured by the resulting sinusoidal torque around the drum axis according to Eq. 2.6. The resulting amplitude $M_{Mu}^{(0)}$ of the sinusoidal excitation moment is listed in Table 31. Based on the relation between the excitation torque $M_{Mu}(t)$ and the location of the rotating unbalanced shafts visualized in Fig. 23, it is assumed that the drum runs at constant speed and performs an alternating high-frequency forward-backward motion.

The considered vertical soil section is a rectangular plain strain domain discretized by Finite Elements (FE), which is embedded in infinite elements. The plane-strain thickness of the vertical soil section corresponds to the thickness of the drum. To the soil section, the *hypoplastic* constitutive law with the extension for intergranular strain as proposed by Niemunis and Herle [1997] is assigned. For a brief overview see Appendix G. This constitutive model allows a realistic description of soil compaction.

In summary, the plane-strain FE model created in *ABAQUS/CAE* and shown in Fig. 31 consists of three subsystems, i.e., the soil, the oscillation drum, and the spring-damper elements between the drum and the roller frame. The origin O of the x (horizontal) and y (vertical) coordinates describing the planar model geometry is located in the center of the free undeformed soil surface, as illustrated in Fig. 31. Note that the coordinate system as defined in *ABAQUS/CAE* is used throughout the subsequently described study. Thus, the vertical axis, unlike in Chapter 2, is defined positively upwards and is subsequently referred to as y.

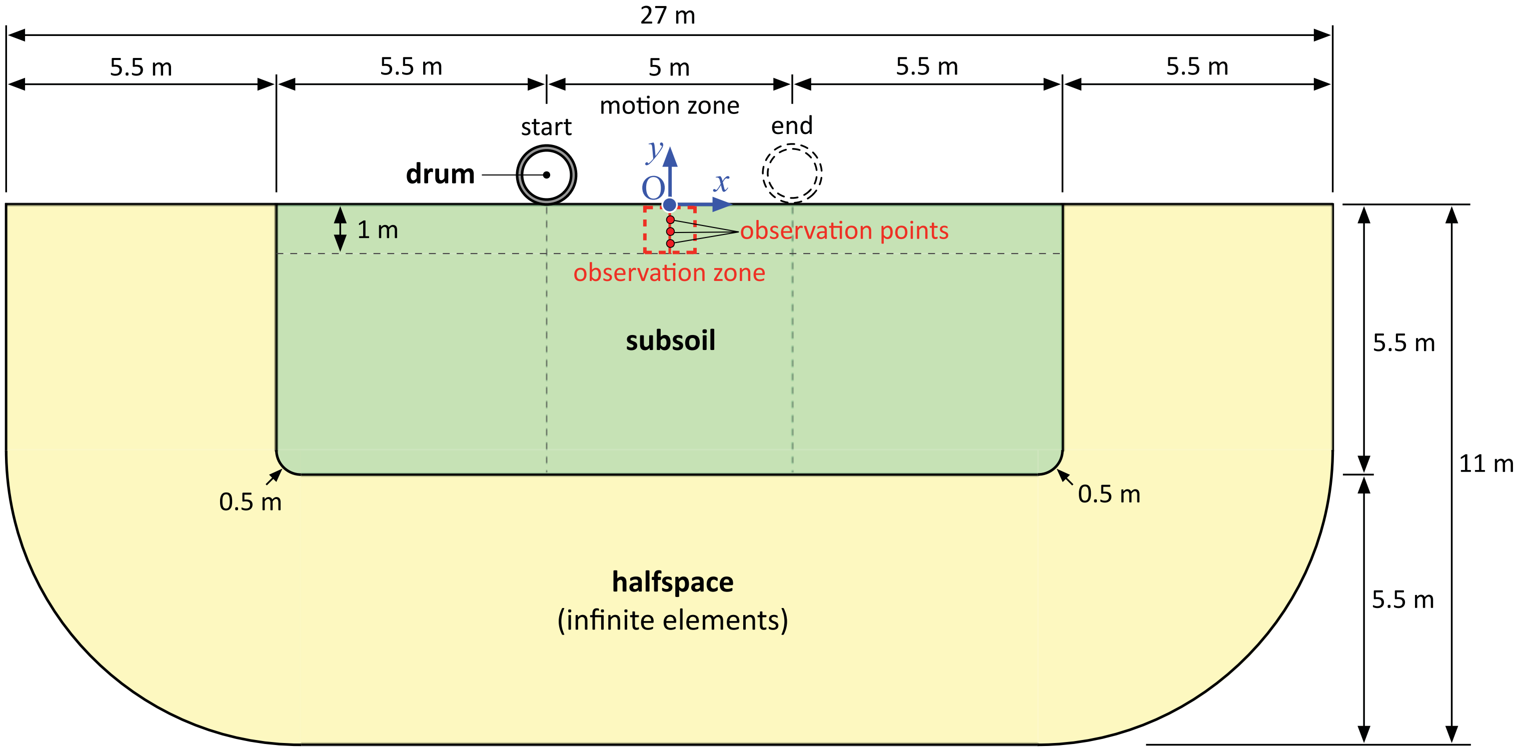
27 m
5.5 m
5.5 m
5 m
5.5 m
5.5 m
motion zone
start
end
drum
y
O
x
1 m
observation points
observation zone
subsoil
0.5 m
0.5 m
halfspace
(infinite elements)
5.5 m
5.5 m
11 m

Figure 31: Sketch of the Finite Element model (without mesh, without suspension)

3.2.2 Spatial and temporal discretization

The soil subsystem subjected to compaction is a rectangular finite domain of the dimension 16 m x 5.5 m, and at its boundaries to the surrounding halfspace, which is not significantly affected by the roller, infinite elements with a length of 5.5 m capture the effects of radiation damping both horizontally and vertically (see Fig. 31). The infinite elements (CINPE4) emulate the halfspace by introducing velocity-proportional damping at the boundaries, and consequently, the impinging compression and shear waves at the model boundaries are not reflected [Smith, 2015]. In the horizontal range -3 m $\leq x \leq 3$ m the subsoil surface (i.e. vertical coordinate $y=0$) is defined as the contact area between drum and soil, and thus, represents for the drum the "motion zone" and for the soil layer the "compaction zone". The soil domain is spatially discretized by four-node bilinear plane-strain quadrilateral elements (CPE4). In the horizontal range of -2.5 m $\leq x \leq 2.5$ m the mesh of the contact and compaction zones consists of elements with the dimension 0.02 m x 0.02 m. The element size of the mesh in the domains -5.5 m $\leq x \leq -2.5$ m, 2.5 m $\leq x \leq 5.5$ m, and -5.5 m $\leq y \leq -1.0$ m increases to 0.1 m x 0.1 m at the semi-infinite boundaries. The model was refined stepwise in the soil domain of potential compaction during its development. The resulting mesh used in this study consists of 37,569 elements including the infinite elements. Additionally, convergence studies were performed with a coarse mesh consisting of 11,795 elements and an even more refined mesh consisting of 46,326 elements and a minimum element size of 0.01 m x 0.01 m.

The drum is modeled as an elastic circular steel ring with the outer radius of 0.60 m, thickness of 0.02 m, density $\rho = 7850\,\mathrm{kg/m^3}$, *Young*'s modulus $E = 210 \times 10^9\,\mathrm{N/m^2}$, and *Poisson*'s ratio $\nu = 0.3$. The FE model of the drum model consists of radially uniformly distributed 376 four-node bilinear plane-strain quadrilateral elements (CPE4). Four dummy elements (see Fig. 32) with the same material properties are added to the quarter points on the inner ring surface to support response visualization. These elements are of dimension 0.01 m x 0.03 m, whereas all other elements have a size of approximately 0.01 m x 0.02 m. The total mass of this model is 993.6 kg and its mass moment of inertia is 344.4 kg m^2. Since according to the manufacturer the actual mass of the drum is larger (see Table 31), a lumped mass of 857.4 kg and an rotary inertia (I_{33}) of 67.4 kg m^2 is added to this model to the reference point at center of the drum ("RP_M"). The reference node RP_M (referred to as "M") and the nodes of the inner drum surface are coupled by defining kinematic coupling constraints for all affected degrees of freedom (nodal degree of freedom in the x-direction "U1", in the y-direction "U2", and in the rotation about z-axis "UR3").

As agreed upon with the manufacturer, the mechanical properties of the suspension elements between the drum and roller frame are described by three lumped parameter spring-dashpot elements (*Kelvin-Voigt* bodies), arranged as shown in Fig. 32. The spring and dashpot elements are defined between the reference point RP_M (drum center M) and the reference nodes RP_{fl}, RP_{fr}, RP_{ft}, respectively, which belong to the quasi-static roller frame. The spring stiffness and the dashpot coefficients as listed in Table 31 are assigned to the vertical *Kelvin-Voigt* body. The stiffness and the dashpot parameters of the horizontal elements only have half of these values, resulting in the same vertical and horizontal global stiffness and dashpot coefficients as used in the lumped parameter modeling in Chapter 2.

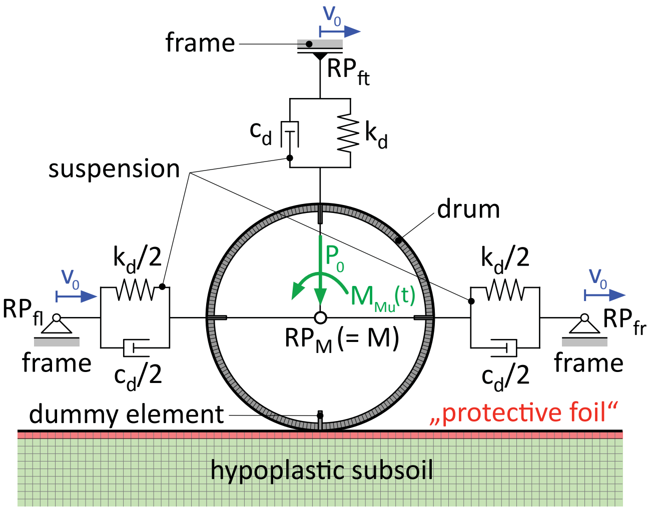

Figure 32: Sketch of the drum and the suspension model

In the course of the model optimization it was found that the maximum time increment $\Delta t = 0.0002\,\mathrm{s}$ maintains the required high resolution accuracy of the predicted response accelerations. The total computation time for simulating one roller pass from the initial drum position at $x = -2.5$ m to the final position at $x = 2.3$ m (time frame of motion 4.5 s) varies from at least one day to about one week (computer with seven processor cores each with a clock rate of 3 GHz).

By employing the FE simulation software *ABAQUS/Standard* (version R2016x), the Hilber-Hughes-Taylor (HHT) [Smith, 2015] implicit integrator is used to solve the present dynamic boundary value problem. The HHT-parameter α, which provides the maximum numerical damping, is set to $-1/3$. The *nohalf* option specifies that the half-increment residual is not checked.

3.2.3 Contact between soil and drum

The contact formulation implemented in *ABAQUS/Standard* [Smith, 2015] is used to model the contact interaction between the outer surface of the drum (*master* surface) and the surface of the soil ($y = 0$) in the range -3 m $\leq x \leq 3$ m (*slave* surface), which represent a so-called “contact pair”. Since the actual behavior of drum-soil contact has never been experimentally investigated in detail, it is assumed that the properties of drum-soil contact can be described sufficiently accurately by the classical isotropic *Coulomb friction model*. In this friction model, the two contact surfaces can carry shear stresses up to a certain limit value (*stick* state) before mutual sliding is initiated (*slip* phase) [Smith, 2015]. The subsequent simulations are performed with a constant coefficient of friction $\mu = 0.50$ (default value).

3.2.4 Initial conditions

Initially, the drum is located at $(x, y) = (-2.5, 0.1)$ m, i.e. there is a gap of 0.1 m between the drum surface and the top of the subsoil (initial uplifted drum position). In the soil domain, an initial stress field is imposed by specifying vertical stresses on the top and the bottom of the subsoil subdomain. In addition, the first coefficient of lateral earth pressure (x-direction) is set to 0.429. In the hypoplastic soil domain, initial values of solution-dependent state variables (SDVs) are specified. In all simulations, the SDVs are set to zero except for the initial void ratio e_0 (SDV7).

3.2.5 Analysis steps

In analysis step 1, the gravitational acceleration $g = 9.81\,\mathrm{m/s}^2$ is applied to the soil domain in negative y-direction to establish equilibrium with the imposed initial soil stresses ("geostatic step"). Then, in a second static analysis step, the raised drum is lowered and pressed 0.005 m into the soil to establish contact between the drum and the soil (analysis step 2, or "displacement step"). In static simulation step 3, the drum is loaded by applying the static axle load P_0 to the reference node RP_M ("vertical loading step"). In dynamic analysis step 4, at the reference nodes RP_{fl}, RP_{fr}, RP_{ft} (shown in Fig. 32) the velocity $v(t) = v_0 \sin^2(2\pi t/\Delta t_{acc})$ is prescribed, with $0 \leq t \leq \Delta t_{acc}$. The time period Δt_{acc} of the "acceleration step" to accelerate the statically loaded drum from $v = 0$ up to the target roller speed v_0 is assumed with 0.5 s. Thus, the drum covers a distance of about 0.3 m during the acceleration phase. In the last dynamic analysis step 5 ("compaction step"), the oscillation moment $M_{Mu}(t)$ is applied to the reference node at the center of the drum, thereby exciting harmonically the statically loaded drum moving at constant speed v_0, as described in the subsequent Section 3.2.6.

Some test simulations were performed where analysis steps 3 and 4 were combined, i.e. acceleration and harmonic excitation of the drum were applied simultaneously. Depending on the soil parameters (especially on void ratio e_0), this combination may lead to such a large soil deflection that the drum need to be driven up afterwards, which yields unrealistic initial conditions for the compaction step.

3.2.6 Loading, movement, and excitation of the oscillation drum

The concentrated static axle load P_0 specified in Table 31 is applied to reference node RP_M, which represents the drum center M. The motion of the drum at constant roller speed is modeled by defining boundary conditions in terms of velocity at the reference nodes RP_{fl}, RP_{fr}, RP_{ft} (see Fig. 32) and the frictional contact between drum and soil. The concentrated periodic moment $M_{Mu}(t)$ according to Eq. 2.5 is applied to the drum center M (reference node RP_M). Due to the alternating high-frequency forward-backward motion of the drum, which is superimposed on the translational roller motion at constant speed $v_0 = 1.11\,\mathrm{m/s}$, the soil is exposed to about 35 oscillations per meter traveled.

3.2.7 Constitutive soil model and numerical implementation

To describe soil compaction, the so-called intergranular strain enhanced extended hypoplastic constitutive model (e.g. [von Wolffersdorff, 1996], [Niemunis and Herle, 1997]) was implemented in *ABAQUS/Standard* via a user-defined subroutine (UMAT), as described in [Gudehus et al, 2008], [Mašín, 2019a]. According to Heiniger [2018], who tested the implementation of this UMAT, the present simulations are based on the constitutive parameters of the so-called *Hochstetten Sand* [Herle, 1997] listed in Table 32 (basic hypoplastic model) and Table 33 (additional parameters of the extended hypoplastic model). The initial void ratio e_0 is varied in the range of 0.90 (very loose soil) to 0.60 (dense soil). The corresponding soil density is calculated assuming a grain density of $\rho_s = 2650\,\mathrm{kg/m^3}$. For an overview on this constitutive soil model see Appendix G. Details on the implementation of this UMAT can be found in Appendix H.

In the hypoplastic soil domain, material damping is considered in terms of *Rayleigh damping*. The *Rayleigh* parameter α is set to 34.3, providing a mass proportional damping of about 7 % at frequency $f = \bar{f}$.

According to Smith [2015], in dynamic analyses the material response in the infinite elements is assumed to be isotropic. In the present simulations the elastic constitutive parameters assigned to the infinite elements are: density $\rho = 2200\,\mathrm{kg/m^3}$, *Young*'s modulus $E = 250 \times 10^6\,\mathrm{N/m^2}$, *Poisson*'s ratio $\nu = 0.3$.

Table 32: Material parameters of "Hochstetten Sand" for basic hypoplasticity [Herle, 1997]

φ_c [°]	h_s [N/m^2]	n	e_{d0}	e_{c0}	e_{i0}	α	β
33	1.5×10^9	0.28	0.55	0.95	1.05	0.25	1.50

Table 33: Additional parameters for hypoplasticity with intergranular strain [Niemunis and Herle, 1997]

R	m_R	m_T	β_r	χ
1×10^{-4}	5	2	0.5	6

3.2.8 Modeling approach to maintain numerical stability

In a hypoplastic constitutive law near-surface tensile strains may lead to positive effective normal stresses, and, as a result, to an abortion of the calculation due to the loss of material stiffness in the hypoplastic constitutive model. The implemented hypoplastic constitutive model can handle only small tensile stresses depending on the assigned "apparent cohesion" p_t. The default value of p_t is $1\,\mathrm{kN/m^2}$ [Gudehus et al, 2008]. Preliminary studies have shown that cyclic compression and expansion of the soil may lead to large displacements in the soil area close to the oscillation drum, which may impede stable numerical simulation. Thus, an "additional measure" must be applied to the stress-free surface, which turned out to be the most challenging problem of the presented modeling approach.

One option to avoid inadmissible tensile effective stresses and ensure better numerical stability known from the literature (e.g. [Chrisopoulos et al, 2016]) is to apply a constant distributed load to the soil surface (hereinafter referred to as "surface pressure"). In preliminary studies the effect of surface protection measures was tested with different values of p_t and additional surface pressure p_{surf}. Neither with an assumed apparent cohesion p_t of $10\,\mathrm{kN/m^2}$ nor with an applied surface pressure p_{surf} of $20\,\mathrm{kN/m^2}$ a whole roller pass could be simulated. The application of an initial static surface pressure larger than $20\,\mathrm{kN/m^2}$ proved to be unfeasible, because the initial soil stiffness increases, and consequently, the prediction of the drum motion and the compaction effect is incorrect.

Therefore, in a second approach the modeling attempt according to Heiniger [2018] has been tested. To this end, the stress-free surface is loaded by dynamically effective nodal forces only, achieved by application of viscous dampers to the nodes of the free surface. By defining additional dashpot dampers ("surface dampers") that *connect* the nodes of the free soil surface *to ground* [Smith, 2015], both in horizontal and vertical direction, the numerical difficulties related with the hypoplastic soil behavior were overcome. The damping coefficients c_x (horizontal) and c_y (vertical) of the surface dampers were found by trial and error (for further details see Appendix I.2 and Appendix I.4). This modeling approach has already been proven by Heiniger [2018], who was able to run a first stable FE simulation using surface dampers with $c_x = 560\,\mathrm{Ns/m}$ and $c_y = 1680\,\mathrm{Ns/m}$. Note that he used a larger value for c_y than for c_x, because the instabilities are related to the vertical soil response, where node velocities are lower than in horizontal direction. Preliminary studies based on the presented model (see Section 3.2.2) have shown that damper coefficients $c_x = c_y = 750\,\mathrm{Ns/m}$ in addition to an apparent cohesion of $p_t = 5\,\mathrm{kN/m^2}$ proved to be a useful combination ($e_0 = 0.90$) to simulate one oscillatory roller pass only. These values allow for a stable numerical analysis, however, they do affect the system response considerably, as shown by the results in Appendix I.4.

Thus, in the present dissertation another novel modeling attempt is pursued to increase the numerical stability associated with the hypoplastic constitutive law. It is proposed to "seal" the free soil surface with an elastic "protective foil" to prevent individual nodes from lifting off so strongly causing the analysis to be aborted. The "protective foil" is realized by assigning a linear elastic isotropic constitutive law to the elements of the first row of the soil mesh with a low *Young*'s modulus $E = 50 \times 10^6\,\mathrm{N/m^2}$ (found by trial and error) and p_t is set to $5\,\mathrm{kN/m^2}$, see Fig. 32. *Rayleigh damping* is assigned to this elastic layer. By setting the *Rayleigh* parameter α and β to 28.6 and 9.52×10^{-5}, respectively, a material damping of about $7\,\%$ is provided at frequency $f = \bar{f}$ and $f = 5\bar{f}$, whereas in between about $5\,\%$ damping is achieved. Also a hypoplastic "protective foil" with parameters $p_t = 500\,\mathrm{kN/m^2}$ and $e_0 = 0.60$ allows for a stable calculation and provides a comparable change of the void ratio. However, this approach affects the predicted drum accelerations to an unacceptable extent, and the computation time increases significantly.

3.3 Results and discussion

In the following, the response of the described model after the first pass of a HAMM HD$^+$ 90 VO tandem roller (see Table 31), is presented and evaluated. In the first study, an initially very loose soil with an initial void ratio of $e_0 = 0.90$ is considered for compaction. The results for the dynamic roller pass (stresses, strains and compaction effect) are compared with the outcomes of a "static" roller run due to the moving drum under the static vertical load P_0 without oscillation ($M_{Mu}(t) = 0$).

Next, the influence of the variation of different model and operating parameters on both compaction effect and response prediction, and in further consequence, on the CCC indicator proposed by Pistrol [2016] is studied. The influence of the initial void ratio e_0 on compaction effect and response prediction is assessed for three further initial void ratios in addition to the standard value of $e_0 = 0.90$ by considering the default value of $\mu = 0.50$. To investigate how the choice of the coefficient of friction μ, which controls the slip phase of the drum, affects the response prediction, and consequently the CCC indicator, in addition to the default value of $\mu = 0.50$, simulations with $\mu = 0.30$ are performed. The effect of the apparent cohesion p_t applied in the numerical model to the "subsoil" domain is analyzed by considering both the default value $p_t = 5\,\mathrm{kN/m^2}$ and the twofold value $p_t = 10\,\mathrm{kN/m^2}$. The corresponding simulations are both conducted for an initially very loose soil with an initial void ratio $e_0 = 0.90$ (standard subsoil) and an initially medium dense soil with $e_0 = 0.70$. In another study, the default value of the static axle load P_0 of the considered roller is varied by ±20 % and ±50 %, respectively. In order to clarify the significance of the roller speed for the effect of the oscillation drum, four additional speeds are considered in addition to the standard roller speed $v_0 = 1.11\,\mathrm{m/s}$. For the largest value of v_0, a second roller pass is simulated.

3.3.1 First observations

Fig. 33 shows the predicted distribution of the void ratio e in the upper soil layer of 1 m thickness after 2 s of compaction (a) with and (b) without oscillation. In the red areas the void ratio e is equal to the initial void ratio e_0. The compaction, i.e. a reduction of the initial void ratio e_0, is indicated by a color in the range from orange to deep blue depending on the predicted value of e. The color gray shows soil domains with loosening (i.e. $e > e_0$). This figure confirms that the oscillating roller has a much larger compaction effect on the subsoil than the static roller.

It is readily seen that the so-called *bow wave* ([Grabe, 1993], [Mooney and Rinehart, 2009], [Pistrol, 2016]) develops in front of both the static and dynamic drum, as it was observed in the field, because in this domain the soil is subjected to a vertical (y-direction) expansion and horizontal (x-direction) compression. The bow wave is a result of the roller motion at speed v_0, and in the case of the dynamic roller it is amplified by the shear waves induced by the oscillating unbalances. Thus, the oscillation drum results in a much larger bow wave and a much larger settlement trough than a static roller, compare the plots (a) and (b) of this figure. Due to the bow wave, the drum center lags behind the center of the contact area between drum and soil, and the distance between these centers becomes larger the larger the bow wave is. In the rear part of the bow wave vertex, the void ratio e decreases to a depth of about 0.7 m below the oscillating drum, whereas in the front of the vertex the soil is affected by the dynamic roller only to a depth of about 0.3 m. In a static roller pass, the soil below the bow wave surface is loosened, as can be seen in Fig. 33 (a). The influence of the settlement trough and the bow wave on the predicted change of the void ratio e will be discussed later in more detail (see Sections 3.3.2 and 3.3.3).

3.3.2 Stress and strain components in the soil

Now the predicted stresses and strains in representative elements at soil depths of 0.15 m, 0.25 m and 0.50 m, respectively, are considered. These elements, also subse-

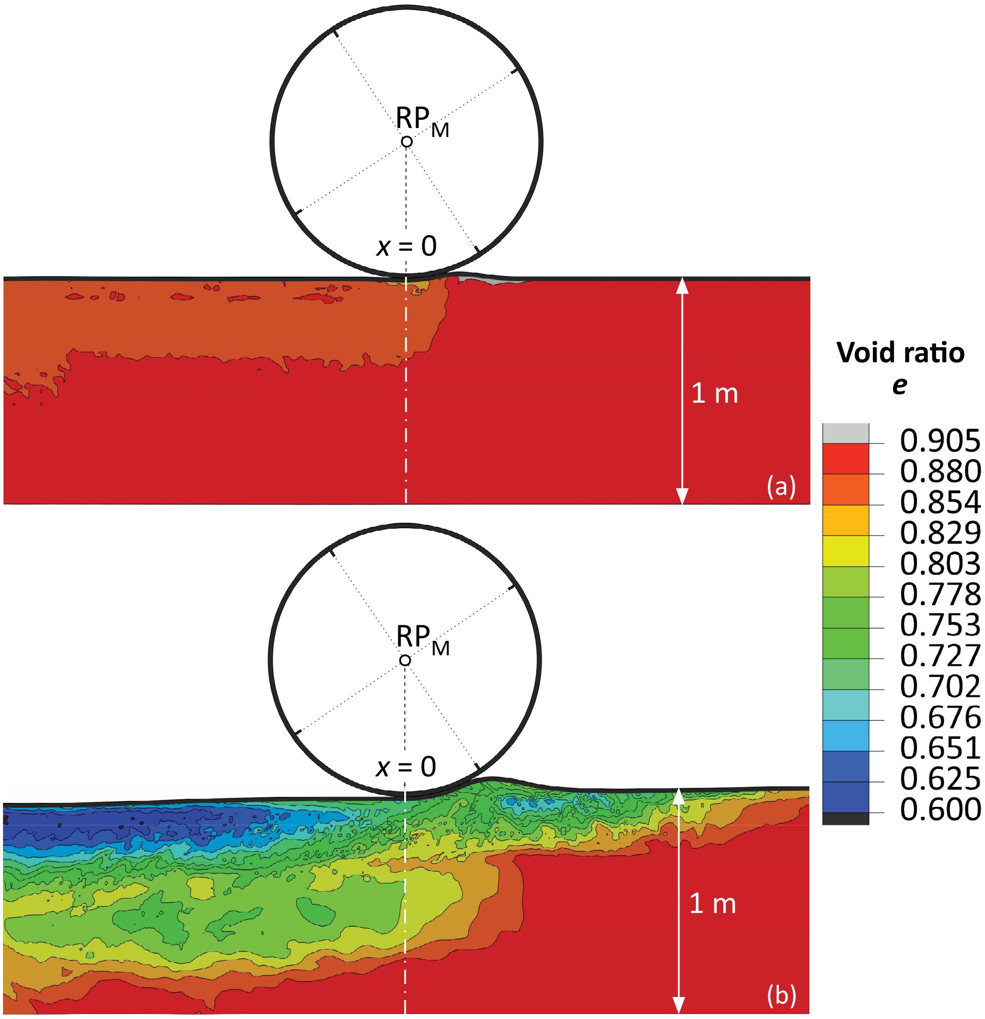

Figure 33: Distribution of void ratio e in the upper soil layer of 1 m thickness during compaction (a) without and (b) with oscillation

quently referred to as "observation points", are on top of each other in the section $x = 0$, as depicted in Fig. 31 by red circular markers. Figs 34, 35 and 36 show the stress and strain components at these observation points during the run of an oscillation roller and a static roller, respectively. In these figures, the abscissa represents the horizontal distance x_M of the drum center (moving at speed v_0) from the observation points. As the roller moves from left to right, a decrease of $-x_M$ indicates that the drum is approaching the element. At $x_M = 0$ the drum center is directly above the observation points, and with increasing $x_M > 0$ the drum moves away from the observation points. In the left plot of these figures, the *Cauchy* stress components "$S11$" (σ_{xx}), "$S22$" (σ_{yy}) and "$S12$" (σ_{xy}) are depicted. The right plot shows the logarithmic strains "LE11" (ϵ_{xx}), "LE22" (ϵ_{yy}) and "LE12" (ϵ_{xy}) according to the *ABAQUS*' convention, where "LE12" represents the engineering shear strain γ [Smith, 2015]. Positive stress and strain values represent tension and expansion, respectively. Blue lines show σ_{xx} and ϵ_{xx}, σ_{yy} and ϵ_{yy} are plotted in green, and σ_{xy} and ϵ_{xy} are depicted by red lines. Solid lines refer to the response quantities induced by the dynamic roller, whereas the outcomes of the static roller are indicated by dashed lines and the corresponding response variables by superscript "s".

The left plots of these figures show that the vertical normal stress component $\sigma_{yy}^{(s)}$ due to the static roller pass has a pulse shape (compression), the horizontal stress component $\sigma_{xx}^{(s)}$ the shape of a double pulse (also compression), and the shear stress $\sigma_{xy}^{(s)}$ the shape of a double pulse with a sign reversal in the vertical and horizontal planes, similar to the outcomes found in [Brown, 1996]. The absolute value of maximum $\sigma_{xy}^{(s)}$ before sign reversal is slightly smaller than the absolute value of minimum $\sigma_{xy}^{(s)}$ after sign reversal. That is, the peak shear stress is larger when the drum approaches the considered element. At x_M, where $\sigma_{xy}^{(s)}$ is zero, $\sigma_{yy}^{(s)}$ is minimum and $\sigma_{xx}^{(s)}$ has a local maximum. The corresponding location of the drum is in the negative x-range, but close to the observation points, i.e. $x_M \approx -0.05\,\text{m}$ to $-0.08\,\text{m}$.

Notably, the stresses induced by the dynamic roller are of the order of magnitude of the stresses from a static roller pass. The observed high-frequency stress oscillations with small amplitudes superimposed on the quasi-static stress regime of σ_{xx}, σ_{yy}, and σ_{xy} are due to the oscillatory excitation moment. The high-frequency stress oscillations σ_{xx} and σ_{yy} mostly oscillate in phase, as can be seen in field tests [Kopf, 1999].

Moreover, the general trend of the quasi-static parts of the components σ_{yy}, σ_{xy} and the corresponding static roller-induced stress components $\sigma_{yy}^{(s)}$, $\sigma_{xy}^{(s)}$ is the same, but with a slight shift to the left that increases with soil depth. Therefore, the minimum of σ_{yy} also occurs during compaction with the dynamic roller before the drum passes the observation point, but at a greater distance to the left depending on the soil depth, i.e. $x_M \approx -0.15\,\text{m}$ ($y = -0.15\,\text{m}$) to $-0.27\,\text{m}$ ($y = -0.50\,\text{m}$). Compared to $\sigma_{xy}^{(s)}$, the asymmetry of σ_{xy} with respect to the axis $y = 0$ is more pronounced for the dynamic roller at a soil depth $\leq 0.25\,\text{m}$. In particular, minimum σ_{xy} is much smaller than minimum $\sigma_{xy}^{(s)}$, and both minimum and maximum $\sigma_{yy}^{(s)}$ are shifted to the left.

The difference between the quasi-static part of the normal stress σ_{xx} (oscillation roller) and the stress component $\sigma_{xx}^{(s)}$ (static roller) is more pronounced than in the previously discussed stress components. In particular at the depth of $y = -0.15\,\text{m}$, in the positive x-range the quasi-static part of σ_{xx} is almost zero, while $|\sigma_{xx}^{(s)}|$ has a maximum. Moreover, at $x_M < -0.4\,\text{m}$, maximum $|\sigma_{xx}|$ is much smaller than maximum $|\sigma_{xx}^{(s)}|$. However, with increasing soil depth the difference between $|\sigma_{xx}|$ and $|\sigma_{xx}^{(s)}|$ diminishes. This numerically observed difference in σ_{xx} was also found in field tests [Kopf, 1999] and can be attributed to the loosening of the soil [Kopf, 1999] and the release of residual ("locked in") stresses (evident in the static roller pass) [Mooney and Rinehart, 2009] by the oscillating drum.

In field tests ([Pistrol, 2016], [Kopf, 1999]), the dynamic vertical normal stress was recorded during compaction by an oscillation roller. As example, Fig. 310 (based on Pistrol [2016]) shows the dynamic soil stresses at the depth of $y = -0.50\,\text{m}$ in a soil medium compacted by the oscillation roller HAMM HD^{+} 90 VO considered in this numerical study. To compare the computed soil stresses with the stresses recorded in the field tests, the dynamic parts of the stress components, $\sigma_{xx}^{(d)}$, $\sigma_{yy}^{(d)}$, and $\sigma_{xy}^{(d)}$, respectively, are extracted by subtracting the quasi-static portions from the total stresses σ_{xx}, σ_{yy}, and σ_{xy}, respectively. The extracted stress quantities are depicted

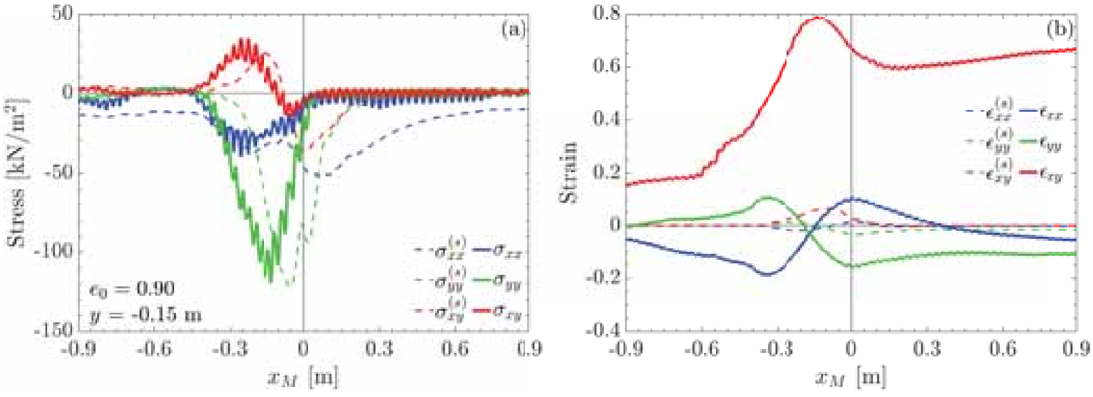

Figure 34: (a) Stress and (b) strain components at $x = 0$ due to an oscillatory (solid lines) and static roller pass (dashed lines), respectively; depth $y = -0.15\,\mathrm{m}$

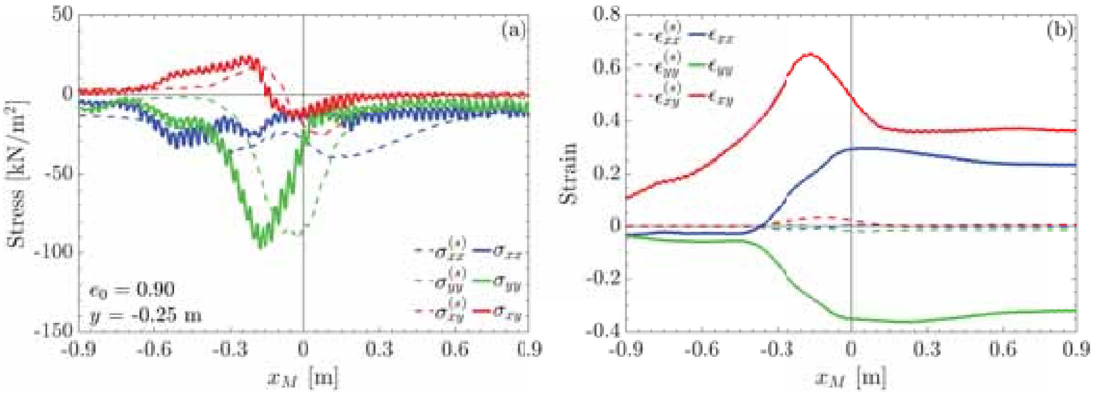

Figure 35: (a) Stress and (b) strain components at $x = 0$ due to an oscillatory (solid lines) and static roller pass (dashed lines), respectively; depth $y = -0.25\,\mathrm{m}$

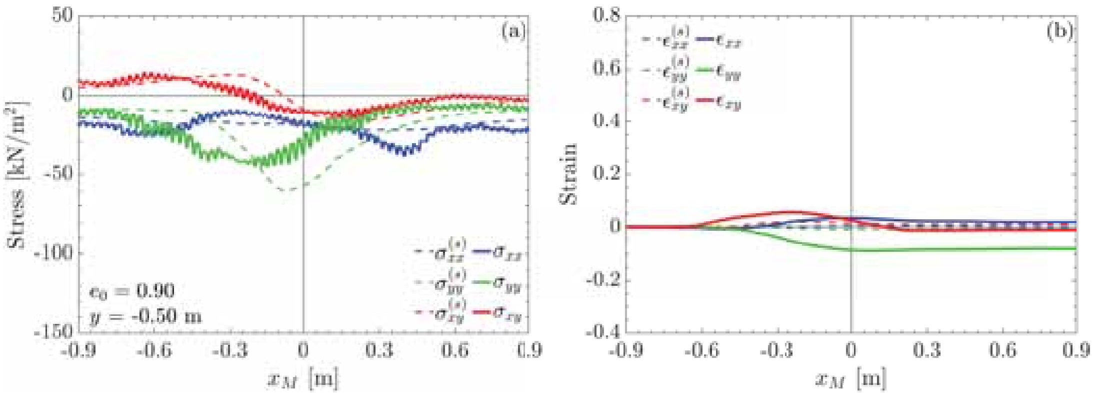

Figure 36: (a) Stress and (b) strain components at $x = 0$ due to an oscillatory (solid lines) and static roller pass (dashed lines), respectively; depth $y = -0.50\,\mathrm{m}$

in Figs 37 ($\sigma_{xx}^{(d)}$), 38 ($\sigma_{yy}^{(d)}$), and 39 ($\sigma_{xy}^{(d)}$) for two selected depths, i.e. $y = -0.15\,\mathrm{m}$ (left plots) and $y = -0.50\,\mathrm{m}$ (right plots). These figures show that the frequency content of $\sigma_{xx}^{(d)}$, $\sigma_{yy}^{(d)}$ and $\sigma_{xy}^{(d)}$ is primarily dominated by the excitation frequency $\bar{f}$. At $x_M \approx -0.2\,\mathrm{m}$ in the depth $y = -0.15\,\mathrm{m}$, the evolution of $\sigma_{xx}^{(d)}$ with respect to x_M has a "node" that indicates the presence of the second harmonic of $\bar{f}$ (see Fig. 37 (a)). In the larger depth of $y = -0.50\,\mathrm{m}$, a node appears at $x_M \approx -0.27\,\mathrm{m}$ (see Fig. 38 (b)). In the normal stress component $\sigma_{xx}^{(d)}$ a node at $x_M \approx -0.23\,\mathrm{m}$, which is more obvious at larger depth, also indicates the presence of the second harmonic of $\bar{f}$. The dynamic shear stress component $\sigma_{xy}^{(d)}$ shows two distinct nodes, one when the drum approaches $x_M = 0$ and one when the drum moves away from the origin. Comparing the left plots of Figs 37 and 39 reveals that at $y = -0.15\,\mathrm{m}$ the maximum amplitude of $\sigma_{xy}^{(d)}$ of about $8\,\mathrm{kN/m^2}$ occurs at the same x_M ($\approx 0.2\,\mathrm{m}$) where the amplitude of $\sigma_{xx}^{(d)}$ is about zero (node). The dynamic horizontal normal stress $\sigma_{xx}^{(d)}$ is approximately zero when the center of the contact zone and the observation point at $y = -0.15\,\mathrm{m}$ are on top of each other, while the dynamic shear stress $\sigma_{xy}^{(d)}$ reaches its maximum. The maximum amplitudes of $\sigma_{xx}^{(d)}$ are about $8.5\,\mathrm{kN/m^2}$ ($y = -0.15\,\mathrm{m}$) and $3.4\,\mathrm{kN/m^2}$ ($y = -0.50\,\mathrm{m}$), respectively, and thus, in the same order of magnitude as the peak amplitudes of $\sigma_{xy}^{(d)}$. The peak amplitudes of the vertical stress component $\sigma_{yy}^{(d)}$ are almost twice as high these values, i.e. $15\,\mathrm{kN/m^2}$ ($y = -0.15\,\mathrm{m}$) and $6.5\,\mathrm{kN/m^2}$ ($y = -0.50\,\mathrm{m}$), respectively.

Comparison of the vertical dynamic stress components $\sigma_{yy}^{(d)}$ at depth $y = -0.50\,\mathrm{m}$ (Fig. 38 (b)) with the experimentally found soil stress at the same depth (Fig. 310, based on Pistrol [2016]) shows that computed and measured stresses are in good qualitative and quantitative agreement. The peak amplitudes differ from each other only by about 7 %. However, the recorded peak stress amplitude occurs in the negative x-domain, while in the computed counterparts at $x_M > 0$. The latter result, however, corresponds with the observations from earlier field tests documented in [Kopf, 1999].

Now the computed soil strains ϵ_{xx}, ϵ_{yy} and ϵ_{xy} depicted in the right plots of Figs 34, 35 and 36 are addressed. As can be observed at first glance, the strains induced by the oscillation roller are magnitudes larger than the strains due to the static roller, in contrast to the stresses. As the drum approaches the considered element, the soil at depth $y = -0.15\,\mathrm{m}$ is exposed to increasing vertical expansion ($\epsilon_{yy} > 0$) and longitudinal compression ($\epsilon_{xx} < 0$). This can be attributed to the bow wave and the settlement trough, which develop during compaction. The peak values of both quantities, $\max \epsilon_{yy} = 0.11$ and $\min \epsilon_{xx} = -0.19$, which are reached at $x_M \approx -0.33\,\mathrm{m}$, are about ten times larger than those resulting from a static roller pass. At about $x_M = -0.15\,\mathrm{m}$, ϵ_{xx} turns into the extension regime, while ϵ_{yy} turns into the compression regime. Local peak values equal to the first peak values are reached at $x_M \approx 0$. In the range of moving away, at about $x_M = 0.4\,\mathrm{m}$ the strain ϵ_{xx} turns back into compression.

As the depth increases, in the approaching zone $-0.9\,\mathrm{m} \leq x_M \leq -0.4\,\mathrm{m}$ the impact of the bow wave and the settlement trough on these strain components diminishes, and thus, ϵ_{xx} and ϵ_{yy} are small and negative (compression). At medium depth $y = -0.25\,\mathrm{m}$, at $x_M \geq -0.4\,\mathrm{m}$ the strain ϵ_{xx} increases and becomes positive. Its maximum $\max \epsilon_{xx} = 0.3$ is reached at $x_M \approx 0.05\,\mathrm{m}$. A further increase of x_M yields ϵ_{xx} almost constant. Remarkably, at this depth $\max \epsilon_{xx}$ is about 2.7 times larger than its maximum at the depth closer to the surface $y = -0.15\,\mathrm{m}$ (compare Figs 35 (b)

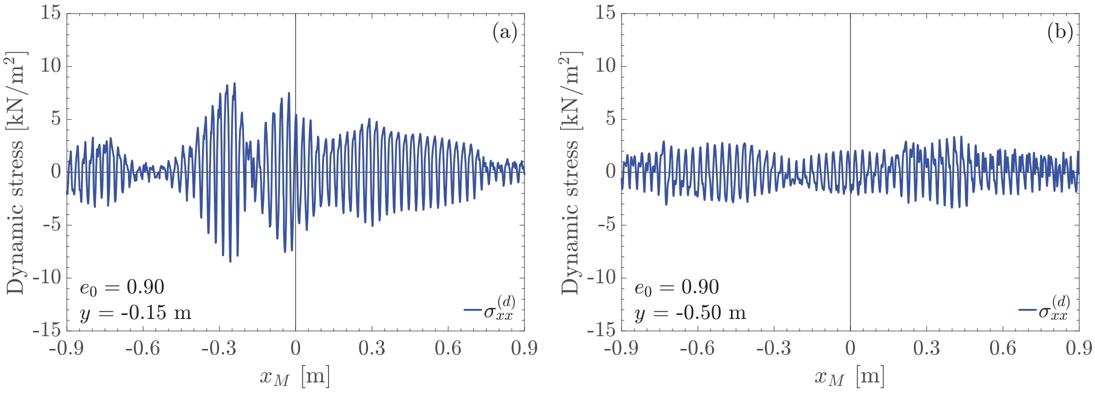

Figure 37: Dynamic part of the horizontal stress $\sigma_{xx}^{(d)}$ at $x = 0$ and a depth of (a) 0.15 m and (b) 0.50 m

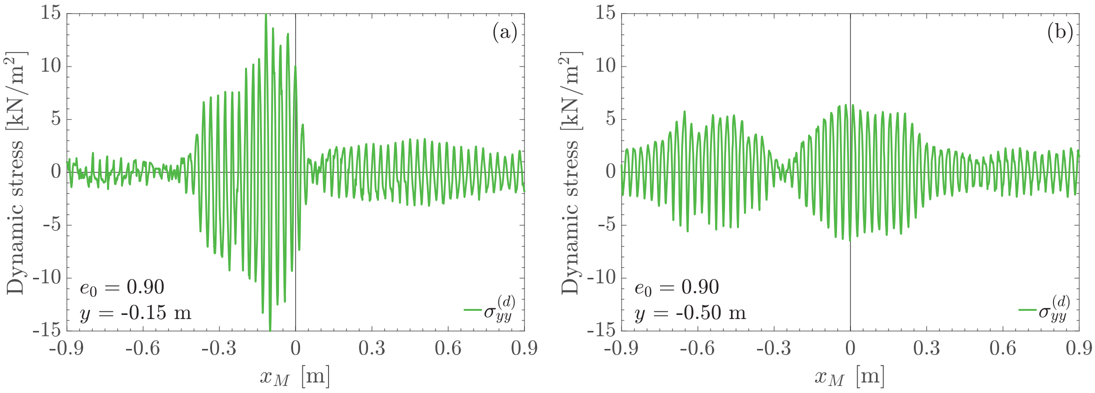

Figure 38: Dynamic part of the vertical stress $\sigma_{yy}^{(d)}$ at $x = 0$ and a depth of (a) 0.15 m and (b) 0.50 m

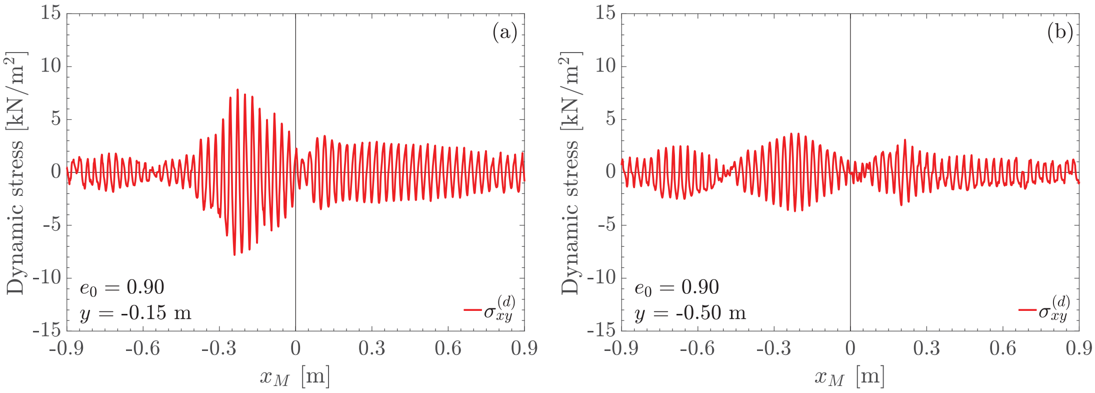

Figure 39: Dynamic part of the shear stress $\sigma_{xy}^{(d)}$ at $x = 0$ and a depth of (a) 0.15 m and (b) 0.50 m

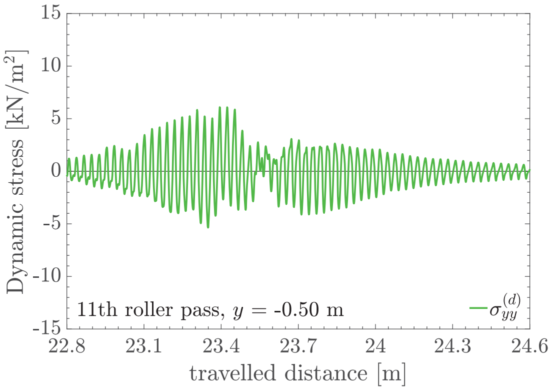

Figure 310: Dynamic part of the vertical stress at a depth of 0.5 m; recorded in field tests on gravel [Pistrol, 2016]

and 34 (b)). The strain component ϵ_{yy} remains in the compressive regime in the entire considered range of x_M. It decreases significantly in the range $-0.40\,\mathrm{m} \leq x_M \leq 0.25\,\mathrm{m}$. The maximum compressive strain min $\epsilon_{yy} = -0.36$ at $x_M \approx 0.25\,\mathrm{m}$ is 2.3 times larger than that at depth $y = -0.15\,\mathrm{m}$. The observed reduction of ϵ_{xx} with further increasing x_M is insignificant. At the largest considered depth $y = -0.50\,\mathrm{m}$, compressive and expansion strains are still observed that are about ten or 13 times larger than those caused by a static roller (see Fig. 36 (b)). However, they are much smaller than the ones at depth $y = -0.25\,\mathrm{m}$.

It is also noteworthy that the shear strains are larger than the normal strain components in the entire considered soil domain subjected to oscillatory loading. While at depth $y = -0.15\,\mathrm{m}$ the maximum shear strain max $\epsilon_{xy} = 0.8$ is reached at $x_M \approx -0.13\,\mathrm{m}$, at depth $y = -0.25\,\mathrm{m}$ max $\epsilon_{xy} = 0.65$ is predicted at $x_M \approx -0.16\,\mathrm{m}$. In the depth $y = -\ 0.50\,\mathrm{m}$, the maximum shear strain max $\epsilon_{xy} = 0.06$ is shifted even further in the negative x-range to $x_M \approx -0.25\,\mathrm{m}$.

At the shallow depth of $y = -0.15\,\mathrm{m}$ the residual shear strain of approximately 0.7 ($x_M = 0.9\,\mathrm{m}$) is about six times larger than $|\epsilon_{yy}|$ and eleven times larger than $|\epsilon_{xx}|$. At depth $y = 0.25\,\mathrm{m}$, the residual shear strain decreases to 0.36 and is therefore only 12 % larger than the residual vertical normal strain ϵ_{yy} (compression), but 56 % larger than the residual horizontal normal strain ϵ_{xx} (extension). The residual compressive strain ϵ_{yy} of about -0.08 at depth $y = 0.50\,\mathrm{m}$ is still 73 % of the residual counterpart at $y = -0.15\,\mathrm{m}$. The numerical results, thus, indicate that one pass of oscillatory loading on loose soil with an initial void ratio $e_0 = 0.90$ results in plastic strains of considerable size to a depth of at least 0.50 m.

3.3.3 Compaction effect in terms of void ratio change

Next, the effect of different parameters in the numerical model on the predicted soil compaction due to the oscillatory load is examined in terms of the void ratio e, which is normalized to its initial value e_0, i.e. e/e_0. The soil section considered is the potential "compaction zone" at depth 0 to 1 m and horizontal extent $-0.5\,\mathrm{m} \leq x \leq 0.5\,\mathrm{m}$, also referred to as "observation zone" in Fig. 31.

Static vs. dynamic roller pass
First, the void ratio e normalized to its initial value $e_0 = 0.90$, i.e. e/e_0, at two different observation points in the soil ($x = 0, y = -0.15$ m and $x = 0, y = -0.50$ m) during the roller motion is considered, similarly to the discussion of soil stress and strain components in the previous Section 3.3.2. Fig. 311 shows the ratio e/e_0 with respect to the horizontal distance x_M of the drum center from the observation points resulting from the oscillatory roller (red line with circular markers) and the static roller (black line), respectively. As can be readily seen, the static roller begins to compact the subsoil when the drum center is at a distance of -0.3 m to -0.4 m from the observation points. Interestingly, at the greater depth of $y = -0.50$ m compaction is initiated earlier than at the lesser depth of $y = -0.15$ m. The largest compaction is achieved when the drum center is directly above the observation point, i.e. $x_M = 0$. When the static roller moves away, a slight soil loosening is observed (i.e. ratio e/e_0 increases slightly), but this is insignificant. At the near-surface observation point, the single static roller pass provides a void ratio reduction (i.e. compaction) of only 4 %, which is approximately four times the predicted reduction at the larger depth of 0.50 m.

In contrast, an oscillating drum reduces the void ratio by 30 % at $y = -0.15$ m and by 13 % at $y = -0.50$ m. While in the deeper observation point the compaction is virtually complete when the oscillating drum is directly above, at the near-surface point more than half of the compaction is achieved after the drum has passed the points at $x = 0$. In contrast to the lower observation spot, soil compaction at the near-surface point does not increase continuously during the dynamic roller pass. At a distance $x_M \approx -0.45$ m, a local minimum of the ratio e/e_0 is observed. As the drum continues to approach the observation point, the ratio e/e_0 becomes larger, up to 7 % at $x = 0$, i.e. the soil is loosened in the range as result of the bow wave developing at the surface. In the subsequent zone $x_M > 0$, the soil is increasingly compacted again. Obviously, the void ratio in the near-surface point was already reduced before the approaching dynamic drum reaches the observation area at $x_M = -0.9$ m, and additional compaction is still achieved after the roller has left the considered area at $x_M = 0.9$ m. That is, the reach of the oscillation roller is at least 1.5 times the drum radius r. In the deeper observation point, the predicted horizontal expansion of the compaction zone is bounded by the drum radius r, i.e. $-r < x_M < r$.

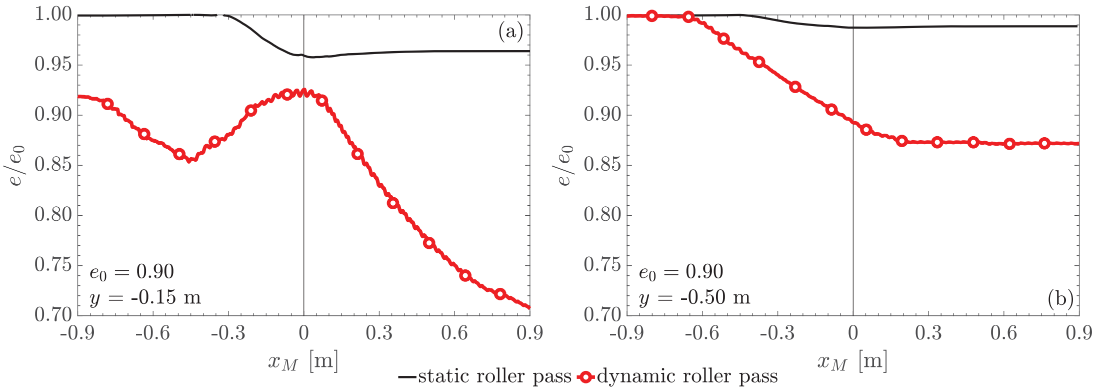

Figure 311: Normalized void ratio e/e_0 at section $x = 0$ at soil depths of (a) 0.15 m and (b) 0.50 m during a static and oscillatory roller pass

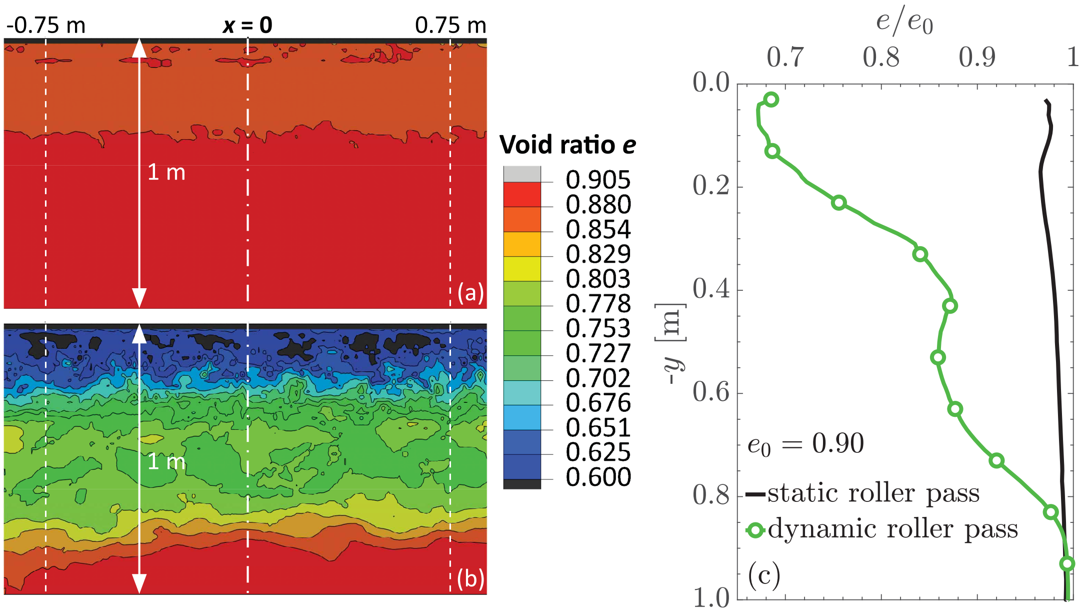

Figure 312: Distribution of void ratio e in the upper soil layer of 1 m thickness after a (a) static and (b) oscillatory roller pass, and (c) corresponding normalized void ratio profile at $x = 0$

After having assessed the void ratio evolution at two selected observation spots, the compaction effect in the entire range of the potential “compaction zone” is investigated. To this end, Fig. 312 shows the distribution of e in the upper soil layer with 1 m thickness in the range $-0.75\,\mathrm{m} \leq x \leq 0.75\,\mathrm{m}$ after a single static roller run (plot (a)) and a single oscillatory roller pass (plot (b)). Red domains indicate a void ratio very close to its initial value $e_0 = 0.90$. The color range from orange to deep blue refers to increased compaction, as specified in the legend. The darker the soil domain is colorized, the more compacted the soil is. In gray domains the soil is loosened, i.e. $e > e_0$. These contour plots illustrate that a single static roller pass reduces e to a depth of about 0.3 m by less than 4 %. In contrast, the oscillation roller reduces e by about 0.8-0.9 m below surface. The largest reduction of e is achieved in the upper soil layer of about 0.2 m. For better readability, Fig. 312 (c) shows for both rollers a profile of the ratio e over e_0 at $x = 0$ with respect to the soil depth. These profiles, subsequently referred to as “normalized void ratio profiles”, represent the mean of e/e_0 in the soil region $-0.5\,\mathrm{m} \leq x \leq 0.5\,\mathrm{m}$ analyzed in steps of 0.05 m. A ratio $e/e_0 < 1$ indicates soil compaction. This figure illustrates the superiority of an oscillation roller over a static roller in terms of compaction efficiency. While the oscillation roller in the upper soil layer of 0.2 m reduces the void ratio by 33 %, a decrease of 13 % (i.e. $e/e_0 = 0.87$) at the depth $y = -0.45\,\mathrm{m}$ is still observed. At a depth of about 0.9 m the effect of the oscillation roller diminishes completely.

Variation of the initial void ratio

In the following, the influence of the *initial void ratio* e_0 on the compaction effect is discussed. To this end, additional computations with $e_0 = 0.80$, 0.70, and 0.60, respectively, were performed, indicating initially loose, medium dense, and dense soil,

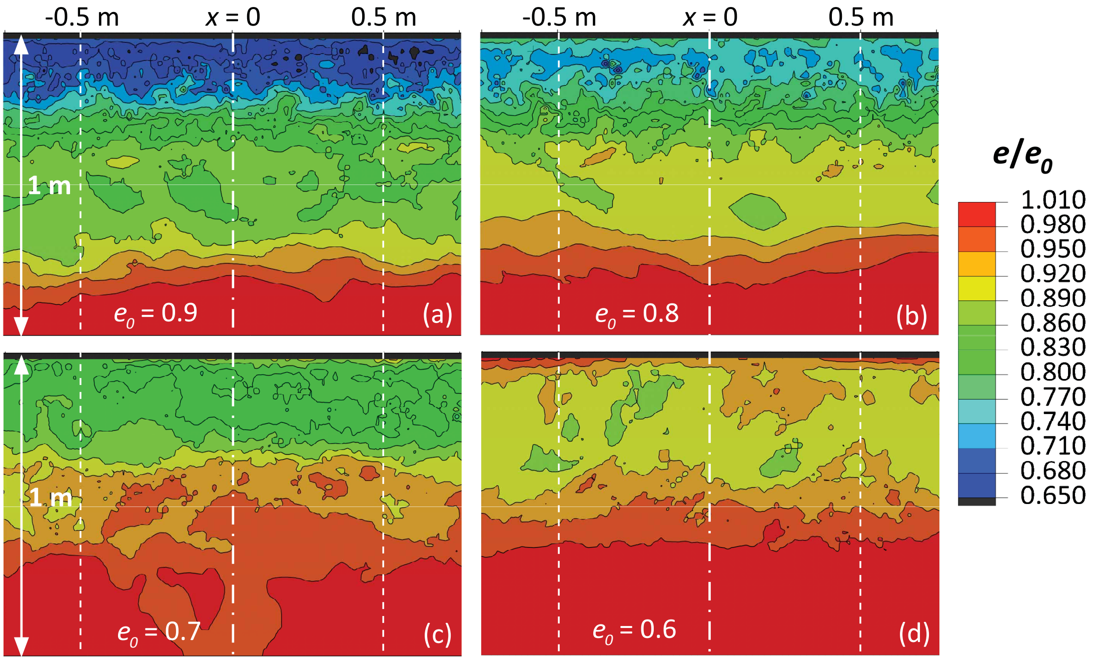

Figure 313: Distribution of normalized void ratio e/e_0 in the upper soil layer of 1 m thickness after an oscillatory roller pass for an initial void ratio e_0 of (a) 0.90, (b) 0.80, (c) 0.70, and (d) 0.60

respectively. Figs 313 illustrate the distribution of the normalized void ratio e/e_0 in the same subsurface area after an oscillatory roller pass on initially (a) very loose ($e_0 = 0.90$), (b) loose ($e_0 = 0.80$), (c) medium dense ($e_0 = 0.70$), and (d) dense soil ($e_0 = 0.60$). As expected, the relative compaction (i.e. e/e_0) decreases with decreasing initial void ratio e_0. The corresponding normalized void ratio profiles e/e_0 at $x = 0$ plotted in Fig. 314 make the effect of e_0 on the compaction achieved more visible. As previously discussed, for the very loose soil with $e_0 = 0.90$ a maximum soil compaction, i.e. $1 - \min(e/e_0)$, of 33 % is predicted, while in an initially dense soil ($e_0 = 0.60$) the maximum compaction is about 10 % only. The corresponding compaction value for $e_0 = 0.80$ is about 26 % and for $e_0 = 0.70$ it is 17 %. For $e_0 = 0.70$ to $e_0 = 0.90$, the maximum compaction is achieved about 0.1 m below the surface. For $e_0 = 0.60$, in contrast, the maximum void ratio reduction is observed at a depth of about 0.3 m.

The 105 % value of $\min(e/e_0)$, which is considered as indicator of uniform high compaction, is observed at depths of ≈ 0.15 m (initially very loose soil) and ≈ 0.2 m (loose soil). In a medium dense soil, the depth range of uniformly high compaction increases to ≈ 0.3 m. This depth increases further for the initially dense soil to ≈ 0.5 m. The mean value of e/e_0 in this depth range (dotted lines in Fig. 314) varies between 0.68 ($e_0 = 0.90$) and 0.91 ($e_0 = 0.60$), i.e. an average compaction of approximately 32 % and 9 %, respectively. These results confirm the assumption that with increasing initial soil density, the maximum compaction to be achieved becomes smaller, but the uniformity of compaction increases over the depth. At depth $y \approx -0.45$ m the profiles for $e_0 = 0.90$, 0.80, and 0.70 show a local maximum with a corresponding void ratio reduction of about 13 % ($e_0 = 0.90$) to 6 % ($e_0 = 0.70$). In contrast, no local maximum

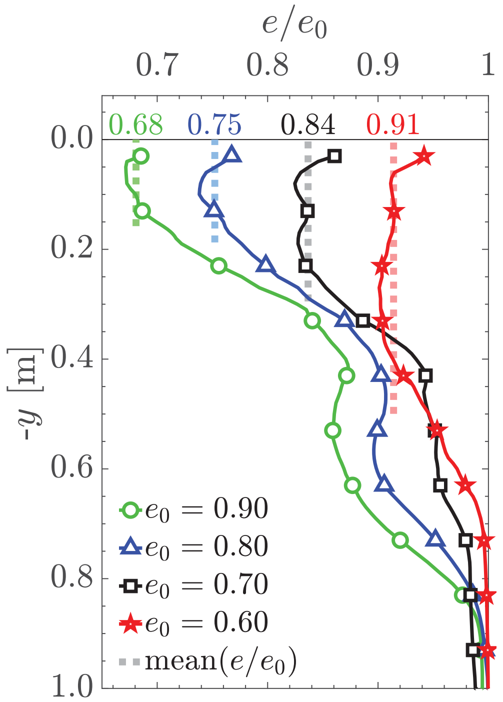

Figure 314: Normalized void ratio profile e/e_0 at $x = 0$ for four different initial void ratios e_0, based on Fig. 313

in the profile is observed for the dense soil at this depth. While for $e_0 = 0.90$, 0.80, and 0.70 the depth effect of the oscillation roller on the void ratio is about 0.95 m, the depth effect in the dense soil is reduced to 0.8 m.

Variation of the coefficient of friction

Next, the influence of the *coefficient of friction* μ, which governs in the numerical model the contact between the drum and the soil surface, is addressed. To this end, Fig. 315 shows the distribution of the normalized void ratio e/e_0 in the compaction zone after a single oscillatory roller pass on initially very loose ($e_0 = 0.90$) (plots a,b) and medium dense ($e_0 = 0.70$) (plots c,d) soil, both for the default value $\mu = 0.50$ (plots a,c) and the reduced value $\mu = 0.30$ (plots b,d). The areas highlighted in red correspond to non-compacted or weakly compacted areas, i.e. e is equal or slightly smaller than its initial value e_0. The largest compaction is achieved in the blue area. In grey areas the soil is loosened, i.e. $e > e_0$. Note that the colour scale that distinguishes the achieved e/e_0-value is the same for all subsequent representations. Fig. 316 shows the corresponding profiles of the normalized void ratio e/e_0 over the soil depth $-y$ for (a) $e_0 = 0.90$ and (b) $e_0 = 0.70$. These profiles in turn represent the mean of e/e_0 in the soil region $-0.5\,\text{m} \leq x \leq 0.5\,\text{m}$. Comparison of Figs 315 (a) and (b) reveals that the model with smaller coefficient of friction predicts a slightly lower compaction of an initially very loose soil in the depth range $0.3\,\text{m} \leq -y \leq 0.7\,\text{m}$, while the other soil zones remain virtually unaffected by the choice of μ. This result is confirmed by the corresponding profile e/e_0 vs. depth shown in Fig. 316 (a). In the depth range $0.3\,\text{m} \leq -y \leq 0.7\,\text{m}$, the compaction effect is at most about 3 % lower for $\mu = 0.30$. The maximum predicted soil compaction, i.e. $1 - \min(e/e_0)$, is almost 33 % for both $\mu = 0.50$ and $\mu = 0.30$. Moreover, the 105 % value of $\min(e/e_0)$, which is considered as an indicator of uniform high compaction, is observed at same the depth of ≈ 0.15 m. The depth, where the subsoil remains virtually unaffected by the oscillation roller ($e/e_0 \approx 1$), referred to as "depth effect", is about 0.95 m for both coefficients of friction.

In contrast, in the case of an initially medium dense soil ($e_0 = 0.70$) the smaller coefficient of friction has a greater impact on the compaction effect. For $\mu = 0.30$, e/e_0 is over the whole considered soil depth smaller compared to the outcomes based on $\mu = 0.50$ (compare Figs 315 (c) and (d)). Thus, the maximum predicted soil compaction is smaller for the lower μ-value, as illustrated in Fig. 316 (b).

Comparison of Figs 316 (a) and (b) also shows the expected result that with increasing initial soil density characterized by e_0 the maximum achieved compaction decreases. The uniformity of compaction, however, increases over the depth, and the 105 % value of $\min(e/e_0)$ is reached at a depth of approximately 0.3 m for both $\mu = 0.50$ and $\mu = 0.30$ if $e_0 = 0.70$.

Variation of the apparent cohesion

Next, the influence of the *apparent cohesion* p_t on the predicted compaction effect is discussed. To this end, the predicted normalized void ratio e/e_0 is evaluated in the same manner for two different values of p_t (default value $p_t = 5\,\mathrm{kN/m^2}$ and increased value $p_t = 10\,\mathrm{kN/m^2}$), and two initial void ratios ($e_0 = 0.90$ and $e_0 = 0.70$). The resulting normalized void ratios e/e_0 are shown in Figs 317 (contour plot) and 318 (corresponding profiles). As can be observed at first glance, the larger apparent cohesion of $10\,\mathrm{kN/m^2}$ predicts a lower ratio e/e_0 to a depth of 0.45 m (very loose soil) and 0.75 m (medium dense soil), respectively, by almost 10 % at most. Thus, in the near-surface soil domain the predicted soil compaction is higher if a larger apparent compaction is assigned to the numerical model. In the initially very loose soil ($e_0 = 0.90$), the maximum predicted soil compaction is about 37 % for the higher value $p_t = 10\,\mathrm{kN/m^2}$, and about 33 % for the default value $p_t = 5\,\mathrm{kN/m^2}$. A roller pass on initially medium dense soil causes a void ratio reduction of about 22 % at most for $p_t = 10\,\mathrm{kN/m^2}$, and 18 % for $p_t = 5\,\mathrm{kN/m^2}$. The depth, where the 105 % value of $\min(e/e_0)$ is observed, increases slightly from 0.15 m to 0.20 m in a very loose soil ($e_0 = 0.90$), while it is virtually unaffected in a medium dense soil ($e_0 = 0.70$) if the simulation is performed with the larger value of p_t. The depth effect of the oscillation roller on the void ratio is about 0.95 m for both very loose and medium dense soil, and thus, almost not affected by the increase of the apparent cohesion.

Variation of the static axle load

Subsequently, the *static axle load* P_0 of the drum is varied to reveal the effect of this quantity on the compaction effect. In particular, the default value of P_0, as listed in Table 31, is varied by ±20 % and ±50 %, respectively. For this study, compaction of a very loose soil characterized by the initial void ratio $e_0 = 0.90$ is considered. The predicted normalized void ratio e/e_0, evaluated in the same way as before, is depicted in Figs 319 (distribution in the observation zone) and 320 (corresponding profiles). Comparison of Figs 319 (a), (b), (c) and (d) reveals that with increasing axle load P_0 the depth effect of the oscillation roller becomes larger. The maximum achievable

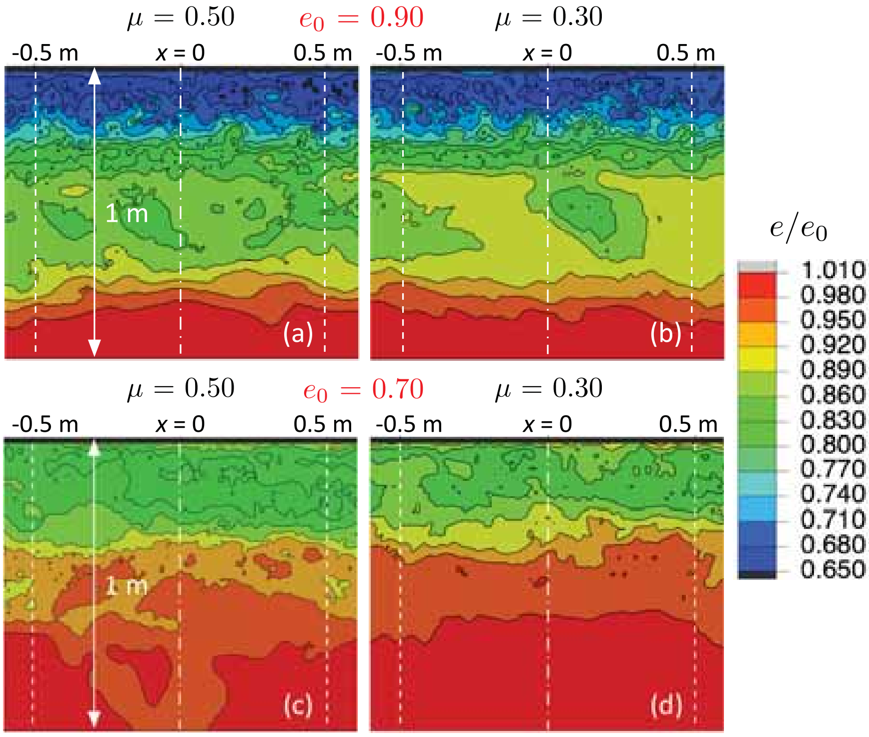

Figure 315: Normalized void ratio after one oscillatory roller pass; initial void ratio (a,b) $e_0 = 0.90$ and (c,d) $e_0 = 0.70$; coefficient of friction (a,c) $\mu = 0.50$ and (b,d) $\mu = 0.30$

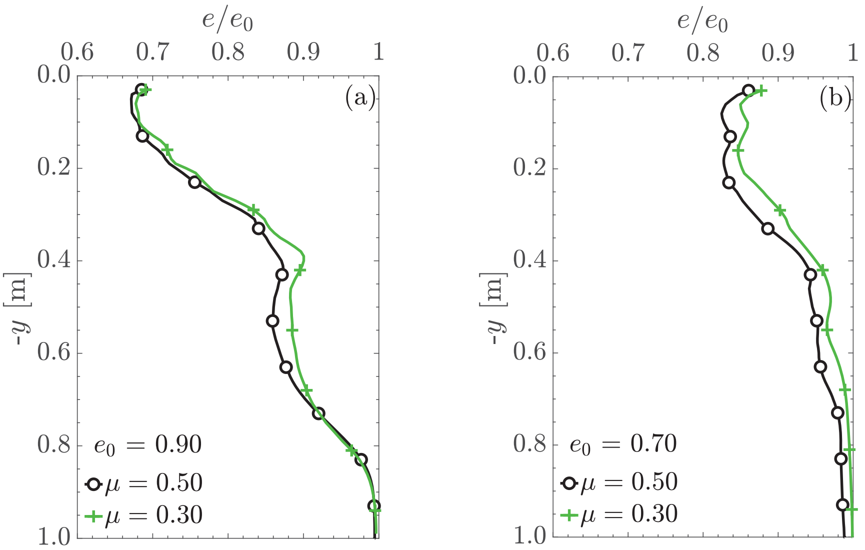

Figure 316: Normalized mean void ratio profile for two values of the coefficient of friction μ; initial void ratio (a) $e_0 = 0.90$ and (b) $e_0 = 0.70$, based on Fig. 315

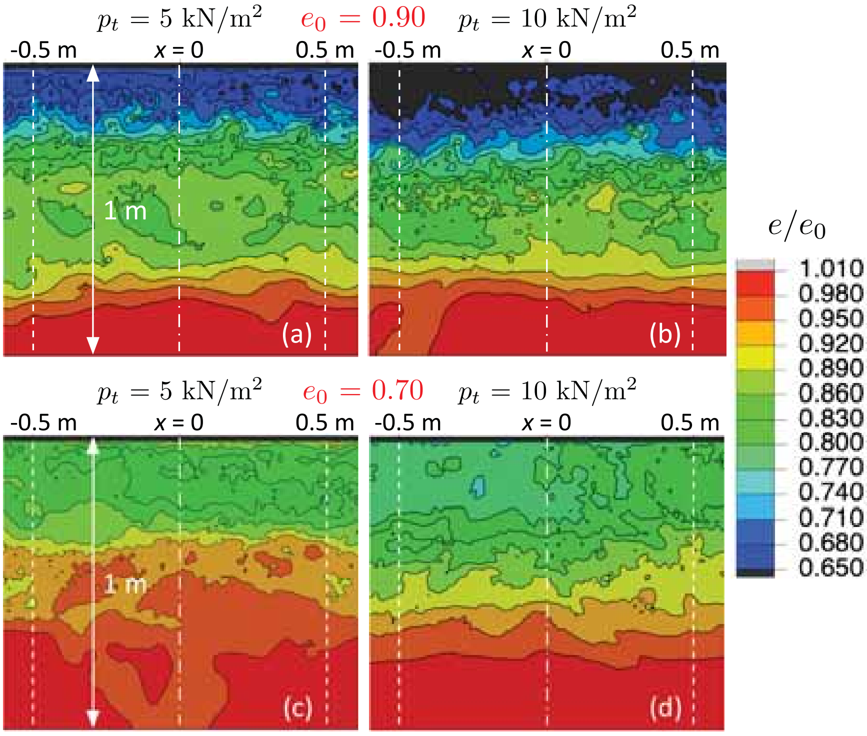

Figure 317: Normalized void ratio after one oscillatory roller pass; initial void ratio (a,b) $e_0 = 0.90$ and (c,d) $e_0 = 0.70$; (a,c) $p_t = 5\,\mathrm{kN/m^2}$ and (b,d) $p_t = 10\,\mathrm{kN/m^2}$

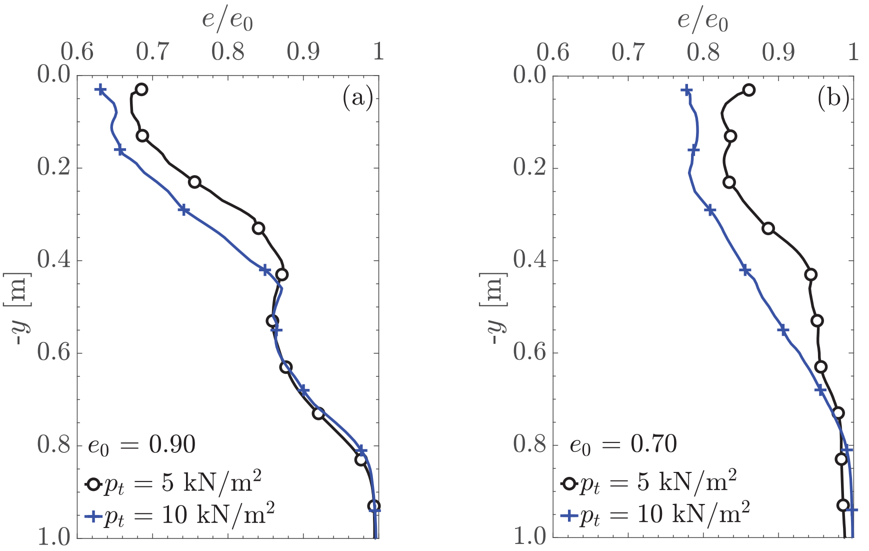

Figure 318: Normalized mean void ratio profile for two values of the apparent cohesion p_t; initial void ratio (a) $e_0 = 0.90$ and (b) $e_0 = 0.70$, based on Fig. 317

void ratio reduction of around 33 % is, however, virtually not affected by the considered variation of P_0. The depth range $0.4\,\mathrm{m} \leq -y \leq 0.9\,\mathrm{m}$ is influenced most by the increased axle load, as shown in Figs 320 (a) and (b). Comparison of Figs 320 (a) and (b) reveals that a reduction of the default static axle load has a significantly stronger impact on the void ratio decrease in the aforementioned depth range than an increase of P_0 by the same amount. Notably, in the soil zone above 0.4 m the normalized void ratios based on the reduced axle load are continuously slightly lower than the ones based on the larger value of P_0, i.e. from the lower axle load results numerically a slightly larger soil compaction, as clearly shown by Fig. 320 (b). The 105 % value of $\min(e/e_0)$ is observed at a depth of about 0.18 m for both reduced and increased axle load by ±20 %, and is, thus, slightly larger compared to the default value of P_0. In the case of the variation of P_0 by ±50 %, the 105 % value of $\min(e/e_0)$ is observed at a depth of about 0.16 m for the reduced and at around 0.13 m for the increased axle load. Mean e/e_0 up to this depth is the lowest for the reduced axle load, and the largest for the increased axle load. Thus, the considered lower values of P_0 lead to a slightly higher and more uniform high compaction compared to the outcomes based on the larger values of P_0, as illustrated by Figs 320 (a) and (b). These results demonstrate that the variation of the axle load in the applied range does not significantly affect the predicted soil compaction up to a depth of about 0.3 m.

Variation of the roller speed

The influence of the *roller speed* v_0 on the predicted void ratio e of an initially very loose soil ($e_0 = 0.90$) is discussed next. In addition to the default speed $v_0 = 1.11\,\mathrm{m/s}$ as listed in Table 31, four additional roller speeds are considered, two below (0.55 m/s and 0.75 m/s) and two above (1.39 m/s and 2.22 m/s) the default value. The results in terms of the normalized void ratio e/e_0 found for the five roller speeds are illustrated in Figs 321 (distribution in the observation zone) and 322 (corresponding profiles). At first glance it can be clearly seen that the roller speed considerably affects the compaction effect of the oscillation drum. Both the maximum predicted void ratio reduction and the soil zone with uniform high compaction, i.e. the zone to the depth corresponding to the 105 % value of $\min(e/e_0)$, increase the lower the roller speed v_0 is. The smallest predicted normalized void ratio $\min(e/e_0)$ decreases from 0.77 for the highest speed ($v_0 = 2.22\,\mathrm{m/s}$) to 0.61 for the lowest speed ($v_0 = 0.55\,\mathrm{m/s}$). This corresponds to a reduction of the void ratio e of 23 % at the highest speed and 39 % at the lowest speed (see Fig. 322). Notably, the maximum predicted soil compaction is virtually the same for the default speed and the lower speed of $v_0 = 0.75\,\mathrm{m/s}$. However, the depth of uniform soil compaction becomes significantly larger if the roller speed v_0 is lower than the default value (0.15 m for $v_0 = 1.11\,\mathrm{m/s}$ and 0.35 m for $v_0 = 0.55\,\mathrm{m/s}$). Moreover, the depth effect increases from 0.95 m ($v_0 = 1.11\,\mathrm{m/s}$) to about 1.3 m ($v_0 = 0.55\,\mathrm{m/s}$).

Effect of a second roller pass

So far, soil compaction has been considered after the first oscillatory roller pass only. Therefore, in the next study the effect of a *second roller pass* of an oscillation roller with the speed $v_0 = 2.22\,\mathrm{m/s}$ on the predicted compaction of initially very loose soil ($e_0 = 0.90$) assuming two selected values of the apparent cohesion p_t is addressed. The

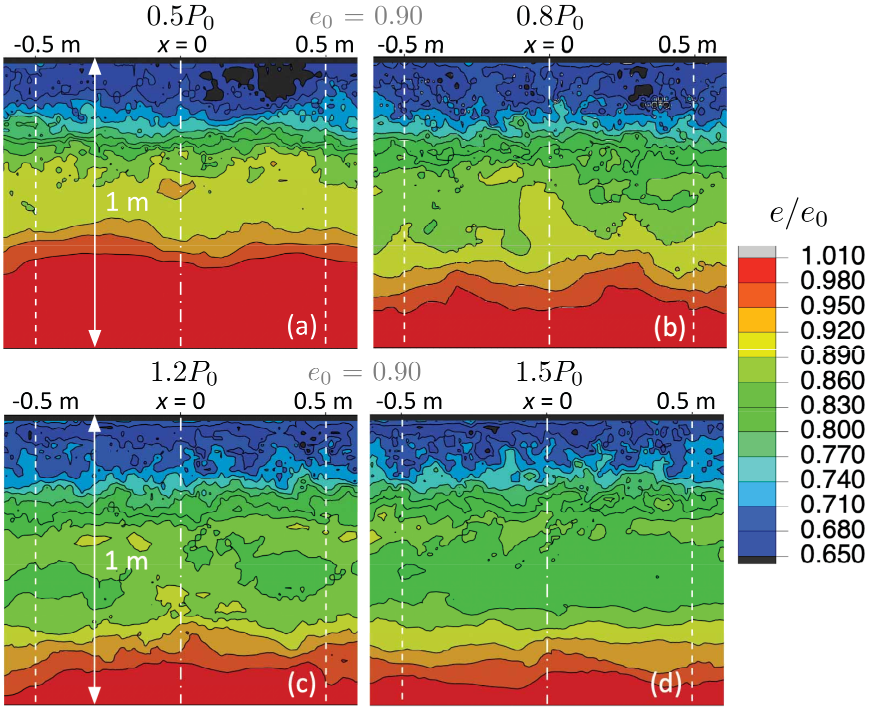

Figure 319: Normalized void ratio up to a soil depth of 1 m after one oscillatory roller pass with (a) 0.5 F_z, (b) 0.8 F_z, (c) 1.2 F_z, and (d) 1.5 F_z; $e_0 = 0.90$

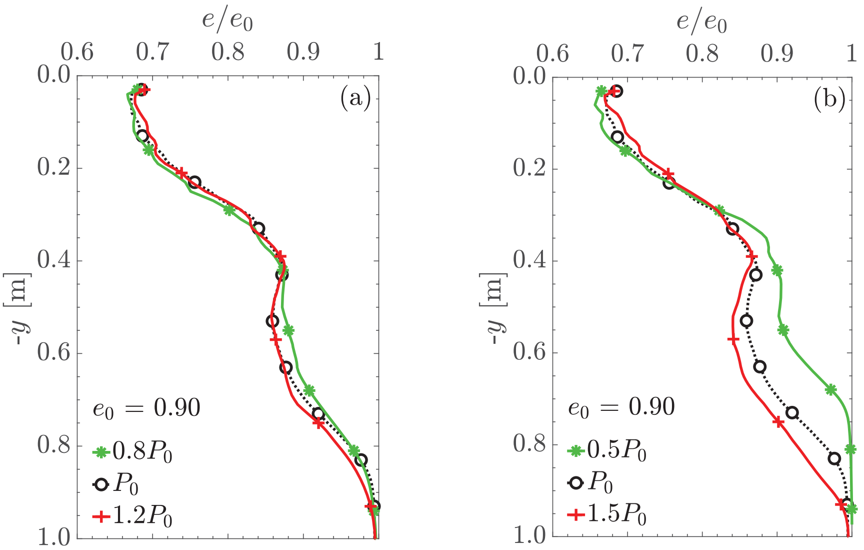

Figure 320: Normalized mean void ratio profile for three different axle loads P_0; variation of P_0 by (a) ±20 % and (b) ±50 %, based on Fig. 319

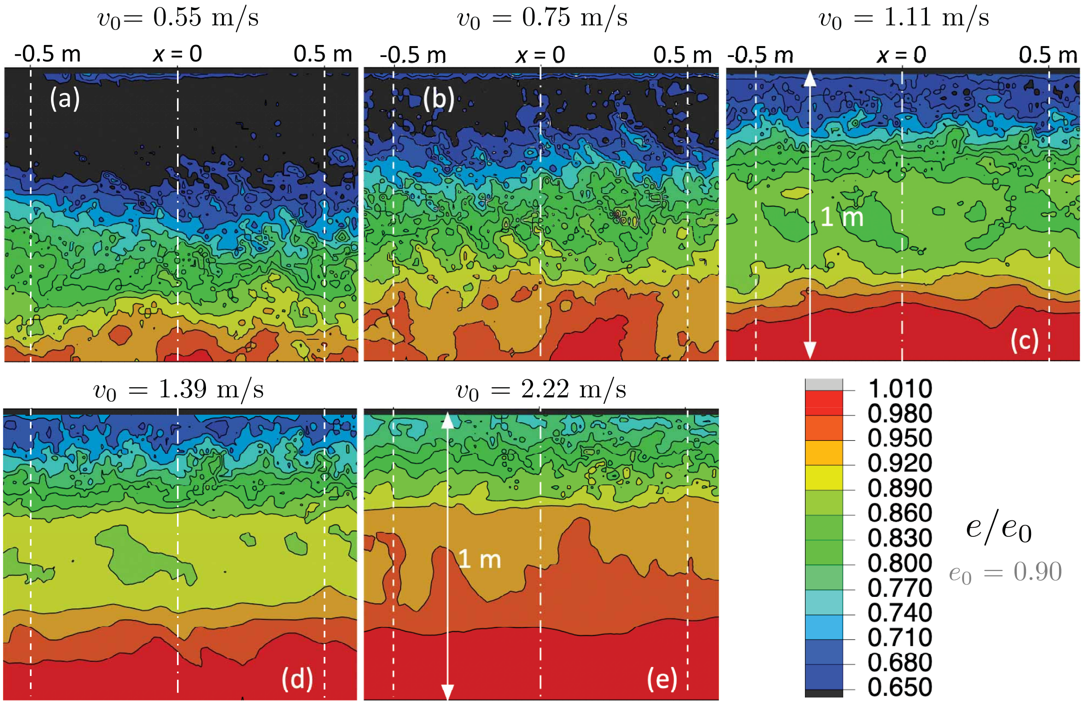

Figure 321: Normalized void ratio after one oscillatory roller pass; roller speed (a) $v_0 = 0.55\,\mathrm{m/s}$, (b) $v_0 = 0.75\,\mathrm{m/s}$, (c) $v_0 = 1.11\,\mathrm{m/s}$, (d) $v_0 = 1.39\,\mathrm{m/s}$, and (e) $v_0 = 2.22\,\mathrm{m/s}$

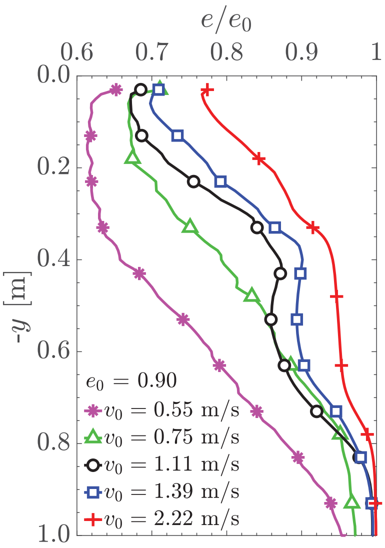

Figure 322: Normalized mean void ratio profile after one oscillatory roller pass at five different speeds v_0 on initially very loose soil, based on Fig. 321

resultant normalized void ratio e/e_0 distribution in the observation zone after the first (Fig. 323 (a,b)) and second pass (Fig. 323 (b,d)) illustrate that the second roller run significantly increases the depth effect of the roller for both $p_t = 5\,\mathrm{kN/m^2}$ (default value) and $p_t = 10\,\mathrm{kN/m^2}$. In the case of the default subsoil conditions, the maximum amount of soil compaction (i.e. the largest reduction of e) predicted after the first pass is, however, not further increased, as can be seen in the corresponding e/e_0-profiles in Fig. 324 (a). That is, the predicted smallest normalized void ratio $\min(e/e_0)$ is about 0.77 after both first and second roller pass, which corresponds to a void ratio reduction of about 23 %. The depth associated with the 105 % value of $\min(e/e_0)$ is 0.14 m (after the first pass) and 0.21 m (after the second pass) below the surface. Thus, with the second crossing the compaction is homogenized over a greater depth. In the case of the considered larger value of p_t, the predicted smallest normalized void ratio $\min(e/e_0)$ of about 0.73 after the first pass becomes 14 % smaller due to a subsequent second roller pass resulting in a predicted void ratio reduction of 34 %. The second pass yields also a deeper homogenized soil zone as the depth corresponding to the 105 % value of $\min(e/e_0)$ is increased to about 0.24 m. Moreover, the depth effect increases from about 1 m (after the first pass) to about 1.15 m (after the second pass). These outcomes qualitatively correspond to the results based on a simplified FE model in which a hypoplastic soil layer with a thickness of 0.25 m covers a linear elastic subsoil. By application of viscous “surface dampers“, as explained in Section 3.2.8, four subsequent roller passes could be simulated. The predicted void ratios show a significant increase in compaction from the first to the second roller run, while passes three and four cause only a slight further compaction, as shown by Figs I3 and I4 in Appendix I.2.

In general, the presented results on compaction effect and influence depth of the oscillation roller confirm qualitatively the observations from field tests and on-site applications. However, it seems that the model with the “protective foil” overestimates slightly the amount of compaction achieved after one oscillatory roller pass (see Appendix I.3).

3.3.4 Drum response

In the following, the dynamic response of the drum during compaction is investigated. In particular, the numerically predicted acceleration components $\ddot{x}_M$ (horizontal) and $\ddot{y}_M$ (vertical) of the drum center M (reference node RP_M) are depicted and evaluated both in the time and frequency domain. Parameters based on the drum center response are also evaluated because they form the basis of the novel CCC methodology for oscillation rollers [Pistrol, 2016] described in the introduction.

Effect of the initial void ratio

Figs 325, 326, and 327 show the horizontal ($\ddot{x}_M$, left plot) and the vertical acceleration component ($\ddot{y}_M$, right plot) for three different initial void ratios ($e_0 = 0.90$, 0.70, and 0.60) in a time frame of one second. As observed, the horizontal response $\ddot{x}_M$ varies only slightly with time. Its amplitude is, however, affected by e_0. This means that with increasing initial soil density the amplitude also increases in the range of about $-9.3\,\mathrm{m/s^2}$ ($e_0 = 0.90$) until about $-12.2\,\mathrm{m/s^2}$ ($e_0 = 0.60$). It is also seen that the response $\ddot{x}_M$ is asymmetrical to the baseline, i.e. the amplitudes in the negative response

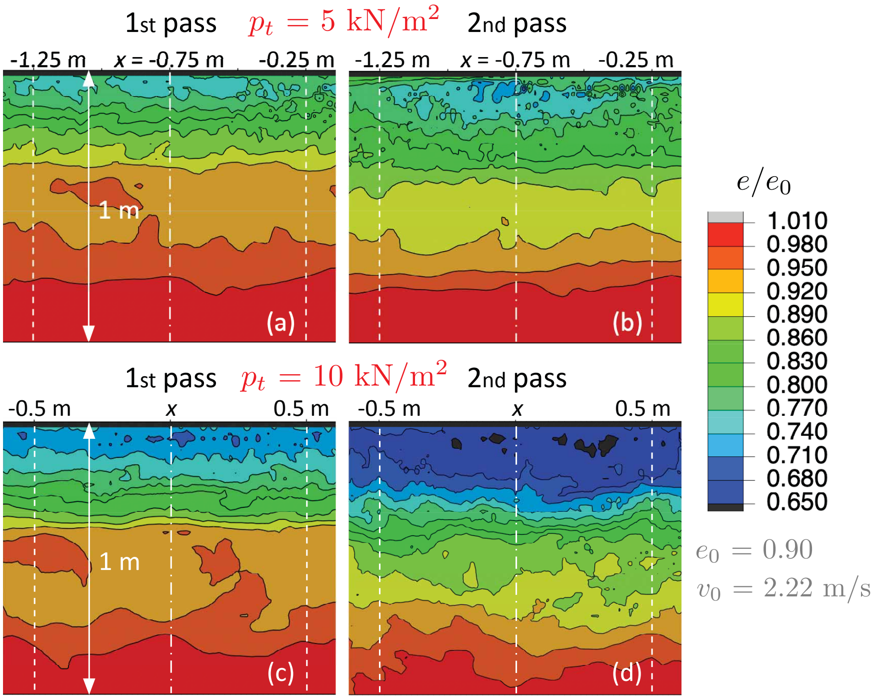

Figure 323: Normalized void ratio after the (a,c) first and (b,d) second roller pass; (a,b) $p_t = 5\,\mathrm{kN/m^2}$ and (c,d) $p_t = 10\,\mathrm{kN/m^2}$

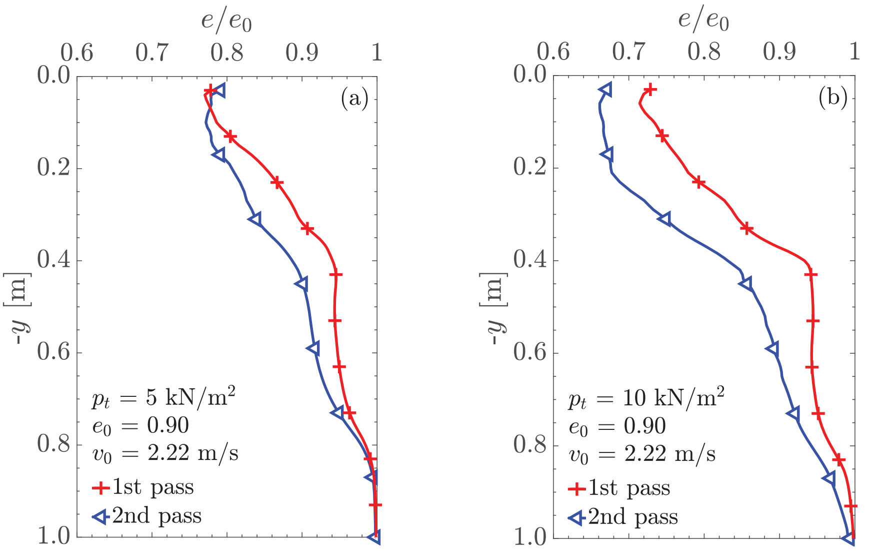

Figure 324: Normalized mean void ratio profile after two subsequent oscillatory roller passes; (a) $p_t = 5\,\mathrm{kN/m^2}$ and (b) $p_t = 10\,\mathrm{kN/m^2}$, based on Fig. 323

range are larger than those in the positive range. This asymmetry, however, decreases with decreasing e_0 (i.e. with increasing initial soil density). The same behavior was predicted in Section 2.4.2, where a simple lumped parameter model of the drum-subsoil interacting is used to study the response of an oscillating drum. It was shown that $\ddot{x}_M$ is asymmetric when the drum operates on the slope of the settlement trough (above its bottom) behind the bow wave (see Section 2.4.2).

The vertical response $\ddot{y}_M$, which essentially results from the up- and downward motion of the drum in the curved contact zone ("settlement trough") during each period of excitation (see Section 2.4), shows a more transient behavior. The mean amplitudes of $\ddot{y}_M$ lie between $-1.3\,\mathrm{m/s^2}$ and $1.3\,\mathrm{m/s^2}$ ($e_0 = 0.70$), and between $-1.8\,\mathrm{m/s^2}$ and $2.3\,\mathrm{m/s^2}$ ($e_0 = 0.90$). The predicted vertical acceleration amplitudes are therefore only one fifth to one tenth of the horizontal amplitudes. Interestingly, the medium initial soil density ($e_0 = 0.70$) yields the smallest vertical peak accelerations, while the largest vertical response amplitudes occur at the largest soil density $e_0 = 0.60$. For $e_0 = 0.90$ and $e_0 = 0.70$, the amplitudes in the positive response regime of $\ddot{y}_M$ are larger than the negative ones. The initial void ratio $e_0 = 0.60$ yields these amplitudes equal. This result also corresponds to the outcomes of the lumped parameter modeling discussed in Section 2.4.2. Another observation is that due to the nonlinearity of the interacting system, the governing period of $\ddot{y}_M$ is half the excitation period, i.e. one excitation period corresponds to two periods of $\ddot{y}_M$. This harmonic depends strongly on the bow wave and the settlement trough, and thus, the response pattern of $\ddot{y}_M$ becomes more transient. A more detailed discussion on the frequency content of the drum response follows later.

A time frame of two periods depicted in Fig. 328 exemplary for $e_0 = 0.70$ reveals that the positive amplitudes of the horizontal acceleration $\ddot{x}_M$ have a "peak cut", which results from the stick-slip motion of the drum. This behavior was also observed in the study based on the proposed lumped parameter model (see Section 2.4.2).

Plotting the vertical component $\ddot{y}_M$ against the horizontal one $\ddot{x}_M$, subsequently referred to as "$\ddot{y}_M$-$\ddot{x}_M$ plot", results in a response representation that is fundamental to the CCC methodology described in [Pistrol, 2016]. In Figs 329, this response representation is depicted by gray lines for the time histories shown in Figs 325, 326, and 327. That is, diagram (a) corresponds to the initial void ratio $e_0 = 0.90$, diagram (b) to $e_0 = 0.80$, diagram (c) to $e_0 = 0.70$, and diagram (d) to $e_0 = 0.60$. For two "representative" excitation periods in this time frame the response is shown in green. The result is a so-called *Lissajous curve* [Klotter, 1981] with an asymmetric pattern, whose shape depends on the initial void ratio. The denser the initial soil, the less asymmetric the response becomes. It can also be seen that the *Lissajous figures* rotate clockwise with decreasing e_0. For the dense soil ($e_0 = 0.60$) the figure resembles a *recumbent eight*. Such a response behavior has recently been discovered in the analysis of field test data [Pistrol, 2016]. As an example, Fig. 330 shows this response representation using the drum acceleration components recorded in a field test described by Pistrol [2016]. It can be seen that the numerically derived drum acceleration qualitatively reproduces the response behavior observed in the field.

Another representative response parameter of the previously discussed CCC methodology is the "area" enclosed in the $\ddot{y}_M$ over $\ddot{x}_M$ figure. This CCC parameter (i.e. the "area") is determined consecutively (in time) for two subsequent periods. In Fig. 331 discrete markers represent this parameter in a window of two seconds with respect to

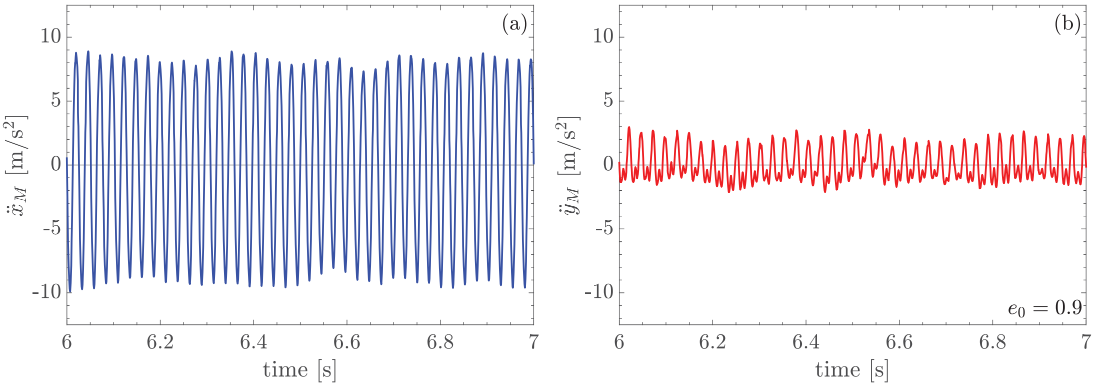

Figure 325: Time history of the (a) horizontal and (b) vertical acceleration in the drum center M during an oscillatory roller pass on initially very loose soil ($e_0 = 0.90$)

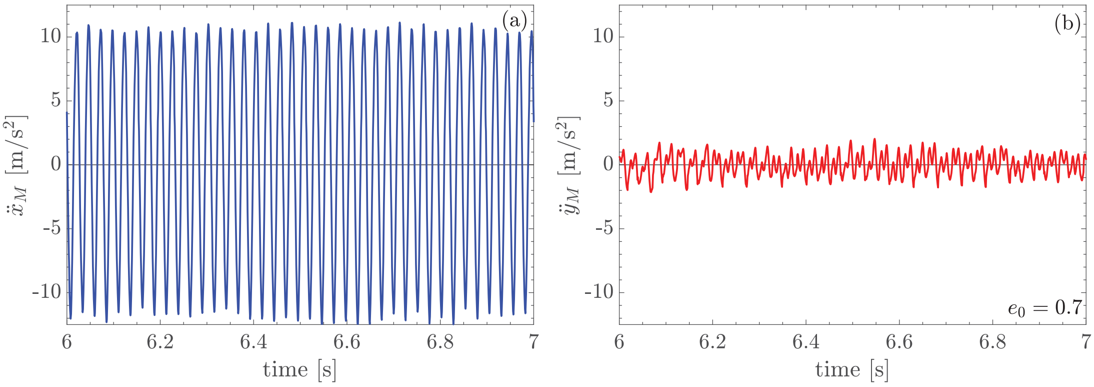

Figure 326: Time history of the (a) horizontal and (b) vertical acceleration in the drum center M during an oscillatory roller pass on initially medium dense soil ($e_0 = 0.70$)

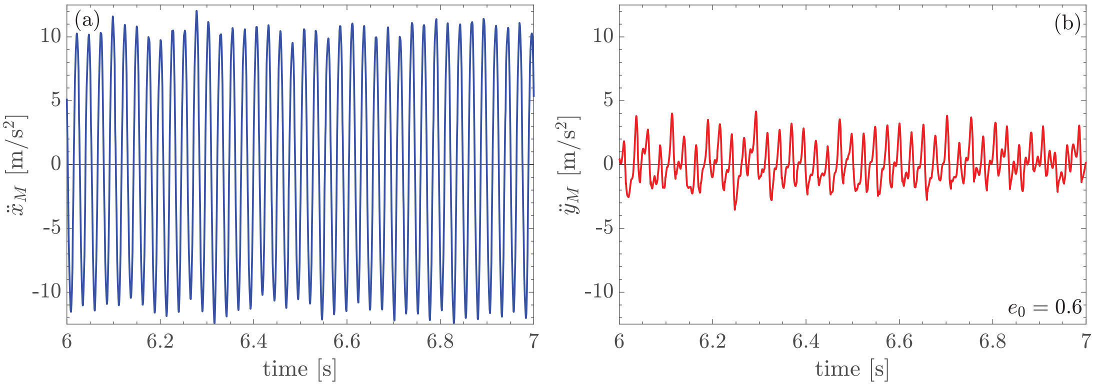

Figure 327: Time history of the (a) horizontal and (b) vertical acceleration in the drum center M during an oscillatory roller pass on initially dense soil ($e_0 = 0.60$)

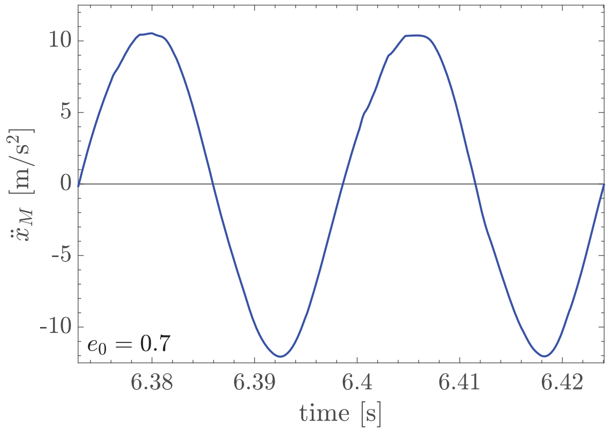

Figure 328: Two periods of the horizontal drum center acceleration for an initial void ratio $e_0 = 0.70$

time. The outcomes shown in green refer to an initially very loose soil ($e_0 = 0.90$), the results for the dense soil ($e_0 = 0.60$) are depicted in red. The imagined connection line between the markers shows a quite large scatter, which is primarily a result of the strong amplitude fluctuation of the vertical accelerations. Therefore, the upper and lower envelopes of this parameter are depicted in this figure, in addition to the mean shown by bold lines. For $e_0 = 0.90$ the mean CCC parameter, based on the "area" enclosed by the "representative" *Lissajous curve* depicted in green in Fig. 329 (a), of about $24\,\mathrm{m}^2/\mathrm{s}^4$ is in very good agreement with the CCC value of about $25\,\mathrm{m}^2/\mathrm{s}^4$, which results from one on-site roller pass on a very loose soil, as documented in [Pistrol, 2016]. It is evident that the lower initial void ratio of $e_0 = 0.60$ leads to a more pronounced CCC parameter scatter. For the initially dense soil (i.e. $e_0 = 0.60$), the mean CCC parameter of about $35\,\mathrm{m}^2/\mathrm{s}^4$ is larger. The increase in this parameter by almost 60 % is mainly due to the increase of the horizontal acceleration amplitudes as the initial subsoil becomes denser. This result is consistent with the findings based on the lumped parameter model of the roller-soil system presented in Section 2.4.2.

To gain a deeper insight into the drum response characteristic, the drum accelerations shown in Figs 325, 326, and 327 are transformed into the frequency domain. The resulting frequency response, normalized to a peak value of one, is plotted against the ratio of frequency f over excitation frequency $\bar{f}$, as illustrated in Figs 332, 333, and 334. It is readily seen that the frequency spectra contain both odd and even harmonics, but in most cases they are dominated by the excitation frequency $\bar{f}$. The additional harmonics in the spectra of the horizontal drum accelerations ($\ddot{x}_M$-spectra) at $f/\bar{f} =$ 2, 3, 4, ..., with amplitudes much smaller than those at $f/\bar{f} = 1$, can be traced back to "peak cut" in the response in the *slip* phases of the drum motion. As the observed "peak cut" is not that significant (see Figs 328), the third harmonic ($f/\bar{f} = 3$) is for all investigated initial void ratios about 0.03 times the amplitude at the dominating frequency ($f/\bar{f} = 1$). The drum operates on the slope of the settlement trough, and thus, the vertical acceleration spectra ($\ddot{y}_M$-spectra) are in most cases dominated by the excitation frequency. The second harmonic in the $\ddot{y}_M$-spectra results from the up- and downward motion of the drum in the curved contact zone between drum and subsoil ("settlement trough"). For the initially very loose soil ($e_0 = 0.90$), the amplitude at

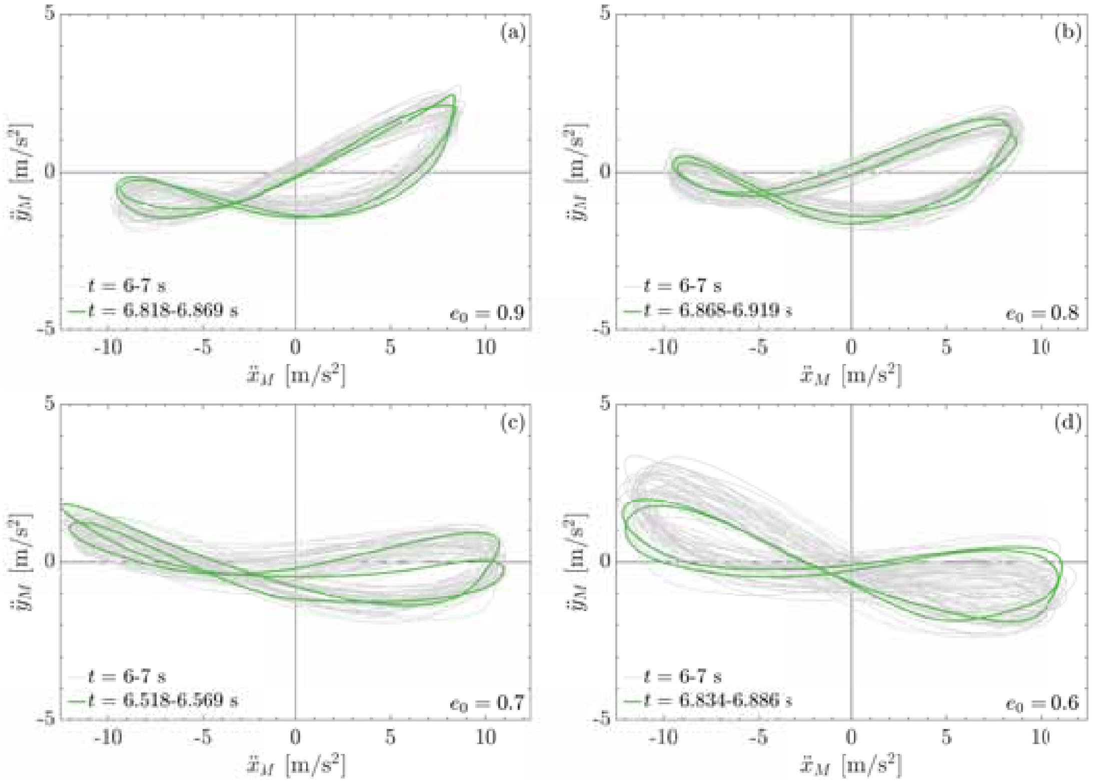

Figure 329: Plot $\ddot{y}_M$ over $\ddot{x}_M$ for an initial void ratio e_0 of (a) 0.90, (b) 0.80, (c) 0.70 and (d) 0.60 for a time window of 1 s (grey lines) and two representative oscillating cycles (green lines)

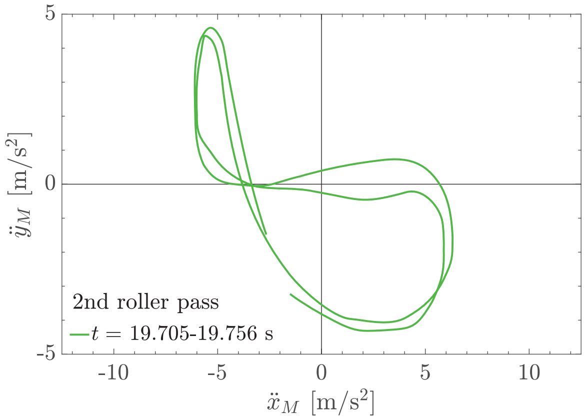

Figure 330: Plot $\ddot{y}_M$ over $\ddot{x}_M$ for two oscillating cycles based on acceleration data recorded in field tests (described by Pistrol [2016])

the second harmonic ($f/\bar{f}=2$) of the vertical accelerations is about 44 % smaller than the amplitude at the dominating frequency ($f/\bar{f}=1$), for the dense soil ($e_0 = 0.60$) it is 35 % only (see Figs 332 (b) and 334 (b)). In contrast, an initial void ratio of $e_0 = 0.70$ yields the amplitude at the second harmonic about 10 % larger than the amplitude at the excitation frequency (see Figs 333 (b)). These outcomes correspond with

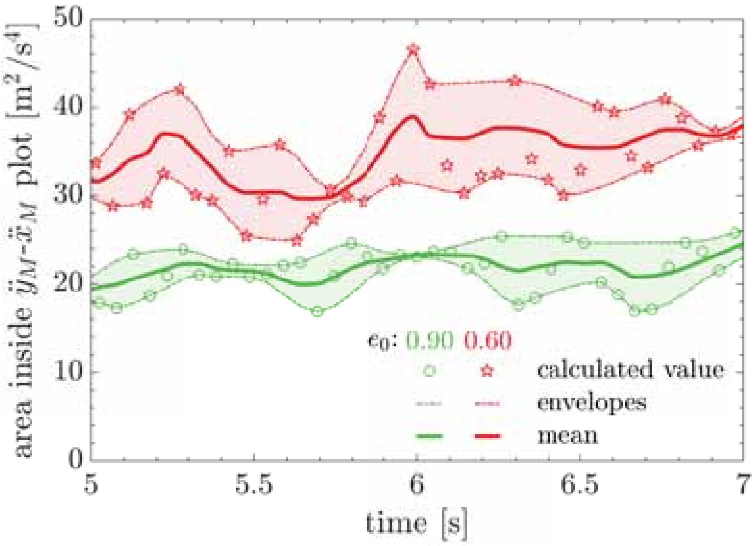

Figure 331: CCC indicator (i.e. area inside the plot $\ddot{y}_M$ over $\ddot{x}_M$) during one oscillatory roller pass at $v_0 = 1.11\,\mathrm{m/s}$ for an initially very loose ($e_0 = 0.90$) and an initially dense soil ($e_0 = 0.60$)

findings presented in Section 2.4.2, where an increase in the response amplitude ratio $\ddot{Y}(2\bar{f})/\ddot{Y}(\bar{f})$ with increasing soil stiffness was observed. Comparison of Figs 332 (b) and 333 (b) shows that both the third and fourth harmonic of the normalized vertical response amplitudes increase with decreasing initial void ratio.

For comparison purposes, Figs 335 and 336 show the frequency response recorded during oscillation compaction of sandy gravel with the HD$^+$ 90 VO roller, whose machine parameters are used for the presented numerical simulations. The overtones in the measured data are also found in the numerically simulated data, and the corresponding amplitudes are of the same magnitude. The only exception is the normalized amplitude at the third harmonic of the vertical accelerations ($f/\bar{f} = 3$), which is 0.45, and thus, about three times larger than the corresponding computed amplitude (compare Figs 332 (b) and 335 (b)). In particular, the presented numerical model predicts the relative increase of the second harmonic in $\ddot{y}_M$ (with respect to the first normalized harmonic) with increasing soil compaction, as can be seen from the field data. The examination of the normalized frequency response reveals that the frequency content of the computed drum accelerations and the accelerations measured in field tests described in [Pistrol, 2016] is in good agreement.

Effect of the coefficient of friction, apparent cohesion and roller speed

The effect of the *coefficient of friction* μ for *Coulomb*'s law of friction between soil and drum and soil surface is studied for an initially very loose soil ($e_0 = 0.90$) and an initially medium dense soil ($e_0 = 0.70$) to be compacted. As before, in two subsequent simulations to the numerical model two coefficient of frictions are assigned, i.e. the default value $\mu = 0.50$ and the smaller value $\mu = 0.30$. Figs 337 (a) and (c) ($e_0 = 0.90$) and Figs 337 (b) and (d) ($e_0 = 0.70$) show $\ddot{x}_M$ (plots a,b) and $\ddot{y}_M$ (plots c,d) in a time frame of two excitation periods. The stick-slip response prediction based on $\mu = 0.50$

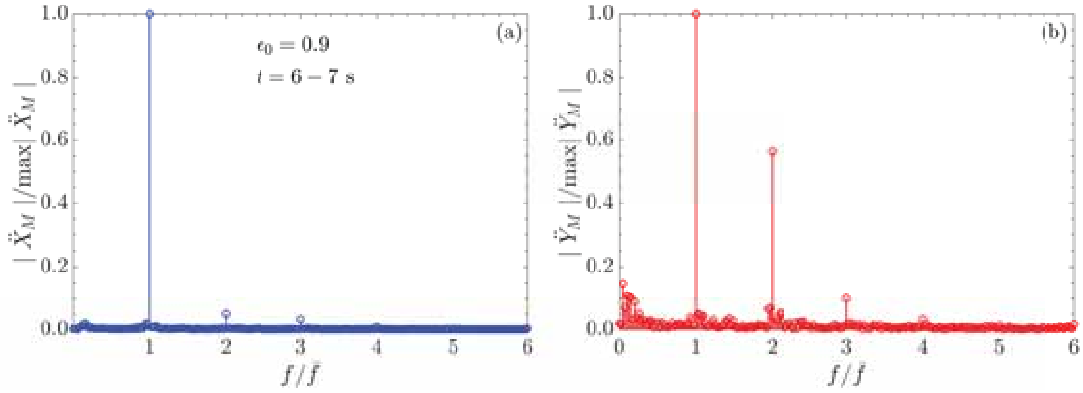

Figure 332: Normalized frequency spectrum of the (a) horizontal and (b) vertical acceleration in the drum center for one second of an oscillatory roller pass; initially very loose soil ($e_0 = 0.90$)

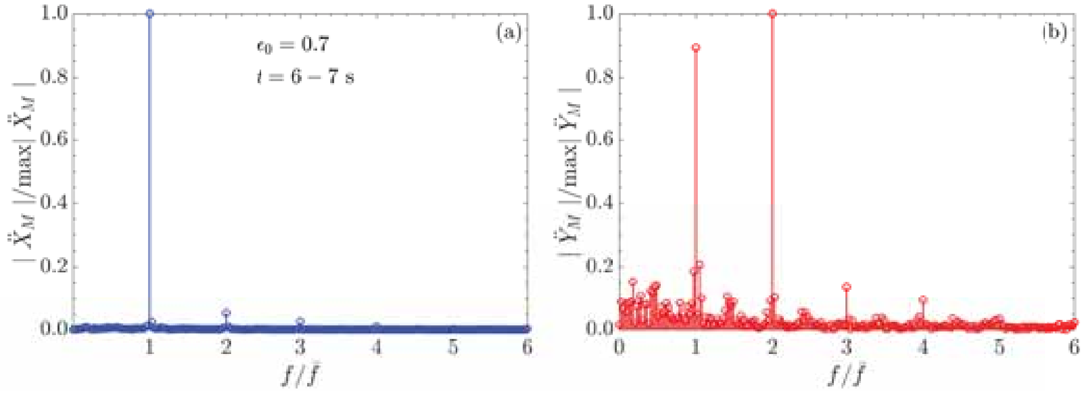

Figure 333: Normalized frequency spectrum of the (a) horizontal and (b) vertical acceleration in the drum center for one second of an oscillatory roller pass; initially medium dense soil ($e_0 = 0.70$)

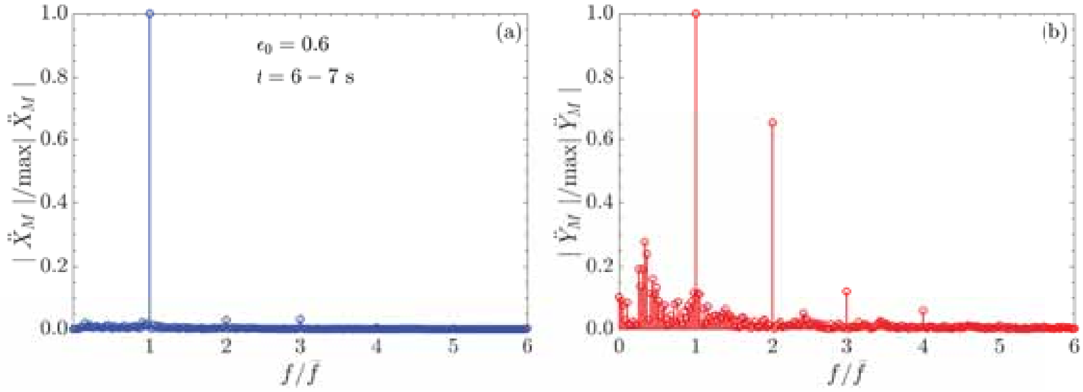

Figure 334: Normalized frequency spectrum of the (a) horizontal and (b) vertical acceleration in the drum center for one second of an oscillatory roller pass; initially dense soil ($e_0 = 0.60$)

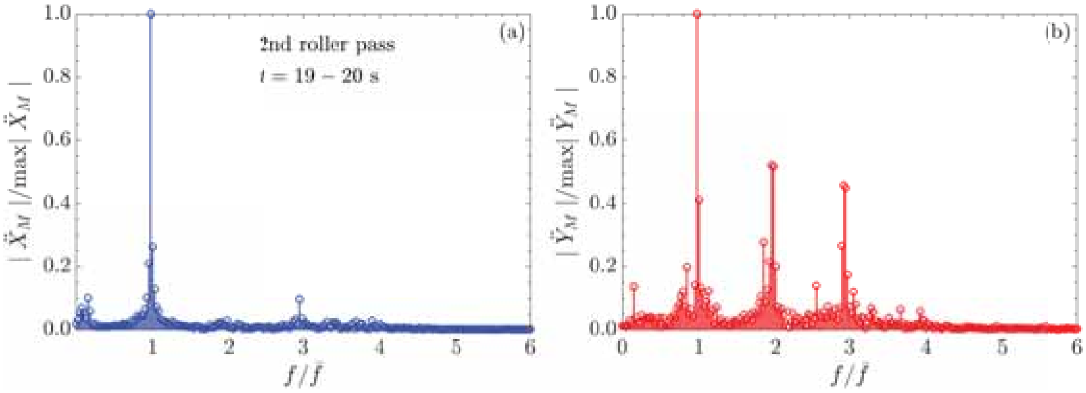

Figure 335: Normalized frequency spectrum of recorded horizontal (a) and vertical (b) accelerations in the drum center during field tests; roller pass no. 2 on gravel (based on Pistrol [2016])

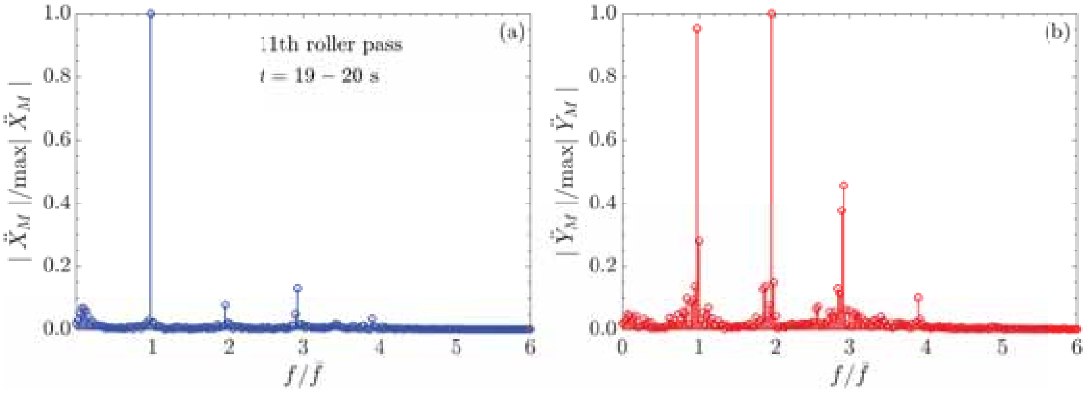

Figure 336: Normalized frequency spectrum of recorded horizontal (a) and vertical (b) accelerations in the drum center during field tests; roller pass no. 11 on gravel (based on Pistrol [2016])

is presented by a black line and "*" markers, and the one based on $\mu = 0.30$ by a red line and circular markers. These results illustrate the grave effect of slip between the drum and the soil surface on the drum response. As can be observed at first glance, the smaller coefficient of friction μ leads to smaller drum center response components $\ddot{x}_M$ and $\ddot{y}_M$ for both subsoil conditions.

It is also seen that the smaller coefficient of friction $\mu = 0.30$ causes the typical "peak cut" of the horizontal response $\ddot{x}_M$ in the *slip* phase, in both positive and negative directions, which is more pronounced for the initially medium dense soil ($e_0 = 0.70$). A kink in the time history of the horizontal acceleration component $\ddot{x}_M$ indicates the transition from the stick into the slip phase and vice versa. Another observation is that the smaller coefficient of friction μ elongates the duration of the slip phase in both the negative and positive horizontal acceleration range. The amplitudes of the horizontal acceleration component $\ddot{x}_M$ in the negative response range are larger than those in the positive range, because the drum operates at the slope of the "settlement trough" in driving direction. Therefore, the slip phase in the negative horizontal acceleration range

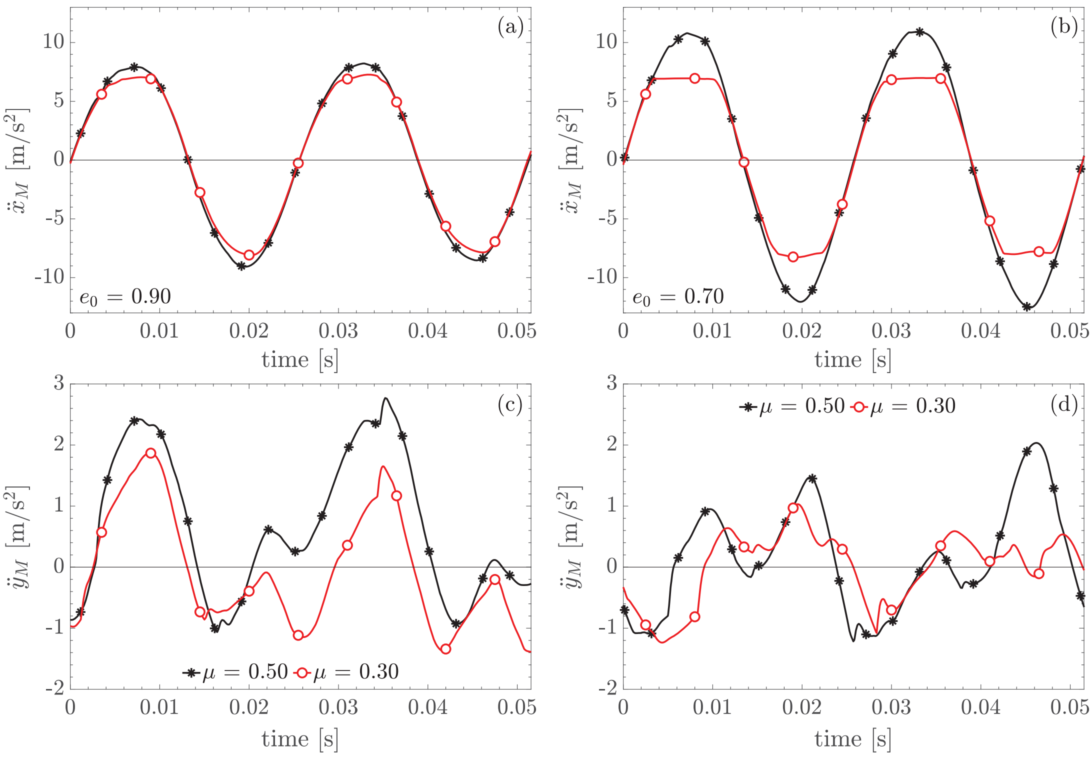

Figure 337: Time history of the (a,b) horizontal and (c,d) vertical acceleration in the drum center for two selected coefficients of friction; initial void ratio (a,c) $e_0 = 0.90$ and (b,d) $e_0 = 0.70$

is smaller than the one in the positive range. For $\mu = 0.50$, the horizontal response $\ddot{x}_M$ is bounded by $-9\,\mathrm{m/s^2}$ ($e_0 = 0.90$) and $-12.5\,\mathrm{m/s^2}$ ($e_0 = 0.70$) in the negative range, and by $8\,\mathrm{m/s^2}$ ($e_0 = 0.90$) and $11\,\mathrm{m/s^2}$ ($e_0 = 0.70$) in the positive range. That is, compaction of the initially medium dense soil induces larger horizontal response amplitudes, compare Figs 337 (a) and (b). The corresponding response amplitudes for the lower coefficient of friction $\mu = 0.30$ are smaller, and in-between $-8\,\mathrm{m/s^2}$ and $7\,\mathrm{m/s^2}$, both for $e_0 = 0.90$ and $e_0 = 0.70$.

The vertical response component of the drum center $\ddot{y}_M$, which essentially results from the up- and down movement of the drum in the curved contact zone ("settlement trough") during each excitation period (see Section 2.4) shows, as already observed in the section before, a more transient behavior, as illustrated in Figs 337 (c) and (d). For $\mu = 0.50$, $\ddot{y}_M$ is in the range between $-1.1\,\mathrm{m/s^2}$ and $2.8\,\mathrm{m/s^2}$ ($e_0 = 0.90$), and $-1.2\,\mathrm{m/s^2}$ and $2\,\mathrm{m/s^2}$ ($e_0 = 0.70$), respectively. In contrast to $\ddot{x}_M$, the compaction of the initially medium dense soil leads to 30-40 % smaller vertical response amplitudes in the positive response range. The smaller coefficient of friction $\mu = 0.30$ further reduces the positive amplitudes of $\ddot{y}_M$, which are at most $1.9\,\mathrm{m/s^2}$ ($e_0 = 0.90$) and $1\,\mathrm{m/s^2}$ ($e_0 = 0.70$), respectively. The predicted vertical acceleration amplitudes are therefore only one third to one tenth of the horizontal amplitudes.

To gain a deeper insight into the drum response characteristics, Fig. 338 shows the drum acceleration components of a time frame of one second in the frequency domain. In these figures, the frequency f is normalized with respect to the excitation frequency

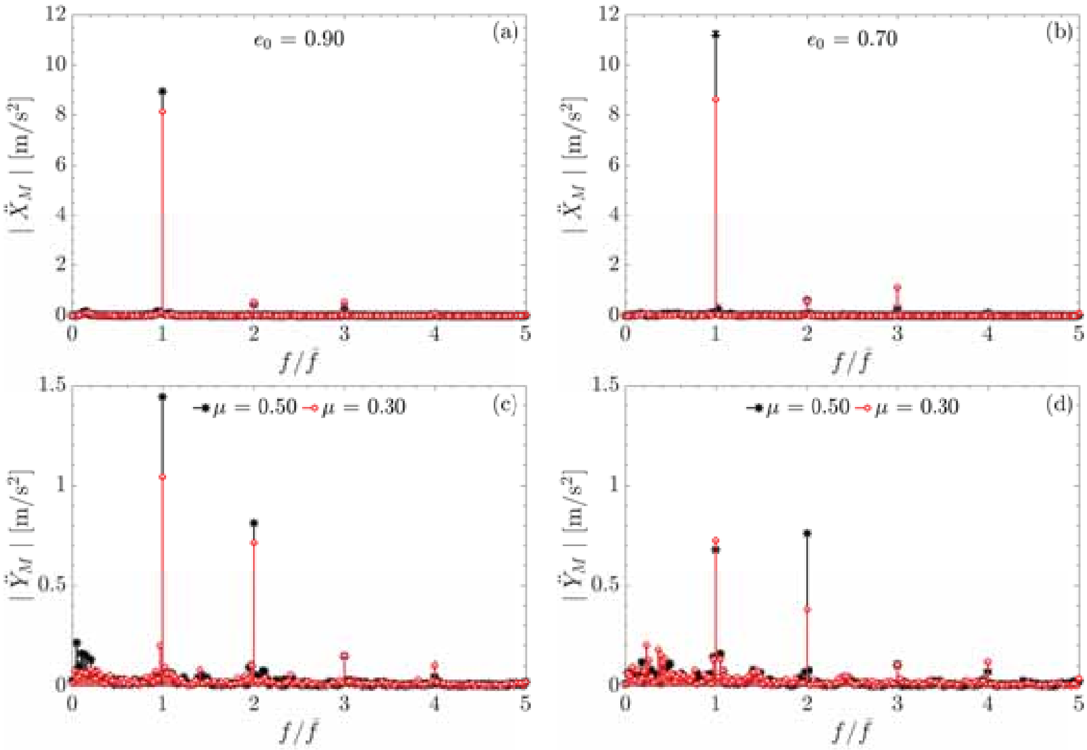

Figure 338: Frequency spectrum of the (a,b) horizontal and (c,d) vertical acceleration in the drum center for two selected coefficients of friction; initial void ratio (a,c) $e_0 = 0.90$ and (b,d) $e_0 = 0.70$

$\bar{f}$. It is readily seen that the absolute values of the frequency spectra of $\ddot{x}_M$ ($|\ddot{X}_M(f)|$) and $\ddot{y}_M$ ($|\ddot{Y}_M(f)|$) contain both odd and even harmonics. An interesting observation is that the frequency content of the response components for all parameter combinations, except $|\ddot{Y}_M|$ for $e_0 = 0.70$ and $\mu = 0.50$, is dominated by the excitation frequency $\bar{f}$. In the latter case, the spectral acceleration is largest at $f = 2\bar{f}$. The additional harmonics in the spectra of the horizontal response $|\ddot{X}_M|$ at $f/\bar{f} =$ 2, 3, 4, ..., with amplitudes much smaller than those at $f/\bar{f} = 1$, can be traced back to aforementioned "peak cut" due to the *slip* phases of the drum motion. The second harmonic in the spectra of the vertical response $\ddot{y}_M$ (i.e. $|\ddot{Y}_M(2\bar{f})|$) reflects the up- and down motion of the drum in the "settlement trough". The additional harmonics at $f/\bar{f} =$ 3, 4, 5, ..., are a result of the slip phases of the drum.

In the case of an initially very loose soil ($e_0 = 0.90$), the horizontal spectral acceleration at the excitation frequency $\bar{f}$ ($|\ddot{X}_M(\bar{f})|$) is 8.9 m/s^2 ($\mu = 0.50$) and 8.1 m/s^2 ($\mu = 0.30$), respectively (see Fig. 338 (a)). The amplitudes at the second ($|\ddot{X}_M(2\bar{f})|$) and at the third harmonic ($|\ddot{X}_M(3\bar{f})|$) are only about 0.449 m/s^2 and 0.512 m/s^2 ($\mu = 0.50$) and 0.292 m/s^2 and 0.529 m/s^2 ($\mu = 0.30$), respectively. These results show that the use of the smaller coefficient of friction ($\mu = 0.30$) reduces the horizontal spectral acceleration at the excitation frequency $|\ddot{X}_M(\bar{f})|$ by about 9 %, while the amplitudes of the second and third harmonics, $|\ddot{X}_M(2\bar{f})|$ and $|\ddot{X}_M(3\bar{f})|$, increase by 14 % and 81 %, respectively. Therefore, the amplitude ratio $|\ddot{X}_M(3\bar{f})|/|\ddot{X}_M(\bar{f})|$ increases by almost 100 % if $\mu = 0.30$. This outcome confirms that the normalized amplitude at the third harmonic $|\ddot{X}_M(3\bar{f})|/|\ddot{X}_M(\bar{f})|$ may be considered as an indicator of the extent of the slip phase in the drum response [Pistrol, 2016].

For the initially medium dense soil ($e_0 = 0.70$), the difference between the results for $\mu = 0.50$ and for $\mu = 0.30$ is larger, as observed from see Fig. 338 (b). Therefore, it is confirmed that at this soil condition the reduction of the coefficient of friction μ has a greater effect on the horizontal drum response due to the more pronounced slip phases.

A closer inspection of the vertical frequency domain response for an initially very loose soil ($e_0 = 0.90$) reveals that spectral acceleration at the excitation frequency $\bar{f}$ ($|\ddot{Y}_M(\bar{f})|$) is $1.44\,\mathrm{m/s^2}$ ($\mu = 0.50$) and $1.04\,\mathrm{m/s^2}$ ($\mu = 0.30$), respectively (see Fig. 338 (c)). For $\mu = 0.50$, at the second harmonic ($|\ddot{Y}_M(2\bar{f})|$) the spectral acceleration is $0.81\,\mathrm{m/s^2}$ (i.e. 0.56 times $|\ddot{Y}_M(2\bar{f})|$), at the third harmonic ($|\ddot{Y}_M(3\bar{f})|$) $0.145\,\mathrm{m/s^2}$, and at the fourth harmonic ($|\ddot{Y}_M(4\bar{f})|$) $0.048\,\mathrm{m/s^2}$. For $\mu = 0.30$, $|\ddot{Y}_M(2\bar{f})| = 0.72\,\mathrm{m/s^2}$, which is 0.69 times $|\ddot{Y}_M(2\bar{f})|$, $|\ddot{Y}_M(3\bar{f})| = 0.149\,\mathrm{m/s^2}$, and $|\ddot{Y}_M(4\bar{f})| = 0.103\,\mathrm{m/s^2}$. Hence, the smaller coefficient of friction reduces $|\ddot{Y}_M(\bar{f})|$ by about 28 % and $|\ddot{Y}_M(2\bar{f})|$ by about 12 %, $|\ddot{Y}_M(3\bar{f})|$ is virtually not affected, and $|\ddot{Y}_M(4\bar{f})|$ increases by 115 %.

In the simulation of the compaction of initially medium dense soil ($e_0 = 0.70$), the coefficient of friction has a very different effect on the general characteristics of the vertical drum response in the frequency domain. As observed, for $\mu = 0.30$ the vertical spectral acceleration at the excitation frequency $|\ddot{Y}_M(\bar{f})|$ is slightly larger than for $\mu = 0.50$, while $|\ddot{Y}_M(2\bar{f})|$ drops significantly by about 50 % (Fig. 338 (d)). The vertical response at the third harmonics is virtually unaffected by μ, similarly to the case with $e_0 = 0.90$. At the fourth harmonics $\mu = 0.30$ even yields a larger spectral acceleration than for $\mu = 0.50$.

In order to validate the numerically predicted drum response with experimental data, the frequency spectra for the lower coefficient of friction $\mu = 0.30$, shown in Fig. 338 in red colour, are normalized to the maximum value of one. In Fig. 339, these spectra are compared with the drum acceleration in the frequency domain recorded during oscillation compaction of sandy gravel [Pistrol, 2016] with the HAMM HD$^+$ 90 VO roller, whose machine parameters are used for the presented numerical simulations. It is readily seen that the overtones in the measured data are also found in the numerically simulated data. Moreover, the corresponding normalized amplitudes are of the same magnitude. The only exceptions are the normalized amplitudes of the vertical accelerations at the third harmonic $f/\bar{f} = 3$ (about three times larger than the corresponding computed amplitudes), and at the fourth harmonic $f/\bar{f} = 4$ (about three times smaller than the corresponding computed amplitude).

The effect of the *roller speed* v_0 is studied for an initially very loose soil ($e_0 = 0.90$) and a coefficient of friction of $\mu = 0.50$. Fig. 340 shows the (a) horizontal ($\ddot{x}_M$) and (c) vertical acceleration component ($\ddot{y}_M$) for three different roller speeds ($v_0 = 0.55\,\mathrm{m/s}$, $1.11\,\mathrm{m/s}$, $2.22\,\mathrm{m/s}$) in a time frame of one second during the first roller pass. It is readily seen that both the horizontal and vertical response, i.e. $\ddot{x}_M$ and $\ddot{y}_M$, are strongly influenced by the roller speed v_0. The amplitudes of $\ddot{y}_M$ increase with decreasing speed v_0 from about $-1 \div 1.5\,\mathrm{m/s^2}$ ($v_0 = 2.22\,\mathrm{m/s}$) until about $-4 \div 4\,\mathrm{m/s^2}$ ($v_0 = 0.55\,\mathrm{m/s}$). Thus, the asymmetry of $\ddot{y}_M$ with respect to the baseline (i.e. the amplitudes in the positive response range are larger than those in the negative range, as observed for $v_0 = 1.11\,\mathrm{m/s}$ and $v_0 = 2.22\,\mathrm{m/s}$), vanishes for the lowest considered speed of $v_0 = 0.55\,\mathrm{m/s}$. The amplitudes of the horizontal response $\ddot{x}_M$ also become larger

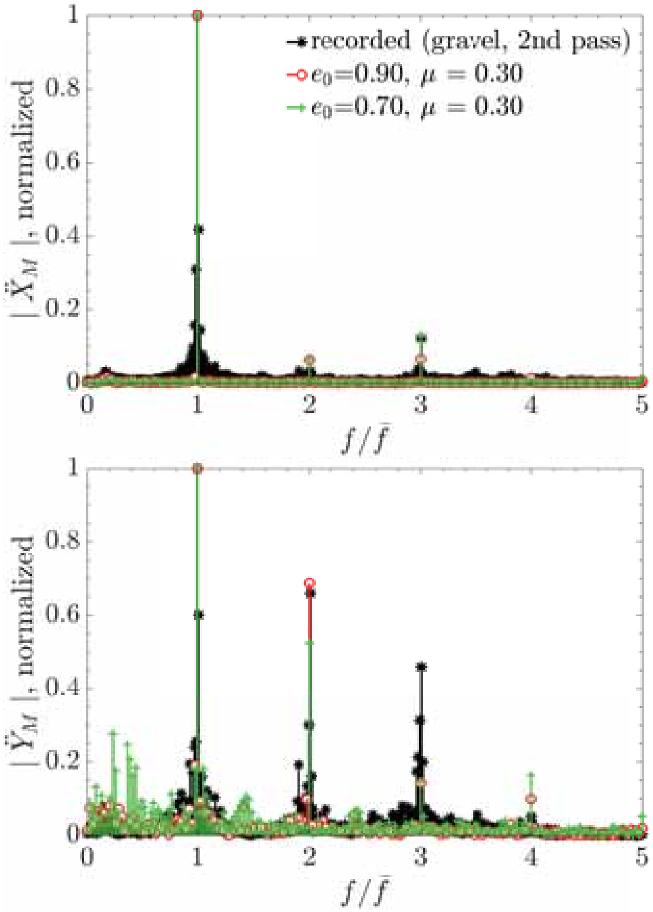

Figure 339: Normalized frequency spectrum of the (a) horizontal and (b) vertical acceleration in the drum center; computed and recorded (based on Pistrol [2016]) response

with decreasing roller speed v_0. At the largest considered value of v_0, the predicted amplitudes of $\ddot{x}_M$ are in the range of about $-8 \div 7\,\mathrm{m/s^2}$ ($v_0 = 2.22\,\mathrm{m/s}$), while the accelerations in the drum center of a roller operating at the lowest speed of $v_0 = 0.55\,\mathrm{m/s}$ vary between $-15\,\mathrm{m/s^2}$ and $12\,\mathrm{m/s^2}$. Thus, the amplitudes in the negative response range are in absolute larger than those in the positive range. In contrast to the behavior of $\ddot{y}_M$, the observed asymmetry of the horizontal response $\ddot{x}_M$ decreases with increasing v_0.

Figs 340 (b) and (d) show the drum acceleration components of a time frame of one second, as discussed above, in the frequency domain. In these figures, the frequency f is normalized with respect to the excitation frequency $\bar{f}$. At first glance it can be observed that the absolute values of both the frequency spectra of $\ddot{x}_M$ ($|\ddot{X}_M(f)|$) and $\ddot{y}_M$ ($|\ddot{Y}_M(f)|$) are dominated by the excitation frequency $\bar{f}$ for all three roller speeds v_0. Moreover, the amplitudes at the excitation frequency $\bar{f}$ of both $\ddot{x}_M$ ($|\ddot{X}_M(\bar{f})|$) and $\ddot{y}_M$ ($|\ddot{Y}_M(\bar{f})|$) become larger with decreasing v_0. Fig. 340 (c) shows that $|\ddot{X}_M(\bar{f})|$ is $7.7\,\mathrm{m/s^2}$ ($v_0 = 2.22\,\mathrm{m/s}$), $8.9\,\mathrm{m/s^2}$ ($v_0 = 1.11\,\mathrm{m/s}$) and $13.5\,\mathrm{m/s^2}$ ($v_0 = 0.55\,\mathrm{m/s}$). The amplitudes at the second harmonic ($|\ddot{X}_M(2\bar{f})|$) are only about $0.39\,\mathrm{m/s^2}$ ($v_0 = 2.22\,\mathrm{m/s}$),

$0.45\,\mathrm{m/s^2}$ ($v_0 = 1.11\,\mathrm{m/s}$) and around $1\,\mathrm{m/s^2}$ ($v_0 = 0.55\,\mathrm{m/s}$). The amplitudes at the third ($|\ddot{X}_M(3\bar{f})|$) and fourth harmonic ($|\ddot{X}_M(4\bar{f})|$) are about $0.92\,\mathrm{m/s^2}$ and $0.48\,\mathrm{m/s^2}$ ($v_0 = 0.55\,\mathrm{m/s}$), respectively. In the case of $v_0 = 1.11\,\mathrm{m/s}$, $|\ddot{X}_M(3\bar{f})|$ is about $0.29\,\mathrm{m/s^2}$, while $|\ddot{X}_M(4\bar{f})|$ is not observed. In the case of the highest considered roller speed ($v_0 = 2.22\,\mathrm{m/s}$), both $|\ddot{X}_M(3\bar{f})|$ and $|\ddot{X}_M(4\bar{f})|$ are not observed in the computed drum response. These results show that the amplitudes of the harmonics of $\ddot{x}_M$ become larger with decreasing v_0 due to more pronounced slip phases. For instance, the amplitude ratio $|\ddot{X}_M(3\bar{f})|/|\ddot{X}_M(\bar{f})|$ increases from about 0.03 ($v_0 = 1.11\,\mathrm{m/s}$) to almost 0.07 ($v_0 = 0.55\,\mathrm{m/s}$), i.e. the ratio more than doubles when the standard operating speed is halved. Thus, the normalized amplitude at the third harmonic ($|\ddot{X}_M(3\bar{f})|/|\ddot{X}_M(\bar{f})|$) can be taken as a slip indicator as already discussed in Section 2.5.1.

A closer inspection of the vertical frequency domain response reveals that spectral acceleration at the excitation frequency $\bar{f}$ ($|\ddot{Y}_M(\bar{f})|$) increases from about $0.7\,\mathrm{m/s^2}$ ($v_0 = 2.22\,\mathrm{m/s}$) to $4\,\mathrm{m/s^2}$ ($v_0 = 0.55\,\mathrm{m/s}$). At the second harmonic ($|\ddot{Y}_M(2\bar{f})|$) the spectral acceleration is about $0.5\,\mathrm{m/s^2}$ for $v_0 = 2.22\,\mathrm{m/s}$ and around $0.8\,\mathrm{m/s^2}$ for both $v_0 = 0.55\,\mathrm{m/s}$ and $v_0 = 1.11\,\mathrm{m/s}$. $|\ddot{Y}_M(2\bar{f})|$ is therefore about 0.7 times $|\ddot{Y}_M(\bar{f})|$ for the largest speed of $v_0 = 2.22\,\mathrm{m/s}$ and only around 0.2 times $|\ddot{Y}_M(\bar{f})|$ for the lowest speed of $v_0 = 0.55\,\mathrm{m/s}$. Thus, the ratio $|\ddot{Y}_M(2\bar{f})|/|\ddot{Y}_M(\bar{f})|$ becomes larger with increasing roller speed v_0. The amplitudes of the third and fourth harmonics of $\ddot{y}_M$ are only about $0.38\,\mathrm{m/s^2}$ and $0.19\,\mathrm{m/s^2}$ for $v_0 = 0.55\,\mathrm{m/s}$ and become even smaller with increasing v_0. For instance, in the case of $v_0 = 1.11\,\mathrm{m/s}$, $|\ddot{Y}_M(3\bar{f})|$ is about $0.14\,\mathrm{m/s^2}$, while $|\ddot{Y}_M(4\bar{f})|$ is not observed.

The effect of a *second roller pass* is studied for the considered oscillation roller operating at speed $v_0 = 2.22\,\mathrm{m/s}$ on initially very loose soil ($e_0 = 0.90$) and an apparent cohesion of $p_t = 10\,\mathrm{kN/m^2}$ assuming a coefficient of friction of $\mu = 0.50$. Fig. 341 shows the (a) horizontal ($\ddot{x}_M$) and (c) vertical acceleration component ($\ddot{y}_M$) in a time frame of one second during the first and a subsequent roller pass. As can readily be observed, the amplitudes of both $\ddot{x}_M$ and $\ddot{y}_M$ increase when a subsequent roller pass is performed. This is clearly illustrated by the frequency spectra depicted in Figs 341 (b) and (d). The amplitude at the excitation frequency $\bar{f}$ of $\ddot{x}_M$ ($|\ddot{X}_M(\bar{f})|$) increases from about $10.2\,\mathrm{m/s^2}$ (first pass) to $13.2\,\mathrm{m/s^2}$ (second pass). The amplitude at the second harmonic ($|\ddot{X}_M(2\bar{f})|$) is only about $0.51\,\mathrm{m/s^2}$ (first pass) and $0.44\,\mathrm{m/s^2}$ (second pass) and thus, virtually not affected by a subsequent roller pass. However, the amplitude at the third harmonic ($|\ddot{X}_M(3\bar{f})|$), which is not observed during the first pass, is about $0.8\,\mathrm{m/s^2}$ after the second pass, i.e. about 0.06 times $|\ddot{X}_M(\bar{f})|$. This result reflects the occurrence of slip phases during the second roller pass due to increased soil stiffness. The amplitude at the excitation frequency $\bar{f}$ of the vertical response $\ddot{y}_M$ ($|\ddot{Y}_M(\bar{f})|$) increases more significantly from about $0.8\,\mathrm{m/s^2}$ (first pass) to $1.4\,\mathrm{m/s^2}$ (second pass). $|\ddot{Y}_M(2\bar{f})|$, however, shows only a slight increase from about $0.25\,\mathrm{m/s^2}$ (first pass) to $0.32\,\mathrm{m/s^2}$ (second pass). Consequently, the ratio $|\ddot{Y}_M(2\bar{f})|/|\ddot{Y}_M(\bar{f})|$ decreases from about 0.31 (first pass) to 0.23 (second pass).

Plotting the vertical component $\ddot{y}_M$ against the horizontal counterpart $\ddot{x}_M$ results in a response representation that is fundamental to the CCC methodology described in [Pistrol, 2016]. In Fig. 342, grey graphs show this response representation for drum acceleration considering a coefficient of friction of $\mu = 0.30$ derived numerically in the context of the present study. Plot (a) depicts the response when compacting initially very loose soil ($e_0 = 0.90$), and plot (b) refers to the response when compacting initially

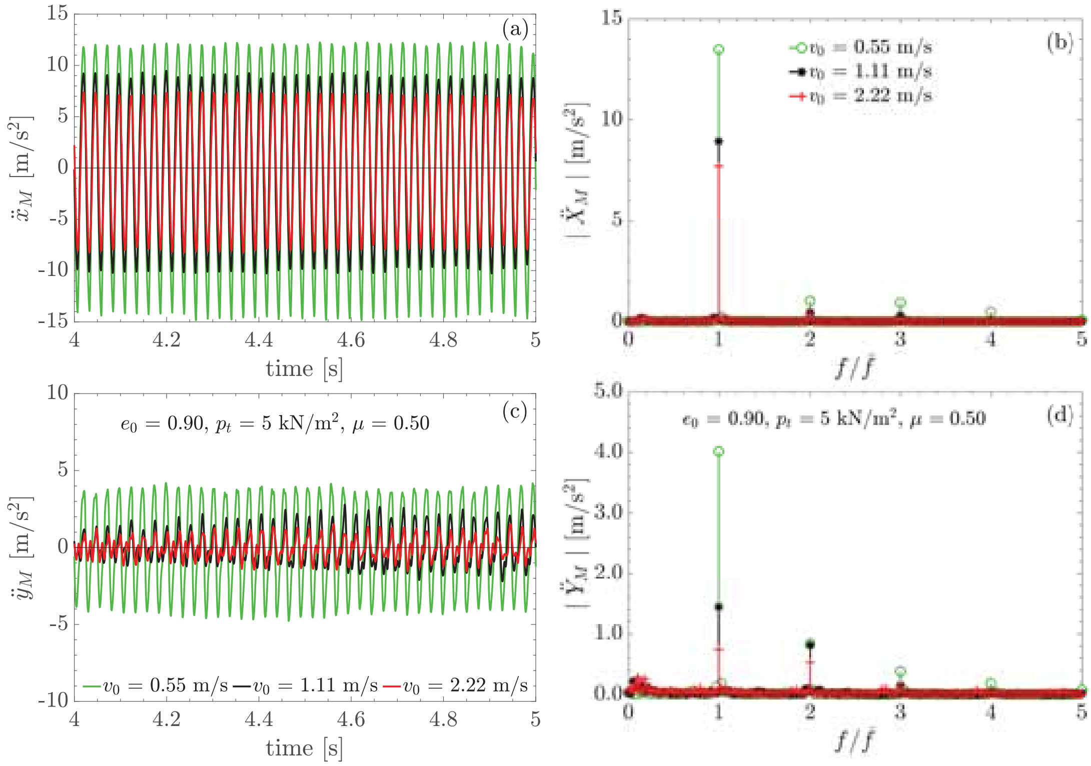

Figure 340: Time history and frequency spectrum of the (a,b) horizontal and (c,d) vertical acceleration in the drum center for three roller speeds; initially very loose soil

medium dense soil ($e_0 = 0.70$). For two "representative" excitation periods in this time frame the response is shown in plot (a) in green, and in plot (b) in green and red. For the initially very loose soil ($e_0 = 0.90$), a figure forms similar to a so-called *Lissajous curve* [Klotter, 1981] with one node and an asymmetric pattern, as the green lines in Fig. 342 (a) illustrate, which resemble a *recumbent eight*. The "area" enclosed in this *Lissajous*-like curve "representative" for $e_0 = 0.90$ is about $15.5\,\mathrm{m}^2/\mathrm{s}^4$. For comparison, Fig. 343 shows this response representation for drum acceleration components recorded in a field test described by Pistrol [2016]. It can be seen that the numerically derived drum acceleration qualitatively reproduces the drum response observed in the field. The amplitude of the horizontal acceleration component is approximately as large as in the field, while the vertical accelerations are underestimated by numerical analysis.

The effect of an initially larger soil density ($e_0 = 0.70$) on the $\ddot{y}_M$-$\ddot{x}_M$ plot is clearly illustrated in Fig. 342 (b). As it can be observed at first glance, the shape of the resulting figure is strongly influenced by the "peak cut" due to the slip phases. In some cases the shape of this figure is now similar to an asymmetric "bow tie" (figure depicted in green), and in other cases degenerated curves without nodes are observed (figure depicted in red with dotted line). This result is consistent with the findings based on the lumped parameter model of the roller-soil system presented in Section 2.4.2. The area enclosed in the figure depicted in green is about $9.6\,\mathrm{m}^2/\mathrm{s}^4$, the one enclosed in the figure depicted by red dotted lines is $23.3\,\mathrm{m}^2/\mathrm{s}^4$. This outcome is another confirmation that the area enclosed in the $\ddot{y}_M$-$\ddot{x}_M$ plot is also affected by the initial void ratio e_0.

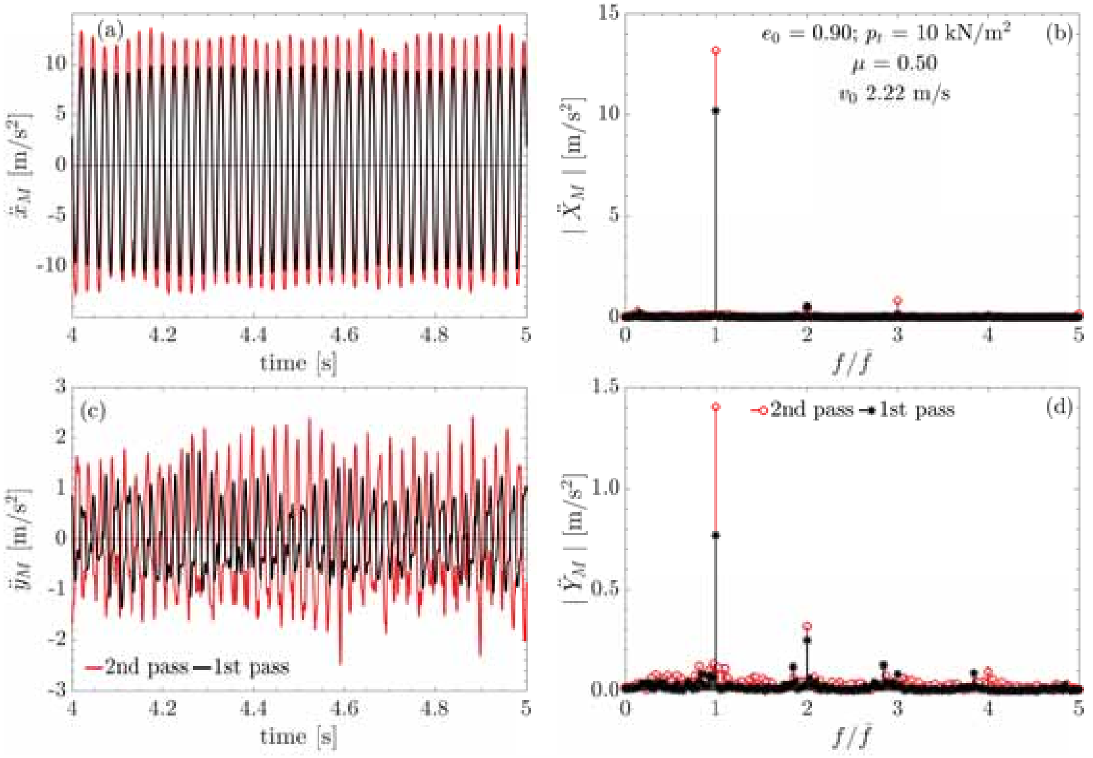

Figure 341: Time history and frequency spectrum of the (a,b) horizontal and (c,d) vertical acceleration in the drum center for two subsequent roller passes on initially very loose soil; $p_t = 10\,\mathrm{kN/m^2}$; $v_0 = 2.22\,\mathrm{m/s}$

The effect of the roller speed v_0 on the $\ddot{y}_M$-$\ddot{x}_M$ plot is illustrated in Fig. 344. That is, diagram (a) corresponds to the roller speed $v_0 = 0.55\,\mathrm{m/s}$, diagram (b) to $v_0 = 0.75\,\mathrm{m/s}$, diagram (c) to $v_0 = 1.11\,\mathrm{m/s}$, and diagram (d) to $v_0 = 2.22\,\mathrm{m/s}$. For two "representative" excitation periods in the depicted time frame of one second (grey lines) the response is shown in green. At first glace it can be seen that the shape of these figures strongly depends on the roller speed and that the area enclosed by these figures decreases with increasing roller speed. For all investigated values of v_0 the result of this response representation is a so-called *Lissajous curve* [Klotter, 1981] with one node and an asymmetric pattern. At the lowest considered speed, the right "lobe" of the eight-shaped figure is almost missing because in this case the ratio $|\ddot{Y}_M(2\bar{f})|/|\ddot{Y}_M(\bar{f})|$ is the smallest. With increasing speed the ratio $|\ddot{Y}_M(2\bar{f})|/|\ddot{Y}_M(\bar{f})|$ becomes larger and consequently, the right "lobe" increases, resulting in a more pronounced and eight-shape. Moreover, the predicted *Lissajous*-like curves rotate clockwise with increasing roller speed v_0.

The effect of a second roller pass on the $\ddot{y}_M$-$\ddot{x}_M$ plot is visualized in Fig. 345a. It is readily seen that the "area" enclosed by the depicted figure evaluated for the second pass is much larger than the one resulting from the first pass. Moreover, the node observed in the $\ddot{y}_M$ over $\ddot{x}_M$ figure during the first pass is no longer present in the figure that represents the CCC indicator during the second pass. Consequently, the resulting shape resembles that of an ellipse.

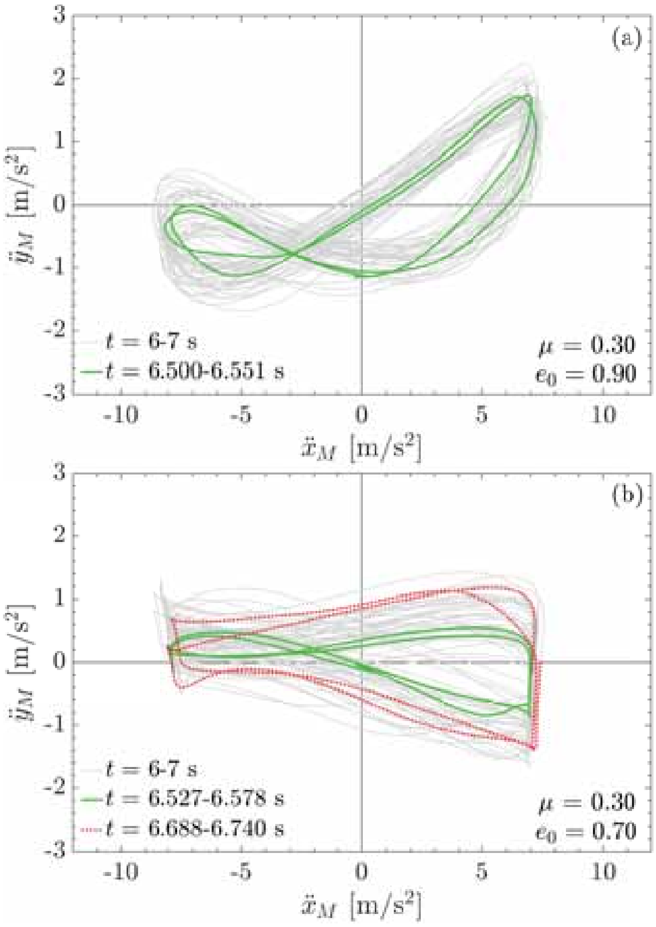

Figure 342: Plot $\ddot{y}_M$ over $\ddot{x}_M$ for a time window of 1 s (grey lines) and two representative oscillating cycles (green and red lines); $\mu = 0.30$; initial void ratio e_0 of (a) 0.90 and (b) 0.70

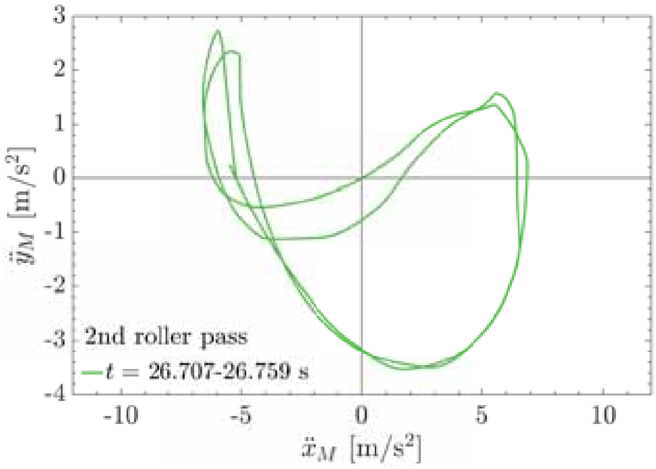

Figure 343: Plot $\ddot{y}_M$ over $\ddot{x}_M$ based on drum center accelerations recorded in field tests (described in [Pistrol, 2016]); two oscillation cycles

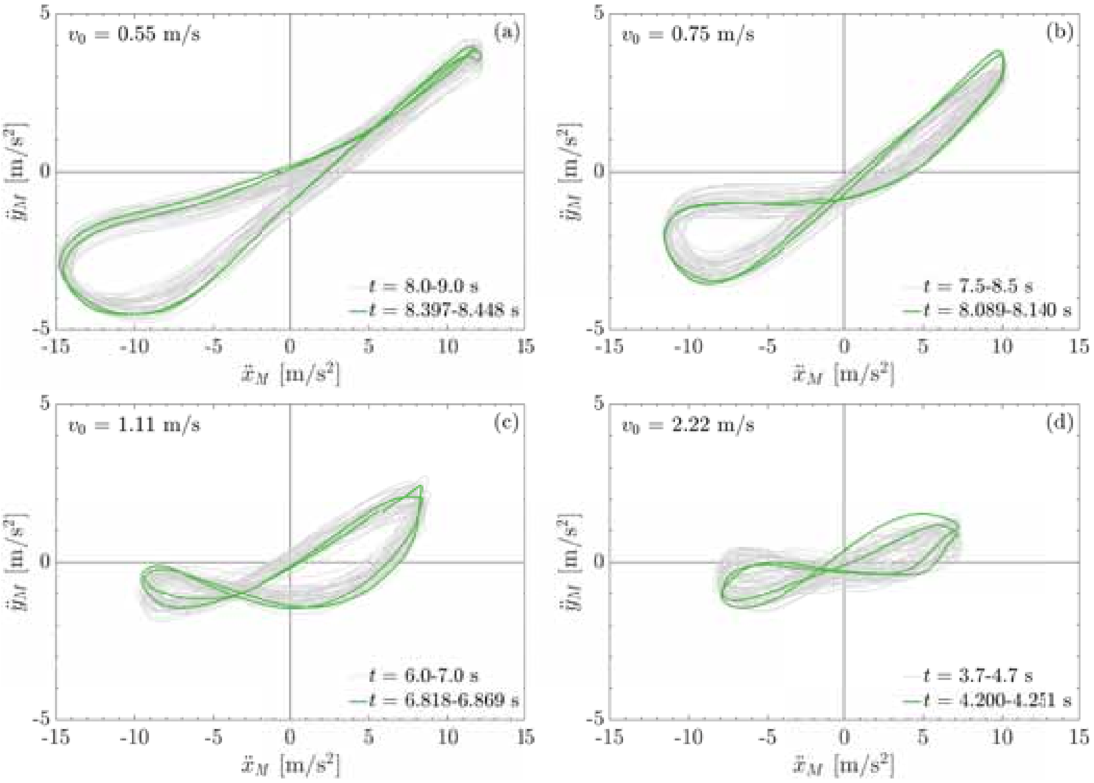

Figure 344: Plot $\ddot{y}_M$ over $\ddot{x}_M$ for roller speed v_0 of (a) 0.55 m/s, (b) 0.75 m/s, (c) 1.11 m/s and (d) 2.22 m/s for a time window of 1 s (grey lines) and two representative oscillating cycles (green lines); initially very loose soil ($e_0 = 0.90$); $p_t = 5\,\mathrm{kN/m^2}$

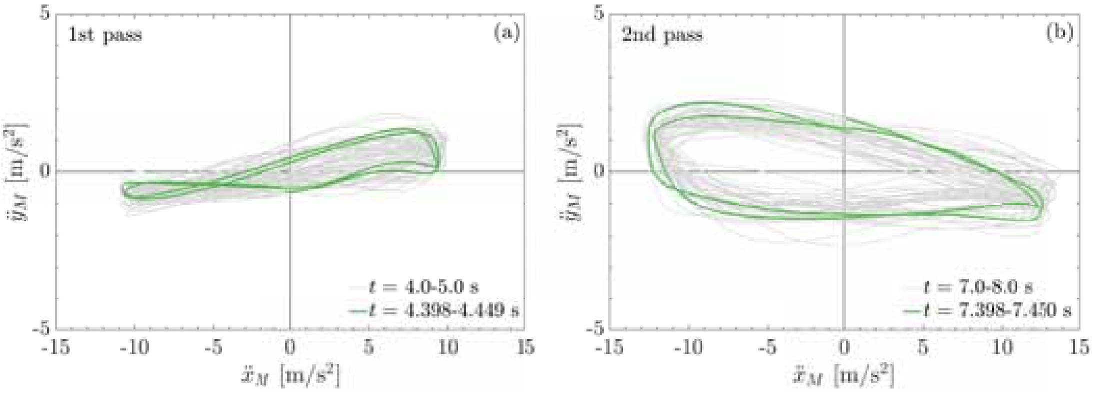

(a) Plot $\ddot{y}_M$ over $\ddot{x}_M$ for two subsequent roller passes on initially very loose soil ($e_0 = 0.90$); $p_t = 10\,\mathrm{kN/m^2}$; $v_0 = 2.22\,\mathrm{m/s}$

During the analysis of field test data, Pistrol [2016] recently identified the "area" enclosed in the $\ddot{y}_M$-$\ddot{x}_M$ response presentation as an indicator for CCC (in the literature also referred to as CCC-value) with oscillation rollers, which becomes larger with increasing soil stiffness. In Fig. 346, this *CCC indicator* (i.e. the aforementioned "area") resulting from one roller pass is plotted as a function of the distance x from the origin of the system of coordinates used to describe the geometry of the numerical model (see Fig 31). In accordance with Pistrol [2016], the compaction parameter is determined consecutively (in time) for five subsequent excitation periods, shown in this figure by discrete markers. The results of this figure are based on various parameter combinations, varying the initial subsoil conditions ($e_0 = 0.90$ and 0.70, respectively), the coefficient of friction ($\mu = 0.50$ and 0.30, respectively), and the apparent cohesion ($p_t = 5\,\mathrm{kN/m^2}$ and $10\,\mathrm{kN/m^2}$, respectively). The scatter of the compaction indicator with respect to x is primarily a result of the strong amplitude fluctuation of the vertical accelerations.

For the initially loose soil ($e_0 = 0.90$) and the "default parameter set" ($\mu = 0.50$ and $p_t = 5\mathrm{kN/m^2}$), the mean compaction indicator, which varies between 21.5 and $31.4\,\mathrm{m^2/s^4}$, is about $26.8\,\mathrm{m^2/s^4}$. This value is in very good agreement with the CCC value of about $25\,\mathrm{m^2/s^4}$, which results from one on-site roller pass on a very loose soil, as documented in [Pistrol, 2016]. For $e_0 = 0.70$ the mean CCC indicator is about $30\,\mathrm{m^2/s^4}$ and thus, 12 % larger compared to the initially very loose soil. Therefore, this indicator captures the increase of stiffness associated with soil compaction if the standard parameter set is used.

As expected, the reduction of μ reduces the amount of the compaction indicator in the range of 12.6-24.6 $\mathrm{m^2/s^4}$ ($e_0 = 0.90$) and 15.0-27.7 $\mathrm{m^2/s^4}$ ($e_0 = 0.70$), respectively. The maximum value for $e_0 = 0.70$ is about 13 % larger than for $e_0 = 0.90$, while the mean value (of approximately $20\,\mathrm{m^2/s^4}$) is virtually the same for both $e_0 = 0.70$ and $e_0 = 0.90$. Thus, for an initially medium dense soil the increase of the simulated stiffness is not that pronounced if the smaller value of μ is assigned to the model.

Using an apparent cohesion p_t that is two times the default value, significantly increases the amount of the compaction indicator. The resultant "area“ varies between 35.8 and $70.7\,\mathrm{m^2/s^4}$ ($e_0 = 0.90$) and between 59.8 and $81.1\,\mathrm{m^2/s^4}$ ($e_0 = 0.70$), respectively. In this case, the mean compaction indicator for the initially medium dense soil of $73.2\,\mathrm{m^2/s^4}$ is about 45 % larger than for the initially very loose soil ($50.5\,\mathrm{m^2/s^4}$). Therefore, the compaction indicator most clearly reflects the higher soil stiffness with a larger apparent cohesion p_t.

Fig. 347 shows the CCC indicator during one oscillatory roller pass on initially very loose soil ($e_0 = 0.90$) for four selected roller speeds v_0 considered already in Section 3.3.3. In the numerical analyses a coefficient of friction of $\mu = 0.50$ has been used. As before, one marker represents the area in the $\ddot{y}_M$-$\ddot{x}_M$ figure determined consecutively (in time) for five subsequent excitation periods. Blue circular markers refer to the results for the default roller speed of $v_0 = 1.11\,\mathrm{m/s}$, and black "x" markers represent the results for $v_0 = 0.55\,\mathrm{m/s}$. Outcomes based on $v_0 = 1.39\,\mathrm{m/s}$ are indicated by red "*" markers. Green "+" markers represent the performance indicator for the roller at twice the default speed ($v_0 = 2.22\,\mathrm{m/s}$). As can be observed at first glance, the simulations based on the highest speed $v_0 = 2.22\,\mathrm{m/s}$, where the soil is exposed to only about 18 oscillations per meter driven, yield the lowest mean compaction indicator of about $17.5\,\mathrm{m^2/s^4}$ with a scatter in the range of 14.1-21.2 $\mathrm{m^2/s^4}$. Notably, the CCC

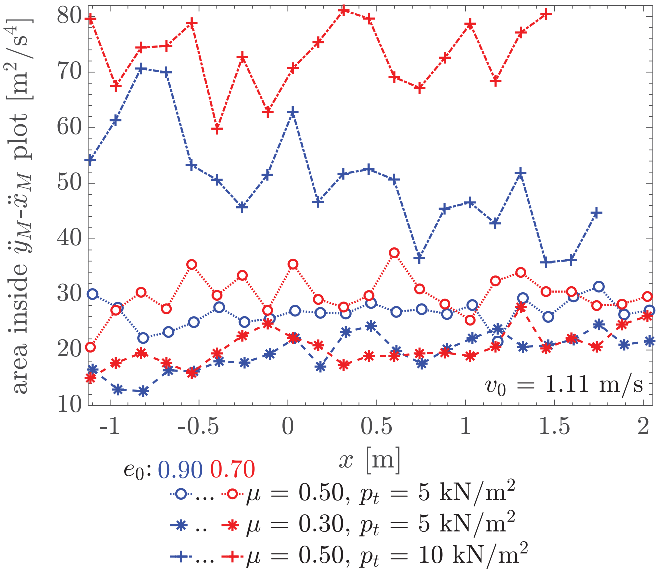

Figure 346: Compaction indicator during the first roller pass; variation of v_0

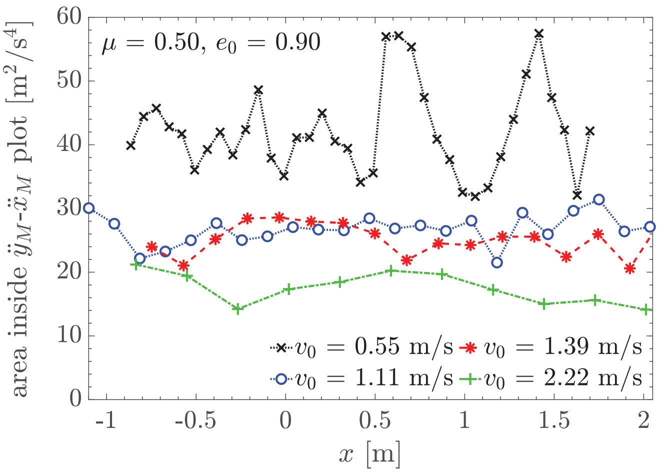

Figure 347: Compaction indicator during the first roller pass; variation of v_0

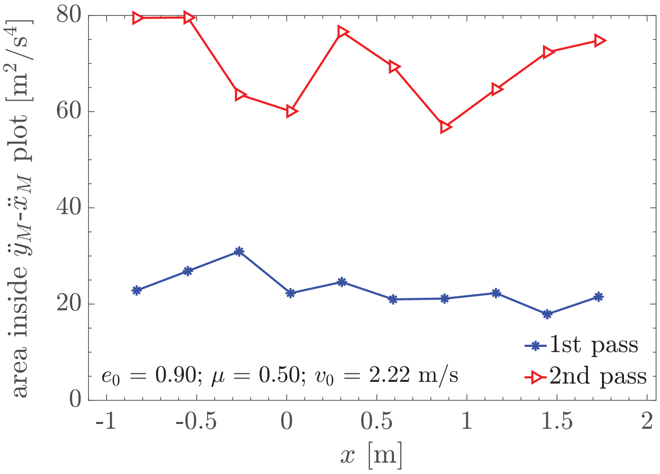

Figure 348: Compaction indicator during two subsequent roller passes on initially very loose soil; $p_t = 10\,\mathrm{kN/m^2}$; $v_0 = 2.22\,\mathrm{m/s}$

indicator based on the lowest roller speed, where the subsoil is subjected to about 70 oscillations per meter driven, shows the largest scatter with a variation between 31.9 and 57.5 $\mathrm{m^2/s^4}$. The corresponding mean value is 42.1 $\mathrm{m^2/s^4}$. The mean values induced by rollers with speeds $v_0 = 1.11\,\mathrm{m/s}$ and $v_0 = 1.39\,\mathrm{m/s}$ are in the same order of magnitude, i.e. 26.8 $\mathrm{m^2/s^4}$ and 25.2 $\mathrm{m^2/s^4}$, respectively. These results essentially show that the considered CCC parameter decreases with increasing roller speed, and thus, with decreasing number of oscillations per meter driven.

The effect of a subsequent second roller pass on the CCC indicator is clearly illustrated in Fig. 348. It can readily be seen that the second pass of an oscillation roller operating at $v_0 = 2.22\,\mathrm{m/s}$ on initially very loose soil ($e_0 = 0.90$) yields a significantly larger CCC value over the whole traveled length. The corresponding "area" varies between 56.8 and 79.6 $\mathrm{m^2/s^4}$. The mean compaction indicator after the second roller pass is about 70 $\mathrm{m^2/s^4}$ and thus, about three times larger than the mean CCC indicator after the first pass, which is about 23 $\mathrm{m^2/s^4}$.

Chapter **4**

Summary, conclusions, and outlook

4.1 Summary and conclusions

In the present work, two modeling strategies have been pursued. On the one hand, *lumped parameter modeling* was applied to investigate the motion behavior of the drum in dependence of a priori defined soil parameters. On the other hand, *Finite Element modeling* was used to assess the compaction effect and the drum motion behavior simultaneously.

4.1.1 Lumped parameter modeling

In the chosen *lumped parameter modeling* strategy, a three degrees-of-freedom model of the interacting oscillation roller-subsoil system has been proposed. The governing highly nonlinear equations of this model have been derived for an asymmetric shape of the underlying soil ("settlement trough") separately for the *stick* and the *slip* phase of the drum motion.

The presented results of the detailed response study based on the HD$^+$ 90 VO tandem roller demonstrate that the proposed model predicts the main outcomes found in previous in-situ tests. The maximum amplitude in the frequency spectrum of the horizontal drum acceleration occurs at the operating frequency $\bar{f}$. The observed overtones at odd multiples of the excitation frequency ($f/\bar{f} = 3, 5, 7, ...$) result from the slip phase of the drum motion. In the frequency spectrum of the vertical drum accelerations the harmonics at even multiples of the excitation frequency ($f/\bar{f} = 4, 6, 8, ...$) indicate slip between drum and soil. In the case of a drum oscillating at the bottom of the settlement trough, the maximum amplitude in the frequency spectrum of the vertical drum response occurs at $f/\bar{f} = 2$, reflecting the up- and down motion of the drum in the settlement trough. If the drum operates on the slope of the settlement trough (above its bottom) by application of a constant driving torque, for most subsoil conditions the dominating frequency of the vertical drum response also corresponds to the excitation frequency $\bar{f}$, and additional harmonics at $f/\bar{f} = 3, 5, 7, ...$ are observed. It was confirmed that the plot vertical drum accelerations over horizontal drum accelerations yields a *Lissajous curve* with one node ("recumbent eight"), and the area enclosed in this figure depends on the soil stiffness (and thus, on the compaction degree) if the drum conducts a pure rolling motion, i.e. the drum sticks on the underlying soil. Application of a constant driving torque, which simulates the effect of the translation motion of the roller speed, yields a distorted and rotated “recumbent eight”, as it is observed from accelerations recorded in field tests. In *stick-slip* drum motion, the observed eight-shaped figure distorted (shape of a twisted “bow tie”) because the maximum horizontal accelerations are confined in the slip phase. The results indicate that relations between the compaction degree of soil layers and the area inside the response representation of vertical drum acceleration vs. horizontal drum acceleration can be established also for stick-slip motion of the drum. If a certain driving torque is applied, the “area” (i.e. the compaction indicator) becomes larger with increasing shear modulus, reaches a maximum and then decreases with further increase of the soil stiffness.

The outcomes of the parametric studies based on four different types of oscillation rollers demonstrate that the compaction indicator for continuous compaction control (CCC) with oscillation rollers proposed by Pistrol [2016] is basically suitable for all considered roller types. The observed increase of the CCC indicator with increasing soil stiffness is mainly due to the amplitudes in the frequency domain of the horizontal drum accelerations at the oscillation frequency $\bar{f}$, which increase continuously with increasing shear modulus for all rollers. In addition, the amplitudes in the frequency domain of the vertical drum accelerations at frequencies $2\bar{f}$ and $3\bar{f}$ affect the area because these harmonics have a strong impact on the shape of the response representation of vertical drum acceleration vs. horizontal drum acceleration. For the standard equipment and operating parameters, the shear modulus, which corresponds to the maximum area increase and thus, represents the application limit of the assessed CCC indicator, is largest for the rollers HD13i VIO and HD$^+$ 140i VO and lowest for the H7i VIO roller. Therefore, the rollers HD13i VIO and HD$^+$ 140i VO are best suited for the proposed CCC application. The conducted sensitivity studies demonstrate that the application limit of this value is positively influenced by an increased operating frequency. Moreover, the suspension stiffness has an impact on the level of increase of the compaction indicator but not on its application limit, while the impact of the suspension damping is negligible. Similarly, the reduction of the coefficient of friction between the drum and the soil surface has virtually no effect on that soil stiffness, where the maximum normalized compaction indicator occurs.

In summary it can be concluded that the developed analytical model facilitates the response simulation of an oscillation drum with the least numerical effort capturing the observed stick-slip motion of the drum. The predicted response matches qualitatively, and partially also quantitatively, the drum response observed in the field during near-surface compaction of non-cohesive soils.

4.1.2 Finite Element modeling

In the chosen *Finite Element modeling* strategy, a plane-strain model of the oscillation roller-soil interaction system during the near-surface compaction of a granular soil was presented. With this FE model, the compaction effect of the roller can be predicted, since the mechanical behavior of the subsoil is described by the intergranular strain enhanced hypoplastic constitutive model. As a novelty, a protective layer, i.e. a thin elastic layer, is applied to the soil surface to improve the numerical stability due to issues related to the hypoplastic law. This model reproduces the bow wave developing in front of the drum as observed in the field. Its influence on the soil compaction and near-surface soil loosening as well as the sensitivity of both the soil compaction achieved with a HD$^+$ 90 VO roller and the drum response to the variation of different model and operating parameters was assessed in detail.

The visualization of the soil stress and strain components has provided novel insight into the soil depth-dependent compaction behavior of oscillation rollers. It could be shown that the quasi-static stresses induced by a single oscillatory roller pass on initially very loose soil are of similar shape and magnitude as the stresses resulting from a static roller with a certain offset. In contrast, the subgrade stain components induced by the oscillatory roller are much larger than those of the static roller. From this it can be concluded that the high-frequency dynamic stresses due to the oscillatory moment impose both considerable shear and compressive deformation in the subsoil although their amplitudes are much smaller than those of the quasi-static stresses. It has been confirmed that not only the dynamic shear stresses but also the normal stresses transferred by the oscillation roller into the subsoil lead to a compaction of the subgrade. Another observation is that the moving oscillation roller has the largest impact on the stress-strain state in the soil when the drum is at a horizontal distance of about $x_M = -0.6 \div 0.9\,\mathrm{m}$ from a selected observation point in the subsoil. This means that the range of influence can be related to the drum radius r of the considered roller as $-r \leq x_M \leq 1.5r$.

The study of the effect of differently packed soil conditions on the change of the void ratio revealed the extent of the achieved compaction with an oscillation roller in terms of soil depth and horizontal distance of the drum from a selected observation spot in the subsoil. Naturally, the largest compaction effect was achieved when the subsoil was initially very loose. Another finding is that the compaction over the depth is more uniform in initially dense subsoils. For all initial soil densities considered, the depth effect of the oscillation roller operating at standard speed was about the same, i.e. nearly one meter. The results of comprehensive studies confirm that a single pass with the considered oscillation roller running at standard speed uniformly reduces the void ratio of the investigated sandy soil up to a depth of 0.15-0.50 m thickness, with the lower limit for an initially very loose soil and the upper limit for a dense soil. This compaction depth is virtually not influenced by the choice of the friction coefficient between the drum, which controls the slip phase in the contact zone between the drum and the soil surface, and the apparent cohesion of the subsoil. Reducing the roller speed results in an increase of this depth as well as the maximum predicted void ratio reduction. With a second roller pass, the maximum compaction remains the same as after the first pass, but the compaction depth is increased. The variation of the static axle load by ±20 % has no significant effect on the achieved soil compaction. Increasing the apparent cohesion of the soil up to $10\,\mathrm{kN/m^2}$, yields a larger void ratio reduction, which is even further increased by a subsequent roller pass, without influencing the depth effect significantly. The presented findings with respect to the compaction effect correspond to the observations from on-site applications of oscillation rollers. However, it seems that the proposed numerical model overestimates the degree of achieved compaction by one dynamic roller pass.

The amplitude of the computed horizontal acceleration component is of the same magnitude as observed in the field. The vertical accelerations are, however, underpredicted by the numerical analysis. The frequency content of the numerically analyzed accelerations of the drum center during compaction is very similar to that of field test data. The overtones in the measured data are also found in the numerically simulated data. Moreover, the corresponding normalized amplitudes are of the same magnitude. By reducing the coefficient of friction, the slip phases of the drum are extended and the amplitudes of the horizontal accelerations of the drum center are reduced. As a result, the higher harmonics are more pronounced in the corresponding frequency spectra. The presented outcomes confirm that the amplitude at the third harmonic of the horizontal drum response normalized by amplitude at the excitation frequency may be considered as an indicator of the extent of the slip phase in the drum response.

When the computed vertical acceleration component of the drum center is plotted against the corresponding horizontal component, a so-called *Lissajous curve* with one node and an asymmetric pattern is obtained that resembles a *recumbent eight*, similar to outcomes based on the proposed lumped parameter model. Thus, the response behavior recently discovered in the analysis of field test data is also supported by this numerical model. Pronounced slip phases by reduction of the coefficient of friction modify the shape of the figure, which now resembles more an asymmetric “bow tie”, or the nodes disappear at all. The presented results of the conducted sensitivity study confirm that the shape and area of representation of the vertical over the horizontal drum center acceleration strongly depend on the subsoil stiffness, characterized by the initial void ratio, the apparent cohesion, the coefficient of friction between drum and subsoil, and the roller speed. Simulations of a subsequent second roller pass on initially very loose soil at the same speed revealed a significant increase of the CCC indicator (i.e. the “area”) over the whole covered length. Thus, these outcomes confirm that quantities derived from this drum response representation are appropriate as indicators for work-integrated continuous compaction control with oscillation rollers.

In summary it can be concluded that the developed numerical model predicts qualitatively, and partially also quantitatively, the drum response and the compaction effect of an oscillation roller observed in the field during near-surface compaction of non-cohesive soils.

4.2 Outlook

The more recently developed CCC technique for oscillation rollers, as described in the introduction, has been verified by the presented results of the detailed response study of one specific roller type and the outcomes of a comprehensive parametric study based on three additional oscillation rollers. Thus, the proposed lumped parameter model predicts both realistically and efficiently the dynamic response of an oscillation drum interacting with the underlying soil during roller compaction. For additional research investigations, the model can be extended in a straightforward manner. For instance, non-linearity of the subsoil and, if necessary, the trapped soil mass can easily be considered. In addition, the model allows the investigation of unbalanced drums by appropriate modeling of the corresponding excitation. Moreover, a modified coefficient of friction can be taken into account, which, for example, is modeled as a function of the slip velocity between drum and soil.

The developed numerical model has provided novel insight into the soil depth-dependent compaction behavior and the resulting compaction effect of oscillation rollers.

Simultaneously, also the capability of oscillation rollers for work-integrated compaction control was verified. The presented findings motivate a series of further numerical studies. For instance, the developed model allows the machine and operating parameters of existing oscillation rollers to be optimized with a view to achieving the best possible compaction result. In addition, the measuring depth of oscillation rollers can be studied by investigating the compaction of layers of varying thickness and stiffness resting on a very stiff and on a very soft subsoil, respectively, and evaluating the predicted drum center accelerations in terms of the assessed CCC indicator. Since this compaction indicator is a relative value, investigations should be carried out focusing on a possible relationship between the area enclosed by the *Lissajous figure*, which represents the drum response in terms of drum center accelerations, and the corresponding soil stiffness. For instance, the simulation of conventional spot like compaction testing methods, such as static and dynamic plate load tests, can be used to compute soil stiffness values corresponding to the determined respective relative CCC indicator. Since the present investigations are based on a sandy soil, supplementary simulations based on a gravelly soil model should tackle the sensitivity of the soil compaction as well as of the drum response to the type of granular subsoil. Future studies should also address the influence of the "protective foil" on the response prediction of the interacting oscillatory-roller system, and alternative measures (such as application of viscous "surface dampers", extension of the user defined material subroutine) for improving the numerical stability should be tested and optimized, respectively.

Appendix **A**

Dynamic decoupling

The dynamic decoupling of drum and roller frame (including the cabin), realized by rubber buffers (suspension), is subsequently analyzed for the HAMM HD^{+} 90 VO tandem roller (roller 1) considered in Section 2.4 using a simplified model. The suspension is idealized as a *Kelvin-Voigt* model consisting of a spring and dashpot damper (stiffness k_d and damping parameter c_d). The frame (including the cabin) is modeled as a lumped mass, yielding in combination with the aforementioned *Kelvin-Voigt* suspension model a SDOF system (see Fig. A1). The lumped mass m_f, identified from the static axle load P_0, represents the effective mass of the roller with respect to the front axle.

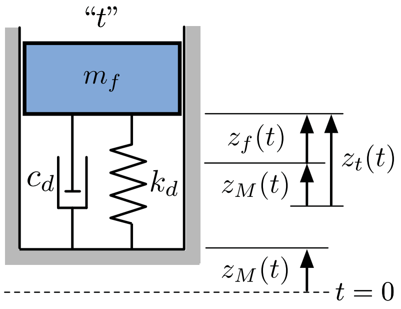

Figure A1: SDOF-model of the front frame supported by the drum suspension

The absolute displacement transmissibility T_p of this SDOF system is assessed according to the subsequent well-known equation [Clough and Penzien, 1993]:

$$T_p = \sqrt{\frac{1+\left(2\zeta\frac{\bar{\nu}}{\omega}\right)^2}{\left[1-\left(\frac{\bar{\nu}}{\omega}\right)^2\right]^2+\left(2\zeta\frac{\bar{\nu}}{\omega}\right)^2}} \tag{A.1}$$

where

$$\zeta = \frac{c_d}{2m_f\omega} \quad , \quad \omega = \sqrt{\frac{k_d}{m_f}} \quad , \quad \bar{\nu} = 2\pi\bar{f} \tag{A.2}$$

For the considered roller 1 with the parameters listed in Table 21, the natural circular frequency ω is 38.1 rad/s, the damping ratio ζ is 0.014 ($c_d = 3\times10^3$ Ns/m) and 0.0014

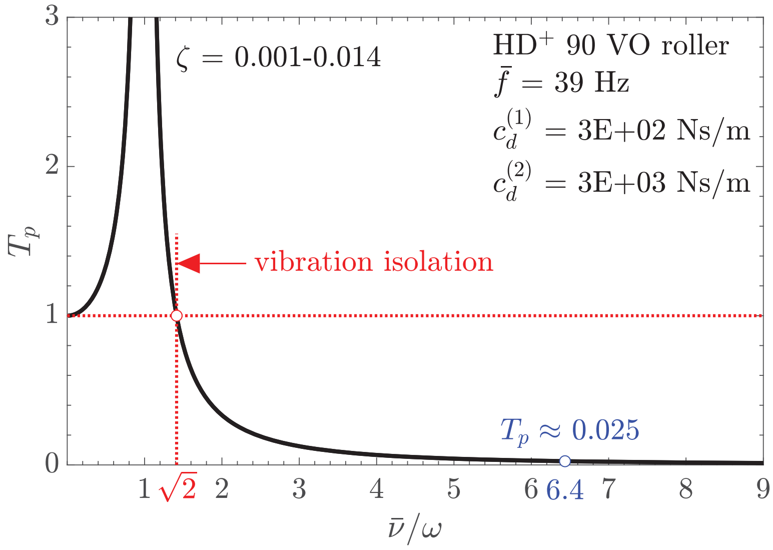

Figure A2: Absolute displacement transmissibility T_p

($c_d = 3 \times 10^2$ Ns/m), respectively, and the excitation frequency $\bar{\nu}$ of base excitation z_M is 245 rad/s. Since the ratio $\bar{\nu}/\omega = 6.4$ is 4.5 times larger than $\sqrt{2}$, the absolute displacement transmissibility T_p is much less than 1. In particular, evaluation of Eq. A.1 yields $T_p \approx 0.025$ for both values of c_d (see Fig. A2). That is, the amplitude of the frame displacement z_f is maximum only about 2.5 % of the amplitude of the displacement z_M imposed at the frame base (according to the model in Fig. A1). Thus, it is confirmed that drum and front frame are dynamically decoupled by the deeply tuned rubber buffers (as desired by the manufacturer and proofed during roller operation on-site).

Appendix B

Coefficients of the discrete soil model

Based on Pistrol [2016], the contact length $2a_0$ is assumed to be four times the contact length according to *Hertzian* theory [Popov, 2017] for non-adhesive elastic contact,

$$2a_0 = 4\left(2\sqrt{\frac{2rP_0\,(1-\nu)}{\pi G b_0}}\right) \tag{B.1}$$

In this equation, r represents the drum radius, P_0 denotes the static (vertical) axle load of the roller, b_0 is the half drum width and a_0 denotes the half contact length between drum and soil surface (see Fig. B1), G and ν are the shear modulus and the *Poisson*'s ratio of the halfspace, respectively.

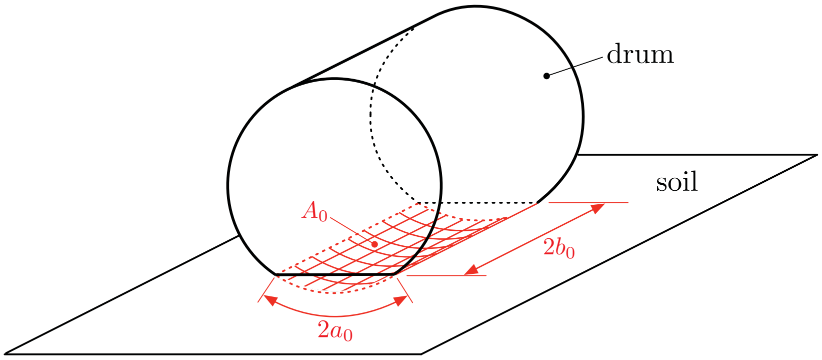

Figure B1: Geometry of the contact area between drum and soil [Pistrol, 2016]

Based on the translational cone models (e.g. [Wolf, 1994]) as shown in Fig. B2, the elastic continuous soil halfspace can be reduced to two spring-dashpot damper elements, as illustrated in Fig. 21, which represent the considered non-cohesive subsoil conditions, i.e. $\nu \leq 1/3$. The corresponding dynamic soil spring coefficients, k_{sh} and k_{sv}, do not depend on the excitation frequency (because $\nu \leq 1/3$), and thus, represent the “frequency-independent coefficients of an ordinary spring (the static stiffness)”, as discussed in [Wolf, 1994]. Instead, the spring coefficients k_{sh} and k_{sv}, which represent

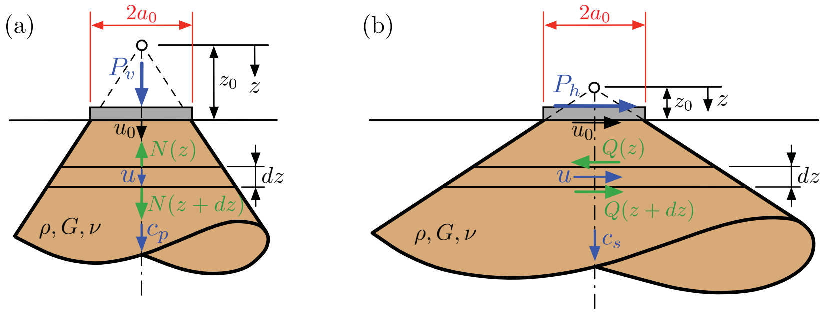

Figure B2: Translational cone for (a) vertical and (b) horizontal motion, based on Wolf [1994]

the subsoil stiffness, depend on the half contact length a_0 between drum and soil as follows ([Pais and Kausel, 1988], [Wolf, 1994]),

$$\begin{aligned} k_{sh} &= \frac{Ga_0}{2-\nu}\left[6.8\left(\frac{b_0}{a_0}\right)^{0.65}+0.8\left(\frac{b_0}{a_0}\right)+1.6\right] \\ k_{sv} &= \frac{Ga_0}{1-\nu}\left[3.1\left(\frac{b_0}{a_0}\right)^{0.75}+1.6\right] \end{aligned} \tag{B.2}$$

The soil damping coefficients c_{sh} and c_{sv} do also not depend on the excitation frequency, and thus, represent “frequency-independent coefficients of an ordinary dashpot” [Wolf, 1994]. The coefficients c_{sh} and c_{sv}, which represent the geometric damping of the subsoil, are two times the coefficients proposed by Wolf [1994],

$$\begin{aligned} c_{sh} &= 2c_{sh}^{(\text{Wolf})} = 2\rho\sqrt{\frac{G}{\rho}}4a_0b_0 \\ c_{sv} &= 2c_{sv}^{(\text{Wolf})} = \sqrt{\frac{2-2\nu}{1-2\nu}}c_{sh} \end{aligned} \tag{B.3}$$

as discussed in [Kopf, 1999]. Variable ρ is the soil density. Substituting for a_0 the expression of Eq. B.1 yields

$$\begin{aligned} c_{sh} &= 32\sqrt{\frac{2\rho r b_0 P_0\,(1-\nu)}{\pi}} \\ c_{sv} &= 64\,(1-\nu)\sqrt{\frac{\rho r b_0 P_0}{(1-2\nu)\,\pi}} \end{aligned} \tag{B.4}$$

According to Wolf [1994] both the dynamic stiffness coefficients and the damping coefficients of the translational cone models are “very accurate in the inter-mediate- and higher-frequency ranges, whereas in the lower-frequency range ($\bar{a}_0 < 2$) and for $\nu \leq 1/3$ [...] the spring-damper soil model overestimates (radiation) damping to a certain extent, especially in the vertical motion”. Note that $\bar{a}_0$ is the non-dimensional frequency parameter defined by Wolf [1994],

$$\bar{a}_0 = \frac{\bar{\nu} r_0}{c_s} \tag{B.5}$$

with the excitation frequency $\bar{\nu}$, the equivalent radius r_0,

$$r_0 = \sqrt{\frac{A_0}{\pi}} = \sqrt{\frac{4a_0 b_0}{\pi}} \tag{B.6}$$

and the shear wave velocity c_s,

$$c_s = \sqrt{\frac{G}{\rho}} \tag{B.7}$$

In the present case, where four selected HAMM rollers with an operating frequency $\bar{f}$ between 33 and 39 Hz are considered (see Table 21), the non-dimensional frequency $\bar{a}_0$ varies between 0.28-0.35 ($G = 70$ MN/m^2) and 2.0-2.5 ($G = 5$ MN/m^2). For $G =$ 10 MN/m^2, $\bar{a}_0 \approx 1.2$-1.5. Thus, $\bar{a}_0 < 2$ except the lowest value of G. The problem is, hence, mostly in the “lower-frequency range”, as defined by Wolf [1994].

			HD$^+$ 90 VO	H7i VIO	H13i VIO	HD$^+$ 140i VO
G [MN/m^2]	ρ [kg/m^3]	ν [ ]	a_0 [m]	a_0 [m]	a_0 [m]	a_0 [m]
5	1,900	0.30	0.215	0.194	0.272	0.245
10	1,900	0.30	0.152	0.137	0.192	0.173
15	1,900	0.30	0.124	0.112	0.157	0.141
20	1,900	0.30	0.107	0.097	0.136	0.122
25	1,900	0.30	0.096	0.087	0.121	0.110
30	1,900	0.30	0.088	0.079	0.111	0.100
35	1,900	0.30	0.081	0.073	0.103	0.093
40	1,900	0.30	0.076	0.069	0.096	0.087
45	1,900	0.30	0.072	0.065	0.091	0.082
50	1,900	0.30	0.068	0.061	0.086	0.077
55	1,900	0.30	0.065	0.059	0.082	0.074
60	1,900	0.30	0.062	0.056	0.078	0.071
65	1,900	0.30	0.060	0.054	0.075	0.068
70	1,900	0.30	0.057	0.052	0.073	0.065

Table B1: Soil parameters (shear modulus G, density ρ, *Poisson*'s ratio ν), and corresponding half contact length a_0 between drum of the four considered oscillation rollers and soil

	HD$^+$ 90 VO		H7i VIO		H13i VIO		HD$^+$ 140i VO	
G [MN/m^2]	k_{sh} [MN/m]	k_{sv} [MN/m]	k_{sh} [MN/m]	k_{sv} [MN/m]	k_{sh} [MN/m]	k_{sv} [MN/m]	k_{sh} [MN/m]	k_{sv} [MN/m]
5	11,4	16,3	10.9	15.8	14.5	20.7	13.8	20.1
10	19,7	29,5	18.9	28.8	25.0	37.5	24.0	36.5
15	27,3	42,1	26.3	41.1	34.6	53.5	33.3	52.3
20	34,5	54,3	33.3	53.2	43.8	69.1	42.2	67.6
25	41,4	66,3	40.0	65.0	52.6	84.3	50.8	82.6
30	48,2	78,1	46.6	76.6	61.2	99.3	59.1	97.4
35	54,8	89,8	53.0	88.1	69.6	114	67.3	112
40	61,2	101	59.3	99.6	77.8	129	75.3	127
45	67,6	113	65.6	111	85.9	144	83.2	141
50	73,9	124	71.7	122	93.9	158	91.0	155
55	80,1	136	77.8	133	102	172	98.7	170
60	86,2	147	83.8	145	110	187	106	184
65	92,3	158	89.7	156	117	201	114	198
70	98,3	169	95.6	167	125	215	121	212
G [MN/m^2]	c_{sh} [kNs/m]	c_{sv} [kNs/m]	c_{sh} [kNs/m]	c_{sv} [kNs/m]	c_{sh} [kNs/m]	c_{sv} [kNs/m]	c_{sh} [kNs/m]	c_{sv} [kNs/m]
5-70	141	263	127	238	227	424	204	382

Table B2: Shear modulus of the soil, and corresponding stiffness and damping parameters of the lumped parameter model

APPENDIX C

Abbreviations

C.1 Spiral-shaped settlement trough

The functions f_1, f_2, f_3, f_4, f_5, and f_6 in the equations of motion of the proposed lumped parameter model (see Section 2.2), which depend on spiral parameters a, k, α, R_0, drum radius r, and angle $\delta(t)$, read as

$$f_1 = R_0 \exp(-k\delta)\Big[k\cos(\alpha+\delta)+\sin(\alpha+\delta)\Big] - r\cos\delta \tag{C.1}$$

$$f_2 = R_0 \exp(-k\delta)\Big[(1-k^2)\cos(\alpha+\delta)-2k\sin(\alpha+\delta)\Big] + r\sin\delta \tag{C.2}$$

$$f_3 = -R_0 \exp(-k\delta)\Big[k\sin(\alpha+\delta)-\cos(\alpha+\delta)\Big] + r\sin\delta \tag{C.3}$$

$$f_4 = -R_0 \exp(-k\delta)\Big[(1-k^2)\sin(\alpha+\delta)+2k\cos(\alpha+\delta)\Big] + r\cos\delta \tag{C.4}$$

$$f_5 = \sqrt{1+k^2}\exp(-k\delta)\frac{R_0}{r} - 1 \tag{C.5}$$

$$f_6 = -k\sqrt{1+k^2}\exp(-k\delta)\frac{R_0}{r} \tag{C.6}$$

C.2 Semi-circular settlement trough

If the logarithmic spiral approaches a semi-circle (see Fig. C1), the first spiral parameter k becomes zero, the second parameter a corresponds to the radius R of the semi-circular curved track, and the angle α becomes $\pi/2$:

$$k = 0 \quad , \quad a = R_0 = R \quad , \quad \alpha = \pi/2 \tag{C.7}$$

Thus, inserting in the relations of Appendix C.1 $k = 0$ and $\alpha = \pi/2$, and replacing a and R_0 by R yields the corresponding expressions for the functions f_i and $\tilde{f}_i$ representing a semi-circular settlement trough,

$$\begin{aligned} &f_1 = -f_4 = l\cos\delta \ , \ f_2 = f_3 = -l\sin\delta \ , \ f_5 = \frac{l}{r} \ , \ f_6 = 0 \\ &\tilde{f}_1 = l \ , \ \tilde{f}_2 = 0 \ , \ \tilde{f}_3 = 0 \ , \ \tilde{f}_4 = -l \end{aligned} \tag{C.8}$$

with

$$l = R - r \tag{C.9}$$

Then, the response of the drum center $(x_M,\, z_M)$ is related to the independent coordinates of motion as

$$x_M = l \sin\delta + x_A \quad , \quad z_M = l(\cos\delta - 1) + s_A \tag{C.10}$$

The second derivative of Eqs C.10 with respect to time t yields the acceleration components $\ddot{x}_M$ and $\ddot{z}_M$,

$$\ddot{x}_M = l\left(\cos\delta\ddot{\delta} - \sin\delta\dot{\delta}^2\right) + \ddot{x}_A \quad , \quad \ddot{z}_M = -l\left(\sin\delta\ddot{\delta} + \cos\delta\dot{\delta}^2\right) + \ddot{s}_A \tag{C.11}$$

The *rolling condition* according to Eq. 2.11, i.e. the relationship between the drum rotation angle φ and the position angle δ in the *stick* phase, simplifies to

$$R\delta = r\,(\delta + \varphi) \tag{C.12}$$

The first and the second time derivative of Eq. C.12 read as

$$\dot{\varphi} = \frac{l}{r}\dot{\delta} \quad , \quad \ddot{\varphi} = \frac{l}{r}\ddot{\delta} \tag{C.13}$$

Based on Eqs C.7 and C.8, the governing equations for the spiral-shaped settlement trough given in Section 3.2.3 can be rewritten for a semi-circular settlement trough, which are subsequently presented.

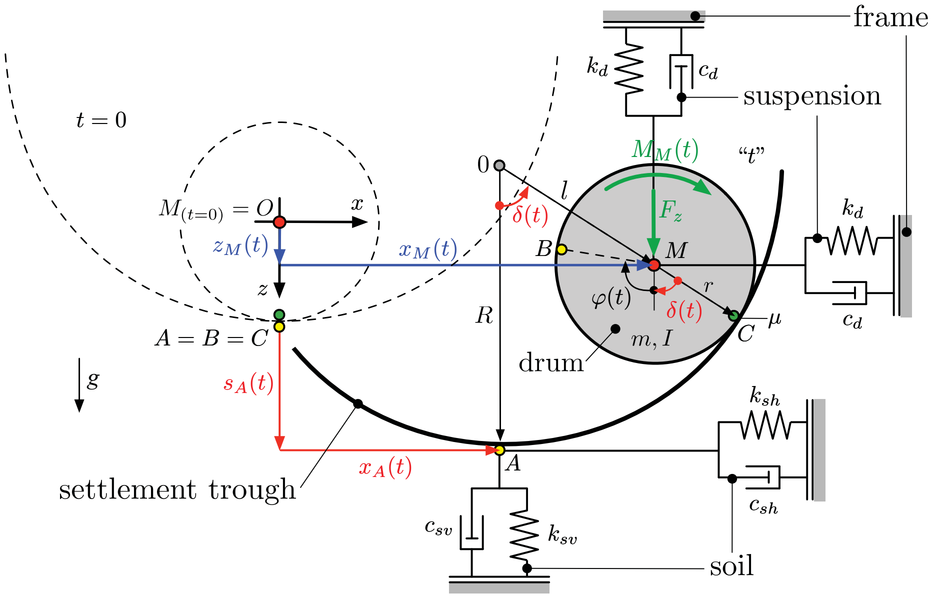
frame
k_d
c_d
suspension
$t = 0$
$M_M(t)$
"t"
0
l
$\delta(t)$
F_z
$M_{(t=0)} = O$
x
$z_M(t)$
$x_M(t)$
B
M
k_d
z
r
$\varphi(t)$
$\delta(t)$
μ
R
C
c_d
$A = B = C$
m, I
drum
g
$s_A(t)$
k_{sh}
$x_A(t)$
A
settlement trough
c_{sh}
c_{sv}
k_{sv}
soil

Figure C1: Lumped parameter model of the interaction system oscillation roller-soil with a semi-circular settlement trough

Stick phase

In the *stick* phase, the equations for the three independent coordinates of motion, i.e. the horizontal (x_A) and the vertical (s_A) displacement of the point A of the curved track and position angle δ (see Fig. C1), read as

$$\begin{aligned} & ml\cos\delta\ddot{\delta} + m\ddot{x}_A - ml\sin\delta\dot{\delta}^2 + c_d l\cos\delta\dot{\delta} + (c_{sh}+c_d)\,\dot{x}_A \\ & \qquad + (k_{sh}+k_d)\,x_A + k_d l\sin\delta = 0 \end{aligned} \tag{C.14}$$

$$\begin{aligned} & -ml\sin\delta\ddot{\delta} + m\ddot{s}_A - ml\cos\delta\dot{\delta}^2 - c_d l\sin\delta\dot{\delta} + (c_{sv}+c_d)\,\dot{s}_A \\ & \qquad + (k_{sv}+k_d)\,s_A + k_d l\,(\cos\delta - 1) = mg + F_z \end{aligned} \tag{C.15}$$

$$\begin{aligned} & \left(1 + \frac{I}{mr^2}\right) ml\ddot{\delta} + m\ddot{x}_A\cos\delta - m\ddot{s}_A\sin\delta + c_d\Big[l\dot{\delta} + \dot{x}_A\cos\delta - \dot{s}_A\sin\delta\Big] \\ & \qquad + k_d\Big[x_A\cos\delta - (s_A - l)\sin\delta\Big] = \frac{M_M(t)}{r} - (mg + F_z)\sin\delta \end{aligned} \tag{C.16}$$

To solve these coupled set of second order nonlinear ordinary differential equations (ODEs), it is written in the state space (see Appendix D.2).

Slip phase

In the *slip* phase, the three equations of motion of the 3DOF lumped parameter model in terms of the four coordinates x_A, s_A, δ and φ read as

$$\begin{aligned} & ml\ddot{\delta} + f_{\mu1}m\ddot{x}_A - f_{\mu2}m\ddot{s}_A + \mathrm{sign}\,(v_{rel})\,\mu ml\dot{\delta}^2 + c_d(l\dot{\delta} + f_{\mu1}\dot{x}_A - f_{\mu2}\dot{s}_A) \\ & \qquad + k_d\Big[-\mathrm{sign}\,(v_{rel})\,\mu l + f_{\mu1}x_A - f_{\mu2}\,(s_A - l)\Big] = -f_{\mu2}(mg + F_z) \end{aligned} \tag{C.17}$$

$$\begin{aligned} & \mathrm{sign}\,(v_{rel})\,\mu m(\ddot{x}_A\sin\delta + \ddot{s}_A\cos\delta) + \frac{I}{r}\ddot{\varphi} - \mathrm{sign}\,(v_{rel})\,\mu\Big\{(mg + F_z)\cos\delta + ml\dot{\delta}^2 \\ & \qquad - c_d\,(\dot{x}_A\sin\delta + \dot{s}_A\cos\delta) - k_d\Big[x_A\sin\delta + s_A\cos\delta + l\,(1 - \cos\delta)\Big]\Big\} = \frac{M_M(t)}{r} \end{aligned} \tag{C.18}$$

$$\begin{aligned} & m\ddot{x}_A\sin\delta + m\ddot{s}_A\cos\delta + (c_{sh}+c_d)\,\dot{x}_A\sin\delta + (c_{sv}+c_d)\,\dot{s}_A\cos\delta - ml\dot{\delta}^2 \\ & \qquad + (k_{sh}+k_d)\,x_A\sin\delta + (k_{sv}+k_d)\,s_A\cos\delta + k_d l\,(1 - \cos\delta) = (mg + F_z)\cos\delta \end{aligned} \tag{C.19}$$

While the angles $\delta(t)$ and $\varphi(t)$ become independent variables in the *slip* phase ($v_{rel} \neq 0$), the variables x_A and s_A are coupled in this phase due to the tangential friction contact according to *Coulomb*'s law at contact point C, yielding a fourth equation,

$$f_{\mu1}\,(c_{sh}\dot{x}_A + k_{sh}x_A) = f_{\mu2}\,(c_{sv}\dot{s}_A + k_{sv}s_A) \tag{C.20}$$

The functions $f_{\mu1}$ and $f_{\mu2}$ in these equations read as,

$$\begin{aligned} f_{\mu1} &= \cos\delta - \mathrm{sign}\,(v_{rel})\,\mu\sin\delta \\ f_{\mu2} &= \sin\delta + \mathrm{sign}\,(v_{rel})\,\mu\cos\delta \end{aligned} \tag{C.21}$$

The state space representation of these nonlinear equations of motion given in Appendix D.2 is solved numerically as described in Section 3.2.4.

C.3 Semi-circular fixed settlement trough

If the horizontal and vertical translation of the settlement trough, i.e. the degrees of freedom of support point A in horizontal (x) and vertical (z) direction, are constrained,

$$x_A = 0 \quad , \quad s_A = 0 \tag{C.22}$$

the 3DOF lumped parameter model presented in Section 2.2 simplifies to a SDOF system. The corresponding model, subsequently referred to as SDOF lumped parameter model with “fixed settlement trough”, is depicted in Fig. C2. In the following, a method is presented to derive efficiently the equation of motion of this SDOF model for the *stick* phase. To this end, in accordance with Williams [2000] the *instant center*, i.e. the contact point between drum and fixed settlement trough (point C), is used as reference point in the *angular momentum theorem* [Ziegler, 1995]. The equation of conservation of angular momentum [Ziegler, 1995] with respect to the contact point C between the rolling drum and the semi-circular bearing surface, i.e. the instant center, reads as

$$\frac{\mathrm{d}\vec{D}_C}{\mathrm{d}t} + m\vec{r}_M \times \vec{a}_C = \vec{M}_C \tag{C.23}$$

where $\vec{D}_C$ denotes the relative angular momentum (or moment of momentum) [Ziegler, 1995] with respect to the contact point C, $\vec{M}_C$ is the moment (with respect to C) of all external forces acting on the rigid drum with mass m,

$$\vec{M}_C = \Big[(mg + F_z) r \sin\delta - M_M(t)\Big] \vec{e}_y \tag{C.24}$$

$\vec{r}_M = \vec{r}_{MC}$ is the position vector representing the position of point M in space in relation to the reference origin C (i.e. the directed line segment from C to M),

$$\vec{r}_M = \vec{r}_{MC} = -r\left(\sin\delta\,\vec{e}_x + \cos\delta\,\vec{e}_z\right) \tag{C.25}$$

and $\vec{a}_C$ denotes the acceleration of point C.

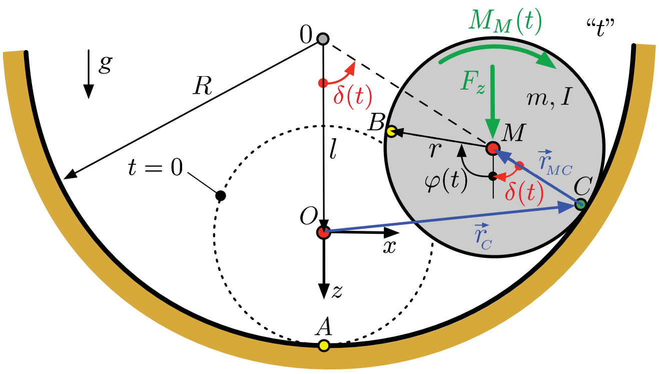

Figure C2: SDOF lumped parameter model of the interaction system oscillation roller-subsoil; pure rolling motion; without suspension; fixed semi-circular settlement trough

The relative angular momentum $\vec{D}_C$ with respect to the contact point C is defined as follows [Ziegler, 1995]:

$$\vec{D}_C = \vec{D}_M + \vec{r}_{MC} \times m\vec{v}_{MC} \tag{C.26}$$

where $\vec{D}_M$ is the relative angular momentum with respect to the drum center M that is determined with the mass moment of inertia I of the drum (with respect to M) and the angular velocity $\dot{\varphi}$ of the drum according to Eq. C.13(1) as follows [Ziegler, 1995]

$$\vec{D}_M = -I\dot{\varphi}\vec{e}_y \tag{C.27}$$

and $\vec{v}_{MC}$ denotes the relative velocity.

When determining the acceleration of point C and the relative velocity $\vec{v}_{MC}$, it is important to distinguish whether C is a point on the drum or a point on the settlement trough [Williams, 2000]. This is illustrated in the following for the example of a drum with radius r rolling without slipping on the inside of a semi-circular bearing surface, i.e. the fixed settlement trough, with radius R.

Contact point C is a point on the drum

The acceleration of point C reads as [Ziegler, 1995]

$$\vec{a}_C = \vec{a}_M + \frac{\mathrm{d}\vec{\omega}}{\mathrm{d}t} \times \vec{r}_{CM} - \omega^2 \vec{r}_{CM} \tag{C.28}$$

where $\vec{a}_M$ is the acceleration of the drum center M,

$$\vec{a}_M = \ddot{x}_M \vec{e}_x + \ddot{z}_M \vec{e}_z \tag{C.29}$$

$\vec{\omega}$ denotes the angular velocity vector,

$$\vec{\omega} = -\dot{\varphi}\vec{e}_y \tag{C.30}$$

and $\vec{r}_{CM}$ is the directed line segment from M to C,

$$\vec{r}_{CM} = -\vec{r}_{MC} = r\left(\sin\delta\vec{e}_x + \cos\delta\vec{e}_z\right) \tag{C.31}$$

Inserting Eq. C.22 into Eq. C.11 yields the acceleration components $\ddot{x}_M$ and $\ddot{z}_M$ for the case of a fixed settlement trough,

$$\ddot{x}_M = l\left(\cos\delta\ddot{\delta} - \sin\delta\dot{\delta}^2\right) \quad , \quad \ddot{z}_M = -l\left(\sin\delta\ddot{\delta} + \cos\delta\dot{\delta}^2\right) \tag{C.32}$$

Inserting Eqs C.29, C.30 and C.31 into Eq. C.28, replacing $\ddot{x}_M$ and $\ddot{z}_M$ by the corresponding expressions according to Eqs C.32 and considering the rolling condition (Eq. C.13) yields after some algebra

$$\vec{a}_C = -\dot{\varphi}^2 r \frac{R}{l}(\sin\delta\vec{e}_x + \cos\delta\vec{e}_z) \tag{C.33}$$

with

$$|\vec{a}_C| = \dot{\varphi}^2 r \frac{R}{l} = R\dot{\varphi}\dot{\delta} \tag{C.34}$$

The relative velocity $\vec{v}_{MC}$ reads as [Ziegler, 1995]

$$\vec{v}_{MC} = \vec{\omega} \times \vec{r}_{MC} \tag{C.35}$$

Inserting Eqs C.30 and C.25 into Eq. C.35 results in

$$\vec{v}_{MC} = r\dot{\varphi}(\cos\delta\vec{e}_x - \sin\delta\vec{e}_z) \tag{C.36}$$

Inserting Eqs C.26 and C.33 into Eq. C.23 and replacing $\vec{D}_M$, $\vec{r}_M$ and $\vec{r}_{MC}$, respectively, and $\vec{v}_{MC}$ by the corresponding expressions according to Eqs C.27, C.25 and C.36, results after some algebra,

$$\vec{D}_C = -(I + mr^2)\dot{\varphi}\vec{e}_y \quad , \quad m\vec{r}_M \times \vec{a}_C = \vec{0} \tag{C.37}$$

in

$$-\left(I + mr^2\right)\ddot{\varphi}\vec{e}_y = \vec{M}_C \tag{C.38}$$

Contact point C is a point on the settlement trough
The acceleration of point C is obtained by double differentiation of the position vector $\vec{r}_C$,

$$\vec{r}_C = R\Big[\sin\delta\vec{e}_x + (\cos\delta - 1)\vec{e}_z\Big] \tag{C.39}$$

with respect to time t,

$$\vec{a}_C = R\Big[(\cos\delta\ddot{\delta} - \sin\delta\dot{\delta}^2)\vec{e}_x - (\sin\delta\ddot{\delta} + \cos\delta\dot{\delta}^2)\vec{e}_z\Big] \tag{C.40}$$

Differentiation of $\vec{r}_{MC}$ (Eq. C.25) with respect to time t yields the relative velocity $\vec{v}_{MC}$

$$\vec{v}_{MC} = -r\dot{\delta}(\cos\delta\vec{e}_x - \sin\delta\vec{e}_z) \tag{C.41}$$

Inserting Eqs C.26 and C.40 into Eq. C.23, replacing $\vec{D}_M$, $\vec{r}_M$ and $\vec{r}_{MC}$, respectively, and $\vec{v}_{MC}$ by the corresponding expressions according to Eqs C.27, C.25 and C.41, and considering the rolling condition (Eq. C.13) results after some algebra

$$\vec{D}_C = -\left(I - m\frac{r^3}{l}\right)\dot{\varphi}\vec{e}_y \quad , \quad m\vec{r}_M \times \vec{a}_C = -m\frac{r^2R}{l}\ddot{\varphi}\vec{e}_y \tag{C.42}$$

in Eq. C.38.

Alternative form of the equation of angular momentum
Inserting Eq. C.26 into Eq. C.23, yields after some algebra an alternative form of the equation of angular momentum:

$$\frac{\mathrm{d}\vec{D}_M}{\mathrm{d}t} + m\vec{r}_{MC} \times \vec{a}_M = \vec{M}_C \tag{C.43}$$

Note, when applying Eq. C.43, the problem of distinguishing point C from being either on the drum or on the settlement trough does not arise. Inserting Eqs C.27 and C.29 into Eq. C.43, replacing $\ddot{x}_M$ and $\ddot{z}_M$ by the corresponding expressions according to Eqs C.32 and $\vec{r}_{MC}$ by the expression according to Eq. C.25, and considering the rolling condition (Eq. C.13) yields after some algebra Eq. C.38.

Equation of motion

To derive the equation of motion, Eqs C.24 and C.13 (rolling condition) are inserted into Eq. C.38. Rearranging finally results in the equation of motion in terms of the position angle $\delta(t)$:

$$\left(1+\frac{I}{mr^2}\right)ml\ddot{\delta}+(mg+F_z)\sin\delta=\frac{M_M(t)}{r} \tag{C.44}$$

APPENDIX D

State-space representation of the equations of motion

D.1 Spiral-shaped settlement trough

Stick phase

The equations of motion for the *stick* phase, Eqs 2.30, 2.31 and 2.32, are rewritten in the state space such that

$$\begin{aligned} q_1 = \delta \quad , \quad q_2 = x_A \quad , \quad q_3 = s_A \\ q_4 = \dot{\delta} \quad , \quad q_5 = \dot{x}_A \quad , \quad q_6 = \dot{s}_A \end{aligned} \tag{D.1}$$

The resulting system of first-order ODEs,

$$\begin{bmatrix} 1 & 0 & 0 & 0 & 0 & 0 \\ 0 & 1 & 0 & 0 & 0 & 0 \\ 0 & 0 & 1 & 0 & 0 & 0 \\ 0 & 0 & 0 & m f_1 & m & 0 \\ 0 & 0 & 0 & m f_3 & 0 & m \\ 0 & 0 & 0 & \left(f_5 \frac{I}{mr} + \tilde{f}_1\right) m & m \cos q_1 & -m \sin q_1 \end{bmatrix} \begin{Bmatrix} \dot{q}_1 \\ \dot{q}_2 \\ \dot{q}_3 \\ \dot{q}_4 \\ \dot{q}_5 \\ \dot{q}_6 \end{Bmatrix} = \begin{Bmatrix} q_4 \\ q_5 \\ q_6 \\ -h_1 \\ mg + F_z - h_2 \\ \frac{M_M(t)}{r} - (mg + F_z) \sin q_1 - h_3 \end{Bmatrix} \tag{D.2}$$

with

$$\begin{aligned} h_1 = {} & f_2 m {q_4}^2 + f_1 c_d q_4 + (c_{sh} + c_d)\, q_5 + (k_{sh} + k_d)\, q_2 \\ & + k_d \Big[-R_0 \exp(-k q_1) \cos(\alpha + q_1) - r \sin q_1 + R_0 \cos\alpha \Big] \end{aligned} \tag{D.3}$$

$$h_2 = f_4 m {q_4}^2 + f_3 c_d q_4 + (c_{sv} + c_d)\, q_6 + (k_{sv} + k_d)\, q_3 \\ + k_d \Big[R_0 \exp(-k q_1) \sin(\alpha + q_1) - r \cos q_1 - (R_0 \sin\alpha - r) \Big] \tag{D.4}$$

$$h_3 = \left(f_6 \frac{I}{mr} + \tilde{f}_2 \right) m {q_4}^2 + c_d \Big[\tilde{f}_1 q_4 + q_5 \cos q_1 - q_6 \sin q_1 \Big] \\ + k_d \Big[\Big(- R_0 \exp(-k q_1) \cos(\alpha + q_1) - r \sin q_1 + R_0 \cos\alpha + q_2 \Big) \cos q_1 \\ - \Big(R_0 \exp(-k q_1) \sin(\alpha + q_1) - r \cos q_1 - (R_0 \sin\alpha - r) + q_3 \Big) \sin q_1 \Big] \tag{D.5}$$

is analyzed numerically by the *ode45* solver of Matlab [Mathworks, 2018]. After having solved Eq. D.2, the response of the drum center ($\ddot{x}_M$, $\ddot{z}_M$), which is of primary interest for the studied CCC indicator, is obtained from Eqs 2.18 with

$$\ddot{\delta} = \frac{M_M(t) + r \Big[h_1 \cos\delta - h_3 + \Big(mg + F_z - h_2 \Big) \sin\delta \Big]}{f_5 I} \tag{D.6}$$

$$\ddot{x}_A = -f_1 \ddot{\delta} - \frac{h_1}{m} \tag{D.7}$$

$$\ddot{s}_A = -f_3 \ddot{\delta} + \frac{1}{m} (mg + F_z - h_2) \tag{D.8}$$

Slip phase

To rewrite the equations of motion for the *slip* phase, Eqs 2.34, 2.36, 2.38, and coupling condition, Eq. 2.39, in the state space, at first the latter equation needs to be differentiated with respect to time and multiplied by m/c_{sh},

$$f_{\mu 1} m \ddot{x}_A - f_{\mu 2} \frac{c_{sv}}{c_{sh}} m \ddot{s}_A + \frac{m}{c_{sh}} \Big\{ f_{\mu 1} \Big[k_{sh} \dot{x}_A - (c_{sv} \dot{s}_A + k_{sv} s_A)\, \dot{\delta} \Big] \\ - f_{\mu 2} \Big[k_{sv} \dot{s}_A + (c_{sh} \dot{x}_A + k_{sh} x_A)\, \dot{\delta} \Big] \Big\} = 0 \tag{D.9}$$

The transformations

$$\begin{aligned} q_1^{(\mathrm{sl})} &= \delta \;,\; & q_2^{(\mathrm{sl})} &= x_A \;,\; & q_3^{(\mathrm{sl})} &= s_A \;,\; & q_4^{(\mathrm{sl})} &= \varphi \\ q_5^{(\mathrm{sl})} &= \dot{\delta} \;,\; & q_6^{(\mathrm{sl})} &= \dot{x}_A \;,\; & q_7^{(\mathrm{sl})} &= \dot{s}_A \;,\; & q_8^{(\mathrm{sl})} &= \dot{\varphi} \end{aligned} \tag{D.10}$$

lead to the first-order ODEs for the *slip* phase,

$$\begin{bmatrix} 1 & 0 & 0 & 0 & 0 & 0 & 0 & 0 \\ 0 & 1 & 0 & 0 & 0 & 0 & 0 & 0 \\ 0 & 0 & 1 & 0 & 0 & 0 & 0 & 0 \\ 0 & 0 & 0 & 1 & 0 & 0 & 0 & 0 \\ 0 & 0 & 0 & 0 & m\,(f_1 f_{\mu 1} - f_3 f_{\mu 2}) & m f_{\mu 1} & -m f_{\mu 2} & 0 \\ 0 & 0 & 0 & 0 & m\tilde{f}_3 & m \sin q_1^{(\mathrm{sl})} & m \cos q_1^{(\mathrm{sl})} & 0 \\ 0 & 0 & 0 & 0 & 0 & m f_{\mu 1} & -\frac{c_{sv}}{c_{sh}} m f_{\mu 2} & 0 \\ 0 & 0 & 0 & 0 & \mathrm{sgn}\mu m \tilde{f}_3 & \mathrm{sgn}\mu m \sin q_1^{(\mathrm{sl})} & \mathrm{sgn}\mu m \cos q_1^{(\mathrm{sl})} & \frac{I}{r} \end{bmatrix} \begin{Bmatrix} \dot{q}_1^{(\mathrm{sl})} \\ \dot{q}_2^{(\mathrm{sl})} \\ \dot{q}_3^{(\mathrm{sl})} \\ \dot{q}_4^{(\mathrm{sl})} \\ \dot{q}_5^{(\mathrm{sl})} \\ \dot{q}_6^{(\mathrm{sl})} \\ \dot{q}_7^{(\mathrm{sl})} \\ \dot{q}_8^{(\mathrm{sl})} \end{Bmatrix} = \begin{Bmatrix} q_5^{(\mathrm{sl})} \\ q_6^{(\mathrm{sl})} \\ q_7^{(\mathrm{sl})} \\ q_8^{(\mathrm{sl})} \\ -f_{\mu 2}\,(mg + F_z) - h_1^{(\mathrm{sl})} \\ (mg + F_z) \cos q_1^{(\mathrm{sl})} - h_3^{(\mathrm{sl})} \\ -h_4^{(\mathrm{sl})} \\ \frac{M_M(t)}{r} - h_2^{(\mathrm{sl})} \end{Bmatrix} \tag{D.11}$$

with

$$\begin{aligned} h_1^{(\mathrm{sl})} = {} & (f_2 f_{\mu 1} - f_4 f_{\mu 2})\, m {q_5^{(\mathrm{sl})}}^2 + c_d \Big[\Big(f_1 f_{\mu 1} - f_3 f_{\mu 2} \Big) q_5^{(\mathrm{sl})} + f_{\mu 1} q_6^{(\mathrm{sl})} - f_{\mu 2} q_7^{(\mathrm{sl})} \Big] \\ & + k_d \Big[f_{\mu 1} \Big(- R_0 \exp(-k q_1^{(\mathrm{sl})}) \cos(\alpha + q_1^{(\mathrm{sl})}) - r \sin q_1^{(\mathrm{sl})} + R_0 \cos\alpha + q_2^{(\mathrm{sl})} \Big) \\ & - f_{\mu 2} \Big(R_0 \exp(-k q_1^{(\mathrm{sl})}) \sin(\alpha + q_1^{(\mathrm{sl})}) - r \cos q_1^{(\mathrm{sl})} - (R_0 \sin\alpha - r) + q_3^{(\mathrm{sl})} \Big) \Big] \end{aligned} \tag{D.12}$$

$$\begin{aligned} {h_2}^{(\mathrm{sl})} = {} & -\mathrm{sgn}\mu \Big\{ (mg + F_z) \cos q_1^{(\mathrm{sl})} - \tilde{f}_4 m {q_5^{(\mathrm{sl})}}^2 - \tilde{f}_3 c_d q_5^{(\mathrm{sl})} \\ & - c_d \Big(q_6^{(\mathrm{sl})} \sin q_1^{(\mathrm{sl})} + q_7^{(\mathrm{sl})} \cos q_1^{(\mathrm{sl})} \Big) - k_d \Big[\Big(- R_0 \exp(-k q_1^{(\mathrm{sl})}) \cos(\alpha + q_1^{(\mathrm{sl})}) \\ & - r \sin q_1^{(\mathrm{sl})} + R_0 \cos\alpha + q_2^{(\mathrm{sl})} \Big) \sin q_1^{(\mathrm{sl})} + \Big(R_0 \exp(-k q_1^{(\mathrm{sl})}) \sin(\alpha + q_1^{(\mathrm{sl})}) \\ & - r \cos q_1^{(\mathrm{sl})} - (R_0 \sin\alpha - r) + q_3^{(\mathrm{sl})} \Big) \cos q_1^{(\mathrm{sl})} \Big] \Big\} \end{aligned} \tag{D.13}$$

$$\begin{aligned} {h_3}^{(\mathrm{sl})} = {} & c_d \tilde{f}_3 q_5^{(\mathrm{sl})} + (c_{sh} + c_d)\, q_6^{(\mathrm{sl})} \sin q_1^{(\mathrm{sl})} + (c_{sv} + c_d)\, q_7^{(\mathrm{sl})} \cos q_1^{(\mathrm{sl})} \\ & + m \tilde{f}_4 {q_5^{(\mathrm{sl})}}^2 + (k_{sh} + k_d)\, q_2^{(\mathrm{sl})} \sin q_1^{(\mathrm{sl})} + (k_{sv} + k_d)\, q_3^{(\mathrm{sl})} \cos q_1^{(\mathrm{sl})} \\ & + k_d \Big[\Big(- R_0 \exp(-k q_1^{(\mathrm{sl})}) \cos(\alpha + q_1^{(\mathrm{sl})}) - r \sin q_1^{(\mathrm{sl})} + R_0 \cos\alpha \Big) \sin q_1^{(\mathrm{sl})} \\ & + \Big(R_0 \exp(-k q_1^{(\mathrm{sl})}) \sin(\alpha + q_1^{(\mathrm{sl})}) - r \cos q_1^{(\mathrm{sl})} - (R_0 \sin\alpha - r) \Big) \cos q_1^{(\mathrm{sl})} \Big] \end{aligned} \tag{D.14}$$

$$\begin{aligned} h_4^{(\mathrm{sl})} = \frac{m}{c_{sh}}\Big\{ & f_{\mu 1}\Big[k_{sh} q_6^{(\mathrm{sl})} - \Big(c_{sv} q_7^{(\mathrm{sl})} + k_{sv} q_3^{(\mathrm{sl})}\Big) q_5^{(\mathrm{sl})}\Big] \\ & - f_{\mu 2}\Big[k_{sv} q_7^{(\mathrm{sl})} + \Big(c_{sh} q_6^{(\mathrm{sl})} + k_{sh} q_2^{(\mathrm{sl})}\Big) q_5^{(\mathrm{sl})}\Big]\Big\} \end{aligned} \tag{D.15}$$

$$\mathrm{sgn} = \mathrm{sign}\left(v_{rel}\right) \tag{D.16}$$

that is solved numerically by the *ode45* solver of Matlab [Mathworks, 2018]. After having solved Eq. D.11, the response of the drum center ($\ddot{x}_M$, $\ddot{z}_M$), is obtained from Eqs 2.18 with

$$\begin{aligned} \ddot{\delta} = \frac{1}{m\Big(f_1 f_{\mu 1} - \frac{c_{sv}}{c_{sh}} f_3 f_{\mu 2}\Big)} \Big\{ & {h_4}^{(\mathrm{sl})} - f_{\mu 1}\Big[{h_1}^{(\mathrm{sl})}\cos\delta + {h_3}^{(\mathrm{sl})} f_{\mu 2}\Big] \\ & - f_{\mu 2}\frac{c_{sv}}{c_{sh}}\Big[mg + F_z + {h_1}^{(\mathrm{sl})}\sin\delta - {h_3}^{(\mathrm{sl})} f_{\mu 1}\Big]\Big\} \end{aligned} \tag{D.17}$$

$$\ddot{x}_A = -f_1\ddot{\delta} - \frac{1}{m}\Big({h_1}^{(\mathrm{sl})}\cos\delta + {h_3}^{(\mathrm{sl})} f_{\mu 2}\Big) \tag{D.18}$$

$$\ddot{s}_A = -f_3\ddot{\delta} + \frac{1}{m}\Big(mg + F_z + {h_1}^{(\mathrm{sl})}\sin\delta - {h_3}^{(\mathrm{sl})} f_{\mu 1}\Big) \tag{D.19}$$

D.2 Semi-circular settlement trough

Stick phase

The equations of motion for the *stick* phase, Eqs C.14, C.15 and C.16, are rewritten in the state space such that

$$\begin{aligned} q_1 = \delta \quad , \quad q_2 = x_A \quad , \quad q_3 = s_A \\ q_4 = \dot{\delta} \quad , \quad q_5 = \dot{x}_A \quad , \quad q_6 = \dot{s}_A \end{aligned} \tag{D.20}$$

The resulting system of first-order ODEs,

$$\begin{aligned} & \begin{bmatrix} 1 & 0 & 0 & 0 & 0 & 0 \\ 0 & 1 & 0 & 0 & 0 & 0 \\ 0 & 0 & 1 & 0 & 0 & 0 \\ 0 & 0 & 0 & ml\cos q_1 & m & 0 \\ 0 & 0 & 0 & -ml\sin q_1 & 0 & m \\ 0 & 0 & 0 & \Big(1+\frac{I}{mr^2}\Big)ml & m\cos q_1 & -m\sin q_1 \end{bmatrix} \begin{Bmatrix} \dot{q}_1 \\ \dot{q}_2 \\ \dot{q}_3 \\ \dot{q}_4 \\ \dot{q}_5 \\ \dot{q}_6 \end{Bmatrix} \\ & = \begin{Bmatrix} q_4 \\ q_5 \\ q_6 \\ -h_1 \\ mg + F_z - h_2 \\ \frac{M_M(t)}{r} - (mg + F_z)\sin q_1 - h_3 \end{Bmatrix} \end{aligned} \tag{D.21}$$

with

$$h_1 \;=\; -ml\sin q_1 q_4^2 \;+\; c_d l\cos q_1 q_4 \;+\; (c_{sh} + c_d)\, q_5 \;+\; (k_{sh} + k_d)\, q_2 \;+\; k_d l\sin q_1 \tag{D.22}$$

$$h_2 = -ml\cos q_1 q_4^2 - c_d l \sin q_1 q_4 + (c_{sv} + c_d)\, q_6 \\ + (k_{sv} + k_d)\, q_3 - k_d l\,(1 - \cos q_1) \quad \text{(D.23)}$$

$$h_3 \quad = \quad c_d\Big[l q_4 \quad + \quad q_5 \cos q_1 \quad - \quad q_6 \sin q_1\Big] \quad + \quad k_d\Big[q_2 \cos q_1 \quad - \quad (q_3 - l)\sin q_1\Big] \quad \text{(D.24)}$$

is analyzed numerically by the *ode45* solver of Matlab [Mathworks, 2018]. After having solved Eq. D.21, the response of the drum center ($\ddot{x}_M$, $\ddot{z}_M$), is obtained from Eqs C.11 with

$$\ddot{\delta} = \frac{M_M(t) + r\Big[h_1 \cos\delta - h_3 + \Big(mg + F_z - h_2\Big)\sin\delta\Big]}{\frac{l}{r} I} \quad \text{(D.25)}$$

$$\ddot{x}_A = -l\cos\delta\ddot{\delta} - \frac{h_1}{m} \quad \text{(D.26)}$$

$$\ddot{s}_A = l\sin\delta\ddot{\delta} + \frac{1}{m}\,(mg + F_z - h_2) \quad \text{(D.27)}$$

Slip phase

To rewrite the equations of motion for the *slip* phase, Eqs C.17, C.18, C.19, and the coupling condition, Eq. C.20, in the state space, at first the latter equation needs to be differentiated with respect to time and multiplied by m/c_{sh},

$$f_{\mu 1} m\ddot{x}_A - f_{\mu 2}\frac{c_{sv}}{c_{sh}} m\ddot{s}_A + \frac{m}{c_{sh}}\Big\{ f_{\mu 1}\left[k_{sh}\dot{x}_A - (c_{sv}\dot{s}_A + k_{sv}s_A)\,\dot{\delta}\right] \\ - f_{\mu 2}\left[k_{sv}\dot{s}_A + (c_{sh}\dot{x}_A + k_{sh}x_A)\,\dot{\delta}\right]\Big\} = 0 \quad \text{(D.28)}$$

Subsequently, the transformations

$$\begin{array}{llll} q_1^{(\mathrm{sl})} = \delta \;, & q_2^{(\mathrm{sl})} = x_A \;, & q_3^{(\mathrm{sl})} = s_A \;, & q_4^{(\mathrm{sl})} = \varphi \\ q_5^{(\mathrm{sl})} = \dot{\delta} \;, & q_6^{(\mathrm{sl})} = \dot{x}_A \;, & q_7^{(\mathrm{sl})} = \dot{s}_A \;, & q_8^{(\mathrm{sl})} = \dot{\varphi} \end{array} \quad \text{(D.29)}$$

lead to the first-order ODEs for the *slip* phase,

$$
\begin{bmatrix}
1 & 0 & 0 & 0 & 0 & 0 & 0 & 0 \\
0 & 1 & 0 & 0 & 0 & 0 & 0 & 0 \\
0 & 0 & 1 & 0 & 0 & 0 & 0 & 0 \\
0 & 0 & 0 & 1 & 0 & 0 & 0 & 0 \\
0 & 0 & 0 & 0 & ml & mf_{\mu 1} & -mf_{\mu 2} & 0 \\
0 & 0 & 0 & 0 & 0 & m\sin q_1^{(\mathrm{sl})} & m\cos q_1^{(\mathrm{sl})} & 0 \\
0 & 0 & 0 & 0 & 0 & mf_{\mu 1} & -\frac{c_{sv}}{c_{sh}} mf_{\mu 2} & 0 \\
0 & 0 & 0 & 0 & 0 & \mathrm{sgn}\mu m\sin q_1^{(\mathrm{sl})} & \mathrm{sgn}\mu m\cos q_1^{(\mathrm{sl})} & \frac{I}{r}
\end{bmatrix}
\left\{\begin{matrix}
\dot{q}_1^{(\mathrm{sl})} \\ \dot{q}_2^{(\mathrm{sl})} \\ \dot{q}_3^{(\mathrm{sl})} \\ \dot{q}_4^{(\mathrm{sl})} \\ \dot{q}_5^{(\mathrm{sl})} \\ \dot{q}_6^{(\mathrm{sl})} \\ \dot{q}_7^{(\mathrm{sl})} \\ \dot{q}_8^{(\mathrm{sl})}
\end{matrix}\right\}
=
\left\{\begin{matrix}
q_5^{(\mathrm{sl})} \\
q_6^{(\mathrm{sl})} \\
q_7^{(\mathrm{sl})} \\
q_8^{(\mathrm{sl})} \\
-f_{\mu 2}\left(mg+F_z\right) - h_1^{(\mathrm{sl})} \\
\left(mg+F_z\right)\cos q_1^{(\mathrm{sl})} - h_3^{(\mathrm{sl})} \\
-h_4^{(\mathrm{sl})} \\
\frac{M_M(t)}{r} - h_2^{(\mathrm{sl})}
\end{matrix}\right\}
\tag{D.30}
$$

with

$$
\begin{aligned}
h_1^{(\mathrm{sl})} = \mathrm{sgn}\mu m l q_5^{(\mathrm{sl})^2} + c_d\left[l q_5^{(\mathrm{sl})} + f_{\mu 1} q_6^{(\mathrm{sl})} - f_{\mu 2} q_7^{(\mathrm{sl})}\right] \\
+ k_d\left[-\mathrm{sgn}\mu l + f_{\mu 1} q_2^{(\mathrm{sl})} - f_{\mu 2}\left(q_3^{(\mathrm{sl})} - l\right)\right]
\end{aligned}
\tag{D.31}
$$

$$
\begin{aligned}
h_2{}^{(\mathrm{sl})} = -\mathrm{sgn}\mu \Big\{ \left(mg+F_z\right)\cos q_1^{(\mathrm{sl})} + m l q_5^{(\mathrm{sl})^2} - c_d\left(q_6^{(\mathrm{sl})}\sin q_1^{(\mathrm{sl})} + q_7^{(\mathrm{sl})}\cos q_1^{(\mathrm{sl})}\right) \\
- k_d\left[q_2^{(\mathrm{sl})}\sin q_1^{(\mathrm{sl})} + q_3^{(\mathrm{sl})}\cos q_1^{(\mathrm{sl})} + l\left(1-\cos q_1^{(\mathrm{sl})}\right)\right]\Big\}
\end{aligned}
\tag{D.32}
$$

$$
\begin{aligned}
h_3{}^{(\mathrm{sl})} = -m l q_5^{(\mathrm{sl})^2} + \left(c_{sh}+c_d\right) q_6^{(\mathrm{sl})}\sin q_1^{(\mathrm{sl})} + \left(c_{sv}+c_d\right) q_7^{(\mathrm{sl})}\cos q_1^{(\mathrm{sl})} \\
+ \left(k_{sh}+k_d\right) q_2^{(\mathrm{sl})}\sin q_1^{(\mathrm{sl})} + \left(k_{sv}+k_d\right) q_3^{(\mathrm{sl})}\cos q_1^{(\mathrm{sl})} + k_d l\left(1-\cos q_1^{(\mathrm{sl})}\right)
\end{aligned}
\tag{D.33}
$$

$$
\begin{aligned}
h_4^{(\mathrm{sl})} = \frac{m}{c_{sh}}\Big\{ f_{\mu 1}\left[k_{sh} q_6^{(\mathrm{sl})} - \left(c_{sv} q_7^{(\mathrm{sl})} + k_{sv} q_3^{(\mathrm{sl})}\right) q_5^{(\mathrm{sl})}\right] \\
- f_{\mu 2}\left[k_{sv} q_7^{(\mathrm{sl})} + \left(c_{sh} q_6^{(\mathrm{sl})} + k_{sh} q_2^{(\mathrm{sl})}\right) q_5^{(\mathrm{sl})}\right]\Big\}
\end{aligned}
\tag{D.34}
$$

$$
\mathrm{sgn} = \mathrm{sign}\left(v_{rel}\right) \tag{D.35}
$$

which are solved numerically by the *ode45* solver of Matlab. After having solved Eq. D.30, the response of the drum center ($\ddot{x}_M$, $\ddot{z}_M$), is obtained from Eqs C.11 with

$$\ddot{\delta} = \frac{1}{ml\Big(\cos\delta f_{\mu 1} + \frac{c_{sv}}{c_{sh}}\sin\delta f_{\mu 2}\Big)}\Big\{h_4{}^{(\mathrm{sl})} - f_{\mu 1}\Big[h_1{}^{(\mathrm{sl})}\cos\delta + h_3{}^{(\mathrm{sl})} f_{\mu 2}\Big] - f_{\mu 2}\frac{c_{sv}}{c_{sh}}\Big[mg + F_z + h_1{}^{(\mathrm{sl})}\sin\delta - h_3{}^{(\mathrm{sl})} f_{\mu 1}\Big]\Big\} \tag{D.36}$$

$$\ddot{x}_A = -l\cos\delta\ddot{\delta} - \frac{1}{m}\Big(h_1{}^{(\mathrm{sl})}\cos\delta + h_3{}^{(\mathrm{sl})} f_{\mu 2}\Big) \tag{D.37}$$

$$\ddot{s}_A = l\sin\delta\ddot{\delta} + \frac{1}{m}\Big(mg + F_z + h_1{}^{(\mathrm{sl})}\sin\delta - h_3{}^{(\mathrm{sl})} f_{\mu 1}\Big) \tag{D.38}$$

Appendix **E**

Lissajous curves

In mathematics, a *Lissajous curve*, also known as *Lissajous figure* or *Bowditch curve* (e.g. [Lawrence, 1972], [Klotter, 1981], [Wikipedia, 2019]), is the pattern that results when two sinusoidal curves,

$$x(t) = x_0 \sin(\omega_x t) \quad , \quad z(t) = z_0 \sin(\omega_z t + \theta_z) \tag{E.1}$$

are plotted against each other, i.e. the plot $z(t)$ versus $x(t)$. Variables x_0 and z_0 are the amplitudes of the sinusoidal curves, ω_x and ω_z denote their corresponding frequencies, and θ_z is the phase difference (phase lag) between these curves. This family of curves was first investigated by Nathaniel *Bowditch* in 1815, and later in much more detail (independently) by Jules-Antoine *Lissajous* in 1857 ([Ferréol, 2017b], [MacTutor History of Mathematics archive, 2019]). The shape of the figure is highly sensitive to the frequency ratio ω_z/ω_x. Visually, the ratio ω_z/ω_x determines the number of “lobes” of the resulting figure [Wikipedia, 2019]. For instance, from a ratio of

$$\frac{\omega_z}{\omega_x} = \frac{2}{1} \tag{E.2}$$

results a figure with two major lobes, as shown in Figs E2, E3 and E4. The amplitude ratio x_0/z_0 determines the ratio of width to height of the curve [Wikipedia, 2019]. For example, a ratio of

$$\frac{x_0}{z_0} = \frac{2}{1} \tag{E.3}$$

produces a figure that is twice as wide ($2z_0$) as it is high (z_0). The value θ_z causes the “rotation” of the curve. Any non-zero θ_z produces a figure that appears to be rotated, either as a left–right or an up–down rotation (depending on the frequency ratio) [Wikipedia, 2019]. The shape of these curves is therefore characteristic of the phase lag and the frequencies of the motion.

$x(t)$ and $z(t)$ according to Eq. E.1 are plotted in Figs E1 to E5 (a) versus time (time histories) and (b) against each other (*Lissajous figure*) for five selected phase lags (θ_z) based on the frequency and amplitude ratio given by Eqs E.2 and E.3. To this end, x_0 and ω_x are assumed as follows:

$$x_0 = 1 \quad , \quad \omega_x = \frac{2\pi}{T_x} = 2\pi\bar{f} = \bar{\nu} \tag{E.4}$$

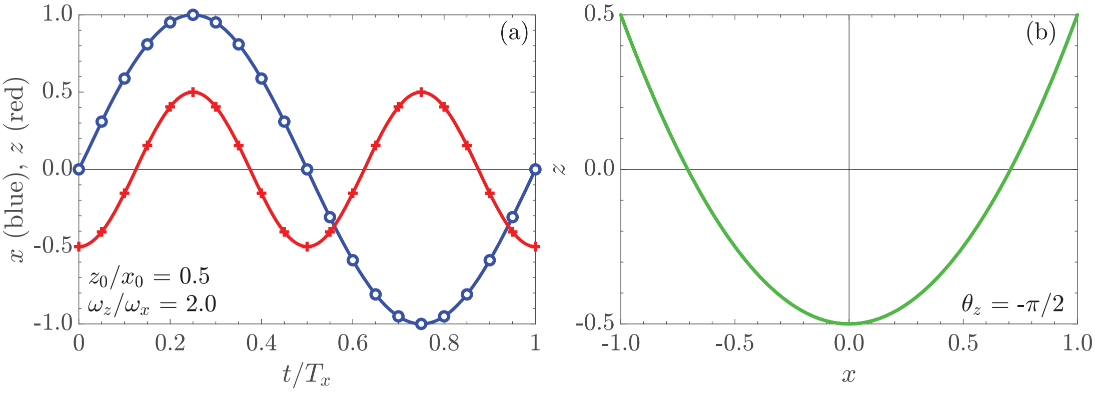

Figure E1: (a) Time history of $x(t)$ and $z(t)$ for a time window of $t = T_x$, and (b) plot $z(t)$ over $x(t)$; $\theta_z = -\pi/2$

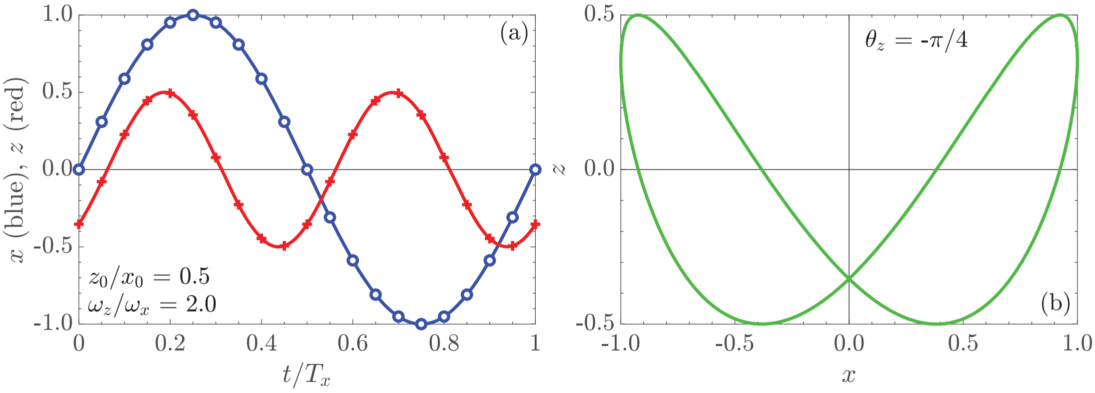

Figure E2: (a) Time history of $x(t)$ and $z(t)$ for a time window of $t = T_x$, and (b) plot $z(t)$ over $x(t)$; $\theta_z = -\pi/4$

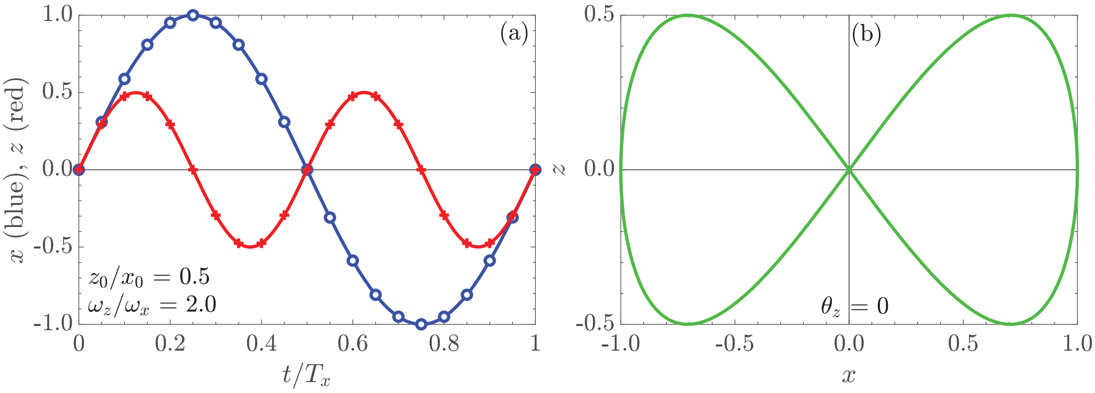

Figure E3: (a) Time history of $x(t)$ and $z(t)$ for a time window of $t = T_x$, and (b) plot $z(t)$ over $x(t)$; $\theta_z = 0$

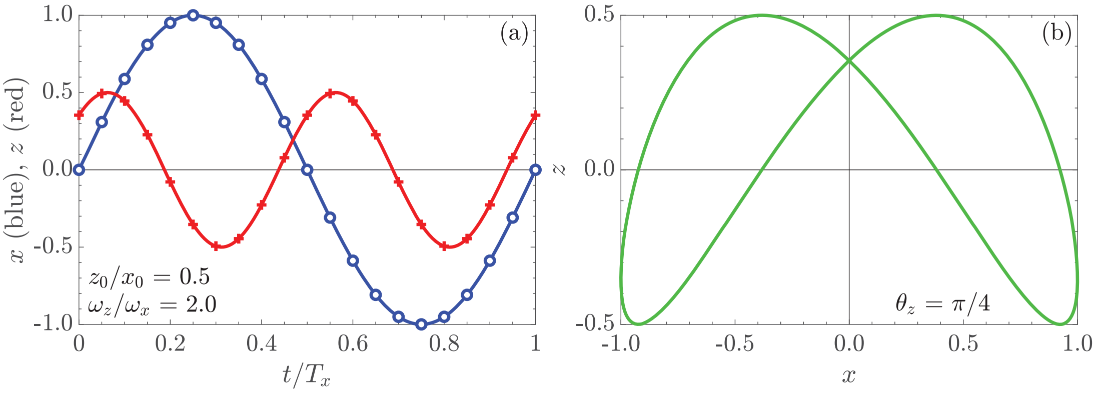

Figure E4: (a) Time history of $x(t)$ and $z(t)$ for a time window of $t = T_x$, and (b) plot $z(t)$ over $x(t)$; $\theta_z = \pi/4$

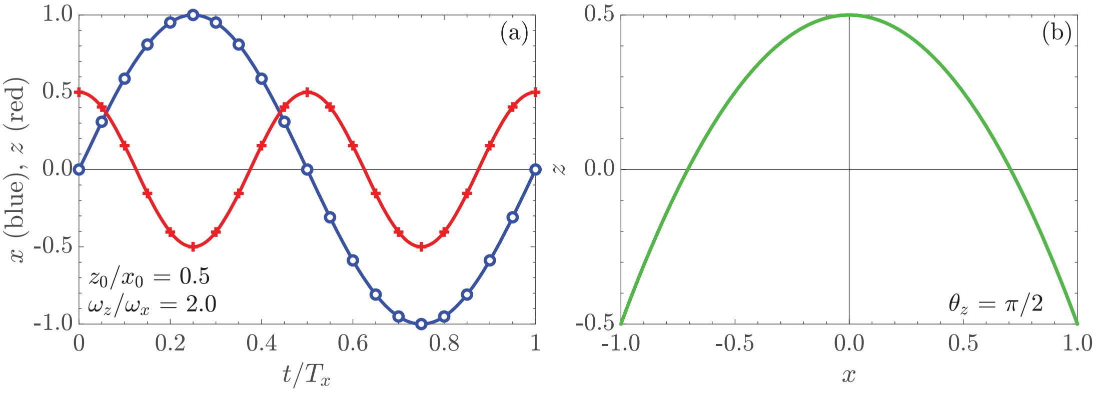

Figure E5: (a) Time history of $x(t)$ and $z(t)$ for a time window of $t = T_x$, and (b) plot $z(t)$ over $x(t)$; $\theta_z = \pi/2$

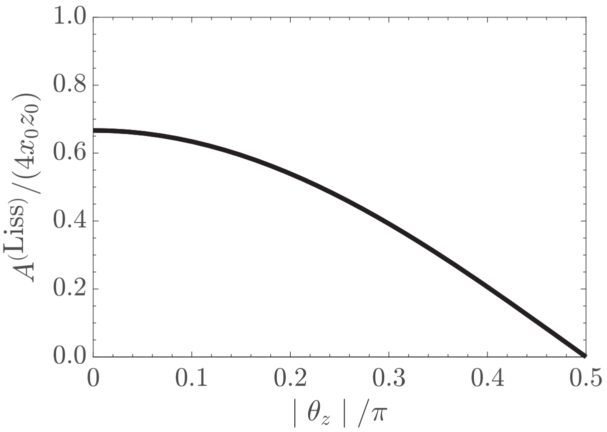

Figure E6: Ratio $A^{(\mathrm{Liss})}/(4x_0z_0)$ in dependence of the phase lag θ_z

Fig. E3 ($\theta_z = 0$) shows a curve that resembles a recumbent figure eight ("lying eight" or *eight curve* [Lawrence, 1972]) or the figure of infinity. With increasing phase lag $\theta_z = 0$, the eight-shaped figure degenerates to a parabola ($\theta_z = \pi/2$) with their vertex at ($x = 0, z = z_0$), see Fig. E5. A study of Figs E2 to E4 reveals that the resultant curve is inscribed in a rectangle of sides $2x_0$ and $2z_0$ [Bajaj, 1988]. The sides of the rectangle are tangential to the *Lissajous curve* at a number of points. The ratio of the numbers of these tangential points along the x-axis to those along the y-axis is the inverse of the ratio of the corresponding frequencies [Bajaj, 1988]. It is also worth mentioning that the area within the curve decreases with increasing or decreasing phase lag $\theta_z = 0$. If $\theta_z = 0$, the resultant curve resembles the aforementioned recumbent figure eight and thus, the area in this figure is maximum. In this case, the area is computed as follows [Nykamp, 2018]:

$$A^{(\mathrm{Liss})} = \frac{2}{3}\,[4x_0 z_0] \quad (\theta_z = 0) \tag{E.5}$$

The area in the *eight curve* illustrated by Fig. E3 is therefore 2/3 of the area in the rectangle of sides $2x_0 = 2$ and $2z_0 = 1$ that encloses the eight-shaped curve, i.e. 4/3. Any non-zero θ_z reduces the ratio $A^{(\mathrm{Liss})}/(4x_0 z_0)$, see Fig. E6. Note that the curve shown in the Fig. E6 can be approximated by the following equation,

$$\frac{A^{(\mathrm{Liss})}}{4x_0 z_0} = 1.858\tilde{\theta}_z^4 + 0.492\tilde{\theta}_z^3 - 3.391\tilde{\theta}_z^2 + 0.007\tilde{\theta}_z + \frac{2}{3} \tag{E.6}$$

where $\tilde{\theta}_z = |\theta_z[\mathrm{rad}]|/\pi$. So to easily compute the area within the *Lissajous curve* resulting from the frequency ratio given by Eq. E.2, only the amplitudes x_0 and z_0, and the phase lag θ_z need to be known.

Appendix **F**

Finite Element model assuming linear elastic soil behavior

The numerical model and the results presented in the following are summarized in paper 3 as discussed in the introduction (Section 1.5).

F.1 Numerical model

To validate the 3DOF lumped parameter model ("LPM"), described in Section 2.2, in *ABAQUS/CAE* a two-dimensional FE model was created that allows the simulation of the response of the drum oscillating in a defined semi-circular notch on the surface of a linear elastic soil halfspace (see Fig. F1). In the contact area between drum and subsoil of this model, a constant coefficient of friction μ is assumed.

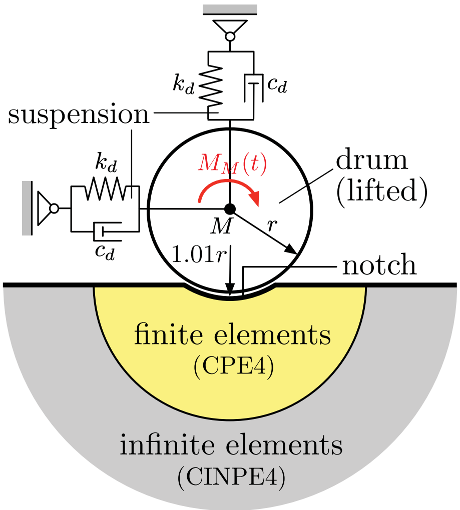
k_d
c_d
suspension
k_d
$M_M(t)$
drum
(lifted)
c_d
M
r
$1.01r$
notch
finite elements
(CPE4)
infinite elements
(CINPE4)

Figure F1: Sketch of the Finite Element model (without mesh)

F.2 Results

The steady state accelerations of the drum center found by the proposed semi-circular 3DOF LPM (see Appendix C.2) are compared both with selected drum accelerations recorded during in situ field tests (4th pass with a HAMM HD$^+$ 90 VO tandem roller on gravel, based on [Pistrol, 2016]) and with outcomes of the linear elastic FE model shown in Fig. F1.

In particular, the frequency content of the drum accelerations $\ddot{x}_M$ and $\ddot{z}_M$ is set in contrast (see Fig. F2 (a) and (b) respectively). The computed drum responses of the 3DOF LPM and the FE model are in good agreement if the contact length resulting from the FE simulations is used when calculating the parameters of the spring-dashpot damper elements, which describe the elastic soil halfspace according to Section 2.2.2 ("LPM-1"). When dividing the damping coefficients c_{sh} and c_{sv} by the factor of two ("LPM-2"), the vertical responses match even better. The amplitudes of the computed accelerations $\ddot{x}_M$ are slightly larger than the ones of the measured response, except at the second harmonic, where the corresponding overtone is overestimated by both the analytical and FE model (see Fig. F2 (a)). In contrast, the amplitudes of the computed accelerations $\ddot{z}_M$ are smaller than the ones of the recorded accelerations (see Fig. F2 (b)). The larger the damping coefficients c_{sh} and c_{sv} are, the better is the prediction of the overtone at the second harmonic (compare "LPM-1" and "LPM-2" in Fig. F2 (b)). The difference between the computed and the measured drum response is mainly due to the fact that in the recorded response the transition from stick to slip phases and vice versa is smoother than in the analytical and numerical model, and consequently, the "peak cut" of the drum accelerations is less pronounced. However, the analytical model is capable of predicting the overall response behavior observed in the field.

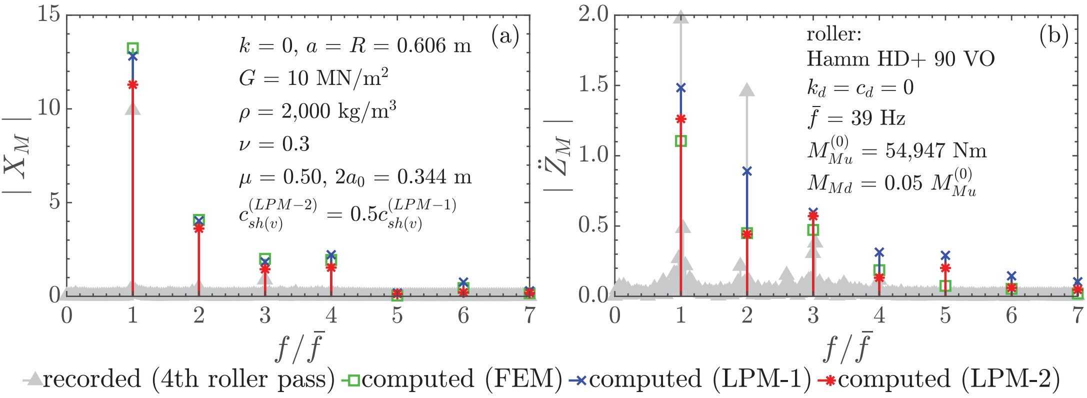

Figure F2: Frequency spectrum of the (a) horizontal and (b) vertical acceleration in the drum center; computed vs. recorded accelerations

Appendix G

Hypoplastic constitutive model

G.1 Basic hypoplastic constitutive model

The notion of *hypoplasticity* has been introduced by Kolymbas [1991], but the ideas behind this constitutive model are much older. Starting in the 1970's (e.g. [Gudehus and Kolymbas, 1979], [Kolymbas, 1978]), hypoplastic rate constitutive equations were developed focusing on granular materials such as sands or gravels with applications in soil mechanics (e.g. [Bauer, 1996], [Gudehus, 1996], [Niemunis and Herle, 1997], [von Wolffersdorff, 1996]). The hypoplastic constitutive model considered in the present paper was developed at the University of Karlsruhe, i.e. the so-called *Karlsruhe hypoplasticity.*

In the following brief summary of this constitutive model, the common sign convention of solid mechanics (compression negative) is adopted throughout. In line with the *Terzaghi principle of effective stress*, all stresses are effective stresses. Tensors of second order are denoted by bold letters (e.g. $\mathbf{T}$, $\mathbf{D}$), and fourth order tensors by calligraphic letters (e.g. $\mathcal{L}$, $\mathcal{M}$). Different types of tensorial multiplication are used: $\mathbf{T}:\mathbf{D}=T_{ij}D_{ij}$, $\mathcal{L}:\mathbf{D}=L_{ijkl}D_{kl}$, $\mathbf{T}\cdot\mathbf{D}=T_{ij}D_{jk}$.

In the hypoplastic constitutive relations the objective (Jaumann) co-rotational stress rate tensor $\mathring{\mathbf{T}}$ is determined by the Cauchy skeleton (effective) stress tensor $\mathbf{T}$, the strain rate (Eulerian stretching) tensor $\mathbf{D}$, and the void ratio in the considered granular material e according to

$$\mathring{\mathbf{T}}=\mathbf{h}(\mathbf{T},\mathbf{D},e) \tag{G.1}$$

where $\mathbf{h}$ is a nonlinear tensor-valued function of $\mathbf{T}$, $\mathbf{D}$ and e, based on the representation theorem for isotropic tensor functions. The function $\mathbf{h}$ is incrementally non-linear in $\mathbf{D}$ to capture the stiffness change in loading and unloading cycles [Fellin and Ostermann, 2002]. Since the behavior of the granular material is assumed to be time independent, basic hypoplastic laws are time-scale invariant Thus, $\mathbf{h}$ is positively homogeneous of the first degree in $\mathbf{D}$ [Fellin and Ostermann, 2002]. Furthermore, $\mathbf{h}$ is homogeneous in $\mathbf{T}$ in order to obtain proportional stress-paths in case of proportional strain-paths [Fellin and Ostermann, 2002]. Eq. G.1 defines the objective (frame-indifferent) velocity, i.e. the velocity perceived by a co-rotated observer, whose change is linked to change of the stress tensor $\mathbf{T}$, i.e. the so-called "co-rotated stress rate tensor" $\mathring{\mathbf{T}}$) [Kelm, 2004] or *Zaremba-Jaumann rate of Cauchy stress* ([Kolymbas, 1991], [Aubram, 2017]).

Note, hypoplastic models use equations of the so-called *rate type*, i.e. incremental or evolution equations, but the material behavior to be described by Eq. G.1 is considered to be rate-independent and, thus, the lack of argotropy is expressed by the fact that the Jaumann rate of Cauchy stress is positively homogeneous of the first degree in $\mathbf{D}$ (Kolymbas [1991], Xu et al [2016]).

The hypoplastic constitutive model proposed by von Wolffersdorff [1996] (subsequently referred to a “basic hypoplastic model”), i.e. the synthesis of the research work carried out in Karlsruhe on this subject, can be expressed through the tensor function

$$\mathring{\mathbf{T}} = f_b f_e \frac{1}{\mathrm{tr}(\hat{\mathbf{T}} \cdot \hat{\mathbf{T}})} \left[F^2 \mathbf{D} + a^2 \hat{\mathbf{T}} \mathrm{tr}(\hat{\mathbf{T}} \cdot \mathbf{D}) + f_d a F (\hat{\mathbf{T}} + \hat{\mathbf{T}}^*) \|\mathbf{D}\| \right] \tag{G.2}$$

and

$$\mathring{\mathbf{T}} = \mathcal{L}(\mathbf{T}, e) : \mathbf{D} + \mathbf{N}(\mathbf{T}, e) \|\mathbf{D}\| \tag{G.3}$$

respectively. The latter represents the hypoplastic equation in its general form. The term $\mathcal{L}(\mathbf{T}, e) : \mathbf{D}$ in Eq. G.3 is linear both in $\mathbf{T}$ and in $\mathbf{D}$ [Kelm, 2004] and equivalent to elasticity producing elliptical response envelope [Mašín, 2019b]. The term $\mathbf{N}(\mathbf{T}, e)\|\mathbf{D}\|$ is linear in $\mathbf{T}$ and nonlinear in $\mathbf{D}$ [Kelm, 2004] and causes translation of the center of the response envelope [Mašín, 2019b]. The linear stiffness tensor of fourth order $\mathcal{L}$ and the nonlinear stiffness tensor of second order $\mathbf{N}$ are calculated as follows:

$$\mathcal{L} := f_b f_e \frac{1}{\mathrm{tr}(\hat{\mathbf{T}} \cdot \hat{\mathbf{T}})} (F^2 \mathcal{I} + a^2 \hat{\mathbf{T}} \hat{\mathbf{T}}) \tag{G.4}$$

$$\mathbf{N} := f_d f_b f_e \frac{F a}{\mathrm{tr}(\hat{\mathbf{T}} \cdot \hat{\mathbf{T}})} (\hat{\mathbf{T}} + \hat{\mathbf{T}}^*) \tag{G.5}$$

The used stress variables, i.e. the non-dimensional stress tensor $\hat{\mathbf{T}}$ and its deviator $\hat{\mathbf{T}}^*$, are defined as follows,

$$\hat{\mathbf{T}} := \frac{\mathbf{T}}{\mathrm{tr}(\mathbf{T})} \quad , \quad \hat{\mathbf{T}}^* := \hat{\mathbf{T}} - \frac{1}{3}\mathbf{I} \tag{G.6}$$

$\mathcal{I}$ is a fourth order unity tensor with components $\mathcal{I}_{ijkl} = \frac{1}{2}(1_{ik}1_{jl} + 1_{il}1_{jk})$. The influence of the mean pressure $p_s = -\mathrm{tr}(\hat{\mathbf{T}})/3$ (barotropy) and void ratio e are considered in the hypoplastic model through three scalar parameters, i.e. the barotropy factor f_b,

$$f_b := \frac{h_s}{n} \left(\frac{e_{i0}}{e_{c0}} \right)^{\beta} \frac{1 + e_i}{e_i} \left(\frac{3 p_s}{h_s} \right)^{1-n} \left[3 + a^2 - a\sqrt{3} \left(\frac{e_{i0} - e_{d0}}{e_{c0} - e_{d0}} \right)^{\alpha} \right]^{-1} \tag{G.7}$$

and the pyknotropy factors f_d and f_e,

$$f_d := \left(\frac{e - e_d}{e_c - e_d} \right)^{\alpha} \quad , \quad f_e := \left(\frac{e_c}{e} \right)^{\beta} \tag{G.8}$$

where e_d is the void ratio for densest packing, e_c the critical void ratio, and e_i the void ratio for loosest packing (for zero mean pressure the corresponding values are denoted by e_{d0}, e_{c0} and e_{i0}). Variable h_s denotes the granular hardness (dimension of stress), the exponent n is a constant ($0.18\ (0.30) < n < 0.50$ [Mašín, 2019b]([Gudehus, 1996])), the parameter α controls the dependency of the peak friction angle on the relative void ratio $\frac{e-e_d}{e_c-e_d}$ ($0 < \alpha < 1$ [Bauer, 1996]), the parameter β controls the increase of stiffness

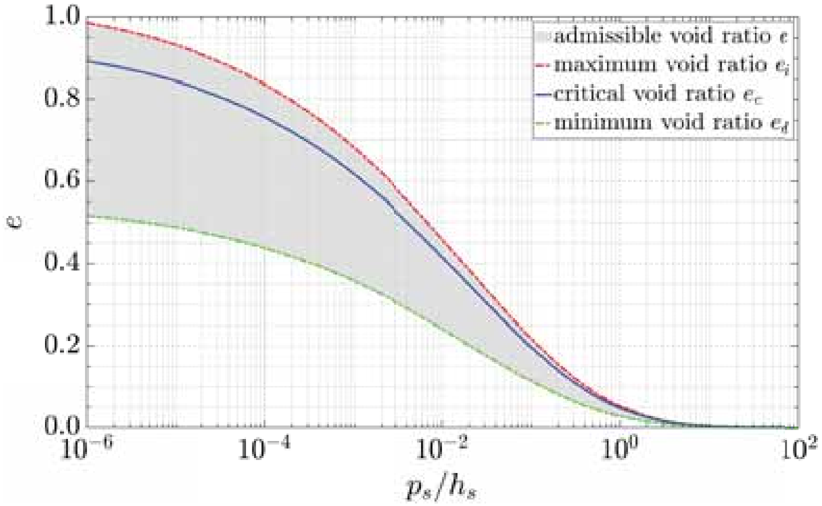

Figure G1: Pressure dependence of void ratios, based on ([Bauer, 1996], [Gudehus, 1996])

with increasing relative density ($1 < \beta < 1.1$ (4) [Gudehus, 1996]([Mašín, 2019b])), and a is a parameter that depends on the critical state friction angle φ_c according to

$$a := \frac{\sqrt{3}(3-\sin\varphi_c)}{2\sqrt{2}\sin\varphi_c} \tag{G.9}$$

With increasing mean pressure p_s a decrease of the characteristic void ratios (maximum (e_i), minimum (e_d) and critical (e_c) void ratio) of a granular material is observed (see Fig. G1) that is described by Bauer [1996] using the following compression law

$$e_i = e_{i0}\exp\left[-\left(\frac{3p_s}{h_s}\right)^n\right] \tag{G.10}$$

where the void ratio e_i is considered as an upper bound for a given mean pressure p_s, as shown in Fig. G1.

Gudehus [1996] postulated that the pressure dependence of e_c and e_d is related to that one for e_i,

$$\frac{e_c}{e_i} = \frac{e_{c0}}{e_{i0}} \quad , \quad \frac{e_d}{e_i} = \frac{e_{d0}}{e_{i0}} \quad , \tag{G.11}$$

The factor F for adapting the failure criterion of Matsuoka–Nakai in the deviator plan is given by

$$F := \sqrt{\frac{1}{8}\tan^2\psi + \frac{2-\tan^2\psi}{2+\sqrt{2}\tan\psi\cos 3\theta}} - \frac{1}{2\sqrt{(2)}}\tan\psi \tag{G.12}$$

with

$$\tan\psi := \sqrt{3}\|\hat{\mathbf{T}}^*\| \tag{G.13}$$

and

$$\cos 3\theta := -\sqrt{6}\frac{\operatorname{tr}(\hat{\mathbf{T}}^*\cdot\hat{\mathbf{T}}^*\cdot\hat{\mathbf{T}}^*)}{[\hat{\mathbf{T}}^*:\hat{\mathbf{T}}^*]^{3/2}} \tag{G.14}$$

With the assumed incompressibility of the grains and constant soil mass, respectively, the evolution of the void ratio e can be described by ([Gudehus, 1981], [Gudehus, 1996], [Fellin et al, 2009])

$$\dot{e} := (1+e)\mathrm{tr}(\mathbf{D}) \tag{G.15}$$

In summary, the basic approach for the hypoplastic constitutive model requires eight parameters: the critical state friction angle φ_c, the granular hardness h_s, the exponent n controlling the shape of the limiting void ratio curves, the reference void ratios e_{i0}, e_{c0} and e_{d0} specifying positions of the limiting void ratio curves, the exponent α controlling the dependency of peak friction angle on relative density, and the exponent β controlling the dependency of soil stiffness on relative density.

G.2 Extended hypoplastic constitutive model

The here used extended version of hypoplasticity with intergranular strain was proposed by Niemunis and Herle [1997]. In this version, the general stress–strain relation is expressed through the following tensor function,

$$\mathring{\mathbf{T}} = \mathcal{M}(\mathbf{T}, \boldsymbol{\delta}, e) : \mathbf{D} \tag{G.16}$$

where $\mathcal{M}$ is the fourth order stiffness tensor of the material (material tangent tensor) that is calculated from the hypoplastic tensors $\mathcal{L}(\mathbf{T}, e)$ and $\mathbf{N}(\mathbf{T}, e)$, and the new state variable intergranular strain $\boldsymbol{\delta}$, which is a strain-like tensor, using the following interpolation function

$$\mathcal{M} := [\rho^{\chi} m_T + (1-\rho^{\chi}) m_R]\mathcal{L} + \begin{cases} \rho^{\chi}(1-m_T)\mathcal{L} : \hat{\boldsymbol{\delta}}\hat{\boldsymbol{\delta}} + \rho^{\chi}\mathbf{N}\hat{\boldsymbol{\delta}} & \hat{\boldsymbol{\delta}} : \mathbf{D} > 0 \\ \rho^{\chi}(m_R - m_T)\mathcal{L} : \hat{\boldsymbol{\delta}}\hat{\boldsymbol{\delta}} & \hat{\boldsymbol{\delta}} : \mathbf{D} \leq 0 \end{cases} \tag{G.17}$$

Parameter m_R controls the magnitude of the very small strain shear modulus in the initial loading, and upon a 180° change in direction of strain path, the parameter m_T controls the initial shear modulus upon 90° strain path reversal and the exponent χ controls the interpolation between the reversible elastic response and nonlinear hypoplastic response [Mašín, 2019b].

In Eq. G.17

$$\rho := \|\boldsymbol{\delta}\| / R \tag{G.18}$$

denotes the normalized length of the intergranular strain with the radius of the elastic strain range R (in the strain space) as maximum value. According to this formulation, the intergranular strain is fully mobilized for $\rho = 1$, and no intergranular strain occurs when $\rho = 0$. The direction of the intergranular strain $\hat{\boldsymbol{\delta}}$ can be calculated as follows,

$$\hat{\boldsymbol{\delta}} := \begin{cases} \boldsymbol{\delta} / \|\boldsymbol{\delta}\| & \boldsymbol{\delta} \neq 0 \\ 0 & \boldsymbol{\delta} = 0 \end{cases} \tag{G.19}$$

The evolution equation for the intergranular strain tensor $\mathring{\boldsymbol{\delta}}$ reads as,

$$\mathring{\boldsymbol{\delta}} = \begin{cases} (\mathcal{I} - \hat{\boldsymbol{\delta}}\hat{\boldsymbol{\delta}}\rho^{\beta_r}) : \mathbf{D} & \hat{\boldsymbol{\delta}} : \mathbf{D} > 0 \\ \mathbf{D} & \hat{\boldsymbol{\delta}} : \mathbf{D} \leq 0 \end{cases} \tag{G.20}$$

where the exponent β_r is a model parameter controlling the rate of the intergranular strain evolution, and consequently, the stiffness degradation curve [Mašín, 2019b] and $\mathcal{I}$ is a fourth order unity tensor.

For the one-dimensional case, Eq. G.20 can be interpreted as follows [Kelm, 2004]: If $\hat{\boldsymbol{\delta}} : \mathbf{D} > 0$, a gradual transition from elastic, intergranular deformation (deformation between the grains) to plastic deformation (contact displacements, i.e. the (hypo-)plastic strains) takes place. If $\hat{\boldsymbol{\delta}} : \mathbf{D} \leq 0$, the deformations are purely elastic. Consequently, after each change in direction of strain path, the material responds first elastically and then gradually plastically again.

In summary, the extended hypoplastic constitutive model [Niemunis and Herle, 1997] requires five additional parameters, i.e. R, m_R, m_T, β_r, and χ.

APPENDIX **H**

UMAT for the extended hypoplastic constitutive model

Here, the basics of the user defined material subroutine, the so-called UMAT, for the extended hypoplastic constitutive model used for the numerical investigations presented in Chapter 3, are briefly described. The original UMAT has been developed by Claudio Tamagnini in 2005. It has since been further developed and updated to new models by David Mašín.

The main program (*ABAQUS/Standard*) passes at time t_a the actual Cauchy stress tensor $\Delta\mathbf{T}(t_a)$ and the time increment Δt to the user defined material subroutine (UMAT) that integrates the constitutive equations, i.e. Eqs H.1 and H.2, with a fully given stretching tensor $\mathbf{D} = \frac{\Delta\epsilon}{\Delta t}$ using an error controlled time sub-stepping. The UMAT returns the co-rotational part of the Cauchy stress tensor $\mathbf{T}(t_a) + \mathring{\mathbf{T}}(t_a) \cdot \Delta t$ at the end of the time step and the Jacobian $\frac{\partial \mathbf{T}(t_a+\Delta t)}{\partial \Delta\epsilon} = \frac{\partial \Delta\mathbf{T}}{\partial \Delta\epsilon}$, i.e. the derivative of the stress increment with respect to the strain increment. Based on these informations (updated stress tensor and consistent tangent stiffness), a new estimate for the strain increment is calculated by ABAQUS and the whole procedure is iterated until convergence is reached. Note that displacement driven finite element methods require the so-called consistent (algorithmic) tangent operator, i.e. the Jacobian of the model, for fast convergence [Fellin et al, 2009].

Since ABAQUS handles large strain effects, the objective rates of the state variables are equal to the time rates in the subroutine [Fellin et al, 2009]. Thus, the evolution equations to be solved by the UMAT for $0 \leq t \leq \Delta t$ are [Fellin et al, 2009]

$$\frac{d}{dt}\mathbf{T} = \mathbf{h}(\mathbf{T}, \mathbf{D}, \mathbf{Q}) \ , \ \mathbf{T}(0) = \boldsymbol{\sigma}(t_a) \tag{H.1}$$

$$\frac{d}{dt}\mathbf{Q} = \mathbf{k}(\mathbf{T}, \mathbf{D}, \mathbf{Q}) \ , \ \mathbf{Q}(0) = \boldsymbol{\delta}(t_a) \tag{H.2}$$

The constitutive equation of the rate of the stress tensor $\mathbf{T}$ is given by Eq. G.16. The rate of the additional state variable $\mathbf{Q}$ is defined by Eq. G.20 (b). In [Fellin et al, 2009] the variational equations

$$\frac{d}{dt}\frac{\partial \mathbf{T}}{\partial \mathbf{D}} = \frac{\partial \mathbf{h}}{\partial \mathbf{T}}\frac{\partial \mathbf{T}}{\partial \mathbf{D}} + \frac{\partial \mathbf{h}}{\partial \mathbf{Q}}\frac{\partial \mathbf{Q}}{\partial \mathbf{D}} + \frac{\partial \mathbf{h}}{\partial \mathbf{D}} \ , \ \frac{\partial \mathbf{T}}{\partial \mathbf{D}}(0) = \mathbf{0} \tag{H.3}$$

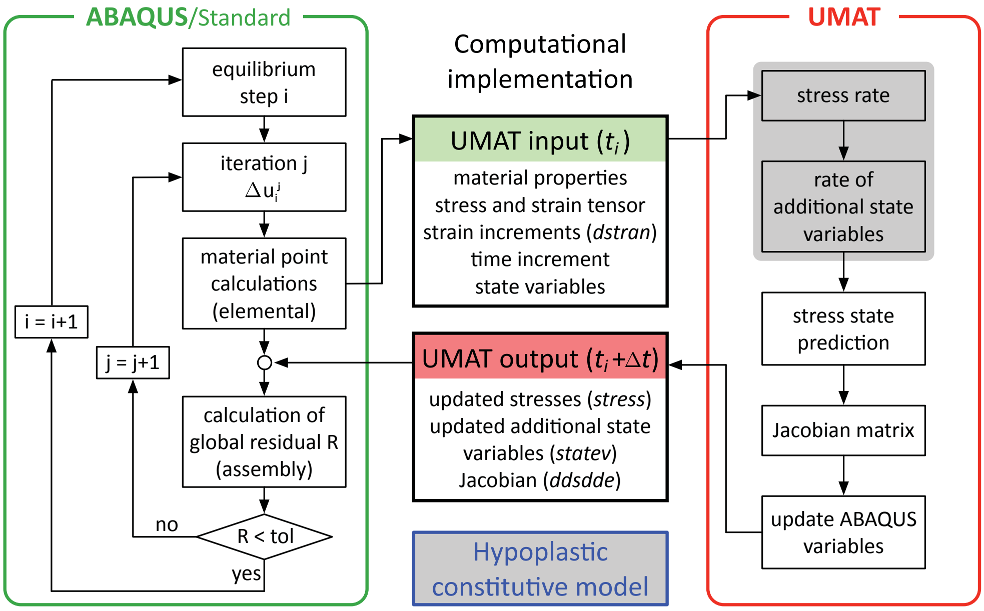
ABAQUS/Standard
equilibrium step i
iteration j Δu_i^j
material point calculations (elemental)
calculation of global residual R (assembly)
R < tol
no
yes
i = i+1
j = j+1
Computational implementation
UMAT input (t_i)
material properties
stress and strain tensor
strain increments (dstran)
time increment
state variables
UMAT output (t_i+Δt)
updated stresses (stress)
updated additional state variables (statev)
Jacobian (ddsdde)
Hypoplastic constitutive model
UMAT
stress rate
rate of additional state variables
stress state prediction
Jacobian matrix
update ABAQUS variables

Figure H1: Flow chart for *ABAQUS* and UMAT intergration, based on Ribeiro et al [2013]

$$\frac{d}{dt}\frac{\partial \mathbf{Q}}{\partial \mathbf{D}} = \frac{\partial \mathbf{k}}{\partial \mathbf{T}}\frac{\partial \mathbf{T}}{\partial \mathbf{D}} + \frac{\partial \mathbf{k}}{\partial \mathbf{Q}}\frac{\partial \mathbf{Q}}{\partial \mathbf{D}} + \frac{\partial \mathbf{k}}{\partial \mathbf{D}} \quad , \quad \frac{\partial \mathbf{Q}}{\partial \mathbf{D}}(0) = \mathbf{0} \tag{H.4}$$

are used to find the Jacobian $\frac{\partial \Delta T_{ij}}{\partial \Delta \epsilon_{kl}}$ by implementation with a numerical approximation according to Fellin and Ostermann [2002]. The Jacobian [Fellin and Ostermann, 2002]

$$\frac{\partial \Delta \mathbf{T}}{\partial \Delta \epsilon} = \frac{\partial \mathbf{T}(t_a + \Delta t)}{\partial \Delta \epsilon} = \frac{1}{\Delta t}\frac{\partial \mathbf{T}}{\partial \mathbf{D}}(\Delta t) \tag{H.5}$$

must be precisely known to achieve fast (quadratic) convergence in the Newton-type iteration performed in ABAQUS. In order to obtain the Jacobian, Eqs H.3 and H.4 must be solved simultaneously with Eqs H.1 and H.2. Due to the complicated structure of the constitutive law, the calculation (and implementation) of the expressions appearing on the right-hand side of Eqs H.3 and H.4 are a tedious task [Fellin and Ostermann, 2002]. Thus, Fellin and Ostermann [2002] recommend to replace Eqs H.3 and H.4 by an approximation that is obtained by numerical differentiation.

The explicit adaptive integration scheme with local sub-stepping implemented in the used UMAT [Gudehus et al, 2008] coincides with the Richardson extrapolation of the explicit Euler method in [Fellin et al, 2009]. The nonlinear initial value problem,

$$\frac{d}{dt}\mathbf{y} = f(\mathbf{y}(t)) \quad , \quad \mathbf{y}(0) = \mathbf{y}_0 \tag{H.6}$$

where $\mathbf{y}$ collects the components of $\mathbf{T}$ and $\mathbf{Q}$, respectively, is solved using the Runge-Kutta method estimating the accuracy of the solution according to Fehlberg [1969] and the new time step according to Hull et al [1972]. For the tolerance, a value of 10^{-3} is used in all numerical simulations.

Note that the effective stress $\mathbf{T}$ used in the model formulation of the UMAT is replaced by $\mathbf{T} - \mathbf{1}p_t$. A non-zero value of the apparent cohesion p_t is needed to overcome problems with the stress-free state. If $p_t = 0$, it is replaced by a default value of 1 kPa in the "PLAXIS implementation of HYPOPLASTICITY including standalone ABAQUS *umat* subroutine" [Gudehus et al, 2008]. If $m_R \leq 0$, in the UMAT [Gudehus et al, 2008] the intergranular strain concept is switched off, and the problem is simulated using the basic hypoplastic model.

Appendix I

Numerical modeling

I.1 Finite Element Models

In the framework of the development of the presented numerical model, test runs have been performed based on a model with a linear elastic, isotropic subsoil that is covered by a hypoplastic soil layer. The “layer” is modeled using the hypoplastic constitutive law as described in Section 3.2.7. This model is subsequently referred to as “model A” (see Fig. I1). The layer thicknesses is increased from 0.25 m (“model $A^{(25)}$”) to 1 m (“model $A^{(100)}$”) in steps of 0.25 m to investigate the influence of the assumed linear elastic subsoil. When assuming linear elastic subsoil behavior, a density ρ of $2200\,\mathrm{kg/m^3}$, a *Young*’s modulus E of $250 \times 10^6\,\mathrm{N/m^2}$ and a *Poisson*’s ratio ν of 0.3 have been defined as standard values (see Section 3.2.7).

Modeling both layer and subsoil using the hypoplasticity model according to Section 3.2.7 results in the model shown in Fig. I2. In the very first computations, for the subsoil up to a depth of 1 m the apparent cohesion p_t is assumed to be $5\,\mathrm{kN/m^2}$ while to the soil below a reduced apparent cohesion of $1\,\mathrm{kN/m^2}$ is assigned. Note that the numerical model described in Section 3.2 corresponds to model B with an apparent cohesion p_t being $5\,\mathrm{kN/m^2}$ in the entire soil domain.

The models were refined stepwise in the soil domain of potential compaction during its development. The resulting mesh consists of 11,795 elements (coarse mesh, subsequently referred to as “mesh I”) and 37,569 elements (medium fine mesh, subsequently referred to as “mesh II”), respectively (including the infinite elements). Additionally, convergence studies were performed with an even more refined mesh using a model with 46,326 elements (fine mesh, subsequently referred to as “mesh III”) and a reduced minimum element size of 0.01 m x 0.01 m. The results have shown that the finer meshed model does not improve accuracy and, moreover, increases not only computation time but also the required disk space considerably. Note, the studies presented in Chapter 3 are therefore based on model B with mesh II.

In the following, selected results (compaction effect, soil stresses and drum response) based on the FE models A and B are presented. Computations using the “surface protective measures” described in Section 3.2.8 are indicated by “PF” for protective foil and “SD” for surface dampers.

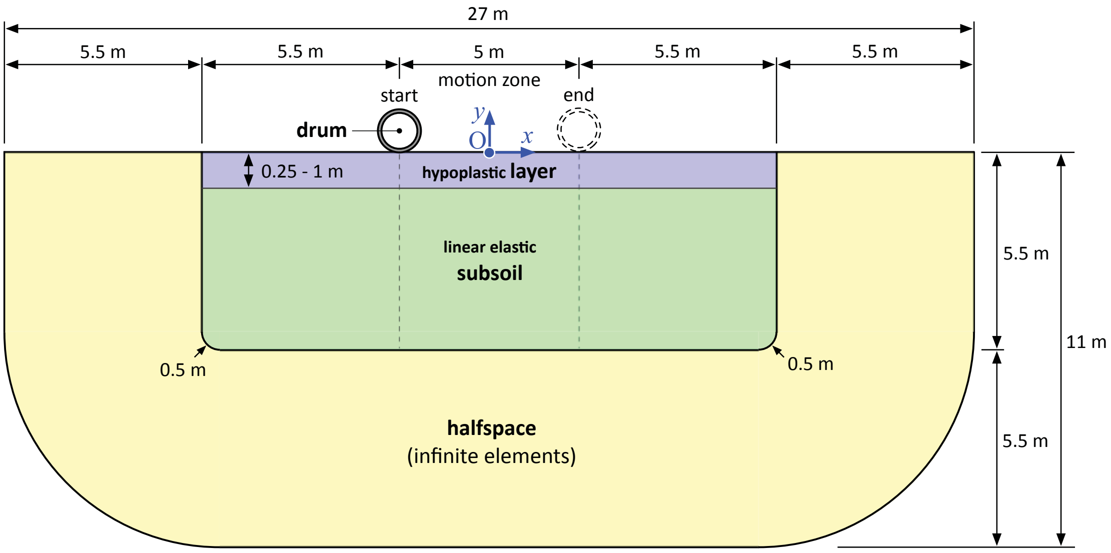
27 m
5.5 m
5.5 m
5 m
5.5 m
5.5 m
motion zone
start
end
drum
y
O
x
0.25 - 1 m
hypoplastic layer
linear elastic
subsoil
0.5 m
0.5 m
halfspace
(infinite elements)
5.5 m
5.5 m
11 m

Figure I1: Sketch of FE “model A” (without mesh, without suspension)

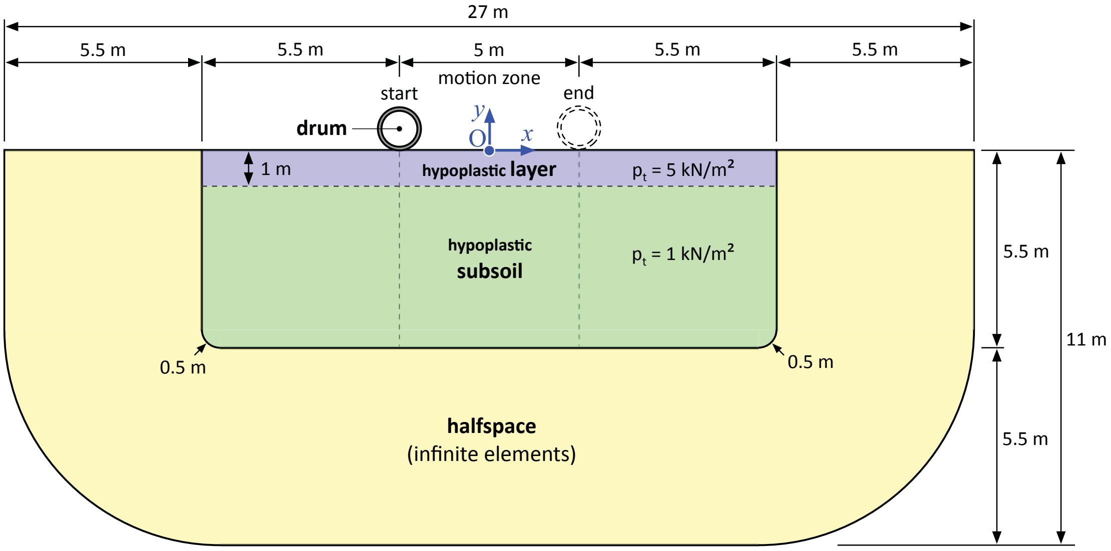
27 m
5.5 m
5.5 m
5 m
5.5 m
5.5 m
motion zone
start
end
drum
y
O
x
1 m
hypoplastic layer
p_t = 5 kN/m²
hypoplastic
subsoil
p_t = 1 kN/m²
0.5 m
0.5 m
halfspace
(infinite elements)
5.5 m
5.5 m
11 m

Figure I2: Sketch of FE “model B” (without mesh, without suspension)

I.2 Results based on “model A” with and without “surface dampers (SD)”

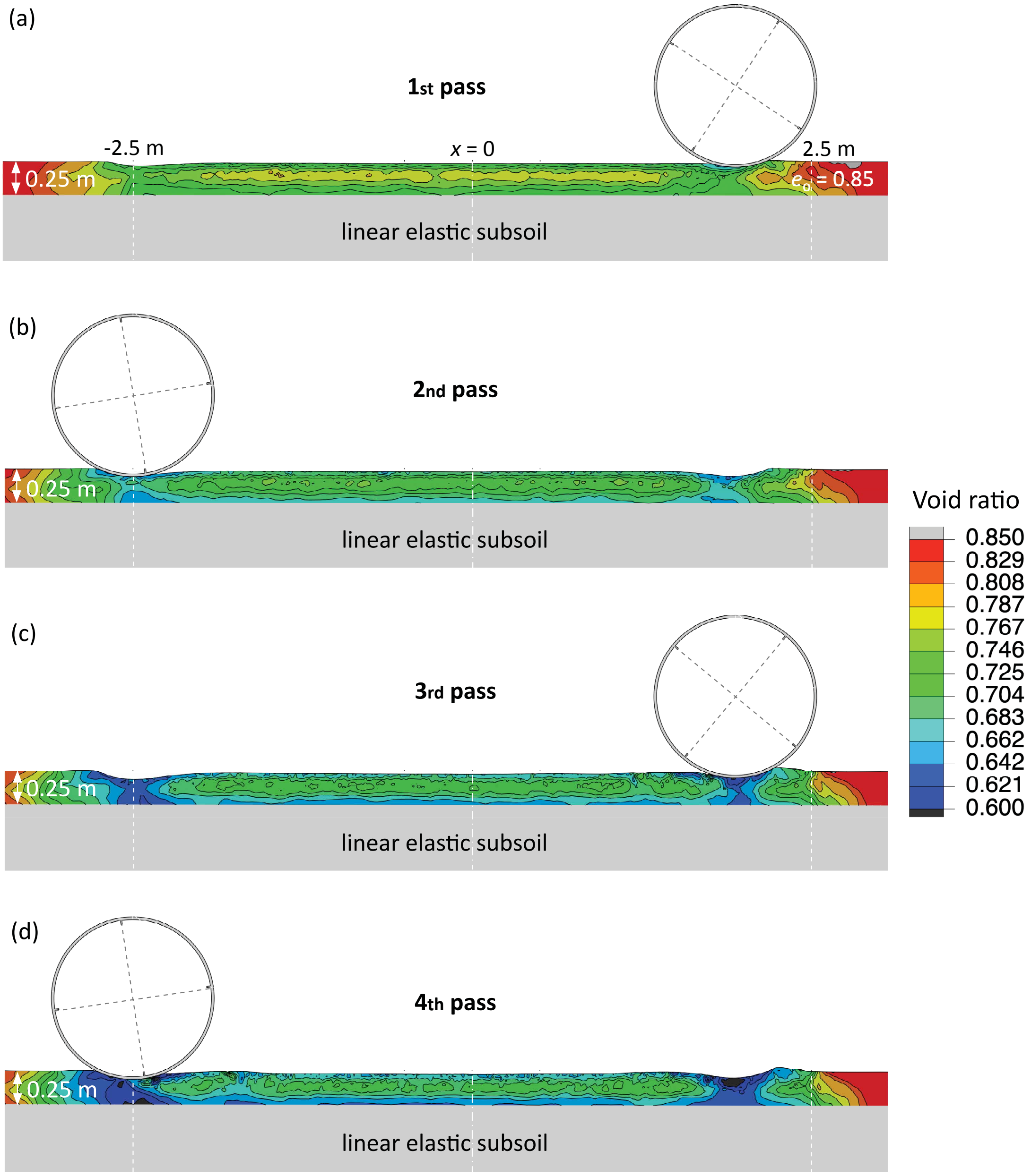

Figure I3: Distribution of void ratio e in the upper soil layer of 0.25 m thickness after the (a) first, (b) second, (c) third and (d) fourth oscillatory roller pass; model $\mathrm{A}^{(25)}$ / mesh I, $e_0 = 0.85$, $\mu = 0.50$, $p_t = 5\,\mathrm{kN/m}^2$, $c_x = c_y = c_{x45} = c_{y45} = 1000\,\mathrm{Ns/m}$

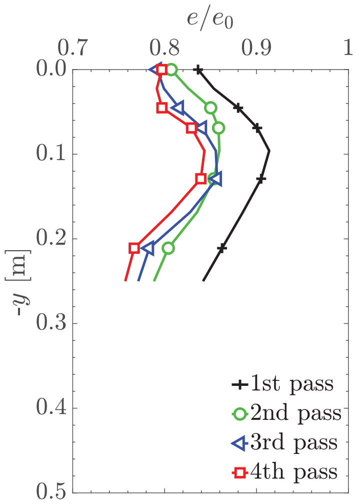

Figure I4: Normalized void ratio profile e/e_0 at $x = 0$, corresponds to Fig. I3

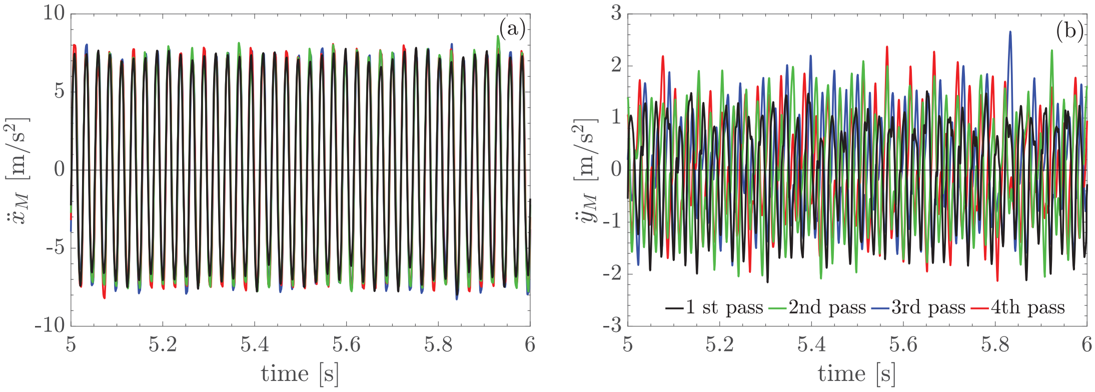

Figure I5: Time history of the (a) horizontal and (b) vertical acceleration in the drum center M during four subsequent oscillatory roller passes; model $A^{(25)}$ / mesh I, $e_0 = 0.85$, $\mu = 0.50$, $p_t = 5\,\mathrm{kN/m^2}$, $c_x = c_y = c_{x45} = c_{y45} = 1000\,\mathrm{Ns/m}$

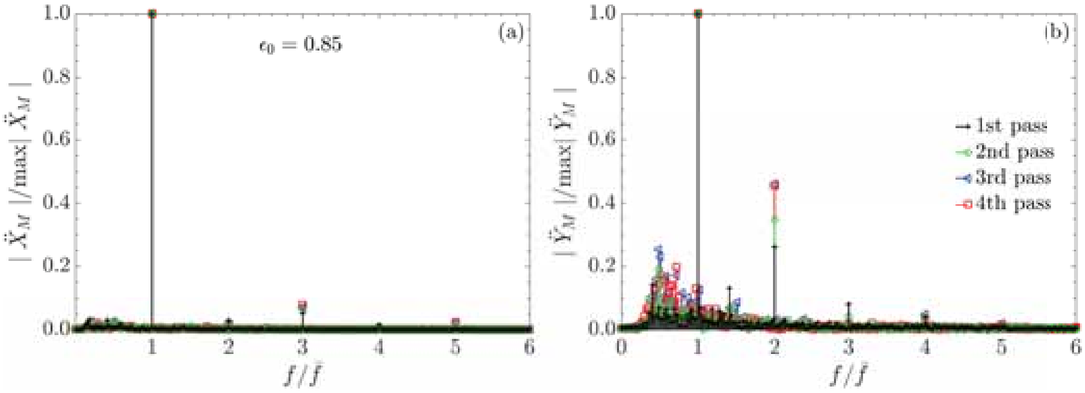

Figure I6: Normalized frequency spectrum of the (a) horizontal and (b) vertical acceleration in the drum center M for one second of the first, second, third, and fourth oscillatory roller pass, based on Fig. I5

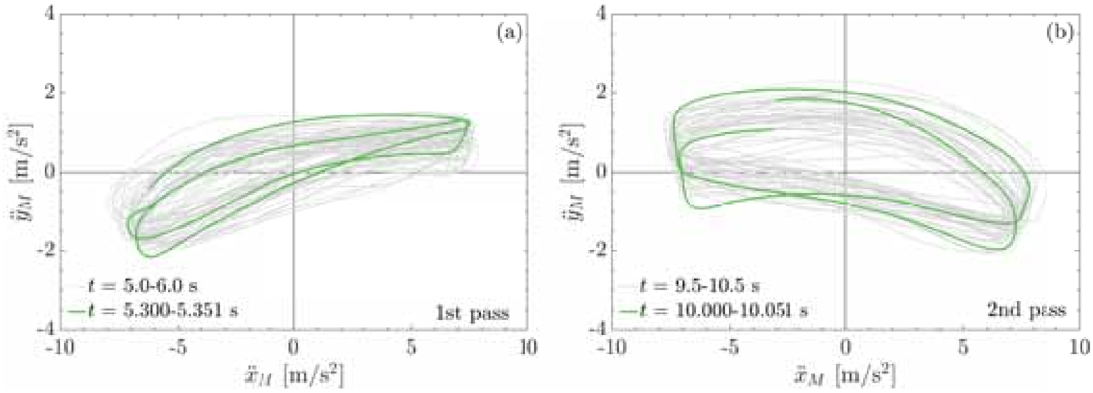

Figure I7: Plot $\ddot{y}_M$ over $\ddot{x}_M$ for a time window of 1 s (grey lines) and two representative oscillating cycles (green lines), based on Fig. I5; (a) first and (b) second roller pass

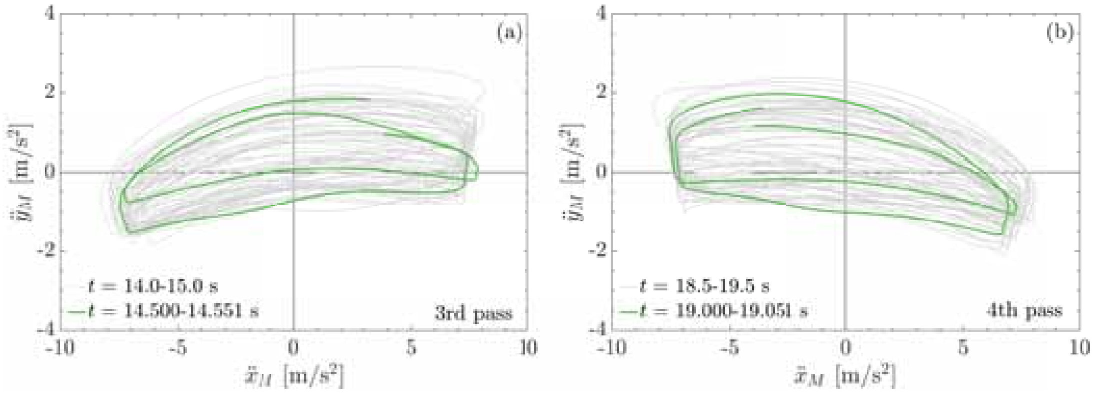

Figure I8: Plot $\ddot{y}_M$ over $\ddot{x}_M$ for a time window of 1 s (grey lines) and two representative oscillating cycles (green lines), based on Fig. I5; (a) third and (b) fourth roller pass

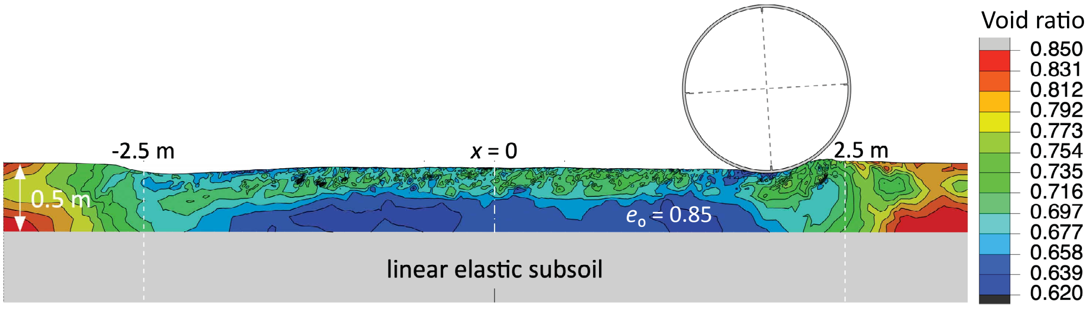
Void ratio
0.850
0.831
0.812
0.792
0.773
0.754
0.735
0.716
0.697
0.677
0.658
0.639
0.620
-2.5 m
x = 0
2.5 m
0.5 m
$e_0 = 0.85$
linear elastic subsoil

Figure I9: Distribution of void ratio e in the upper soil layer of 0.5 m thickness after an oscillatory roller pass; model $A^{(50)}$ / mesh I, $e_0 = 0.85$, $\mu = 0.50$, $p_t = 10\,\mathrm{kN/m^2}$

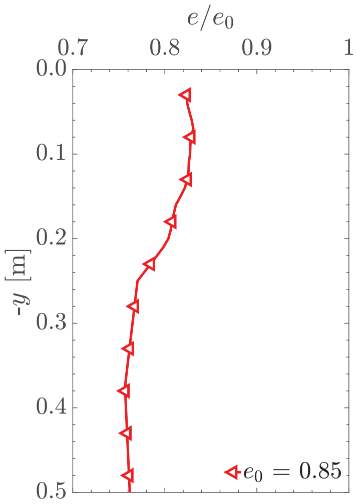

Figure I10: Mean normalized void ratio profile e/e_0 in the soil region $-0.5\,\mathrm{m} \leq x \leq 0.5\,\mathrm{m}$, corresponds to Fig. I9

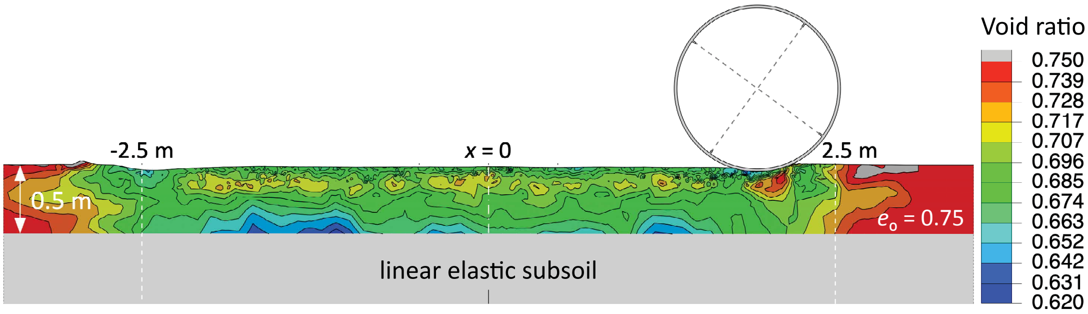

Figure I11: Distribution of void ratio e in the upper soil layer of 0.5 m thickness after an oscillatory roller pass; model A$^{(50)}$ / mesh I / SD, $e_0 = 0.75$, $\mu = 0.50$, $p_t = 5\,\mathrm{kN/m^2}$, $c_x = c_y = c_{x45} = c_{y45} = 1000\,\mathrm{Ns/m}$

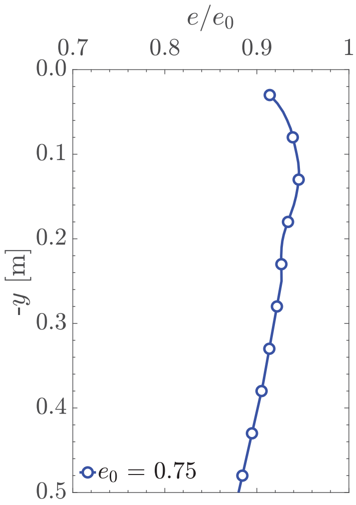

Figure I12: Mean normalized void ratio profile e/e_0 in the soil region $-0.5\,\mathrm{m} \leq x \leq 0.5\,\mathrm{m}$, corresponds to Fig. I11

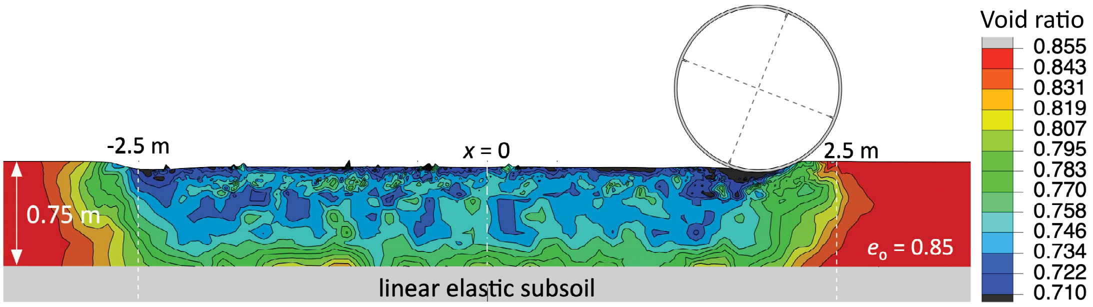

Figure I13: Distribution of void ratio e in the upper soil layer of 0.75 m thickness after an oscillatory roller pass; model $\mathrm{A}^{(75)}$ / mesh I / SD, $e_0 = 0.85$, $\mu = 0.50$, $p_t = 5\,\mathrm{kN/m^2}$, $c_x = c_y = 2500\,\mathrm{Ns/m}$

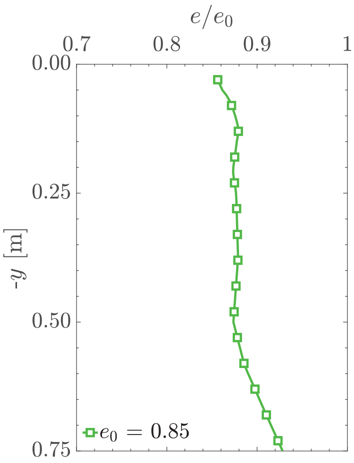

Figure I14: Mean normalized void ratio profile e/e_0 in the soil region $-0.5\,\mathrm{m} \leq x \leq 0.5\,\mathrm{m}$, corresponds to Fig. I13

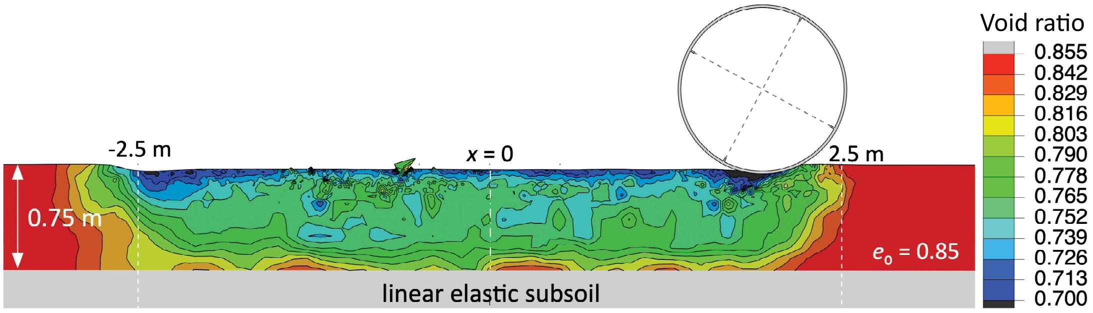

Figure I15: Distribution of void ratio e in the upper soil layer of 0.75 m thickness after an oscillatory roller pass; model $\mathrm{A}^{(75)}$ / mesh I / SD, $e_0 = 0.85$, $\mu = 0.50$, $p_t = 5\,\mathrm{kN/m^2}$, $c_x = c_y = 3500\,\mathrm{Ns/m}$

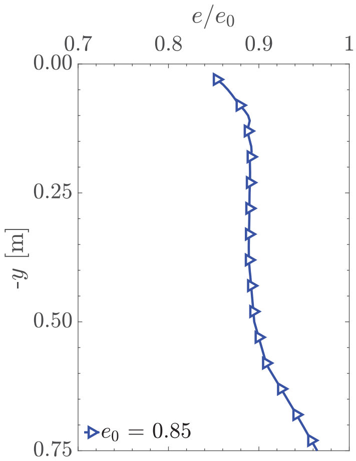

Figure I16: Mean normalized void ratio profile e/e_0 in the soil region $-0.5\,\mathrm{m} \leq x \leq 0.5\,\mathrm{m}$, corresponds to Fig. I15

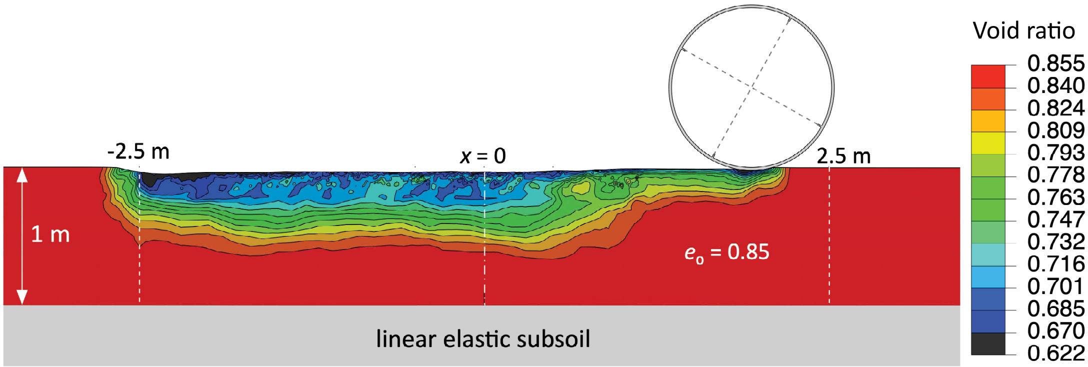

Figure I17: Distribution of void ratio e in the upper soil layer of 1 m thickness after an oscillatory roller pass; model $A^{(100)}$ / mesh I / SD, $e_0 = 0.85$, $\mu = 0.50$, $p_t = 10\,\mathrm{kN/m^2}$, $c_x = c_y = 10{,}000\,\mathrm{Ns/m}$

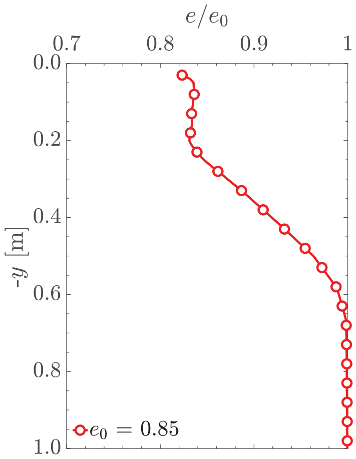

Figure I18: Mean normalized void ratio profile e/e_0 in the soil region $-1\,\mathrm{m} \leq x \leq 0$, corresponds to Fig. I17

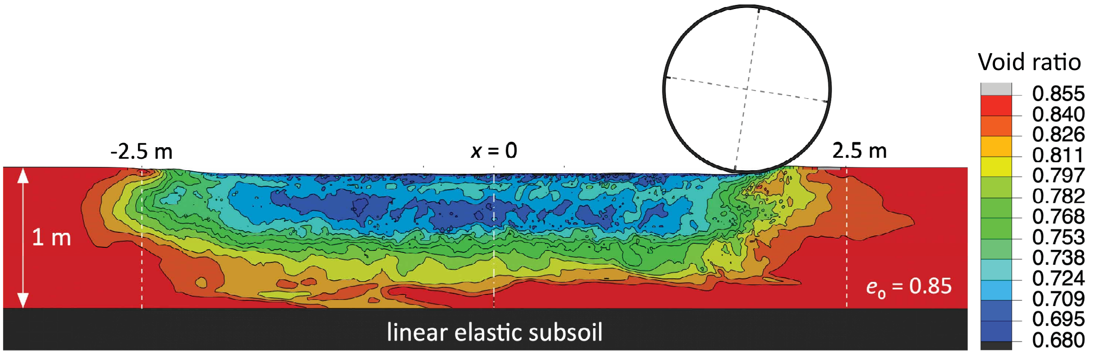

Figure I19: Distribution of void ratio e in the upper soil layer of 1 m thickness after an oscillatory roller pass; model $\mathrm{A}^{(100)}$ / mesh II / SD, $e_0 = 0.85$, $\mu = 0.50$, $p_t = 10\,\mathrm{kN/m^2}$, $c_x = c_y = 500\,\mathrm{Ns/m}$

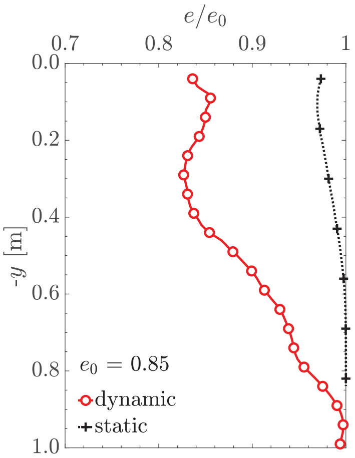

Figure I20: Mean normalized void ratio profile e/e_0 in the soil region $-0.5\,\mathrm{m} \leq x \leq 0.5$, corresponds to Fig. I19

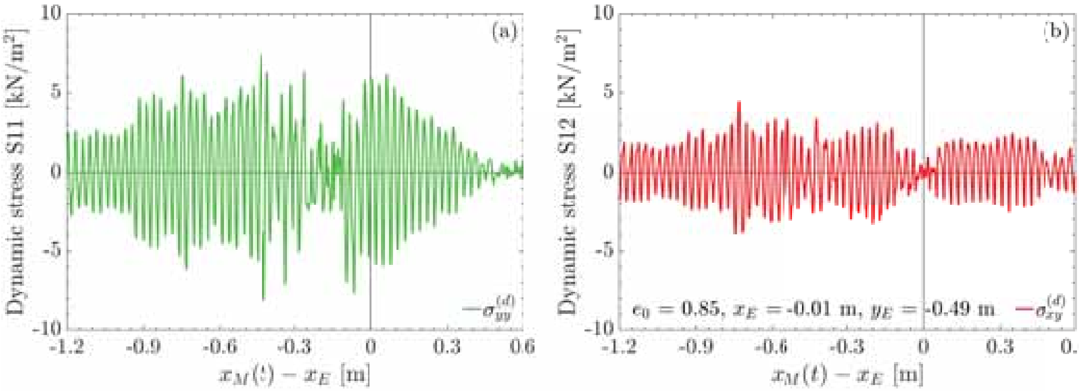

Figure I21: Dynamic part of the (a) vertical and (b) shear stress component at a depth of 0.49 m; model $\mathrm{A}^{(100)}$ / mesh II / SD, $e_0 = 0.85$, $\mu = 0.50$, $p_t = 10\,\mathrm{kN/m^2}$, $c_x = c_y = 500\,\mathrm{Ns/m}$

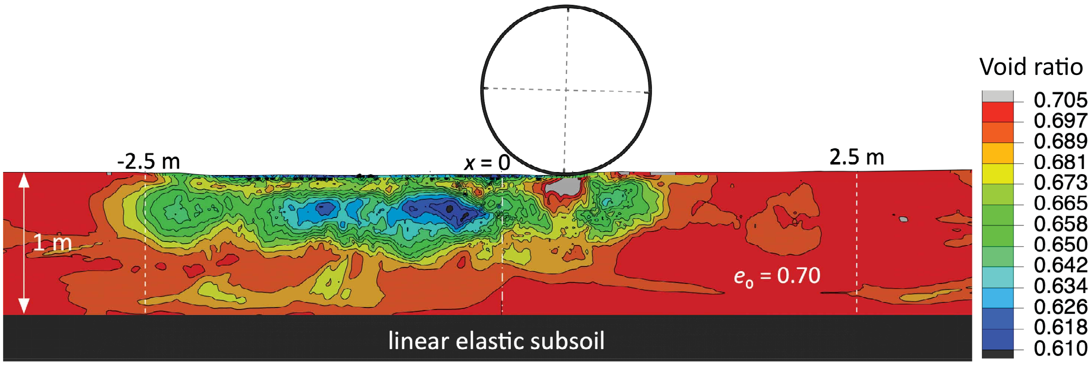

Figure I22: Distribution of void ratio e in the upper soil layer of 1 m thickness after an oscillatory roller pass; model $\mathrm{A}^{(100)}$ / mesh II / SD, $e_0 = 0.70$, $\mu = 0.50$, $p_t = 10\,\mathrm{kN/m^2}$, $c_x = c_y = 500\,\mathrm{Ns/m}$

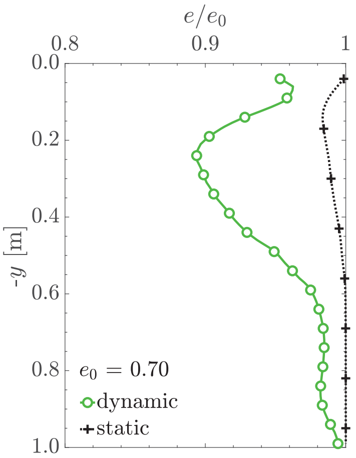

Figure I23: Mean normalized void ratio profile e/e_0 in the soil region $-1.3\,\mathrm{m} \le x \le -0.3$, corresponds to Fig. I22

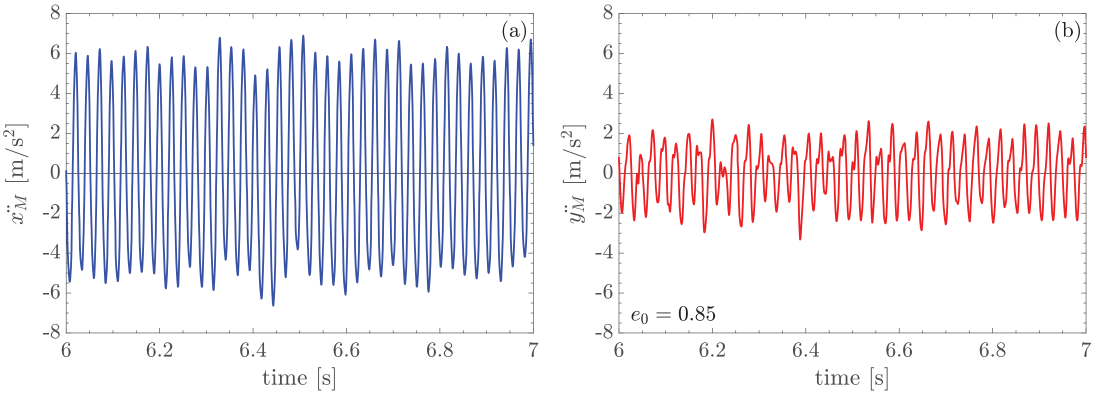

Figure I24: Time history of the (a) horizontal and (b) vertical acceleration in the drum center M during an oscillatory roller pass on initially loose soil; model $\mathrm{A}^{(100)}$ / mesh II / SD, $e_0 = 0.85$, $\mu = 0.50$, $p_t = 10\,\mathrm{kN/m^2}$, $c_x = c_y = 500\,\mathrm{Ns/m}$

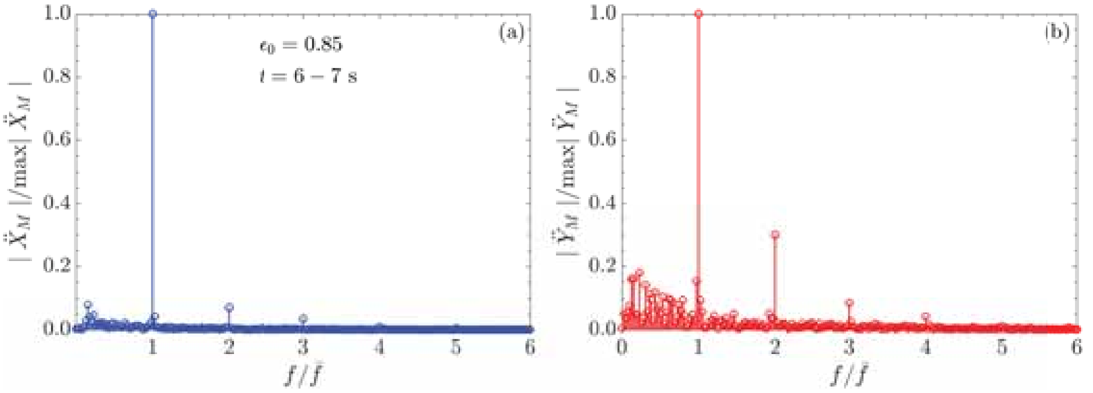

Figure I25: Normalized frequency spectrum of the (a) horizontal and (b) vertical acceleration in the drum center M for one second of an oscillatory roller pass, based on Fig. I24

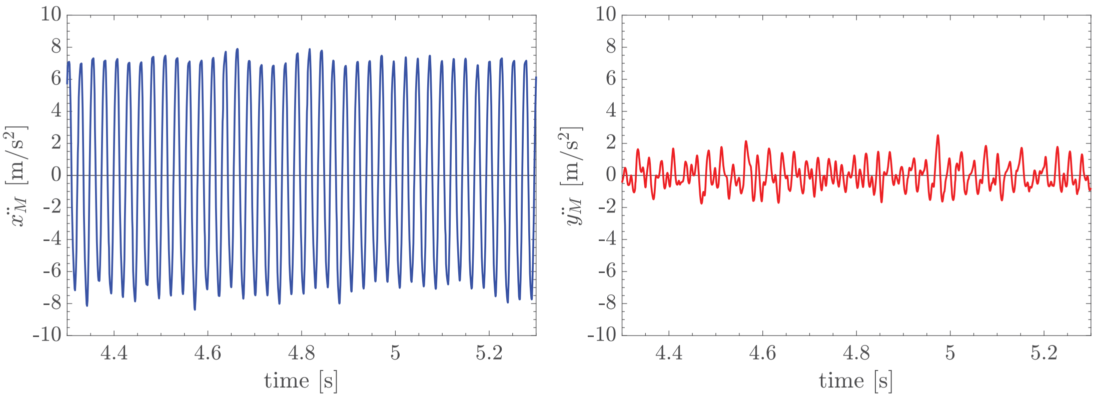

Figure I26: Time history of the (a) horizontal and (b) vertical acceleration in the drum center M during an oscillatory roller pass on initially dense soil; model A$^{(100)}$ / mesh II / SD, $e_0 = 0.70$, $\mu = 0.50$, $p_t = 10\,\mathrm{kN/m^2}$, $c_x = c_y = 500\,\mathrm{Ns/m}$

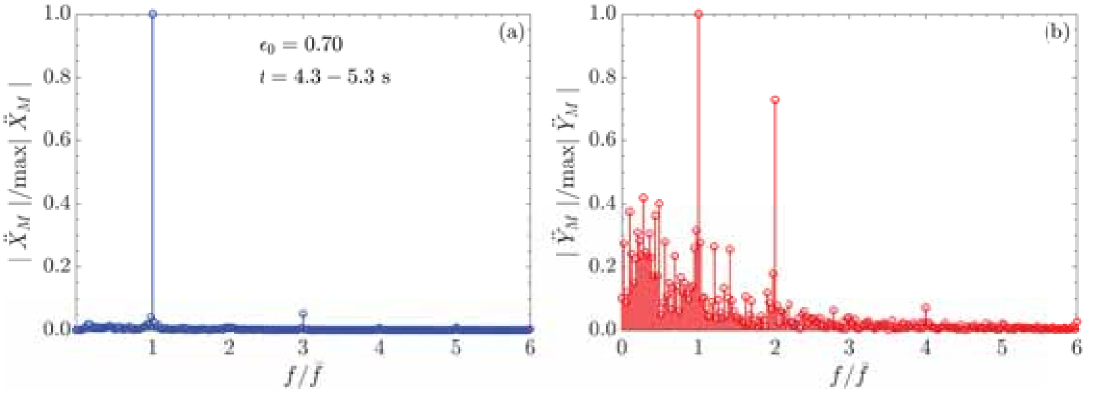

Figure I27: Normalized frequency spectrum of the (a) horizontal and (b) vertical acceleration in the drum center M for one second of an oscillatory roller pass, based on Fig. I26

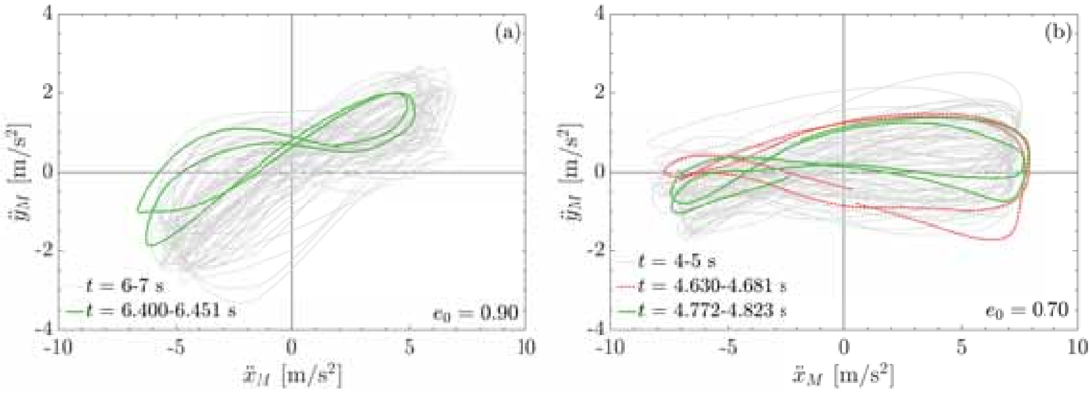

Figure I28: Plot $\ddot{y}_M$ over $\ddot{x}_M$ for a time window of 1 s (grey lines) and two representative oscillating cycles (green and red lines) based on (a) Fig. I24 and (b) Fig. I26

I.3 Results based on “model B” without “protective measures”

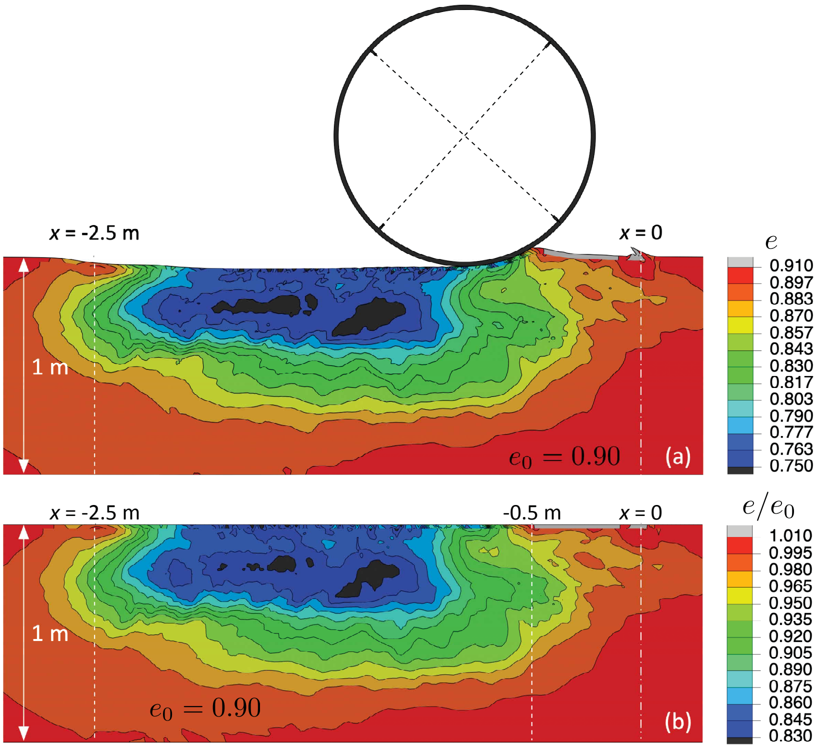

Figure I29: Distribution of (a) void ratio e and (b) normalized void ratio e/e_0 in the upper soil layer of 1 m thickness during an oscillatory roller pass; $t = 1.286$ s (model B / mesh II, $e_0 = 0.90$, $\mu = 0.50$, $p_t = 5(1)$ kN/m^2)

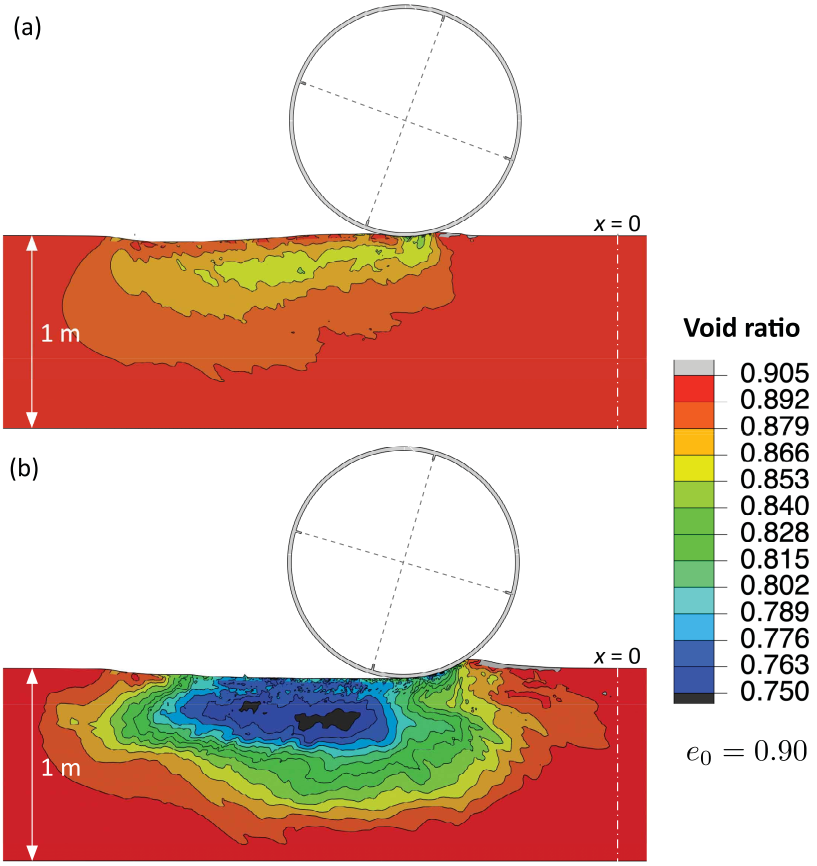

Figure I30: Distribution of void ratio e in the upper soil layer of 1 m thickness during compaction (a) without and (b) with oscillation; model B / mesh III, $e_0 = 0.90$, $\mu = 0.50$, $p_t = 5(1)$ kN/m^2

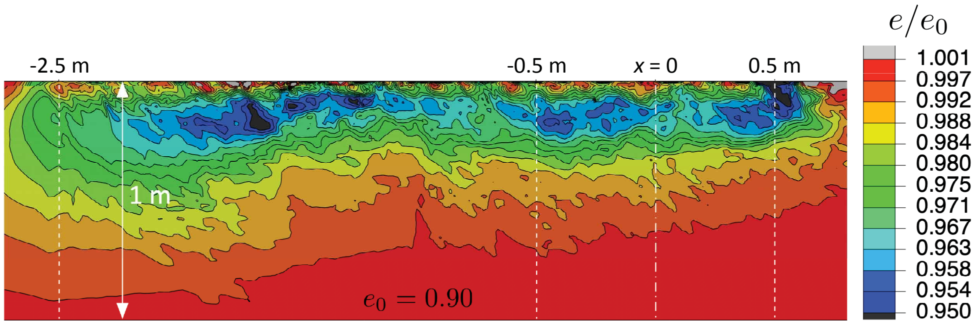

Figure I31: Distribution of the normalized void ratio e/e_0 in the upper soil layer of 1 m thickness after a static roller pass; model B / mesh III, $e_0 = 0.90$, $\mu = 0.50$, $p_t = 5(1)$ kN/m^2

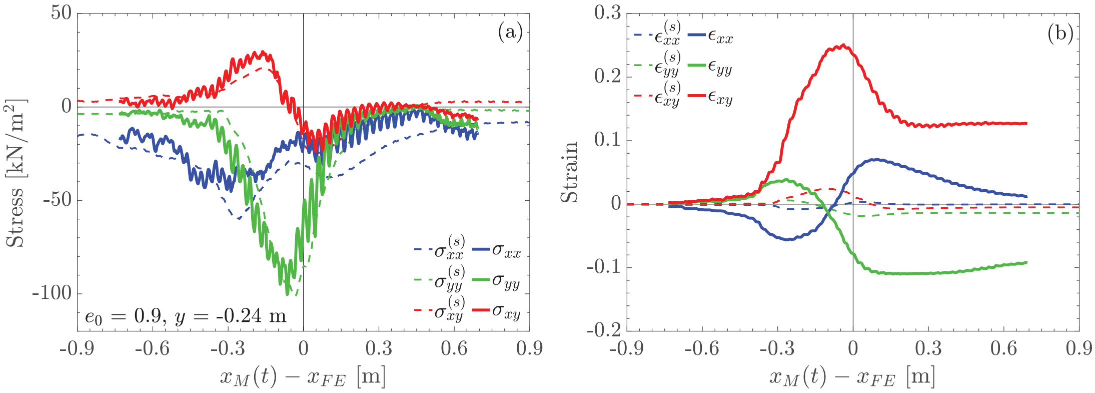

Figure I32: (a) Stress and (b) strain components due to an oscillatory (solid lines) and a static roller pass (dashed lines), respectively; depth $y = -0.24$ m; model B / mesh II, $e_0 = 0.90$, $\mu = 0.50$, $p_t = 5(1)$ kN/m^2

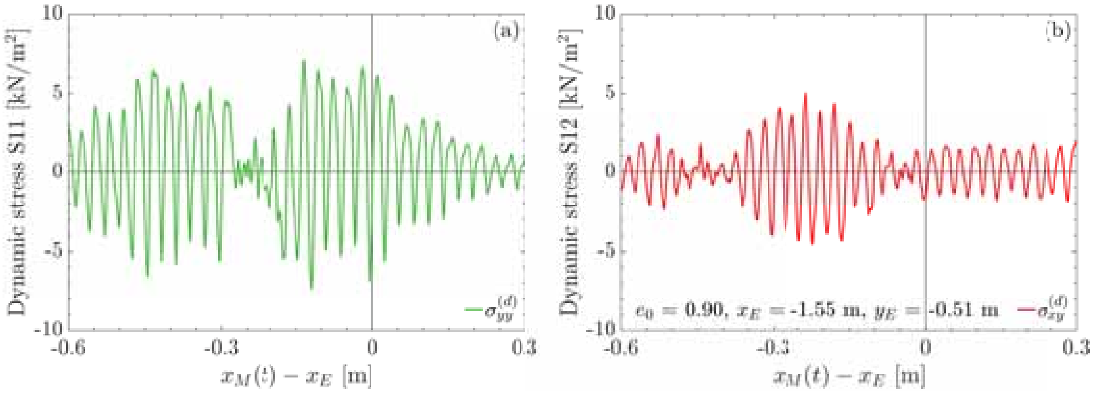

Figure I33: Dynamic part of the (a) vertical and (b) shear stress component at a depth of 0.51 m; model B / mesh III, $e_0 = 0.90$, $\mu = 0.50$, $p_t = 5(1)$ kN/m^2

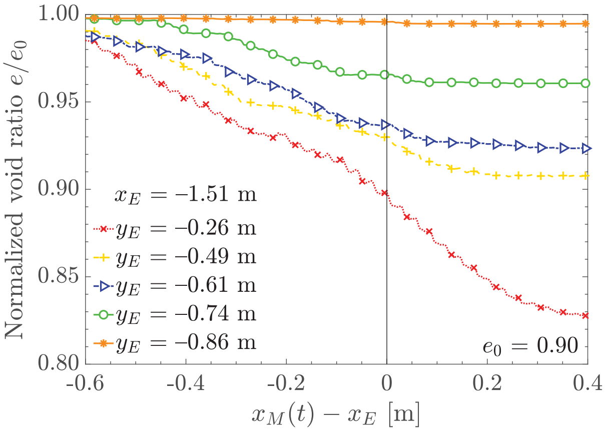

Figure I34: Normalized void ratio e/e_0 vs. horizontal distance from a selected observation point (“E”) at selected soil depths during an oscillatory roller pass; model B / mesh III, $e_0 = 0.90$, $\mu = 0.50$, $p_t = 5(1)$ kN/m^2

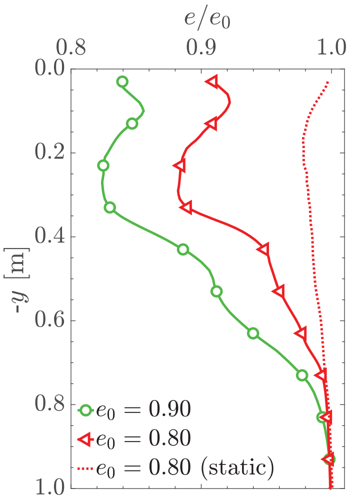

Figure I35: Normalized void ratio profile e/e_0 for two different initial void ratios e_0; $\mu = 0.50$; model B / mesh II, corresponds to Fig. I29

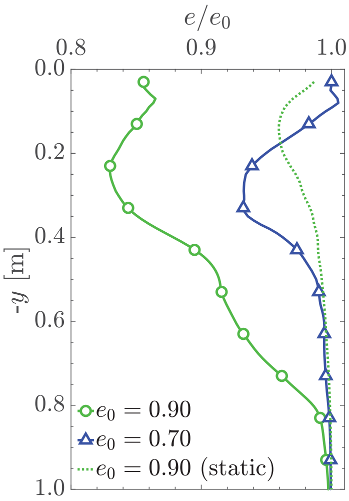

Figure I36: Normalized void ratio profile e/e_0 for two different initial void ratios e_0; $\mu = 0.50$; model B / mesh III, corresponds to Fig. I30

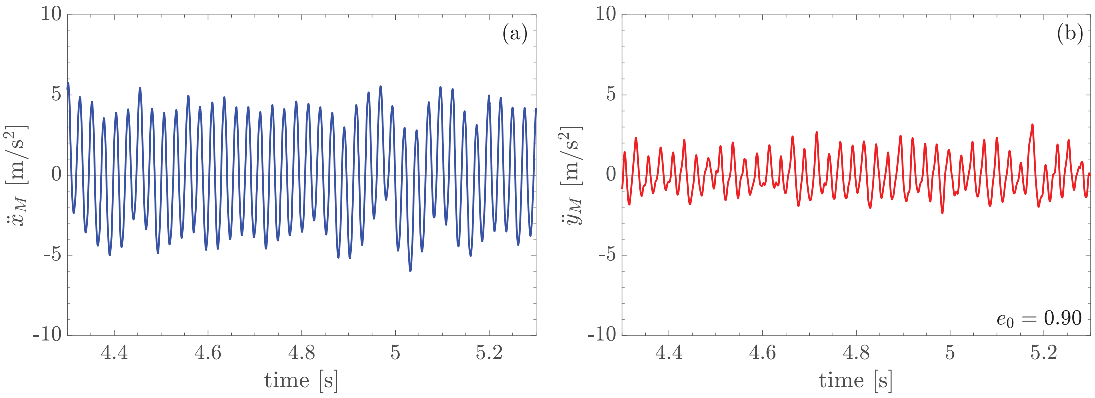

Figure I37: Time history of the (a) horizontal and (b) vertical acceleration in the drum center M; model B / mesh II, $e_0 = 0.90$, $\mu = 0.50$, $p_t = 5(1)$ kN/m^2

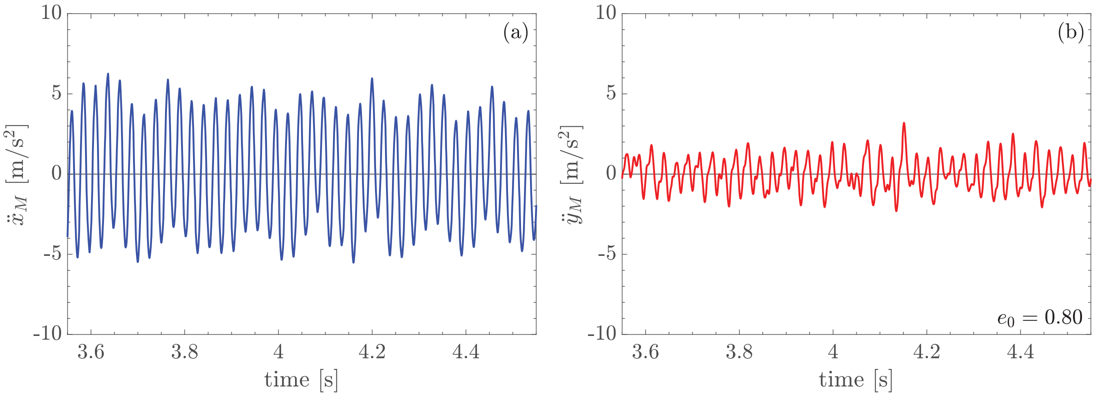

Figure I38: Time history of the (a) horizontal and (b) vertical acceleration in the drum center M; model B / mesh II, $e_0 = 0.80$, $\mu = 0.50$, $p_t = 5(1)$ kN/m^2

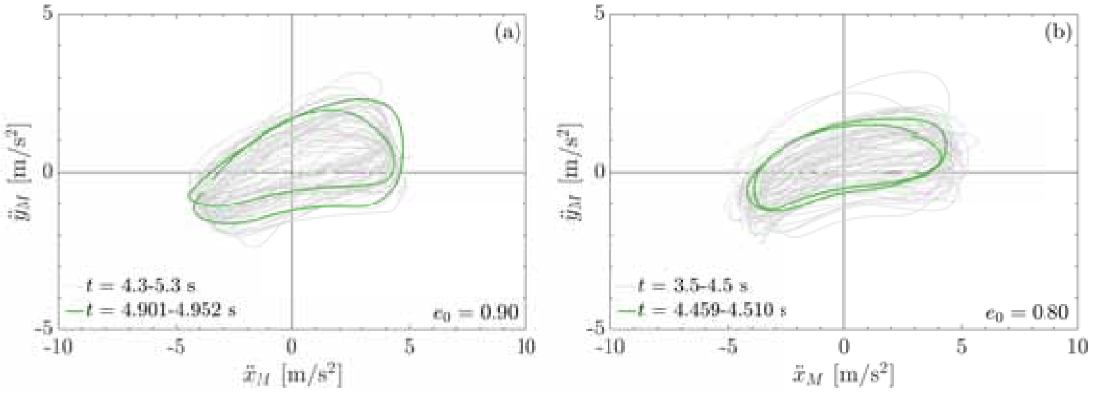

Figure I39: Plot $\ddot{y}_M$ over $\ddot{x}_M$ for an initial void ratio e_0 of (a) 0.90 and (b) 0.80 for a time window of 1 s (grey lines) and two representative oscillating cycles (green lines), based on Figs I37 and I38

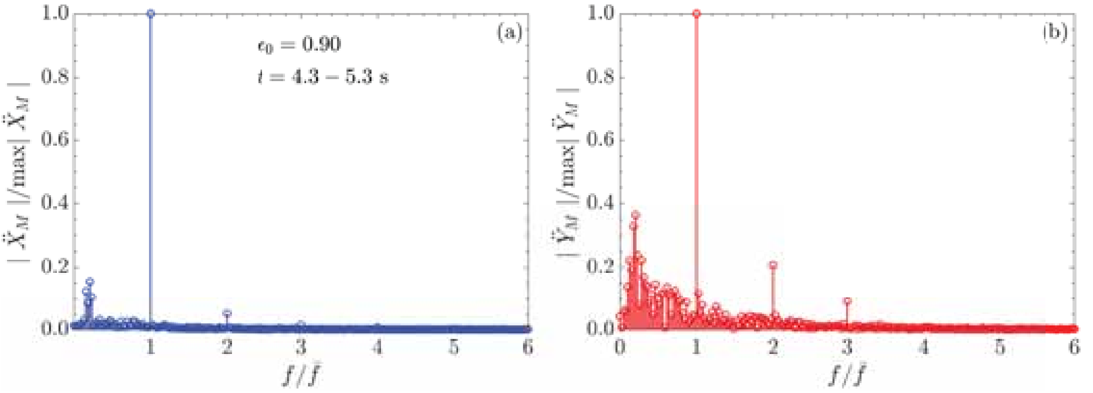

Figure I40: Normalized frequency spectrum of the (a) horizontal and (b) vertical acceleration in the drum center M for one second of an oscillatory roller pass; initially very loose soil ($e_0 = 0.90$); corresponds to Fig. I37

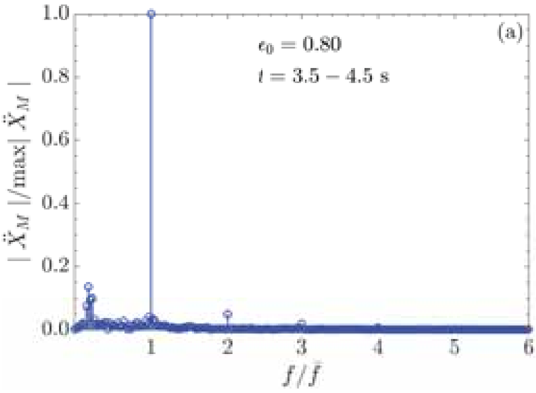

Figure I41: Normalized frequency spectrum of the (a) horizontal and (b) vertical acceleration in the drum center M for one second of an oscillatory roller pass; initially loose soil ($e_0 = 0.80$); corresponds to Fig. I38

I.4 Results based on "model B" with "surface dampers (SD)"

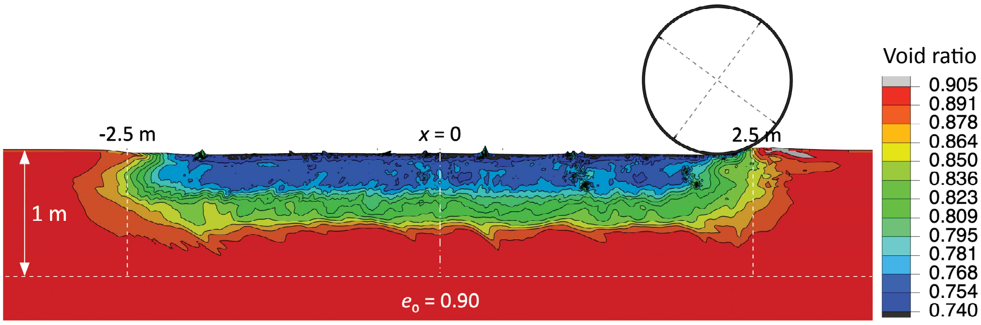

Figure I42: Distribution of void ratio e in the upper soil layer of 1 m thickness after an oscillatory roller pass; model B / mesh II / SD, $e_0 = 0.90$, $\mu = 0.50$, $p_t = 5\,\mathrm{kN/m^2}$, $c_x = c_y = 750\,\mathrm{Ns/m}$

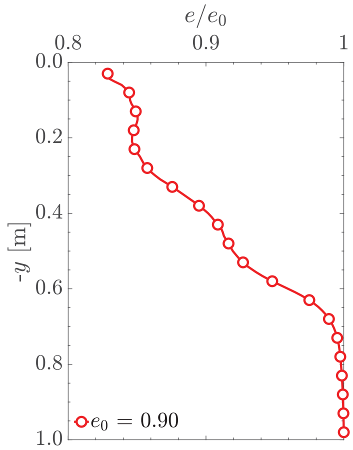

Figure I43: Mean normalized void ratio profile e/e_0 in the soil region $-0.5\,\mathrm{m} \leq x \leq 0.5\,\mathrm{m}$, corresponds to Fig. I42

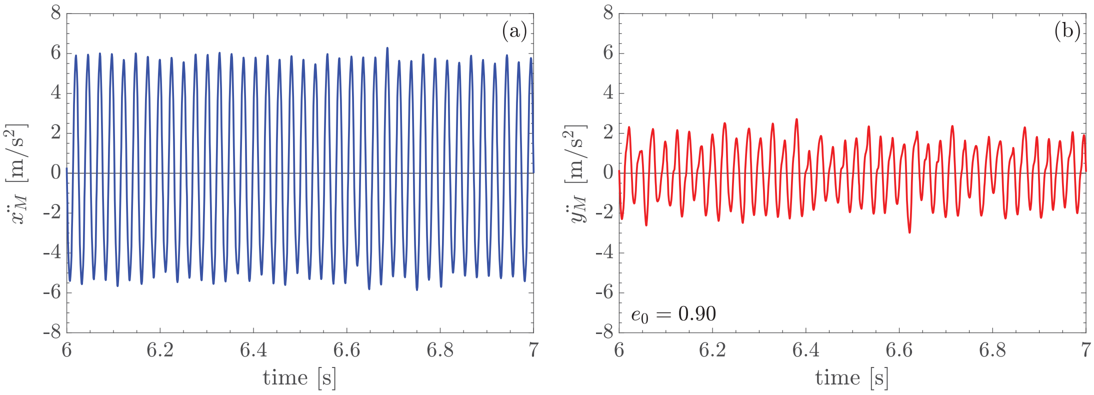

Figure I44: Time history of the (a) horizontal and (b) vertical acceleration in the drum center M during an oscillatory roller pass on initially very loose soil; model B / mesh II / SD, $e_0 = 0.90$, $\mu = 0.50$, $p_t = 5\,\mathrm{kN/m^2}$, $c_x = c_y = 750\,\mathrm{Ns/m}$

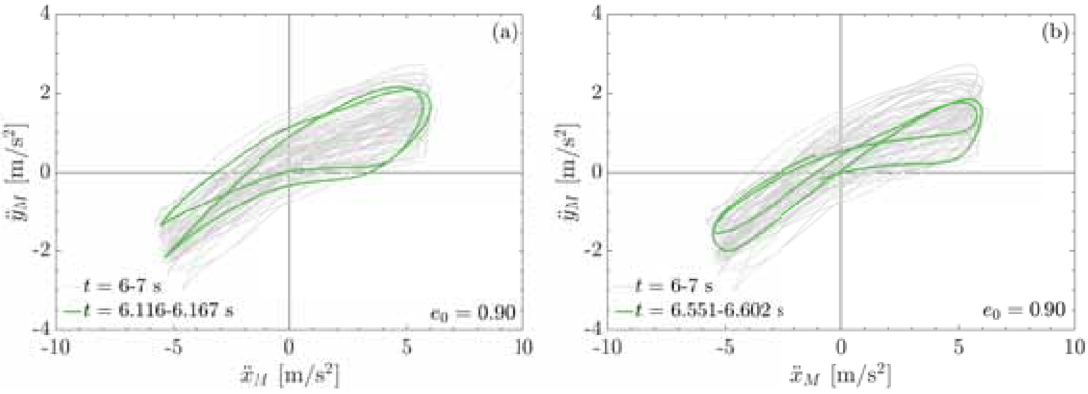

Figure I45: Plot $\ddot{y}_M$ over $\ddot{x}_M$ for a time window of 1 s (grey lines) and two representative oscillating cycles (green lines), based on Fig. I44; (a) without and (b) with node

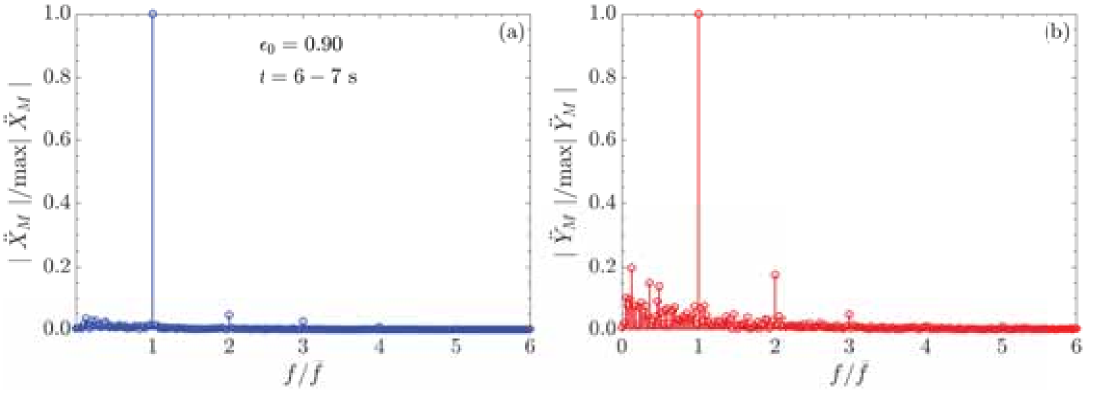

Figure I46: Normalized frequency spectrum of the (a) horizontal and (b) vertical acceleration in the drum center M for one second of an oscillatory roller pass, corresponds to Fig. I44

I.5 Results based on “model B” with “protective foil (PF)”

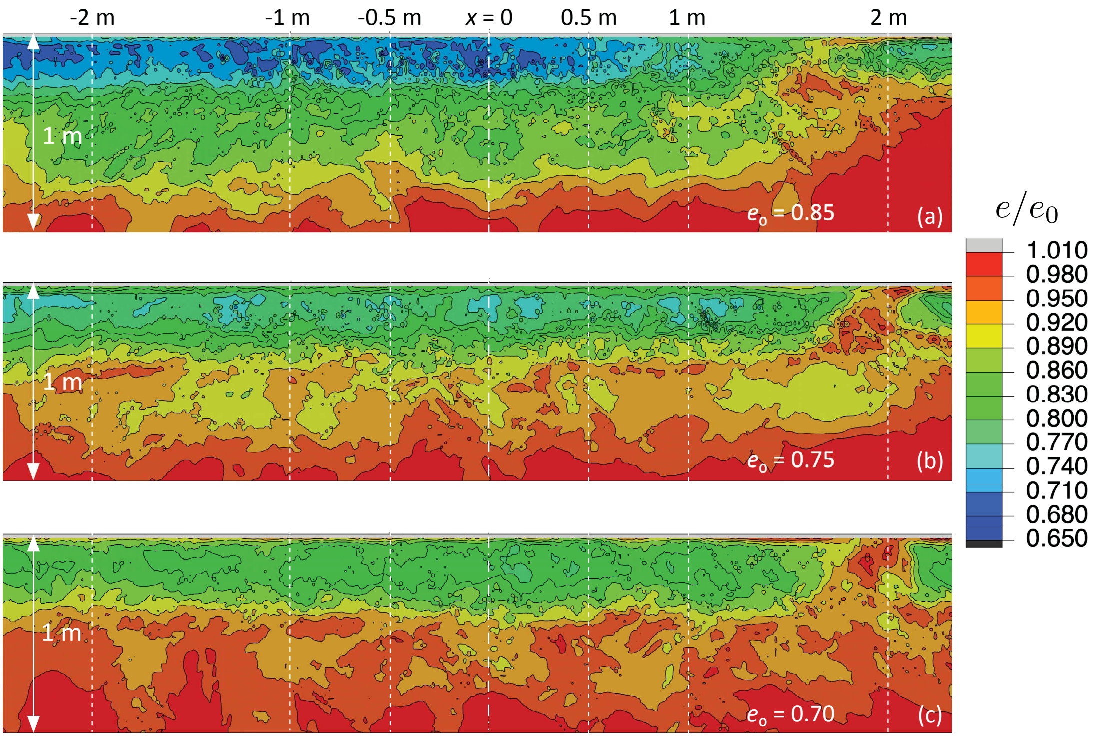

Figure I47: Distribution of the normalized void ratio e/e_0 in the upper soil layer of 1 m thickness after an oscillatory roller pass on a soil with an initial void ratio e_0 of (a) 0.85, (b) 0.75, and (c) 0.70; model B / mesh II / PF, $\mu = 0.30$, $p_t = 5(1)$ kN/m^2

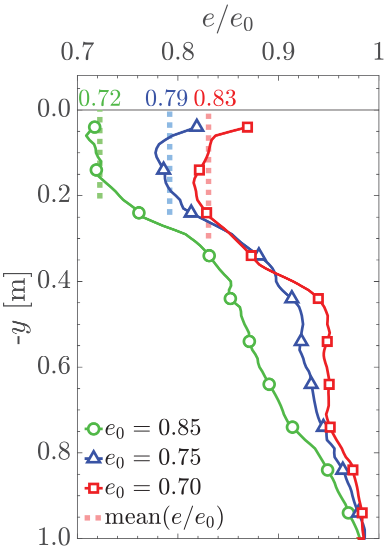

Figure I48: Mean normalized void ratio profile e/e_0 in the soil region $-1\,\mathrm{m} \leq x \leq 0$, corresponds to Fig. I47

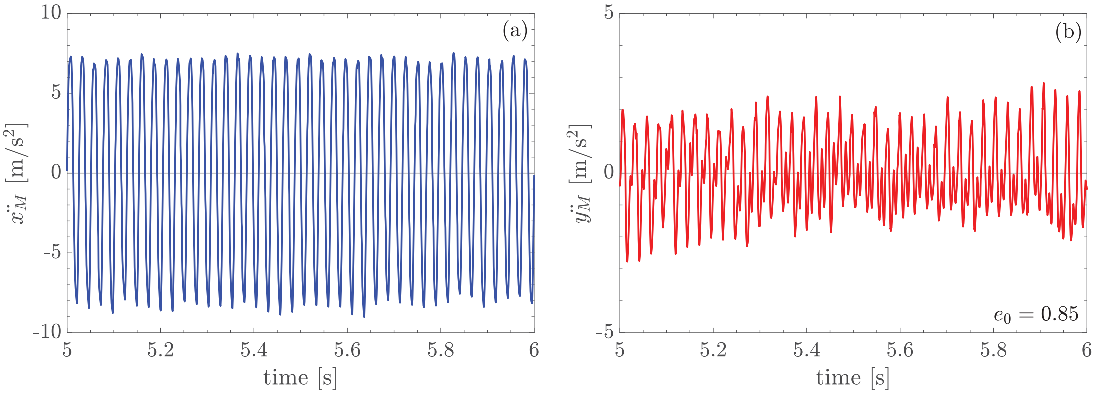

Figure I49: Time history of the (a) horizontal and (b) vertical acceleration in the drum center M during an oscillatory roller pass; model B / mesh II / PF, $e_0 = 0.85$, $\mu = 0.30$, $p_t = 5(1)$ kN/m^2; time window: $t = 5{-}6$ s

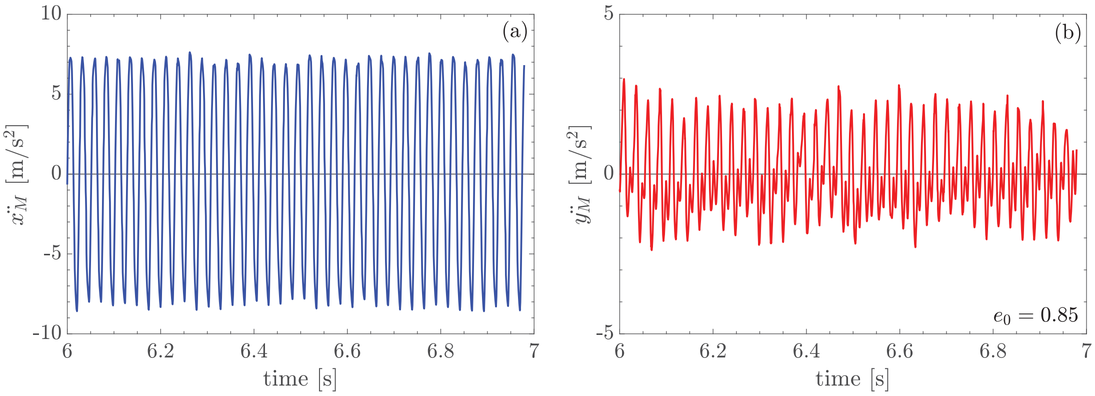

Figure I50: Time history of the (a) horizontal and (b) vertical acceleration in the drum center M during an oscillatory roller pass; model B / mesh II / PF, $e_0 = 0.85$, $\mu = 0.30$, $p_t = 5(1)$ kN/m^2; time window: $t = 6{-}7$ s

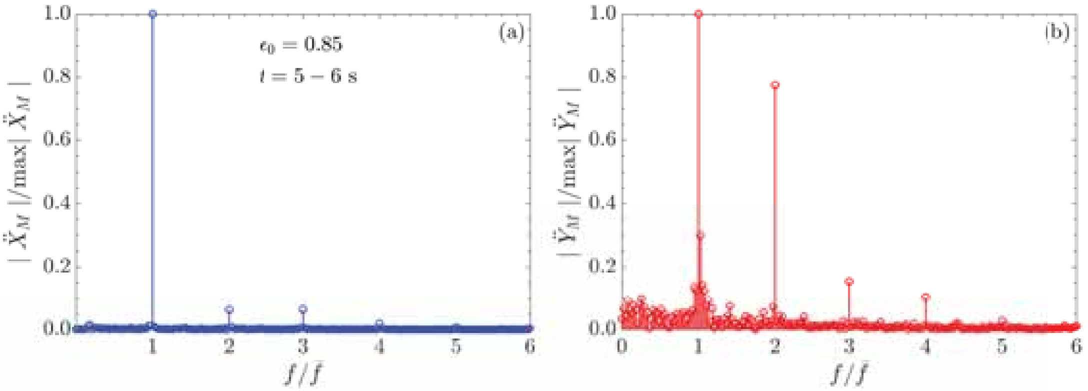

Figure I51: Normalized frequency spectrum of the (a) horizontal and (b) vertical acceleration in the drum center M, corresponds to Fig. I49

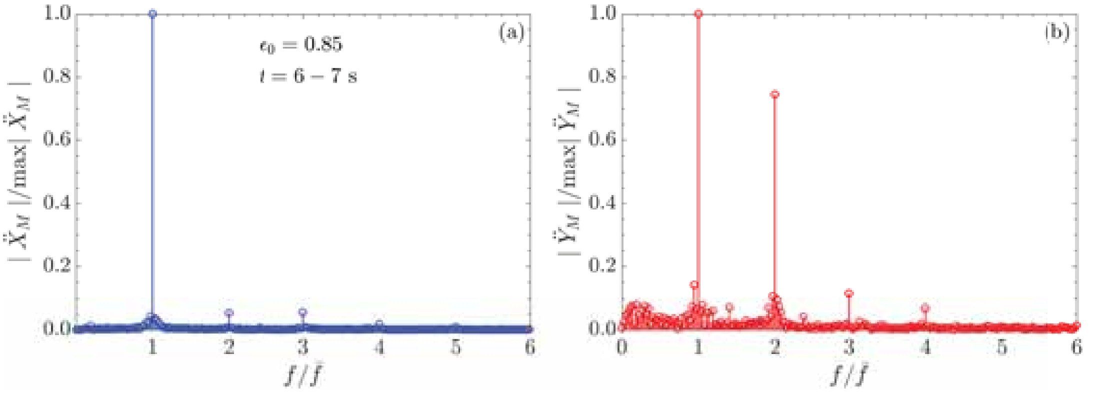

Figure I52: Normalized frequency spectrum of the (a) horizontal and (b) vertical acceleration in the drum center M, corresponds to Fig. I50

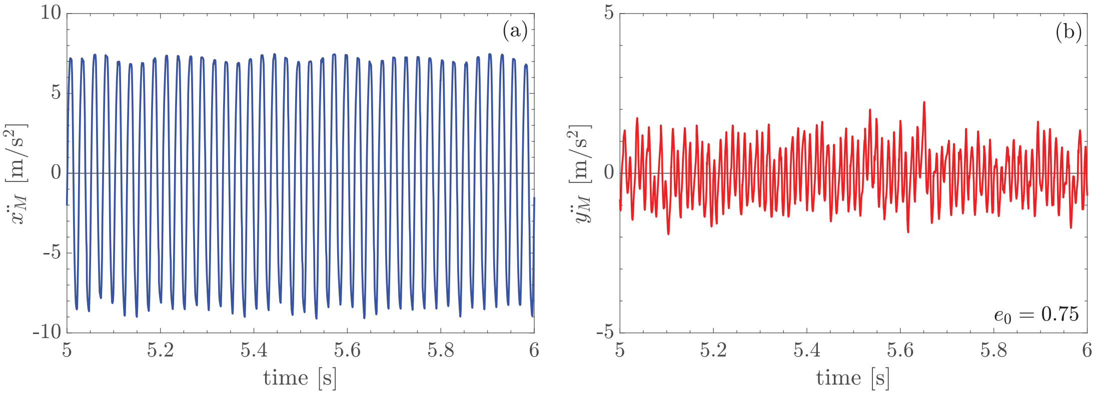

Figure I53: Time history of the (a) horizontal and (b) vertical acceleration in the drum center M during an oscillatory roller pass; model B / mesh II / PF, $e_0 = 0.75$, $\mu = 0.30$, $p_t = 5(1)$ kN/m^2; time window: $t = 5-6$ s

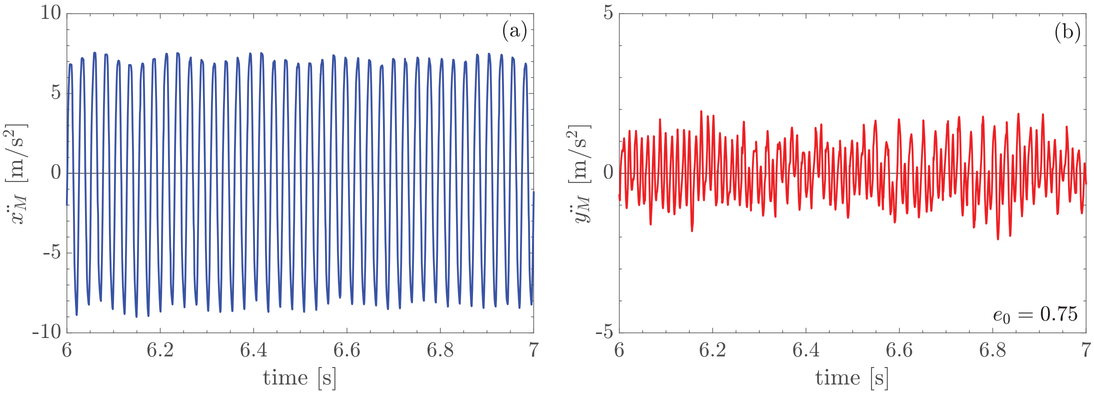

Figure I54: Time history of the (a) horizontal and (b) vertical acceleration in the drum center M during an oscillatory roller pass; model B / mesh II / PF, $e_0 = 0.75$, $\mu = 0.30$, $p_t = 5(1)$ kN/m^2; time window: $t = 6-7$ s

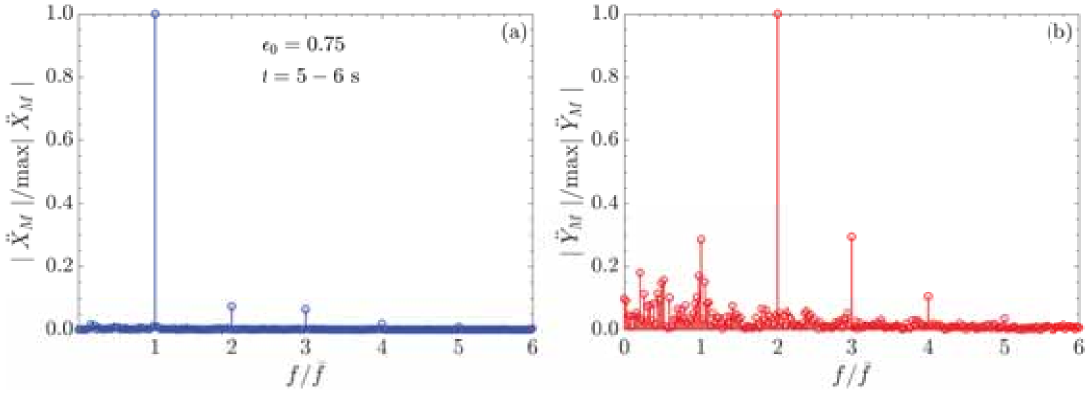

Figure I55: Normalized frequency spectrum of the (a) horizontal and (b) vertical acceleration in the drum center M, corresponds to Fig. I53

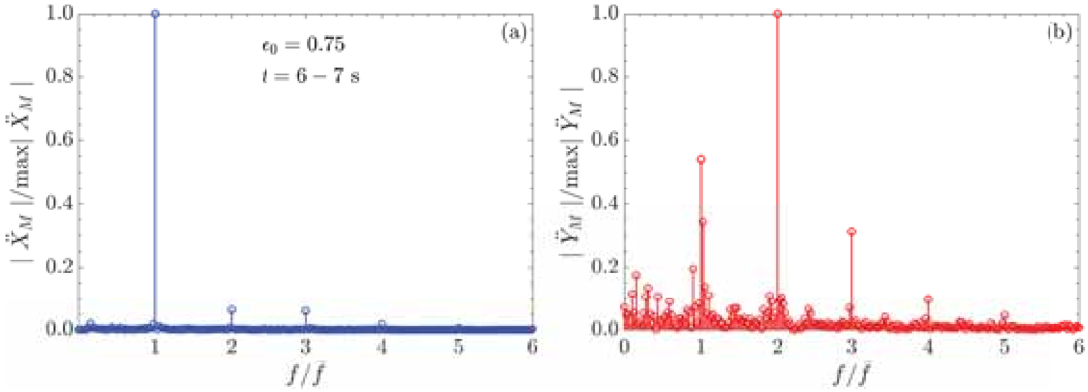

Figure I56: Normalized frequency spectrum of the (a) horizontal and (b) vertical acceleration in the drum center M, corresponds to Fig. I54

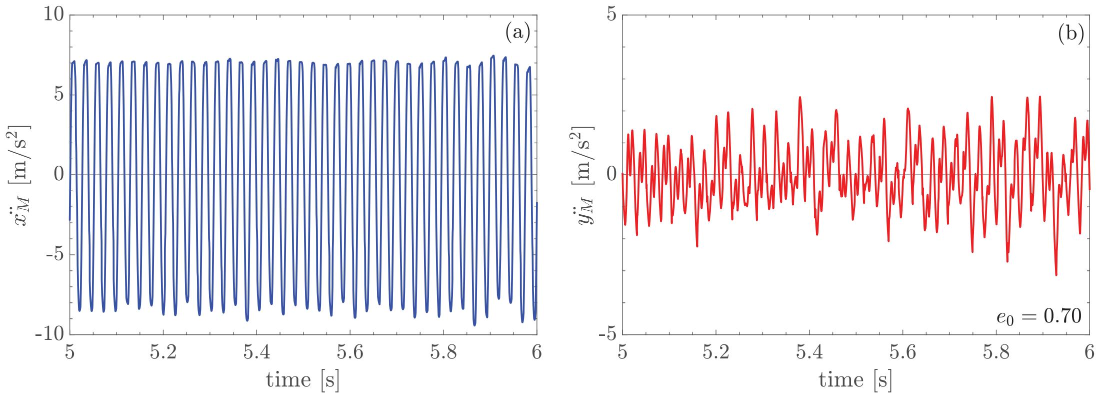

Figure I57: Time history of the (a) horizontal and (b) vertical acceleration in the drum center M during an oscillatory roller pass; model B / mesh II / PF, $e_0 = 0.70$, $\mu = 0.30$, $p_t = 5(1)$ kN/m^2; time window: $t = 5$–6 s

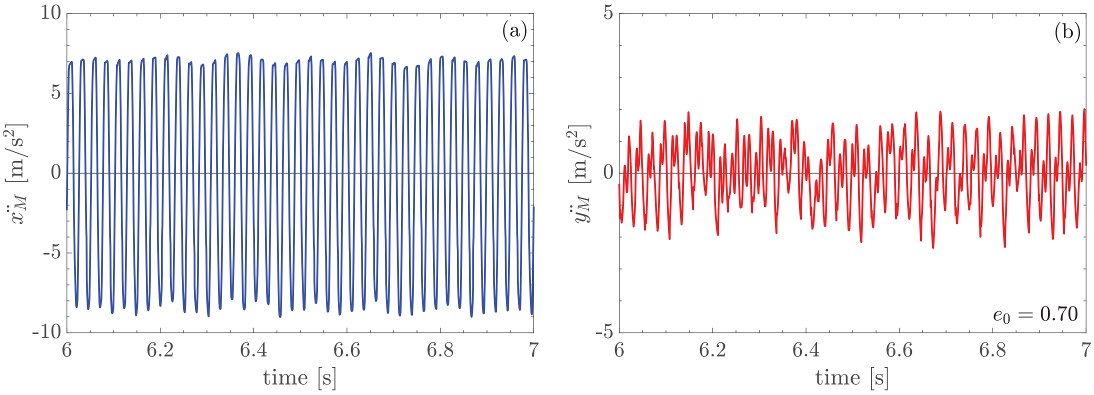

Figure I58: Time history of the (a) horizontal and (b) vertical acceleration in the drum center M during an oscillatory roller pass; model B / mesh II / PF, $e_0 = 0.70$, $\mu = 0.30$, $p_t = 5(1)$ kN/m^2; time window: $t = 6{-}7$ s

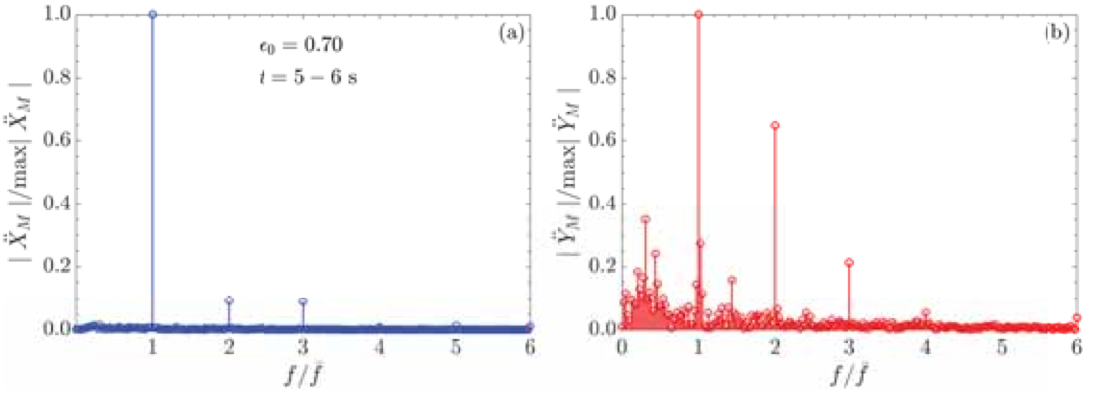

Figure I59: Normalized frequency spectrum of the (a) horizontal and (b) vertical acceleration in the drum center M, corresponds to Fig. I57

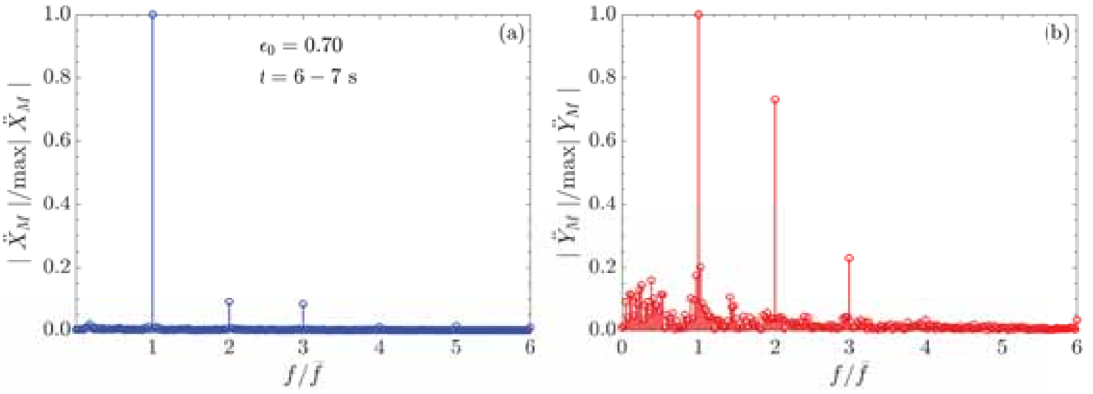

Figure I60: Normalized frequency spectrum of the (a) horizontal and (b) vertical acceleration in the drum center M, corresponds to Fig. I58

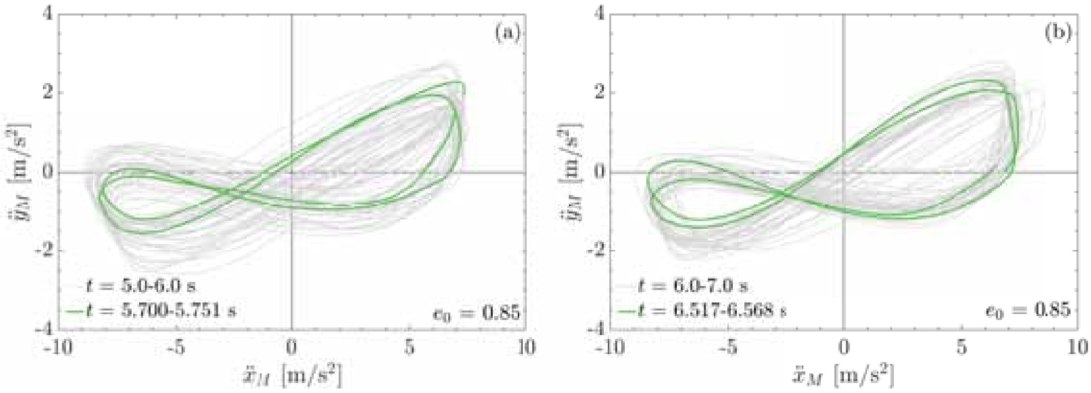

Figure I61: Plot $\ddot{y}_M$ over $\ddot{x}_M$ for an initial void ratio e_0 of 0.85 for a time window of 1 s (grey lines) and two representative oscillating cycles (green lines), based on (a) Fig. I49 and (b) Fig. I50

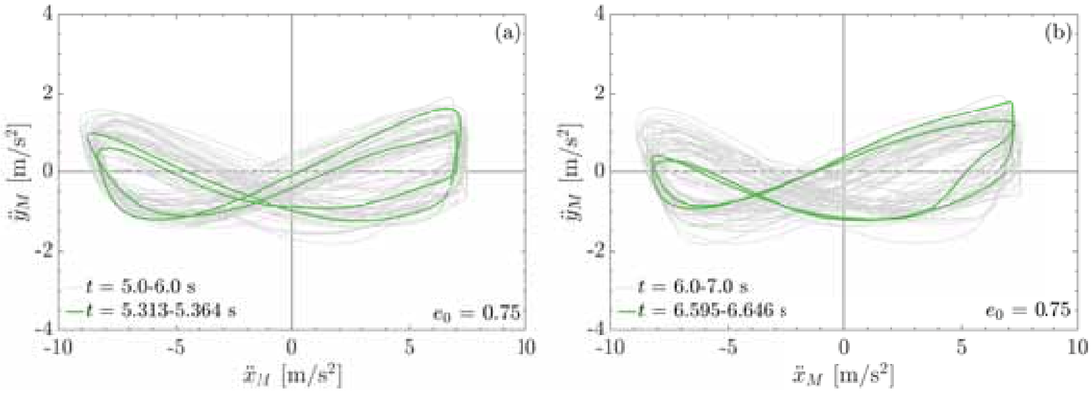

Figure I62: Plot $\ddot{y}_M$ over $\ddot{x}_M$ for an initial void ratio e_0 of 0.75 for a time window of 1 s (grey lines) and two representative oscillating cycles (green lines), based on (a) Fig. I53 and (b) Fig. I54

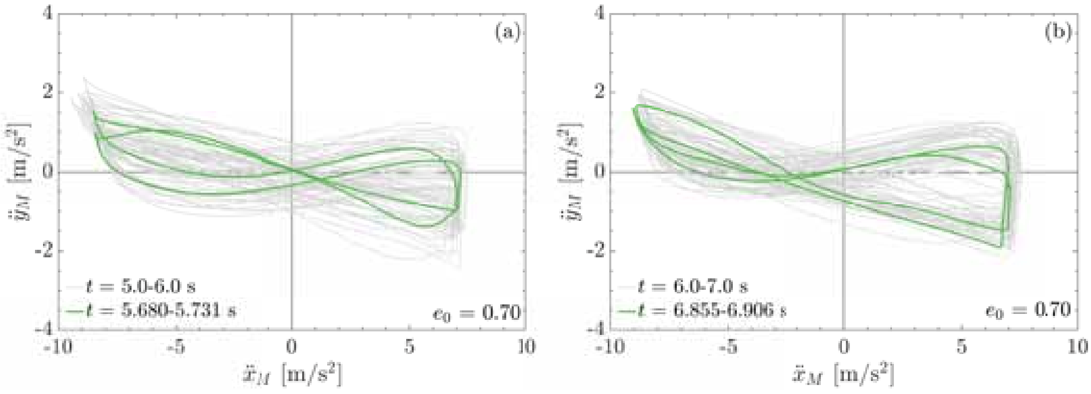

Figure I63: Plot $\ddot{y}_M$ over $\ddot{x}_M$ for an initial void ratio e_0 of 0.70 for a time window of 1 s (grey lines) and two representative oscillating cycles (green lines), based on (a) Fig. I57 and (b) Fig. I58

Abbreviations

CCC	Continuous Compaction Control
DOF	degree of freedom
FE	Finite Element
LPM	lumped parameter model
PF	protective foil
SD	surface dampers
SDOF	single degree of freedom

Lumped parameter modeling

0	origin of the logarithmic spiral representing the settlement trough or center of the semi-circular settlement trough
1	start of the logarithmic spiral
a	size parameter of the logarithmic spiral, i.e. the distance from the spiral start to the origin 0 ($a > 0$)
a_0	half contact length between drum and soil
b	drum width
c_d	viscous damping coefficient of the dashpot dampers representing the damping effect of the suspension between drum and roller frame
c_{sh}	viscous damping coefficient of the dashpot damper representing the geometric damping of the soil in horizontal direction
c_{sv}	viscous damping coefficient of the dashpot damper representing the geometric damping of the subsoil in vertical direction
e_u	distance of one eccentric lumped mass from the axis of the unbalanced shaft (unbalance eccentricity)
e_w	distance of the unbalanced shaft from the drum center (shaft eccentricity)
f_i	function depending on $\delta(t)$, a, k, α, R_0, and r ($i = 1, 2, \ldots, 6$)
$f_{\mu 1}$, $f_{\mu 2}$	functions depending on μ, $\delta(t)$ and the sign of v_{rel}
$\bar{f}$	excitation frequency of the oscillation drum

g	acceleration of gravity
h_i	abbreviation used in the state-space representation of the equations of motion of the *stick* phase ($i = 1,2,3$)
$h_i^{(sl)}$	abbreviation used in in the state-space representation of the equations of motion of the *slip* phase ($i = 1,2,3,4$)
k	shape parameter of the logarithmic spiral ($k > 0$)
k_d	spring stiffness representing the suspension stiffness between drum and roller frame
k_{sh}	spring stiffness representing the horizontal soil stiffness
k_{sv}	spring stiffness representing the vertical soil stiffness
l	distance between 0 and the drum center M ($= R - r$)
m	mass of the drum
m_u	mass of one imbalance (eccentric lumped mass)
n_u	number of unbalanced masses per shaft
r	drum radius
$s_A(t)$	vertical displacement component of support point A
$\text{sign}(v_{rel})$	signum function of v_{rel}
t	time
$v_{rel}(t)$	slip velocity between drum and soil at point C
x	horizontal axis (abscissa) pointing right
$x_A(t)$	horizontal displacement component of the support point A
$x_M(t)$	horizontal displacement component of the drum center M
$x_M^{(\text{roll})}(t)$	horizontal displacement component of the drum center M relative to the settlement trough
$\dot{x}_M(t)$	horizontal velocity component of the drum center M
$\ddot{x}_M(t)$	horizontal acceleration component of the drum center M
z	vertical axis (ordinate) pointing down
$z_M(t)$	vertical displacement component of the drum center M
$z_M^{(\text{roll})}(t)$	vertical displacement component of the drum center M relative to the settlement trough
$\dot{z}_M(t)$	vertical velocity component of the drum center M
$\ddot{z}_M(t)$	vertical acceleration component of the drum center M
A	support point of the settlement trough
B	point on the drum; corresponds to point A at $t = 0$
C	contact point between drum and settlement trough
F_z	vertical load applied to the drum center M representing the static axle load P_0 minus drum weight mg
G	shear modulus of the soil
I	mass moment of inertia of the drum (with respect to M)

M	drum center (axis) and, if $t = 0$, M corresponds to O
M_{Md}	constant driving torque (around the drum axis)
$M_{Mu}(t)$	sinusoidal excitation torque (unbalanced shaft moment around the drum axis)
$M_{Mu}^{(0)}$	amplitude of the excitation torque $M_{Mu}(t)$
N	normal component of the interface force at point C
O	origin of the defined x-z coordinate system
P_0	static axle load
R	radius of the semicircular settlement trough
R	radius of a spiral-shaped ($k > 0$, $a = R_0$, $R(\bar{\varphi})$ with $\bar{\varphi}(t)$) or semicircular ($k = 0$, $a = R_0 = R = \text{const}$) settlement trough
R_0	distance from 0 to the bottom A of the spiral-shaped settlement trough
T	tangential component of the interface force at point C
T_f	sliding friction force between drum and soil
$\lvert\ddot{X}_M(f)\rvert$	absolute value of horizontal spectral acceleration of M at frequency f
$\lvert\ddot{Z}_M(f)\rvert$	absolute value of vertical spectral acceleration of M at frequency f
α	angle between the tangent line at A and the radial line 0-A $(= \arctan \frac{1}{k})$
$\delta(t)$	angle defining the drum position in the settlement trough
$\dot{\delta}$	position angle velocity
$\varphi(t)$	absolute rotation angle of the drum
$\bar{\varphi}(t)$	angle between a and $R(t)$ of the logarithmic spiral
$\bar{\varphi}_0$	angle between a and R_0 of the logarithmic spiral
$\dot{\varphi}$	rotation angle velocity
μ	coefficient of friction according to *Coulomb*'s law of dry friction
ν	*Poisson*'s ratio of the soil
$\bar{\nu}$	angular velocity $(= 2\pi\bar{f})$
ρ	soil density

Finite Element modeling

b	drum width
c_d	viscous damper coefficient of the suspension between drum and roller frame
c_x	viscous damping coefficient of the dashpot dampers that *connect* the nodes of the free soil surface *to ground* in horizontal direction
c_y	viscous damping coefficient of the dashpot dampers that *connect* the nodes of the free soil surface *to ground* in vertical direction
e	void ratio of the soil
e_0	initial void ratio of the soil
e_u	distance of one eccentric lumped mass from the axis of the unbalanced shaft (unbalance eccentricity)

e_w	distance of the unbalanced shaft from the drum center (shaft eccentricity)
f	frequency
$\bar{f}$	excitation frequency of the oscillation drum
g	acceleration of gravity
k_d	stiffness coefficient of the suspension between drum and roller frame
m	mass of the drum
m_u	mass of one imbalance (eccentric lumped mass)
p_t	apparent cohesion of the soil
r	radius of the drum
t	time
v_0	roller speed
x	horizontal axis (abscissa) pointing right
$\ddot{x}_M(t)$	horizontal acceleration component of the drum center M
y	vertical axis (ordinate) pointing up
$\ddot{y}_M(t)$	vertical acceleration component of M
E	*Young*'s modulus
I	mass moment of inertia of the drum (with respect to M)
M	drum center (axis)
$M_{Mu}(t)$	sinusoidal excitation torque around the drum axis
$M_{Mu}^{(0)}$	amplitude of the excitation torque $M_{Mu}(t)$
O	origin of the defined x-y coordinate system
P_0	static axle load applied to the drum center M
$\lvert\ddot{X}_M(f)\rvert$	absolute value of horizontal spectral acceleration of M at frequency f
$\lvert\ddot{Y}_M(f)\rvert$	absolute value of vertical spectral acceleration of M at frequency f
μ	coefficient of friction (*Coulomb*'s law of dry friction)
$\bar{\nu}$	angular velocity ($= 2\pi\bar{f}$)
ν	*Poisson*'s ratio of the soil
ρ	soil density
	Parameters of the hypoplastic constitutive law
φ_c	critical state friction angle
h_s	granular hardness (dimension of stress)
n	constant
e_{d0}	void ratio for densest packing for zero mean pressure
e_{c0}	critical void ratio for zero mean pressure
e_{i0}	void ratio for loosest packing for zero mean pressure
α	parameter that controls the dependency of the peak friction angle on the relative void ratio
β	controls the increase of stiffness with increasing relative density
R	radius of the elastic strain range

m_R	controls the magnitude of the very small strain shear modulus in the initial loading, and upon a 180° change in direction of strain path
m_T	controls the initial shear modulus upon 90° strain path reversal
β_r	model parameter
χ	controls the interpolation between the reversible elastic response and non-linear hypoplastic response

List of Figures

11 Principal components of an oscillation roller compactor with smooth drum 2

21 3DOF lumped parameter model of the interaction system oscillation roller-subsoil (spiral-shaped settlement trough) 12
22 Drum with unbalanced shafts (left), and circular motion of one unbalance mass with constant circular frequency $\bar{\nu}$ (right) 13
23 Excitation torque $M_{Mu}(t)$ in an oscillation drum and corresponding location of the unbalance at discrete time instants, based on Zuwang et al [1997] . . 14
24 Subsystem I (oscillation drum with suspension) and subsystem II (subsoil with settlement trough) 18
25 Time history of the (a) horizontal and (b) vertical acceleration in the drum center; soft soil $G = 5$ MN/m^2; $M_{Md} = 0$; pure rolling motion; symmetric vs. asymmetric settlement trough 22
26 Time history of (a) position angle δ and (b) plot $\ddot{z}_M$ vs. $\ddot{x}_M$; soft soil $G = 5$ MN/m^2; $M_{Md} = 0$; pure rolling motion; symmetric vs. asymmetric settlement trough 23
27 Peak of the (a) horizontal and (b) vertical acceleration in the drum center as a function of soil shear modulus G for selected radii R of a semicircular settlement trough; $M_{Md} = 0$; pure rolling motion 24
28 Phase lag between excitation torque $M_{Mu}(t)$ (dashed line) and drum rotation φ - (a) time histories for four selected soil shear moduli G, and (b) phase lag for the entire range of G; $M_{Md} = 0$; pure rolling motion 25
29 Steady state (a) horizontal and (b) vertical acceleration in the drum center for four selected soil shear moduli G; $M_{Md} = 0$; pure rolling motion 25
210 Phase lag between $\ddot{x}_M$ and $\ddot{z}_M$ as a function of shear modulus G; $M_{Md} = 0$; pure rolling motion 26
211 Plot $\ddot{z}_M$ over $\ddot{x}_M$; (a) $M_{Md} = 0$ vs. (b) $M_{Md} = 0.05M_{Mu}^{(0)}$; pure rolling motion 27
212 Frequency spectrum of the (a) horizontal and (b) vertical acceleration in the drum center for four selected shear moduli G; pure rolling motion; $M_{Md} = 0$ 27
213 Frequency spectrum of the (a) horizontal and (b) vertical acceleration in the drum center for four selected shear moduli G; pure rolling motion; $M_{Md} = 0.05M_{Mu}^{(0)}$ 27

214 Area inside the $\ddot{z}_M$-$\ddot{x}_M$ figure as a function of soil shear modulus G; pure rolling motion; $M_{Md} = 0$ and $M_{Md} = 0.05M_{Mu}^{(0)}$, respectively 28
215 Steady state (a) horizontal and (b) vertical acceleration in the drum center for four selected soil shear moduli G; stick-slip motion ($\mu = 0.50$); $M_{Md} = 0$ 29
216 Steady state (a) horizontal and (b) vertical acceleration in the drum center for four selected soil shear moduli G; stick-slip motion ($\mu = 0.50$); $M_{Md} = 0.05M_{Mu}^{(0)}$ 29
217 Frequency spectrum of the (a) horizontal and (b) vertical acceleration in the drum center for four selected shear moduli G; stick-slip motion ($\mu = 0.50$); $M_{Md} = 0$ 30
218 Frequency spectrum of the (a) horizontal and (b) vertical acceleration in the drum center for four selected shear moduli G; stick-slip motion ($\mu = 0.50$); $M_{Md} = 0.05M_{Mu}^{(0)}$ 30
219 Vertical ($\ddot{z}_M$) over horizontal ($\ddot{x}_M$) acceleration in the drum center; stick-slip motion ($\mu = 0.50$); (a) $M_{Md} = 0$ and (b) $M_{Md} = 0.05M_{Mu}^{(0)}$ 31
220 Area inside the $\ddot{z}_M$-$\ddot{x}_M$ figure as a function of soil shear modulus G; stick slip motion ($\mu = 0.50$); $M_{Md} = 0$ and $M_{Md} = 0.05M_{Mu}^{(0)}$, respectively 31
221 Frequency spectrum of the (a) horizontal and (b) vertical acceleration in the drum center; computed ($G = 25$ MN/m^2; $\mu = 0.50$; $M_{Md} = 0.05M_{Mu}^{(0)}$) vs. recorded (in field tests, dense gravel, based on Pistrol [2016]) accelerations 32
222 (a) Horizontal and (b) vertical acceleration in the drum center with respect to time; roller 1; soft soil; pure rolling motion vs. stick-slip motion 34
223 Frequency spectrum of the (a) horizontal and (b) vertical acceleration in the drum center; roller 1; soft soil; pure rolling motion vs. stick-slip motion 35
224 Plot vertical over horizontal acceleration in the drum center; roller 1; soft soil; pure rolling motion vs. stick-slip motion 36
225 Plot vertical over horizontal acceleration in the drum center; roller 2 36
226 Plot vertical over horizontal acceleration in the drum center; roller 4 37
227 Amplitude of the horizontal drum accelerations at the excitation frequency as a function of soil stiffness 38
228 Amplitude of the second harmonic of the horizontal acceleration normalized by the amplitude at the excitation frequency as a function of soil stiffness . 38
229 Amplitude of the third harmonic of the horizontal acceleration normalized by the amplitude at the excitation frequency as a function of soil stiffness . 38
230 Amplitude of the vertical drum accelerations at the excitation frequency as a function of soil stiffness 39
231 Amplitude of the second harmonic of the vertical acceleration normalized by the amplitude at the excitation frequency as a function of soil stiffness . 39
232 Amplitude of the third harmonic of the vertical acceleration normalized by the amplitude at the excitation frequency as a function of soil stiffness . . . 39
233 Compaction indicator as a function of soil stiffness 42
234 Normalized compaction indicator as a function of soil stiffness 42
235 Normalized compaction indicator as a function of soil stiffness; variation of operating frequency for roller 1 42
236 Normalized compaction indicator as a function of soil stiffness; variation of operating frequency for roller 4 43

237 Normalized compaction indicator as a function of soil stiffness; variation of the suspension stiffness of roller 1 44
238 Normalized compaction indicator as a function of soil stiffness; variation of the suspension damping of roller 1 44
239 Normalized compaction indicator as a function of soil stiffness; standard operating frequency; coefficient of friction $\mu = 0.30$ 44

31 Sketch of the Finite Element model (without mesh, without suspension) . . 47
32 Sketch of the drum and the suspension model 49
33 Distribution of void ratio e in the upper soil layer of 1 m thickness during compaction (a) without and (b) with oscillation 54
34 (a) Stress and (b) strain components at $x = 0$ due to an oscillatory (solid lines) and static roller pass (dashed lines), respectively; depth $y = -0.15$ m 56
35 (a) Stress and (b) strain components at $x = 0$ due to an oscillatory (solid lines) and static roller pass (dashed lines), respectively; depth $y = -0.25$ m 56
36 (a) Stress and (b) strain components at $x = 0$ due to an oscillatory (solid lines) and static roller pass (dashed lines), respectively; depth $y = -0.50$ m 56
37 Dynamic part of the horizontal stress $\sigma_{xx}^{(d)}$ at $x = 0$ and a depth of (a) 0.15 m and (b) 0.50 m 58
38 Dynamic part of the vertical stress $\sigma_{yy}^{(d)}$ at $x = 0$ and a depth of (a) 0.15 m and (b) 0.50 m 58
39 Dynamic part of the shear stress $\sigma_{xy}^{(d)}$ at $x = 0$ and a depth of (a) 0.15 m and (b) 0.50 m 58
310 Dynamic part of the vertical stress at a depth of 0.5 m; recorded in field tests on gravel [Pistrol, 2016] 59
311 Normalized void ratio e/e_0 at section $x = 0$ at soil depths of (a) 0.15 m and (b) 0.50 m during a static and oscillatory roller pass 60
312 Distribution of void ratio e in the upper soil layer of 1 m thickness after a (a) static and (b) oscillatory roller pass, and (c) corresponding normalized void ratio profile at $x = 0$ 61
313 Distribution of normalized void ratio e/e_0 in the upper soil layer of 1 m thickness after an oscillatory roller pass for an initial void ratio e_0 of (a) 0.90, (b) 0.80, (c) 0.70, and (d) 0.60 62
314 Normalized void ratio profile e/e_0 at $x = 0$ for four different initial void ratios e_0, based on Fig. 313 63
315 Normalized void ratio after one oscillatory roller pass; initial void ratio (a,b) $e_0 = 0.90$ and (c,d) $e_0 = 0.70$; coefficient of friction (a,c) $\mu = 0.50$ and (b,d) $\mu = 0.30$ 65
316 Normalized mean void ratio profile for two values of the coefficient of friction μ; initial void ratio (a) $e_0 = 0.90$ and (b) $e_0 = 0.70$, based on Fig. 315 . . . 65
317 Normalized void ratio after one oscillatory roller pass; initial void ratio (a,b) $e_0 = 0.90$ and (c,d) $e_0 = 0.70$; (a,c) $p_t = 5\,\mathrm{kN/m^2}$ and (b,d) $p_t = 10\,\mathrm{kN/m^2}$ 66
318 Normalized mean void ratio profile for two values of the apparent cohesion p_t; initial void ratio (a) $e_0 = 0.90$ and (b) $e_0 = 0.70$, based on Fig. 317 . . . 66
319 Normalized void ratio up to a soil depth of 1 m after one oscillatory roller pass with (a) 0.5 F_z, (b) 0.8 F_z, (c) 1.2 F_z, and (d) 1.5 F_z; $e_0 = 0.90$ 68

320 Normalized mean void ratio profile for three different axle loads P_0; variation of P_0 by (a) $\pm 20\,\%$ and (b) $\pm 50\,\%$, based on Fig. 319 68
321 Normalized void ratio after one oscillatory roller pass; roller speed (a) $v_0 = 0.55\,\mathrm{m/s}$, (b) $v_0 = 0.75\,\mathrm{m/s}$, (c) $v_0 = 1.11\,\mathrm{m/s}$, (d) $v_0 = 1.39\,\mathrm{m/s}$, and (e) $v_0 = 2.22\,\mathrm{m/s}$ 69
322 Normalized mean void ratio profile after one oscillatory roller pass at five different speeds v_0 on initially very loose soil, based on Fig. 321 69
323 Normalized void ratio after the (a,c) first and (b,d) second roller pass; (a,b) $p_t = 5\,\mathrm{kN/m^2}$ and (c,d) $p_t = 10\,\mathrm{kN/m^2}$ 71
324 Normalized mean void ratio profile after two subsequent oscillatory roller passes; (a) $p_t = 5\,\mathrm{kN/m^2}$ and (b) $p_t = 10\,\mathrm{kN/m^2}$, based on Fig. 323 71
325 Time history of the (a) horizontal and (b) vertical acceleration in the drum center M during an oscillatory roller pass on initially very loose soil ($e_0 = 0.90$) 73
326 Time history of the (a) horizontal and (b) vertical acceleration in the drum center M during an oscillatory roller pass on initially medium dense soil ($e_0 = 0.70$) 73
327 Time history of the (a) horizontal and (b) vertical acceleration in the drum center M during an oscillatory roller pass on initially dense soil ($e_0 = 0.60$) 73
328 Two periods of the horizontal drum center acceleration for an initial void ratio $e_0 = 0.70$ 74
329 Plot $\ddot{y}_M$ over $\ddot{x}_M$ for an initial void ratio e_0 of (a) 0.90, (b) 0.80, (c) 0.70 and (d) 0.60 for a time window of 1 s (grey lines) and two representative oscillating cycles (green lines) 75
330 Plot $\ddot{y}_M$ over $\ddot{x}_M$ for two oscillating cycles based on acceleration data recorded in field tests (described by Pistrol [2016]) 75
331 CCC indicator (i.e. area inside the plot $\ddot{y}_M$ over $\ddot{x}_M$) during one oscillatory roller pass at $v_0 = 1.11\,\mathrm{m/s}$ for an initially very loose ($e_0 = 0.90$) and an initially dense soil ($e_0 = 0.60$) 76
332 Normalized frequency spectrum of the (a) horizontal and (b) vertical acceleration in the drum center for one second of an oscillatory roller pass; initially very loose soil ($e_0 = 0.90$) 77
333 Normalized frequency spectrum of the (a) horizontal and (b) vertical acceleration in the drum center for one second of an oscillatory roller pass; initially medium dense soil ($e_0 = 0.70$) 77
334 Normalized frequency spectrum of the (a) horizontal and (b) vertical acceleration in the drum center for one second of an oscillatory roller pass; initially dense soil ($e_0 = 0.60$) 77
335 Normalized frequency spectrum of recorded horizontal (a) and vertical (b) accelerations in the drum center during field tests; roller pass no. 2 on gravel (based on Pistrol [2016]) 78
336 Normalized frequency spectrum of recorded horizontal (a) and vertical (b) accelerations in the drum center during field tests; roller pass no. 11 on gravel (based on Pistrol [2016]) 78
337 Time history of the (a,b) horizontal and (c,d) vertical acceleration in the drum center for two selected coefficients of friction; initial void ratio (a,c) $e_0 = 0.90$ and (b,d) $e_0 = 0.70$ 79

338 Frequency spectrum of the (a,b) horizontal and (c,d) vertical acceleration in the drum center for two selected coefficients of friction; initial void ratio (a,c) $e_0 = 0.90$ and (b,d) $e_0 = 0.70$ 80

339 Normalized frequency spectrum of the (a) horizontal and (b) vertical acceleration in the drum center; computed and recorded (based on Pistrol [2016]) response 82

340 Time history and frequency spectrum of the (a,b) horizontal and (c,d) vertical acceleration in the drum center for three roller speeds; initially very loose soil 84

341 Time history and frequency spectrum of the (a,b) horizontal and (c,d) vertical acceleration in the drum center for two subsequent roller passes on initially very loose soil; $p_t = 10\,\mathrm{kN/m^2}$; $v_0 = 2.22\,\mathrm{m/s}$ 85

342 Plot $\ddot{y}_M$ over $\ddot{x}_M$ for a time window of 1 s (grey lines) and two representative oscillating cycles (green and red lines); $\mu = 0.30$; initial void ratio e_0 of (a) 0.90 and (b) 0.70 86

343 Plot $\ddot{y}_M$ over $\ddot{x}_M$ based on drum center accelerations recorded in field tests (described in [Pistrol, 2016]); two oscillation cycles 86

344 Plot $\ddot{y}_M$ over $\ddot{x}_M$ for roller speed v_0 of (a) 0.55 m/s, (b) 0.75 m/s, (c) 1.11 m/s and (d) 2.22 m/s for a time window of 1 s (grey lines) and two representative oscillating cycles (green lines); initially very loose soil ($e_0 = 0.90$); $p_t = 5\,\mathrm{kN/m^2}$ 87

346 Compaction indicator during the first roller pass; variation of v_0 89

347 Compaction indicator during the first roller pass; variation of v_0 89

348 Compaction indicator during two subsequent roller passes on initially very loose soil; $p_t = 10\,\mathrm{kN/m^2}$; $v_0 = 2.22\,\mathrm{m/s}$ 89

A1 SDOF-model of the front frame supported by the drum suspension 97

A2 Absolute displacement transmissibility T_p 98

B1 Geometry of the contact area between drum and soil [Pistrol, 2016] 99

B2 Translational cone for (a) vertical and (b) horizontal motion, based on Wolf [1994] 100

C1 Lumped parameter model of the interaction system oscillation roller-soil with a semi-circular settlement trough 106

C2 SDOF lumped parameter model of the interaction system oscillation roller-subsoil; pure rolling motion; without suspension; fixed semi-circular settlement trough 108

E1 (a) Time history of $x(t)$ and $z(t)$ for a time window of $t = T_x$, and (b) plot $z(t)$ over $x(t)$; $\theta_z = -\pi/2$ 122

E2 (a) Time history of $x(t)$ and $z(t)$ for a time window of $t = T_x$, and (b) plot $z(t)$ over $x(t)$; $\theta_z = -\pi/4$ 122

E3 (a) Time history of $x(t)$ and $z(t)$ for a time window of $t = T_x$, and (b) plot $z(t)$ over $x(t)$; $\theta_z = 0$ 122

E4 (a) Time history of $x(t)$ and $z(t)$ for a time window of $t = T_x$, and (b) plot $z(t)$ over $x(t)$; $\theta_z = \pi/4$ 123

E5 (a) Time history of $x(t)$ and $z(t)$ for a time window of $t = T_x$, and (b) plot $z(t)$ over $x(t)$; $\theta_z = \pi/2$ 123
E6 Ratio $A^{(\mathrm{Liss})}/(4x_0z_0)$ in dependence of the phase lag θ_z 123

F1 Sketch of the Finite Element model (without mesh) 125
F2 Frequency spectrum of the (a) horizontal and (b) vertical acceleration in the drum center; computed vs. recorded accelerations 126

G1 Pressure dependence of void ratios, based on ([Bauer, 1996], [Gudehus, 1996]) 129

H1 Flow chart for *ABAQUS* and UMAT intergration, based on Ribeiro et al [2013] 134

I1 Sketch of FE “model A” (without mesh, without suspension) 138
I2 Sketch of FE “model B” (without mesh, without suspension) 138
I3 Distribution of void ratio e in the upper soil layer of 0.25 m thickness after the (a) first, (b) second, (c) third and (d) fourth oscillatory roller pass; model A$^{(25)}$ / mesh I, $e_0 = 0.85$, $\mu = 0.50$, $p_t = 5\,\mathrm{kN/m^2}$, $c_x = c_y = c_{x45} = c_{y45} = 1000\,\mathrm{Ns/m}$ 139
I4 Normalized void ratio profile e/e_0 at $x = 0$, corresponds to Fig. I3 140
I5 Time history of the (a) horizontal and (b) vertical acceleration in the drum center M during four subsequent oscillatory roller passes; model A$^{(25)}$ / mesh I, $e_0 = 0.85$, $\mu = 0.50$, $p_t = 5\,\mathrm{kN/m^2}$, $c_x = c_y = c_{x45} = c_{y45} = 1000\,\mathrm{Ns/m}$ 140
I6 Normalized frequency spectrum of the (a) horizontal and (b) vertical acceleration in the drum center M for one second of the first, second, third, and fourth oscillatory roller pass, based on Fig. I5 140
I7 Plot $\ddot{y}_M$ over $\ddot{x}_M$ for a time window of 1 s (grey lines) and two representative oscillating cycles (green lines), based on Fig. I5; (a) first and (b) second roller pass 141
I8 Plot $\ddot{y}_M$ over $\ddot{x}_M$ for a time window of 1 s (grey lines) and two representative oscillating cycles (green lines), based on Fig. I5; (a) third and (b) fourth roller pass 141
I9 Distribution of void ratio e in the upper soil layer of 0.5 m thickness after an oscillatory roller pass; model A$^{(50)}$ / mesh I, $e_0 = 0.85$, $\mu = 0.50$, $p_t = 10\,\mathrm{kN/m^2}$ 141
I10 Mean normalized void ratio profile e/e_0 in the soil region $-0.5\,\mathrm{m} \leq x \leq 0.5\,\mathrm{m}$, corresponds to Fig. I9 142
I11 Distribution of void ratio e in the upper soil layer of 0.5 m thickness after an oscillatory roller pass; model A$^{(50)}$ / mesh I / SD, $e_0 = 0.75$, $\mu = 0.50$, $p_t = 5\,\mathrm{kN/m^2}$, $c_x = c_y = c_{x45} = c_{y45} = 1000\,\mathrm{Ns/m}$ 142
I12 Mean normalized void ratio profile e/e_0 in the soil region $-0.5\,\mathrm{m} \leq x \leq 0.5\,\mathrm{m}$, corresponds to Fig. I11 142
I13 Distribution of void ratio e in the upper soil layer of 0.75 m thickness after an oscillatory roller pass; model A$^{(75)}$ / mesh I / SD, $e_0 = 0.85$, $\mu = 0.50$, $p_t = 5\,\mathrm{kN/m^2}$, $c_x = c_y = 2500\,\mathrm{Ns/m}$ 143
I14 Mean normalized void ratio profile e/e_0 in the soil region $-0.5\,\mathrm{m} \leq x \leq 0.5\,\mathrm{m}$, corresponds to Fig. I13 143

I15 Distribution of void ratio e in the upper soil layer of 0.75 m thickness after an oscillatory roller pass; model $\mathrm{A}^{(75)}$ / mesh I / SD, $e_0 = 0.85$, $\mu = 0.50$, $p_t = 5\,\mathrm{kN/m^2}$, $c_x = c_y = 3500\,\mathrm{Ns/m}$ . . . 143

I16 Mean normalized void ratio profile e/e_0 in the soil region $-0.5\,\mathrm{m} \leq x \leq 0.5\,\mathrm{m}$, corresponds to Fig. I15 . . . 144

I17 Distribution of void ratio e in the upper soil layer of 1 m thickness after an oscillatory roller pass; model $\mathrm{A}^{(100)}$ / mesh I / SD, $e_0 = 0.85$, $\mu = 0.50$, $p_t = 10\,\mathrm{kN/m^2}$, $c_x = c_y = 10{,}000\,\mathrm{Ns/m}$ . . . 144

I18 Mean normalized void ratio profile e/e_0 in the soil region $-1\,\mathrm{m} \leq x \leq 0$, corresponds to Fig. I17 . . . 144

I19 Distribution of void ratio e in the upper soil layer of 1 m thickness after an oscillatory roller pass; model $\mathrm{A}^{(100)}$ / mesh II / SD, $e_0 = 0.85$, $\mu = 0.50$, $p_t = 10\,\mathrm{kN/m^2}$, $c_x = c_y = 500\,\mathrm{Ns/m}$ . . . 145

I20 Mean normalized void ratio profile e/e_0 in the soil region $-0.5\,\mathrm{m} \leq x \leq 0.5$, corresponds to Fig. I19 . . . 145

I21 Dynamic part of the (a) vertical and (b) shear stress component at a depth of 0.49 m; model $\mathrm{A}^{(100)}$ / mesh II / SD, $e_0 = 0.85$, $\mu = 0.50$, $p_t = 10\,\mathrm{kN/m^2}$, $c_x = c_y = 500\,\mathrm{Ns/m}$ . . . 145

I22 Distribution of void ratio e in the upper soil layer of 1 m thickness after an oscillatory roller pass; model $\mathrm{A}^{(100)}$ / mesh II / SD, $e_0 = 0.70$, $\mu = 0.50$, $p_t = 10\,\mathrm{kN/m^2}$, $c_x = c_y = 500\,\mathrm{Ns/m}$ . . . 146

I23 Mean normalized void ratio profile e/e_0 in the soil region $-1.3\,\mathrm{m} \leq x \leq -0.3$, corresponds to Fig. I22 . . . 146

I24 Time history of the (a) horizontal and (b) vertical acceleration in the drum center M during an oscillatory roller pass on initially loose soil; model $\mathrm{A}^{(100)}$ / mesh II / SD, $e_0 = 0.85$, $\mu = 0.50$, $p_t = 10\,\mathrm{kN/m^2}$, $c_x = c_y = 500\,\mathrm{Ns/m}$ . . . 146

I25 Normalized frequency spectrum of the (a) horizontal and (b) vertical acceleration in the drum center M for one second of an oscillatory roller pass, based on Fig. I24 . . . 147

I26 Time history of the (a) horizontal and (b) vertical acceleration in the drum center M during an oscillatory roller pass on initially dense soil; model $\mathrm{A}^{(100)}$ / mesh II / SD, $e_0 = 0.70$, $\mu = 0.50$, $p_t = 10\,\mathrm{kN/m^2}$, $c_x = c_y = 500\,\mathrm{Ns/m}$ . . . 147

I27 Normalized frequency spectrum of the (a) horizontal and (b) vertical acceleration in the drum center M for one second of an oscillatory roller pass, based on Fig. I26 . . . 147

I28 Plot $\ddot{y}_M$ over $\ddot{x}_M$ for a time window of 1 s (grey lines) and two representative oscillating cycles (green and red lines) based on (a) Fig. I24 and (b) Fig. I26 148

I29 Distribution of (a) void ratio e and (b) normalized void ratio e/e_0 in the upper soil layer of 1 m thickness during an oscillatory roller pass; $t = 1.286\,\mathrm{s}$ (model B / mesh II, $e_0 = 0.90$, $\mu = 0.50$, $p_t = 5(1)\ \mathrm{kN/m^2}$) . . . 148

I30 Distribution of void ratio e in the upper soil layer of 1 m thickness during compaction (a) without and (b) with oscillation; model B / mesh III, $e_0 = 0.90$, $\mu = 0.50$, $p_t = 5(1)\ \mathrm{kN/m^2}$ . . . 149

I31 Distribution of the normalized void ratio e/e_0 in the upper soil layer of 1 m thickness after a static roller pass; model B / mesh III, $e_0 = 0.90$, $\mu = 0.50$, $p_t = 5(1)$ kN/m^2 . . . 149

I32 (a) Stress and (b) strain components due to an oscillatory (solid lines) and a static roller pass (dashed lines), respectively; depth $y = -0.24$ m; model B / mesh II, $e_0 = 0.90$, $\mu = 0.50$, $p_t = 5(1)$ kN/m^2 . . . 150

I33 Dynamic part of the (a) vertical and (b) shear stress component at a depth of 0.51 m; model B / mesh III, $e_0 = 0.90$, $\mu = 0.50$, $p_t = 5(1)$ kN/m^2 . . . 150

I34 Normalized void ratio e/e_0 vs. horizontal distance from a selected observation point ("E") at selected soil depths during an oscillatory roller pass; model B / mesh III, $e_0 = 0.90$, $\mu = 0.50$, $p_t = 5(1)$ kN/m^2 . . . 150

I35 Normalized void ratio profile e/e_0 for two different initial void ratios e_0; $\mu = 0.50$; model B / mesh II, corresponds to Fig. I29 . . . 151

I36 Normalized void ratio profile e/e_0 for two different initial void ratios e_0; $\mu = 0.50$; model B / mesh III, corresponds to Fig. I30 . . . 151

I37 Time history of the (a) horizontal and (b) vertical acceleration in the drum center M; model B / mesh II, $e_0 = 0.90$, $\mu = 0.50$, $p_t = 5(1)$ kN/m^2 . . . 151

I38 Time history of the (a) horizontal and (b) vertical acceleration in the drum center M; model B / mesh II, $e_0 = 0.80$, $\mu = 0.50$, $p_t = 5(1)$ kN/m^2 . . . 152

I39 Plot $\ddot{y}_M$ over $\ddot{x}_M$ for an initial void ratio e_0 of (a) 0.90 and (b) 0.80 for a time window of 1 s (grey lines) and two representative oscillating cycles (green lines), based on Figs I37 and I38 . . . 152

I40 Normalized frequency spectrum of the (a) horizontal and (b) vertical acceleration in the drum center M for one second of an oscillatory roller pass; initially very loose soil ($e_0 = 0.90$); corresponds to Fig. I37 . . . 152

I41 Normalized frequency spectrum of the (a) horizontal and (b) vertical acceleration in the drum center M for one second of an oscillatory roller pass; initially loose soil ($e_0 = 0.80$); corresponds to Fig. I38 . . . 153

I42 Distribution of void ratio e in the upper soil layer of 1 m thickness after an oscillatory roller pass; model B / mesh II / SD, $e_0 = 0.90$, $\mu = 0.50$, $p_t = 5$ kN/m^2, $c_x = c_y = 750$ Ns/m . . . 153

I43 Mean normalized void ratio profile e/e_0 in the soil region $-0.5\,\mathrm{m} \leq x \leq 0.5\,\mathrm{m}$, corresponds to Fig. I42 . . . 153

I44 Time history of the (a) horizontal and (b) vertical acceleration in the drum center M during an oscillatory roller pass on initially very loose soil; model B / mesh II / SD, $e_0 = 0.90$, $\mu = 0.50$, $p_t = 5$ kN/m^2, $c_x = c_y = 750$ Ns/m . . . 154

I45 Plot $\ddot{y}_M$ over $\ddot{x}_M$ for a time window of 1 s (grey lines) and two representative oscillating cycles (green lines), based on Fig. I44; (a) without and (b) with node . . . 154

I46 Normalized frequency spectrum of the (a) horizontal and (b) vertical acceleration in the drum center M for one second of an oscillatory roller pass, corresponds to Fig. I44 . . . 154

I47 Distribution of the normalized void ratio e/e_0 in the upper soil layer of 1 m thickness after an oscillatory roller pass on a soil with an initial void ratio e_0 of (a) 0.85, (b) 0.75, and (c) 0.70; model B / mesh II / PF, $\mu = 0.30$, $p_t = 5(1)$ kN/m^2 . . . 155

I48 Mean normalized void ratio profile e/e_0 in the soil region $-1\,\mathrm{m} \leq x \leq 0$, corresponds to Fig. I47 155
I49 Time history of the (a) horizontal and (b) vertical acceleration in the drum center M during an oscillatory roller pass; model B / mesh II / PF, $e_0 = 0.85$, $\mu = 0.30$, $p_t = 5(1)$ kN/m^2; time window: $t = 5{-}6\,\mathrm{s}$ 156
I50 Time history of the (a) horizontal and (b) vertical acceleration in the drum center M during an oscillatory roller pass; model B / mesh II / PF, $e_0 = 0.85$, $\mu = 0.30$, $p_t = 5(1)$ kN/m^2; time window: $t = 6{-}7\,\mathrm{s}$ 156
I51 Normalized frequency spectrum of the (a) horizontal and (b) vertical acceleration in the drum center M, corresponds to Fig. I49 156
I52 Normalized frequency spectrum of the (a) horizontal and (b) vertical acceleration in the drum center M, corresponds to Fig. I50 157
I53 Time history of the (a) horizontal and (b) vertical acceleration in the drum center M during an oscillatory roller pass; model B / mesh II / PF, $e_0 = 0.75$, $\mu = 0.30$, $p_t = 5(1)$ kN/m^2; time window: $t = 5{-}6\,\mathrm{s}$ 157
I54 Time history of the (a) horizontal and (b) vertical acceleration in the drum center M during an oscillatory roller pass; model B / mesh II / PF, $e_0 = 0.75$, $\mu = 0.30$, $p_t = 5(1)$ kN/m^2; time window: $t = 6{-}7\,\mathrm{s}$ 157
I55 Normalized frequency spectrum of the (a) horizontal and (b) vertical acceleration in the drum center M, corresponds to Fig. I53 158
I56 Normalized frequency spectrum of the (a) horizontal and (b) vertical acceleration in the drum center M, corresponds to Fig. I54 158
I57 Time history of the (a) horizontal and (b) vertical acceleration in the drum center M during an oscillatory roller pass; model B / mesh II / PF, $e_0 = 0.70$, $\mu = 0.30$, $p_t = 5(1)$ kN/m^2; time window: $t = 5{-}6\,\mathrm{s}$ 158
I58 Time history of the (a) horizontal and (b) vertical acceleration in the drum center M during an oscillatory roller pass; model B / mesh II / PF, $e_0 = 0.70$, $\mu = 0.30$, $p_t = 5(1)$ kN/m^2; time window: $t = 6{-}7\,\mathrm{s}$ 159
I59 Normalized frequency spectrum of the (a) horizontal and (b) vertical acceleration in the drum center M, corresponds to Fig. I57 159
I60 Normalized frequency spectrum of the (a) horizontal and (b) vertical acceleration in the drum center M, corresponds to Fig. I58 159
I61 Plot $\ddot{y}_M$ over $\ddot{x}_M$ for an initial void ratio e_0 of 0.85 for a time window of 1 s (grey lines) and two representative oscillating cycles (green lines), based on (a) Fig. I49 and (b) Fig. I50 160
I62 Plot $\ddot{y}_M$ over $\ddot{x}_M$ for an initial void ratio e_0 of 0.75 for a time window of 1 s (grey lines) and two representative oscillating cycles (green lines), based on (a) Fig. I53 and (b) Fig. I54 160
I63 Plot $\ddot{y}_M$ over $\ddot{x}_M$ for an initial void ratio e_0 of 0.70 for a time window of 1 s (grey lines) and two representative oscillating cycles (green lines), based on (a) Fig. I57 and (b) Fig. I58 160

List of Tables

21 Roller parameters [Pistrol, 2016] and suspension properties ([HAMM AG, 2017], [HAMM AG, 2018b]) 10

31 HD$^+$ 90 VO tandem roller parameters (based on Pistrol [2016]) 45
32 Material parameters of “Hochstetten Sand” for basic hypoplasticity [Herle, 1997] 51
33 Additional parameters for hypoplasticity with intergranular strain [Niemunis and Herle, 1997] 51

B1 Soil parameters (shear modulus G, density ρ, *Poisson*’s ratio ν), and corresponding half contact length a_0 between drum of the four considered oscillation rollers and soil 102
B2 Shear modulus of the soil, and corresponding stiffness and damping parameters of the lumped parameter model 103

Bibliography

Adam D (1996) Continuous Compaction Control (CCC) with vibrating rollers (in German) (Flächendeckende Dynamische Verdichtungskontrolle (FDVK) mit Vibrationswalzen). PhD thesis, TU Wien

Adam D, Pistrol J (2016) Dynamic roller compaction for earthworks and roller-integrated Continuous Compaction Control: State of the art overview and recent developments. In: Manassero M, Dominijanni A, Foti S, Musso G (eds) Conf. di Geotecnica di Torino, XXIV Ciclio, Turin, pp 1–41

Anderegg R, Kaufmann K (2004) Intelligent compaction with vibratory rollers: Feedback control systems in automatic compaction and compaction control. Transportation Research Record 1868(1):124–134

Aubram D (2017) Notes on rate equations in nonlinear continuum mechanics. arXiv:170910048 [physicsclass-ph] pp 1–47

Bajaj N (1988) The Physics of Waves and Oscillations. Tata McGraw-Hill

Bauer E (1996) Calibration of a comprehensive hypoplastic model for granular materials. Soils and Foundations 36(1):13–26

Beainy F, Commuri S, Zaman M (2013) Dynamical response of vibratory rollers during the compaction of asphalt pavements. Journal of Engineering Mechanics 140(7):04014039

Brown SF (1996) Soil mechanics in pavement engineering. Géotechnique 46(3):383–426

Cao YW, Xiang L, Ma LY, Li ZJ (2013) Application analysis of vibrating wheel-soil model based on ABAQUS. In: Advanced Research on Intelligent Systems and Mechanical Engineering, Trans Tech Publications, Advanced Materials Research, vol 644, pp 366–369

Capraru C, Pistrol J, Villwock S, Völkel W, Kopf F, Adam D (2014) Numerical simulation of soil compaction with oscillatory rollers. In: Brandl H, Adam D (eds) Proc. XV Danube - European Conference on Geotechnical Engineering (DECGE 2014), Vienna, Austria, pp 283–290

Chrisopoulos S, Osinov VA, Triantafyllidis T (2016) Dynamic Problem for the Deformation of Saturated Soil in the Vicinity of a Vibrating Pile Toe, Springer International Publishing, Cham, pp 53–67. Lecture Notes in Applied and Computational Mechanics 80

Clough R, Penzien J (1993) Dynamics of structures, 2nd edn. McGraw-Hill, New York

Erdmann P, Adam D (2014) Numerical simulation of dynamic soil compaction with vibratory compaction equipment. In: Brandl H, Adam D (eds) Proc. XV Danube - European Conference on Geotechnical Engineering (DECGE 2014), Vienna, Austria, pp 243–248

Facas NW, van Susante PJ, Mooney MA (2010) Influence of rocking motion on vibratory roller-based measurement of soil stiffness. Journal of Engineering Mechanics 136(7):898–905

Fehlberg E (1969) Low-order classical Runge-Kutta formulas with stepsize control and their application to some heat transfer problems. NASA Technical Report 315, 1969

Fellin W, Ostermann A (2002) Consistent tangent operators for constitutive rate equations. International Journal for Numerical and Analytical Methods in Geomechanics 26(12):1213–1233

Fellin W, Mittendorfer M, Ostermann A (2009) Adaptive integration of constitutive rate equations. Computers and Geotechnics 36(5):698–708

Ferréol R (2017a) Besace. URL `https://www.mathcurve.com/courbes2d.gb/besace/besace.shtml`, last accessed on 2019-09-30

Ferréol R (2017b) Lissajous curve or Bowditch curve. URL `https://www.mathcurve.com/courbes2d.gb/lissajous/lissajous.shtml`, last accessed on 2019-09-30

Forssblad L (1980) Compaction meter on vibrating rollers for improved compaction control. In: Proceedings of the international conference on compaction, Paris, France, Ecole Nationale des Ponts et Chaussées and Laboratoire Central des Ponts et Chaussées, vol 2, pp 541–546

Gazetas G (1983) Analysis of machine foundation vibrations: State of the art. International Journal of Soil Dynamics and Earthquake Engineering 2(1):2–42

Gazetas G (1991) Formulas and charts for impedances of surface and embedded foundations. Journal of Geotechnical Engineering 117(9):1363–1381

Geodynamik AB (1982) Oscillatory roller, Stockholm

Geodynamik AB (2018) The company. Innovations. URL `http://www.geodynamik.com`, last accessed on 2018-06-07

Grabe J (1993) Continuous inverse calculation of soil stiffness from the dynamic behavior of a driving vibratory roller (in German) (Fortlaufend inverse Berechnung der Bodensteifigkeit aus dem Schwingungsverhalten einer fahrenden Vibrationswalze). Archive of Applied Mechanics 63(7):472–478

Gudehus G (1981) Soil mechanics (in German) (Bodenmechanik). Enke, Stuttgart

Gudehus G (1996) A comprehensive constitutive equation for granular materials. Soils and Foundations 36(1):1–12

Gudehus G, Kolymbas D (1979) A constitutive law of the rate-type for soils. In: Wittke W (ed) Proc. 3rd Int. Conf. on Numerical Methods in Geomechanics, Aachen, Germany, A. A. Balkema, pp 319–329

Gudehus G, Amorosi A, Gens A, Herle I, Kolymbas D, Mašín D, Muir Wood D, Niemunis A, Nova R, Pastor M, Tamagnini C, Viggiani G (2008) The soilmodels.info project. International Journal for Numerical and Analytical Methods in Geomechanics 32(12):1571–1572

HAMM AG (2011) Data sheet HD+ 90 VO

HAMM AG (2017) Additional data HD+ 90i 130mm

HAMM AG (2018a) 35 years of oscillation: Tried and tested solutions for asphalt and earthwork. URL `https://www.hamm.eu/en/news-media/news-jobreports/2017/03-35-years-oscillation.php`, last accessed on 2018-06-07

HAMM AG (2018b) Additional data HD+ 90i 130mm (Rev.01)

Heiniger R (2018) Contributions to the numerical simulation of the compaction of non-cohesive soils with oscillation rollers (in German) (Beiträge zur numerischen Simulation der Verdichtung von nichtbindigen Böden mit Oszillationswalzen). Master's thesis, University of Innsbruck

Herle I (1997) Hypoplasticity and particle size analysis of simple soil skeletons (in German) (Hypoplastizität und Granulometrie einfacher Korngerüste). PhD thesis, Institute of Soil Mechanics and Rock Mechanics, Universität Fridericiana, Karlsruhe

Hull T, Enright W, Fellen B, Sedgwick A (1972) Comparing numerical methods for ordinary differential equations. SIAM Journal on Numerical Analysis 9(4):603–637

Imran SA, Commuri S, Barman M, Zaman M, Beainy F (2017) Modeling the Dynamics of Asphalt-Roller Interaction during Compaction. Journal of Construction Engineering and Management 143(7):04017015

Kappel M (2012) Applied road construction. Road pavers in use (in German) (Angewandter Straßenbau. Straßenfertiger im Einsatz), 1st edn. Vieweg+Teubner Verlag

Kearney EJ (2006) Oscillatory compaction of hot-mix asphalt. In: Factors affecting compaction of asphalt pavements, Transportation Research Board, no. E-C105 in Transportation Research Circular, pp 49–53

Kelm M (2004) Numerical simulation of the compaction of granular soils by vibratory rollers (in German) (Nummerische Simulation der Verdichtung rolliger Böden mittels Vibrationswalzen), 6th edn. Publication of the Institute of Geotechnical and Construction Engineering, Technische Universität Hamburg

Kenneally B, Musimbi OM, Wang J, Mooney MA (2015) Finite element analysis of vibratory roller response on layered soil systems. Computers and Geotechnics 67:73–82

Klotter K (1981) Vibration theory. Volume 2: Multi-degrees-of-freedom oscillator (in German: Technische Schwingungslehre, 2. Band: Schwinger von mehreren Freiheitsgraden). Springer

Kolymbas D (1978) A nonlinear viscoplastic constitutive law for soils (in German) (Ein nichtlineares viskoplastisches Stoffgesetz für Böden). PhD thesis, Institute of Soil Mechanics and Rock Mechanics, Universität Fridericiana, Karlsruhe

Kolymbas D (1991) An outline of hypoplasticity. Archive of Applied Mechanics 61(3):143–151

Kopf F (1999) Continuous Compaction Control (CCC) during compaction of soil by means of dynamic rollers with different kinds of excitation (in German) (Flächendeckende Dynamische Verdichtungskontrolle (FDVK) bei der Verdichtung von Böden durch dynamische Walzen mit unterschiedlichen Anregungsarten). PhD thesis, TU Wien

Kröber W, Floss R, Wallrath W (2001) Dynamic soil stiffness as quality criterion for soil compaction. In: Correia A, Brandl H (eds) Geotechnics for Roads, Rail Tracks, and Earth Structures, Taylor and Francis, pp 189–199

Lawrence JD (1972) A catalog of special plane curves. Dover Publications

Leine R, van Campen D, de Kraker A, van den Steen L (1998) Stick-slip vibrations induced by alternate friction models. Nonlinear Dynamics 16(1):41–54

Li J, Lu L, Zhou Z, Xu L (2018) Dynamic modeling simulation and analysis of amplitude frequency characteristics on tandem-heavy oscillating rollers. IOP Conference Series: Materials Science and Engineering 382:032040

Lysmer J, Richart FE (1966) Dynamic response of footings to vertical loading. Journal of the Soil Mechanics and Foundations Division 92(1):65–91

MacTutor History of Mathematics archive (2019) Lissajous Curves. URL `http://www-groups.dcs.st-and.ac.uk/~history/Curves/Lissajous.html`, last accessed on 2019-09-30

Marguerre K (1968) Mechanics. 3rd Part: Kinetics (in German) (Technische Mechanik. Dritter Teil: Kinetik). Heidelberger Taschenbücher, Springer

Mašín D (2019a) Clay and sand hypoplasticity umat and plaxis implementations, including umat-plaxis interface. URL `https://soilmodels.com`, last accessed on 2019-05-30

Mašín D (2019b) Modelling of Soil Behaviour with Hypoplasticity. Springer Series in Geomechanics and Geoengineering, Springer International Publishing

Mathworks (2018) Matlab (version: R2018b)

Mooney MA, Adam D (2007) Vibratory roller integrated measurement of earthwork compaction: An overview. In: Proc. 7th Int. Symp. Field Measurements in Geomechanics, ASCE, Boston, pp 1–12

Mooney MA, Rinehart RV (2007) Field monitoring of roller vibration during compaction of subgrade soil. Journal of Geotechnical and Geoenvironmental Engineering 133(3):257–265

Mooney MA, Rinehart RV (2009) In situ soil response to vibratory loading and its relationship to roller-measured soil stiffness. Journal of Geotechnical and Geoenvironmental Engineering 135(8):1022–1031

National Academies of Sciences, Engineering, and Medicine (2010) Intelligent Soil Compaction Systems. The National Academies Press, Washington, DC, DOI 10.17226/22922

Niemunis A, Herle I (1997) Hypoplastic model for cohesionless soils with elastic strain range. Mechanics of Cohesive-frictional Materials 2(4):279–299

Nykamp D (2018) Using Green's theorem to find area. URL `https://mathinsight.org/greens_theorem_find_area`, last accessed on 2018-06-11

Pais A, Kausel E (1988) Approximate formulas for dynamic stiffnesses of rigid foundations. Soil Dynamics and Earthquake Engineering 7(4):213–227

Pietzsch D, Poppy W (1992) Simulation of soil compaction with vibratory rollers. Journal of Terramechanics 29(6):585–597

Pistrol J (2016) Compaction with oscillating rollers. Motion behaviour, roller integrated compaction control and assessment of wear (in German) (Verdichtung mit Oszillationswalzen - Bewegungsverhalten, walzenintegrierte Verdichtungskontrolle und Verschleißbeurteilung). PhD thesis, TU Wien

Pistrol J, Adam D (2018) Fundamentals of roller integrated compaction control for oscillatory rollers and comparison with conventional testing methods. Transportation Geotechnics 17:75–84

Popov VL (2017) Contact Mechanics and Friction: Physical Principles and Applications, 2nd edn. Springer

Ribeiro ML, Vandepitte D, Tita V (2013) Damage model and progressive failure analyses for filament wound composite laminates. Applied Composite Materials 20(5):975–992

Sandström Å (1993) Oscillatory compaction. In: Proceedings of XII IRF World Congress, Madrid, pp 957–961

Smith M (2015) ABAQUS 2016 Documentation Collection. Simulia

Steiner W (2014) The use of Castigliano's theorem in Coulomb friction problems. Acta Mechanica 225(9):2471–2483 van Susante P, Mooney M (2008) Capturing nonlinear vibratory roller compactor behavior through lumped parameter modeling. Journal of Engineering Mechanics 134(8):684–693

Thurner H, Sandström Å (1980) A new device for instant compaction control. In: Proceedings of the international conference on compaction, Paris, France, Ecole Nationale des Ponts et Chaussées and Laboratoire Central des Ponts et Chaussées, vol 2, pp 611–614

Thurner H, Sandström Å (2000) Continuous Compaction Control, CCC. In: European Workshop Compaction of Soils and Granular Materials, Paris, May 19th, pp 237–245

Weisstein EW (2018) Logarithmic spiral. URL `http://mathworld.wolfram.com/LogarithmicSpiral.html`, last accessed on 2018-06-11

White DJ, Vennapusa PK (2010) A review of roller-integrated compaction monitoring technologies for earthworks. Final report er10-04, Earthworks Engineering Research Center (EERC), Iowa State University

Wikipedia (2019) Lissajous curve. URL `https://en.wikipedia.org/wiki/Lissajous_curve`, last accessed on 2019-09-30

Williams HE (2000) A note on the use of the instant center as a reference point for angular momentum theorems. International Journal of Mechanical Engineering Education 28(2):185–186

Wolf J (1994) Foundation Vibration Analysis Using Simple Physical Models. Prentice-Hall, Inc.

von Wolffersdorff PA (1996) A hypoplastic relation for granular materials with a pre-defined limit state surface. Mechanics of Cohesive-frictional Materials 1(3):251–271

Xu G, Wu W, Qi J (2016) An extended hypoplastic constitutive model for frozen sand. Soils and Foundations 56(4):704–711

Yoo TS, T Selig E (1977) Fundamentals of vibratory roller behavior. In: Proc. 9th Int. Conf. Soil Mech., Tokyo, pp 375–380

Yoo TS, T Selig E (1979) Dynamics of vibratory-roller compaction. Journal of the Geotechnical Engineering Division 105(10):1211–1231

Ziegler F (1995) Mechanics of Solids and Fluids, 2nd edn. Springer Science+Business Media Wien New York

Zuwang S, Shirley W, Que W (1997) The dynamic process of oscillatory compaction and its computer simulation. In: Asia-Pacific Vibration Conference, The Korean Society of Mechanical Engineers, pp 532–537

Verpflichtungs- und Einverständniserklärung

Ich erkläre, dass ich meine Dissertation selbständig verfasst und alle in ihr verwendeten Unterlagen, Hilfsmittel und die zugrunde gelegte Literatur genannt habe.

Ich nehme zur Kenntnis, dass auch bei auszugsweiser Veröffentlichung meiner Dissertation die Universität, das/die Institut/e und der/die Arbeitsbereich/e, an dem/denen die Dissertation ausgearbeitet wurde, und die Betreuerin/nen bzw. der/die Betreuer zu nennen sind.

Ich nehme zur Kenntnis, dass meine Dissertation zur internen Dokumentation und Archivierung sowie zur Abgleichung mit der Plagiatssoftware elektronisch im Dateiformat pdf ohne Kennwortschutz bei der/dem Betreuer/in einzureichen ist, wobei auf die elektronisch archivierte Dissertation nur die/der Betreuerin/Betreuer der Dissertation und das studienrechtliche Organ Zugriff haben.

Innsbruck am ....
Dipl.-Ing. Ivan Paulmichl